İSTANBUL TECHNICAL UNIVERSITY ★ INSTITUTE OF SCIENCE AND TECHNOLOGY

MEASUREMENT, MODELLING AND MODAL ANALYSES OF HELICOPTER STRUCTURES

M.Sc. Thesis by

Hasan KÖRÜK, B.Sc.

Department: Mechanical Engineering

Programme: Machine Dynamics, Vibration & Acoustics

JUNE 2008

İSTANBUL TECHNICAL UNIVERSITY ★ INSTITUTE OF SCIENCE AND TECHNOLOGY

MEASUREMENT, MODELLING AND MODAL ANALYSES OF HELICOPTER STRUCTURES

M.Sc. Thesis by
Hasan KÖRÜK, B.Sc.
(503051408)

Date of submission : 5 May 2008

Date of defence examination : 13 June 2008

Supervisor (Chairman) : Prof. Dr. Kenan Y. ŞANLITÜRK

Members of the Examining Committee Prof. Dr. H. Temel BELEK

Prof. Dr. A. Rüstem ASLAN

JUNE 2008

İSTANBUL TEKNİK ÜNİVERSİTESİ ★ FEN BİLİMLERİ ENSTİTÜSÜ

HELİKOPTER YAPILARININ ÖLÇÜM, MODELLEME VE MODAL ANALİZLERİ

YÜKSEK LİSANS TEZİ
Makine Müh. Hasan KÖRÜK
(503051408)

Tezin Enstitüye Verildiği Tarih : 5 Mayıs 2008

Tezin Savunulduğu Tarih : 13 Haziran 2008

Tez Danışmanı : Prof. Dr. Kenan Y. ŞANLITÜRK

Diğer Jüri Üyeleri Prof. Dr. H. Temel BELEK

Prof. Dr. A. Rüstem ASLAN

HAZİRAN 2008

ACKNOWLEDGMENTS

I would like to thank and express my deepest gratitude to my supervisor, Prof. Dr. Kenan Yüce Şanlıtürk, for his sustained stimulus, invaluable guidance and suggestions, and intimate support. His scientific knowledge and engineering institution always strikes me with admiration.

This thesis is performed in the scope of Aviation Research and Development Project (HAGU) which is supported by DPT (Turkish Government Planning Organization) and managed by ITU (Istanbul Technical University) rectorship. I would like to specially thank to the project manager Prof. Dr. H. Temel Belek and assistant manager Prof. Dr. A. Rüstem Aslan for their all supports and encouragements. Also, I would like to thank to all the member of the project, and special thanks to Emin Erensoy, Kenan Gürses, Suat Kay and Evren Öner for their assistances.

I would like to thank to Yavuz Güleç and all the people in his group from Turkish Aerospace Industries (TAI), Inc., and Middle East Technical University, for their help during my trips to Ankara for performing experiments. I want also specially thank to Mr. Ali Öge from A-z Tech., Inc., for his intimate help in finite element modelling and analyses.

I also would like to thank to my dear friend Fatih Aruk, for his enthusiasm, encouragement and sophisticated discussions. Thanks are extended to my co-workers Ersin Öztürk, Gökhan Bulut, İlker Altay and Sinem Öztürk.

To my mother and father, my dear sisters: Selver, Gülten, Fatma, and youngest sweet brother Ali, for their huge love.

June 2008 Hasan KÖRÜK

TABLE OF CONTENTS

	Page No
ABBREVIATIONS	**vi**
LIST OF TABLES	**vii**
LIST OF FIGURES	**viii**
LIST OF SYMBOLS	**xii**
SUMMARY	**xii**
ÖZET	**xiiv**
1. INTRODUCTION	**1**
1.1. Introduction	1
1.2. Helicopter Structures	2
1.2.1. A Short history of helicopter structures	3
1.2.2. Principle of operation	5
1.3. Problem	7
1.4. Literature Review	9
1.4.1. General theory of helicopters	9
1.4.2. Theoretical modelling	9
1.4.3. Vibration tests and parameter estimation	12
1.4.4. Correlation, validation and updating	15
1.4.5. Concluding remarks	16
1.5. Motivation, Objective and Scope	16
2. THEORY	**19**
2.1. Finite Element Modelling	19
2.1.1. Introduction	19
2.1.2. Single degree of freedom systems	21
2.1.2.1. Undamped SDOF systems	21
2.1.2.2. Damped SDOF systems	22
2.1.3. Multiple degree of freedom systems	24
2.1.4. Finite Element Modelling	25
2.1.4.1. Introduction	25
2.1.4.2. FE formulation	26
2.1.4.3. Dynamic analysis of FE models	31
2.1.4.4. Solution methods	34
2.1.4.5. Properties of mode shapes	35
2.2. Experimental Modal Analysis Approach	37
2.2.1. Introduction	37

2.2.2. Experimental modal analysis 38
2.2.3. Peak-Peacking method 39
2.2.4. Circle-Fit method 40
2.2.5. Line-Fit method 44
2.3. Comparison and Correlation 47
2.3.1. Introduction 47
2.3.2. Comparison of natural frequencies 48
2.3.3. Comparison of mode shapes 48
2.3.3.1. Visual comparison of mode shapes 48
2.3.3.2. Modal Scale Factor (MSF) 48
2.3.3.3. Modal Assurance Criteria (MAC) 49
2.3.3.4. Coordinate Modal Assurance Criteria (COMAC) 50
2.3.4. Comparison of Frequency Response Functions (FRFs) 50
2.3.4.1. Overlaying individual FRFs 51
2.3.4.2. Frequency Domain Assurance Criterion (FDAC) 51
2.3.4.3. Frequency Response Scale Factor (FRSF) 52
2.3.4.4. Frequency Response Assurance Criterion (FRAC) 52
2.3.5. Orthogonality based comparisons 53
2.3.5.1. Normalised Cross Orthogonality (NCO) 53
2.3.5.2. SEREP-Based Normalised Cross Orthogonality (SCO) 53
2.3.5.3. Pseudo Orthogonality Check (POC) 54
2.3.5.3. Coordinate Orthogonality Check (CORTHOG) 55
2.4. Model Updating 55
2.4.1. Direct Methods 56
2.4.2. Iterative Methods 58
2.4.3. Improving theoretical models using manual correction method 60

3. MODAL ANALYSES OF HELICOPTER STRUCTURES 61
3.1. Introduction 61
3.2. Validation of FE Models of Simple Structures with Riveted Joints 62
3.2.1. Introduction 62
3.2.2. Definition of the problem and the proposed approach 62
3.2.3. Model validation of a riveted L-plate 64
3.2.3.1. Introduction 64
3.2.3.2. Modal tests of L-plates 65
3.2.3.3. FE models of L-plates 67
3.2.3.4. Validation of material properties 67
3.2.3.5. FE model validation of the riveted L-plate 71
3.2.4 Model validation of a riveted beam 75
3.2.4.1. Introduction 75
3.2.4.2. Weighting methods 77
3.2.4.3. Numerical applications 78
3.2.4.4. Experimental applications and comparisons 83
3.3. Tail Boom Section 90

3.3.1. Introduction 90
3.3.2. Experimental study 90
3.3.2.1. Experimental setup and preliminary tests 90
3.3.2.2. Experimental modal analysis 97
3.3.3. Corralation, validation and updating 100
3.3.3.1. Preliminary FE models 100
3.3.3.2. Improved FE models 106
3.4. Tail Boom 108
3.4.1. Introduction 108
3.4.2. Preliminary Tests 110
3.4.3. Initial FE models 114
3.4.4. Detailed tests and experimental modal analysis 116
3.4.4.1. Test planning 116
3.4.4.2. Detailed modal tests and analysis 118
3.4.5. Improved FE model 120
3.4.6. Comparison and correlation 124

4. MODAL ANALYSES OF HELICOPTER AIRFRAME 128
4.1. Introduction 128
4.2. Modelling Helicopter Airframe 129
4.3. Measurement of FRFs on Helicopter Airframe 130
4.3.1. Experimental setup and preliminary tests 130
4.3.2. Measurements 130135
4.3.2.1. Complete airframe 135
4.3.2.2. Isolated engine 137
4.5. Experimental Modal Analysis 138
4.6. Comparison and Correlation of Theoretical and Experimental Results 146
4.6.1. Initial FE models 146
4.6.2. Improved FE model 148
4.6.3. Latest FE model 151
4.6.4. Determination of the appropriate Boundary Conditions (BCs) 152
4.6.5. Concluding Remarks 159

5. CONCLUDING REMARKS AND SUGGESTIONS FOR FUTURE WORK 160
REFERENCES 163
CIRRUCULUM VITAE 172

ABBREVIATIONS

MAC	**:** Modal Assurance Criteria
FE	**:** Finite Element
FEM	**:** Finite Element Method
FRF(s)	**:** Frequency Response Function(s)
IRF(s)	**:** Impulse Response Function(s)
SIMO	**:** Single Input Single Output
MIMO	**:** Multi Input Multi Output
SDOF	**:** Single Degree of Freedom
MDOF	**:** Multi Degree of Freedom
ECD	**:** Effective Clamping Diameter
MSF	**:** Modal Scale Factor
COMAC	**:** Coordinate Modal Assurance Criteria
FRSF	**:** Frequency Response Scale Factor
FDAC	**:** Frequency Domain Assurance Criterion
NCO	**:** Normalised Cross Orthogonality
POC	**:** Pseudo Orthogonality Check
CORTHOG	**:** Coordinate Orthogonality Check
DOF(s)	**:** Degree(s) of Freedom
EMA	**:** Experimental Modal Analysis
dB	**:** decibel
FFT	**:** Fast Fourier Transform
ITU	**:** Istanbul Technical University
LCH	**:** Light Commercial Helicopter
BC(s)	**:** Boundary Condition(s)
TB	**:** Tail Boom

LIST OF TABLES

Page No

Table 3.1 Theoretical and Experimental Natural Frequencies of the Plate Without Rivets 68
Table 3.2 Theoretical and Experimental Natural Frequencies of the Riveted Plate 71
Table 3.3 Theoretical Natural Frequencies of the Riveted Beam for Various Weighting Methods and Clamping Cases....79
Table 3.4 Theoretical Natural Frequencies of the Riveted Beam for Various Weighting Methods (10 mm Clamping Diameter) 81
Table 3.5 Mesh Density Effect (Effective Clamping Diameter is 10 mm) 82
Table 3.6 Experimentally Obtained Natural Frequencies [Hz] 87
Table 3.7 MAC Table (Riveted Beam) 89
Table 3.8 Experimental Obtained Natural Frequencies 100
Table 3.9 Theoretical Natural Frequencies (1st FE Model) and Differences from Experimental Ones....101
Table 3.10 Theoretical Natural Frequencies (2nd FE Model) and Differences from Experimental Ones....104
Table 3.11 Theoretical Natural Frequencies of Improved FE Model (3rd) and Differences from Experimental Ones 107
Table 3.12 Experimentally Obtained Natural Frequencies of the Tail Boom 120
Table 3.13 Comparison of Three Different Mesh-sized FE Models of the Tail Boom....122
Table 3.14 Experimentally Obtained Natural Frequencies of the Tail Boom 123
Table 3.15 Some Properties of Five FE Models of the Tail Boom 124
Table 3.16 Differences between Natural Frequencies of the First FE Models and Experimental Ones [%]....125
Table 3.17 Differences between Natural Frequencies of the Improved FE Model and Experimental ones [%]....127
Table 4.1 Experimentally Obtained Damping Values....146
Table 4.2 Some Properties of the Improved FE Model of the Airframe 149
Table 4.3 Some Properties of the Latest FE Model of the Airframe....151
Table 4.4 Comparison of Experimental and Theoretical Results [%] 152
Table 4.5 Boundary Condition Types and Their Settings 154
Table 4.6 Comparison of Experimental and Theoretical Results (Vertical-Constrained)..154
Table 4.7 Comparison of Experimental and Theoretical Results (Half-Clamped) 155
Table 4.8 Comparison of Experimental and Theoretical Results (Fully-Clamped) 155
Table 4.9 'Optimum' Boundary Conditions....156
Table 4.10 Comparison of Experimental and Theoretical Results (Optimum BCs) 158

LIST OF FIGURES

Page No

Figure 1.1 : Major Components of a Typical Helicopter [4] 3
Figure 1.2 : a) The Chinese Top – B.C. 400, b) Leonardo da Vinci – 1485, c) George De Bothezat-1922 , d) Lois Brequet–1935, e) Igor Skorsky–1940s, f) Bell 206-Today 5
Figure 1.3 : Forces Acting on a Helicopter 6
Figure 1.4 : A Typical Airfoil 7
Figure 1.5 : All Excitation Frequencies on a Typical Helicopter Airframe 7
Figure 1.6 : Main Excitation Frequencies on a Typical Helicopter Airframe 8
Figure 1.7 : Huge Number of Rivets in the Helicopter Structures 8
Figure 1.8 : a) UH-60A FE Model [14], b) UH-60A FE Model [15] 10
Figure 2.1 : a) A Discrete System, b) A Continuous System – Circular Shaft 20
Figure 2.2 : A MDOF System 24
Figure 2.3 : Approximation of an Arbitrarily Shaped Structure by Idealized Elements 26
Figure 2.4 : A General Solid Body under Loads 27
Figure 2.5 : A Typical Circle-Fit Analysis Procedure 43
Figure 2.6 : A Typical Line-Fit Analysis Procedure 46
Figure 3.1 : a) FE Model of a Rivet, b) Joining Nodes within the Effective Clamping Diameter 63
Figure 3.2 : Flowchart for Obtaining a Validated Linear Model of a Structure with Riveted Joints 64
Figure 3.3 : The Riveted Plate and the Plate without Rivets 65
Figure 3.4 : Experimental Meshes for Plates with and without Rivets 66
Figure 3.5 : a) Measured 84 FRFs on the Plate without Rivets b) Measured 91 FRFs on the Riveted Plate 66
Figure 3.6 : a) FE Model of the Plate without Rivets, b) FE Model of the Riveted Plate 67
Figure 3.7 : Comparison of Predicted and Measured Natural Frequencies 69
Figure 3.8 : Comparison of Theoretically Generated and Measured Point FRF 69
Figure 3.9 : MAC for the Plate without Rivets 70
Figure 3.10 : Comparison of Experimental and Theoretical Mode Shapes of the L-Plate without Riveted Joints 70
Figure 3.11 : Difference between Theoretical and Experimental Natural Frequencies of The Riveted Plate 72
Figure 3.12 : Comparison of Theoretically Generated and Measured Natural Frequencies 73
Figure 3.13 : Comparison of Theoretically Generated and Measured Point FRF 73
Figure 3.14 : MAC for the Riveted Plate 74
Figure 3.15 : Comparison of Experimental and Theoretical Mode Shapes of the Riveted Plate 74
Figure 3.16 : Designed Riveted Beam 75
Figure 3.17 a) Picture of the Riveted Beam and b) Magnified FE Model of the Riveted

Beam 76
Figure 3.18 : FE Modelling Parameters of a Riveted Joint....76
Figure 3.19 : Effect of Rotational DOF of the Reference Point for Various Weighting Cases 79
Figure 3.20 : Effect of Weighting Methods (cubic weighting case is taken as reference 80
Figure 3.21 : Effect of Weighting Methods (cubic weighting case is taken as reference 81
Figure 3.22 : Mesh Density Effect (Effective Clamping Diameter is 10 mm) 82
Figure 3.23 : Effect of Effective Clamping Diameter for Different Weighting Functions (6 mm ECD is taken as reference) 83
Figure 3.24 : Best Suspension, Impact Excitation and Accelerometer Locations 84
Figure 3.25 : All Measured FRFs on the Structure 85
Figure 3.26 : All the Measured FRFs on the Structure (exciting at 110 nodes) 85
Figure 3.27 : The First 8th and 17th Theoretical and Experimental Mode Shapes 86
Figure 3.28 : Difference between Experimental and Theoretical Natural Frequencies Obtained for Different Weighting Functions (ECD=6 mm) 87
Figure 3.29 : Difference between Experimental and Theoretical Natural Frequencies Obtained for Different Weighting Functions (ECD=10 mm) 88
Figure 3.30 : Comparison of Measured and Theoretically Generated FRFs for ECD=6 mm and 90
Figure 3.31 : Tail Boom Section 91
Figure 3.32 : Experimental Setup 91
Figure 3.33 : Measurement Points 92
Figure 3.34 : Calibration Cylinder 93
Figure 3.35 : Calibration Results 93
Figure 3.36 : Time Signal 94
Figure 3.37 : Effect of Application of Windowing to the Acceleration Signal on FRF 95
Figure 3.38 : Repeatability Tests 95
Figure 3.39 : Reciprocity Control 96
Figure 3.40 : Nonlinearity Control (excitation at 72nd point, response at 36th point)....97
Figure 3.41 : All Measured FRFs on the Structure (Point FRF 23)....98
Figure 3.42 : All Measured FRFs on the Structure (Point FRF 72)....98
Figure 3.43 : A Typical Experimental Modal Analysis Procedure....99
Figure 3.44 : MIMO Multivariate MIF 99
Figure 3.45: Some Experimentally Obtained Mode Shapes of the Tail Boom Section....100
Figure 3.46 : Approach in Building up FE Model of the Structures....100
Figure 3.47 : First FE Model of the Tail Boom Section 101
Figure 3.48 : Comparison of Measured and Theoretically Generated (1st FE Model) FRFs (Excitation at 75th Point in x Dir., Response at 31st Point in x Dir....102
Figure 3.49 : Comparison of Theoretically Generated (1st FE Model) and Measured Natural Frequencies 103
Figure 3.50 : 2nd FE Model of the Boom Section 104
Figure 3.51 : Comparison of Predicted (2nd FE Model) and Measured Natural Frequencies 105
Figure 3.52 : Comparison of Measured and Theoretically Generated (2nd FE Model) FRFs (Excitation at 75th Point in x Dir., Response at 31st Point in x Dir....105
Figure 3.53 : Comparison of Measured and Theoretically Generated (2nd FE Model) FRFs (Excitation at 31st Point in x Dir., Response at 86th Point in y Dir.) 106

Figure 3.54 : Improved FE Model (3rd) of the Tail Boom Section 106
Figure 3.55 : Natural Frequencies of 10 Modes of Imroved (3rd) FE Model of the Boom Section for Different Mesh Sizes 107
Figure 3.56 : Some Theoretical Mode Shapes of the Tail Boom Section.....108
Figure 3.57 : Helicopter Tail Boom Components.....109
Figure 3.58 : Manufactured Tail Boom of ITU-LCH 109
Figure 3.59 : Experimental Setup for the First Modal Tests of the Tail Boom 110
Figure 3.60 : Calibration Results of a Typical 3-D Accelerometer 111
Figure 3.61 : Time Signals of Force and Accelerations in Three Response Directions 111
Figure 3.62 : Autospectrum of the Force Signal.....112
Figure 3.63 : A Typical Coherence Example.....112
Figure 3.64 : Measurement Points of the Tail Boom.....113
Figure 3.65 : All Measured FRFs on the Structure.....113
Figure 3.66 : Hybrid MIF up to 280 Hz.....114
Figure 3.67 : Initial FE Model of the Tail Boom (TB MODEL 1) 115
Figure 3.68 : Magnified Picture of Improved FE Models of the Tail Boom 116
Figure 3.69 : a) Best Suspension and b) Best Excitation locations.....117
Figure 3.70 : AutoMAC (Tail Boom).....118
Figure 3.71 : Measurement Points 118
Figure 3.72 : All Measured FRFs 119
Figure 3.73 : A Step in a Typical Experimental Modal Analysis Procedure.....119
Figure 3.74 : Experimentally Obtained Some Mode Shapes of the Tail Boom.....120
Figure 3.75 : FE Models of the Tail Boom with Various Mesh Sizes 121
Figure 3.76 : Natural Frequencies of Three Different Mesh Sized FE Models 122
Figure 3.77 : Improved FE Model of the Tail Boom 123
Figure 3.78 : Theoretical Mode Shapes of the Tail Boom.....124
Figure 3.79 : First Eight Modes of Some Initial FE Models of the Tail Boom 125
Figure 3.80 : MAC for 15 Modes (Tail Boom) 127
Figure 4.1 : Main Components of the Helicopter Airframe Tested 128
Figure 4.2 : Helicopter Airframe and the Experimental Setup 129
Figure 4.3 : FE Model of the Helicopter Airframe 130
Figure 4.4 : FE Model of the Airframe Including Rivets.....130
Figure 4.5 : Calibration Results 131
Figure 4.6 : a) Time and b) Autospectrum of the Force Signal 131
Figure 4.7 : Time Signal of the Response.....132
Figure 4.8 : a) FRF and b) Related Coherence of a Typical Signal.....132
Figure 4.9 : Repeatability Tests 133
Figure 4.10 : Repeatability Tests (on the Engine in z Direction) 134
Figure 4.11 : Repeatability Tests (on the Engine in x Direction) 134
Figure 4.12 : Excitation Points 135
Figure 4.13 : Measurement Points 135
Figure 4.14 : Measured FRFs in x Direction 136
Figure 4.15 : Measured FRFs in z Direction.....136
Figure 4.16 : a) Experimental Setup and b) Measurement Points of the Isolated Engine ...137
Figure 4.17 : Measured FRFs on the Engine in x the Direction 137
Figure 4.18 : Measured FRFs on the Engine in y the Direction 138
Figure 4.19 : Measured FRFs on the Engine in z the Direction.....138

Figure 4.20 : A Typical Experimental Modal Analysis Step 139
Figure 4.21 : Tail Boom Rolling (Left-and-Right) Mode 139
Figure 4.22 : Tail Boom Rocking (Up-and-Down) Mode 140
Figure 4.23 : Measured FRFs in the x and z Directions 140
Figure 4.24 : Measured FRFs in the x and z Directions at the Point 189 141
Figure 4.25 : First Rolling Mode (Using Measurements in the x Direction) 141
Figure 4.26 : Second Rolling Mode (Using Measurements in z Direction) 142
Figure 4.27 : Measured FRFs on the Engine in the y Direction 142
Figure 4.28 : A Forward-Backward Mode (Using the Measurements in the y Direction) 143
Figure 4.29 : An Engine Dominated Mode (Up-and-Down) in y-z plane: Using the Measurements on the a) Complete Airframe, b) Isolated Engine 143
Figure 4.30 : An Engine Dominated Mode (Left-and-Right) in x-y plane: Using the Measurements on the a) Complete Airframe, b) Isolated Engine 144
Figure 4.31 : An Engine and Tail Dominated Mode in y-z plane: Using the Measurements on the a) Complete Airframe, b) Isolated Engine 144
Figure 4.32 : A Global Bending Mode in y-z Plane 144
Figure 4.33 : Nose Dominated Modes a) in x-y Plane b) in y-z Plane 145
Figure 4.34 : An Important Global Bending Mode of the Helicopter Airframe 145
Figure 4.35 : Some other Modes of the Helicopter Airframe 145
Figure 4.36 : Two Local Modes of the Helicopter Airframe 146
Figure 4.37 : First Three Mode Shapes of the Initial FE Model of the Helicopter Airframe 147
Figure 4.38 : The First Three Mode Shapes of the Initial FE Model of the Helicopter Airframe 148
Figure 4.39 : Improved FE model of the Helicopter Airframe 149
Figure 4.40 : Some Modes of the Improved FE Model of the Helicopter Airframe 150
Figure 4.41 : Some Modes of the Latest FE Model of the Helicopter Airframe 152
Figure 4.42 : Skid of the Helicopter 153
Figure 4.43 : Some Modes of the Latest FE Model of the Helicopter Airframe with Optimum BCs 157
Figure 4.44 : Comparison of Some Experimentally Found Local Modes of the Helicopter Airframe with the FE Results of the Helicopter Tail Cone 158

LIST OF SYMBOLS

x, y, z	**:** Translational of Degrees of Freedom/Coordinates
$\theta_x, \theta_y, \theta_z$	**:** Rotational of Degrees of Freedom/Coordinates
N	**:** Total Number of Degrees of Freedom/Coordinates
n	**:** Number of Primary/Master/Measured Degrees of Freedom
m	**:** Number of Included Modes
L	**:** Number of Correlated Mode Pairs
r	**:** Current Mode Number
$\vec{b}$	**:** Body Forces per Unit Volume
$\vec{T}$	**:** Surface Loads per Unit Area
$\vec{F}_{ci}$	**:** Concentrated Force at Point i
$[\ ]$	**:** Matrix
$[\ ]^T$	**:** Transpose of a Matrix
$[\ ]^{-1}$	**:** Inverse of a Matrix
$\{\ \}$	**:** Column Vector
$\{\ \}^T$	**:** Transpose of a Column Vector
$\|\ \|$	**:** Norm of a Matrix/Vector
$\{\varepsilon\}$	**:** Strain Vector
$[\partial]$	**:** Derivative Matrix
$\{d\}$	**:** Displacement Vector
$[D]$	**:** Matrix of Elastic Coefficients
$\{\sigma\}$	**:** Stress Vector
$[N]$	**:** Shape Function Matrix
$\{q\}$	**:** Nodal Displacement Vector
$[B]$	**:** Strain Function Matrix
U_e	**:** Strain Energy of an Element
$[k]$	**:** Element Stiffness Matrix
W_e	**:** Work Done by External Forces
$\{f_B\}$	**:** Element Body Force Vector
$\{f_S\}$	**:** Element Surface Load Vector
Π	**:** Potential Energy
$\{Q\}$	**:** Vector of Nodal Displacements
$[K]$	**:** Global Stiffness Matrix

$\{F\}$: Global Load Vector
T : Kinetic Energy
V : Volume
ρ : Density
$\{\dot{d}\}$: Velocity Vector of a Mass Distributed Point
$[m]^e$: Element Mass Matrix
λ : Eigenvalue
ε : Value of an Error
$\mathbf{c}$: Viscous Damping Coefficient
c_{cr} : Critical Damping Coefficient
ξ : Viscous Damping Coefficient
$\mathbf{k}$: Spring Stiffness Coefficient
$[M]$: Mass Matrix
$[C]$: Viscous Damping Matrix
$[M_T]$: Theoretical Mass Matrix
$[M_E]$: Experimental Mass Matrix
$[M_U]$: Updated Mass Matrix
ω_r : Angular Natural Frequency of r^{th} Mode
ω_d : Angular Damped Natural Frequency of r^{th} Mode
η_r : Structural Damping Loss Factor of r^{th} Mode
$\mathbf{m_r}$: Modal/Effective Mass of r^{th} Mode
k_r : Modal/Effective Stiffness of r^{th} Mode
$\alpha(\omega)$: Receptance Frequency Response Function
$\{\Psi_r\}$: Mode Shape Vector of r^{th} Mode
$[\Psi]$: Mode Shape Matrix
$[\phi]$: Normalized Mode Shape Matrix

MEASUREMENT, MODELLING AND MODAL ANALYSES OF HELICOPTER STRUCTURES

SUMMARY

Although modern tools are available for developing numerical models in order to predict the dynamic behaviour of structures, it is still quite difficult to obtain such models that will yield results with acceptable accuracy for complex structures such as helicopters and airplanes. In such situations, it is often necessary to obtain a mathematical model from measured data so as to describe the dynamic properties of structures. This makes the experimental modal analysis quite suitable and valuable. The mathematical model obtained using measured data can be used for assessing the quality of the numerical models. The experimentally derived models can also be used for model updating purposes. In this thesis, first of all, helicopter structures are introduced and a literature survey on the theory, modelling, measurement and analysis of helicopter and similar structures is given. After that, acceptable linear Finite Element (FE) models are built for relatively simple structures with riveted joints by adjusting the FE models using the measured modal properties of those structures. Then, the validated FE model for riveted joints is successfully applied to a helicopter tail boom section. As the helicopter tail boom is quite complex and has very similar structural features with other parts of helicopter airframe, obtaining a validated FE model for this structure is important. Therefore, very detailed and comprehensive tests are performed on a helicopter tail boom and the experimental results are used to develop improved FE models of the tail boom. Furthermore, vibration tests are also performed on an existing real helicopter airframe in order to determine its modal properties experimentally. Utilising the experimental results obtained from such tests and the experience gained from previous studies on helicopter structures, some FE models of the airframe are developed. At the end, a more realistic and representative FE model of the helicopter airframe is obtained. Such a model can be used for design optimisation and certification purposes.

HELİKOPTER YAPILARININ ÖLÇÜM, MODELLEME VE MODAL ANALİZLERİ

ÖZET

Yapıların dinamik davranışını modellemek için ileri modelleme ve analiz yöntemleri mevcut olmasına rağmen, karmaşık yapıların kabul edilebilir seviyede hassasiyete sahip teorik modellerinin oluşturulması hala büyük zorluklar içermektedir. Böyle durumlarda, kritik yapıların dinamik modellerinin deneysel verilere dayanılarak oluşturulması gerekebilmektedir. Bu bağlamda, deneysel modal analiz, yapıların dinamik modellerinin oluşturulması için oldukça güvenilir bir yaklaşım sunmaktadır. Buna ilave olarak yapının deneysel verilerine dayanılarak elde edilen matematiksel modeli, sayısal (teorik) model veya modellerin doğruluğunun sınanması ve bu model veya modellerin güncellenmesi için de kullanılabilmektedir. Bu tez kapsamında, ilk önce helicopter yapıları tanıtılmış, ve helicopter ve benzeri yapılarının teori, modelleme, ölçüm ve analizleri ile ilgili bir literatür araştırması yapılmıştır. Daha sonra, bazı basit perçinli yapılar üzerinde ölçülen modal veriler yardımıyla, perçinli bağlantılar için, lineer Sonlu Eleman (SE) modelleri elde edilmiştir. Takibinde, doğrulanmış perçin modeli başarıyla bir helicopter kuyruk konisi kesitine uygulanmıştır. Helikopter kuyruk konisi, diğer helicopter yapılarındakine benzer parçalar içerdiğinden ve oldukça karmaşık olduğundan, bu yapının doğrulanmış bir SE modelinin oluşturulması önemlidir. Bu yüzden, bir helicopter kuyruk konisi üzerinde çok detaylı testler gerçekleştirilmiş ve yapıyı çok iyi temsil eden bir SE modeli inşa edilmiştir. Bundan başka, gerçek bir helicopter gövdesinin dinamik yapısını belirlemek için, bu yapı üzerinde titreşim testleri gerçekleştirilmiştir. Bu testlerden elde edilen deneysel verilerden ve diğer helikopter yapılarında kazanılmış olan tecrübelerden yararlanılarak, helicopter gövdesinin bazı SE modelleri oluşturulmuştur. Sonunda, daha gerçekçi olan ve yapıyı iyi temsil eden bir SE modeli oluşturulmuştur. Elde edilen bu model tasarım optimizasyonu amacına yönelik olarak kullanılabilir.

1. INTRODUCTION

1.1 Introduction

Helicopters are known as planes with rotating wings. They are capable of moving forward, backward and side ways, moving up and down and hovering in the air, etc. The operating environment of the helicopter is such that the parts of the airframe are subjected to high levels of excitation forces. These forces come from the main and tail rotors and the unsteady aerodynamic loadings on the surfaces [1]. Therefore, vibration considerations are at the top of the importance during the design of these structures. There is hardly any other measurable parameter in practice that gives information as much as vibration signature gives. Vibration signature includes information about the health and operating characteristics of the structure [2]. Thus, it is vital to establish a reliable model of the airframe in order to predict vibration levels so that undesirable fuselage vibratory responses can be predicted and avoided.

Design optimisation often requires that the theoretical model represents the real structure with acceptable accuracy. This usually leads to manufacturing a prototype and performing experiments for correlation and model updating purposes. However, if it is not feasible to manufacture a prototype for the complete structure due to time limitations and economical constraints, it is possible to perform similar tasks on a simplified but representative prototype in terms of manufacturing processes and construction.

A helicopter is an assembly of thousand of sub parts, and these parts are joined together using tens of thousands of riveted joints. Even today, accurate modelling of such structures including the interactions of all the parts and related nonlinear behaviours is not possible with existing theoretical tools. In practice, it is not possible to perform all the tasks or sceneries experimentally and it is very important to have a validated theoretical model. Once a validated model is available, various types of

analyses can be performed quite cost effectively as it will be too expensive to do the same using experimental approach. Furthermore, performing some of these tasks may not be a viable option experimentally in many cases: e.g., it may not be possible to perform the experiments without damaging the structure, or it may be too difficult or too expensive to satisfy the physical requirements. In those cases, it is more appropriate to obtain a validated theoretical model of the structure so as to perform many design iterations and optimisation tasks. This validation process is done by acquiring appropriate experimental data and comparing with the theoretical model(s). The modal data obtained experimentally have been found to be quite effective for validation purposes.

1.2 Helicopter Structures

The helicopter is an aircraft that uses rotating wings to provide lift, propulsion and control [3]. Helicopters are classified as rotorcraft which distinguishes them from fixed-wing aircraft because the helicopter derives its source of lift from the rotor blades rotating around a mast. A helicopter mainly consists of a fuselage on a skid, a tail connected to the fuselage, main and tail rotor blades, and a transmission system that transmits power from helicopter motor(s) to the main and tail rotor. Some of the main components a helicopter are given in Figure 1.1 [4].

Helicopter and also other air vehicle structures are constructed primarily from sheet metals and thin composite materials. These thin metal sheets and composites are very efficient in resisting the shear or tension loads. On the other hand, sheet metal parts should also resist compression loads and normal-to-surface loads. For this reasons, they are generally stiffened with some other parts [4]. Usually, all these parts are assembled with riveted joints.

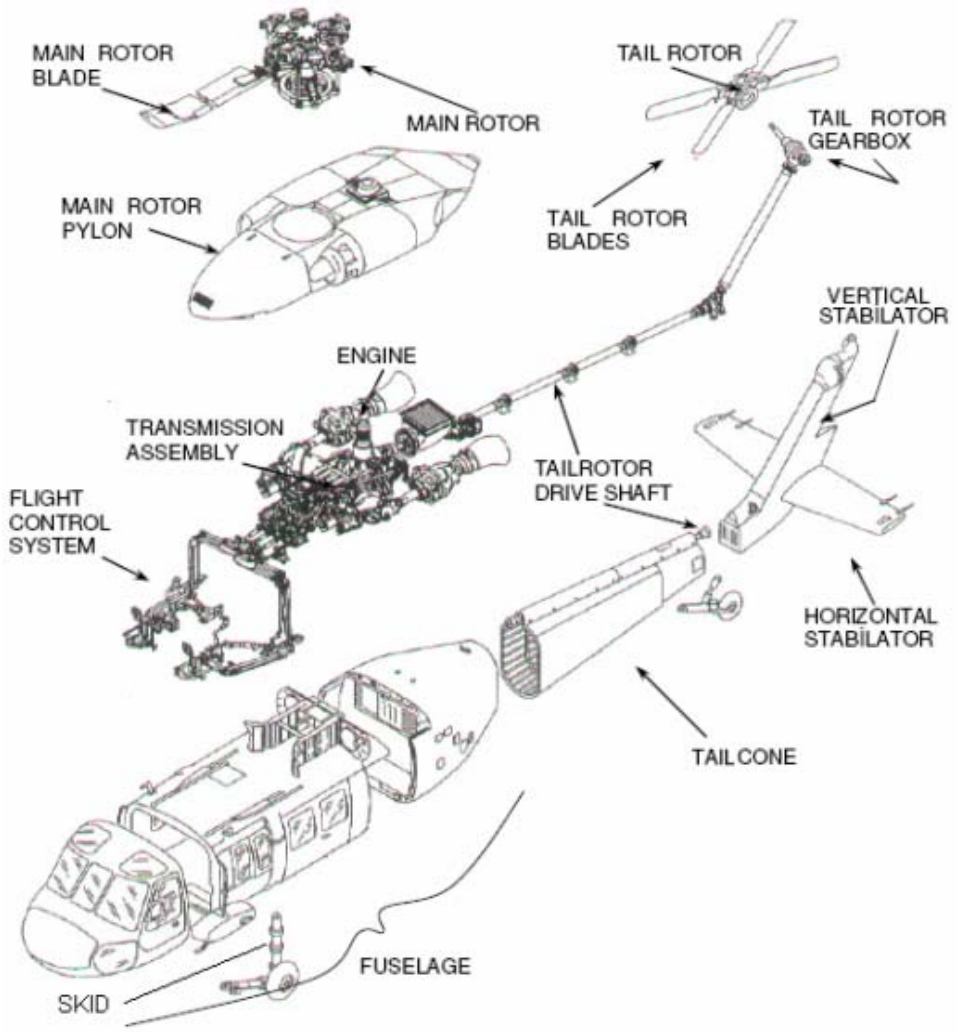

Figure 1.1 : Major Components of a Typical Helicopter [4]

1.2.1 A Short history of helicopter structures

The history of helicopter development is said to begin with the mention of the Chinese top (B.C. 400) a stick with a propeller on top, which was spun by the hand and released (Figure 1.2a). In 1485, Leonardo Da Vinci drew a helicopter [3] which is a machine for vertical flight utilizing a screw-type propeller (Figure 1.2b).

In 1784, Christian de Launoy and Bienvenu in France made a model comprising a pair of counter-rotating rotors using turkey's flight feathers as rotor blades. In 1861, Gustave de Ponton, a French inventor, coined his own models “helicopter” that is linked to the Greek words helix (spiral) and pteron (wing). From 1860 to 1890, many small helicopter models were designed and made (France 1870’s, Italy 1878, United States, 1880’s etc.).

In 20th century, the dream of flying was realised and especially in last several decades, it has been an important transporter vehicle. First man-carrying helicopter was made by Paul Cornu in France in 1907 and it flew with a motor of 24 HP. But, because of some stabilization and other engineering problems, helicopters were not improved in those years. In 1909, Emile and Henry Berliner (United States) built a two-engine coaxial helicopter [4]. Igor Sikorsky (Russia), built a helicopter with two coaxial three-bladed rotor but it was not successful to lift its own weight (including the weight of the pilot)

In 1922, Russian emigrant George De Bothezat (United States) made the biggest machine up to that time (Figure 1.2c). This machine had 4 rotors and could carry 3 people. In 1923, Spanish Juan La Cierva added his name to this field by designing and manufacturing a rotorcraft. In 1930, Corradino d'Ascanio (Italy) built a relatively successful coaxial helicopter which flew under good control. His relatively large machine had two two-bladed counter rotating rotors [5].

In 1935, Lois Brequet (Figure 1.2d) made a helicopter which had blades similar to those used nowadays and his helicopter flew about 44 km [6].

Henrich Focke in 1936 in Germany, C.G. Pullin in 1938 in Britain and Anton Flettner in 1940 in Germany developed some new helicopters. On the other hand, in the United States Igor Skorsky built the VS-300 helicopter that was one of the first most successful helicopter in the world at Sikorsky Aircraft Co in 1941 [3]. He could manage to excite the main and tail rotors properly at the same time and later he managed to add pitch control to his helicopter [6]. In 1942, developed from the VS-300, Sikorsky's R-4 became the first mass produced helicopter with a production order for 100 aircraft. From this date some new models of Sikorsky were developed and manufactured (Figure 1.2e) that lead the helicopter sector [5, 7].

In 1943, Lawrance Bell at Bell Helicopter Company in the United States built a helicopter utilizing Arthur Young work in 1930s. 1945, a tandem rotor helicopter developed by Frank N. Piasecki from Piasecki Helicopter Corporation in the United States. In 1951, the first helicopter with turbine power and in 1954 the first twin-engine turbine powered helicopter were developed by Karman Aircraft Company in United States [3].

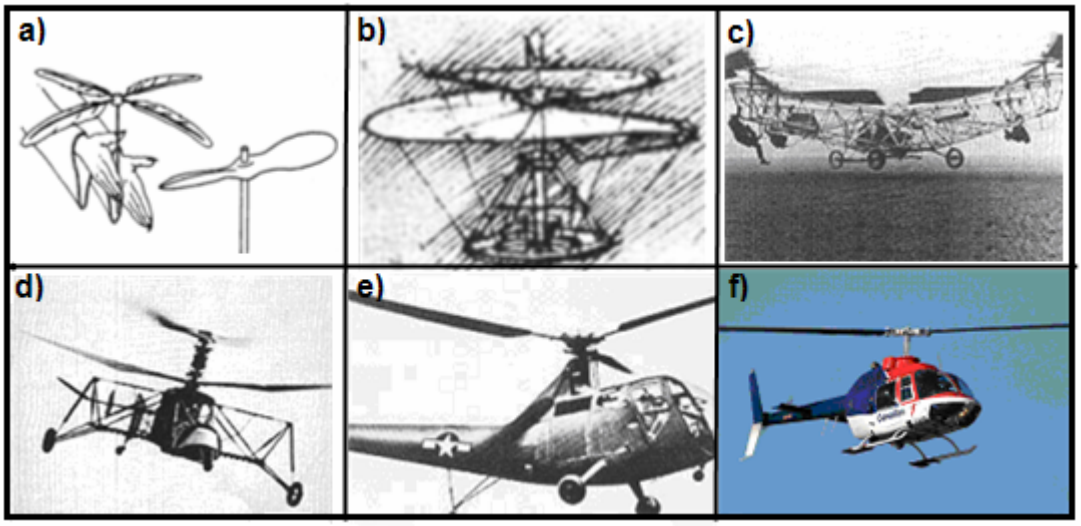

Figure 1.2 : a) The Chinese Top – B.C. 400, b) Leonardo da Vinci – 1485, c) George De Bothezat–1922, d) Lois Brequet–1935, e) Igor Skorsky–1940s, f) Bell 206-Today

Johnson [3] stated that the invention of the helicopter may be considered complete by the early 1950's. In the years that followed, some very large and successful helicopters were developed and constructed although their main principles were from helicopters of 1950s. In Figure 1.2f, such a modern helicopter of a Canadian Helicopter Corporation, Bell 206 is given. Today, many helicopter manufacturers such as Agusta, Boing, Kaman, Robinson, Sikorsky, Bell, Enstrom, Lancair (CH7), Rotorway, Westland, Brantly, Eurocopter, MD and Schwiezer are manufacturing various kinds of helicopters.

1.2.2 Principle of operation

Different from fixed-wing aircraft, the airfoil of a helicopter is a rotating blade assembly (see Figure 1.1). The blade assembly is mounted to the top of the fuselage on a hinged shaft. At the same time this shaft is connected to the engine of the helicopter and its flight control system.

The main rotor blades rotate about a vertical axis. They provide lift for the helicopter as a result of the aerodynamic forces due to relative motion of the surface of the wings with respect to air. On the other hand, when the main rotor turns, it also produces reaction torque that could make the helicopter spin. On most helicopters, there is a small anti-torque rotor fitted with tail rotor blades to provide anti-torque so as to hold the helicopter straight. Tail rotor is linked to the main rotor via a system of

gearboxes and drive shafts that provide power to the tail rotor from the transmission. Although tail rotor is mostly used to compensate the reaction torque of main rotor, in practice, some other systems such as, NOTAR (No Tail Rotor), tip jets, etc. are also used for this purpose.

A helicopter can lift itself by having its main rotor blades move through the air although its body can stay still. Depending on design, main rotor may be fitted with two or more blades. There are four forces acting on a helicopter or airplane: lift, drag, thrust and weight (Figure 1.3). Mainly, the rotor of a helicopter provide three functions: the generation of a vertical lifting force called thrust in opposition to the weight of the helicopter; the generation of a horizontal propulsive force for forward flight; and control the attitude and position of the helicopter in space by generating some forces and moments [5].

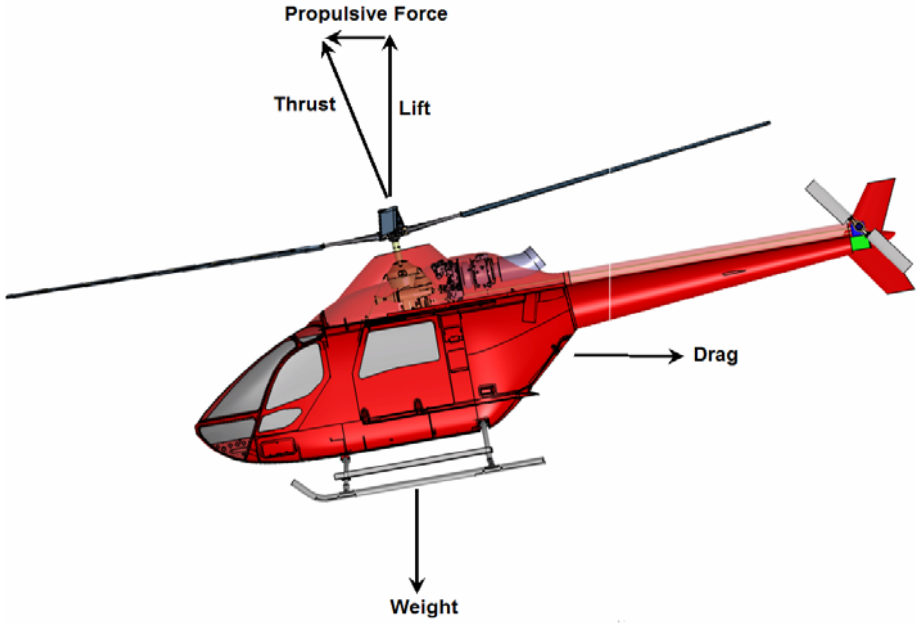

Figure 1.3 : Forces Acting on a Helicopter (ITU-LCH)

The profile of the blades is designed in such a way that the required functions are realized. In a typical airfoil, velocity of the air is low on the lower chamber of the profile, while velocity of the air is high on the upper chamber of the profile. Bernoulli's principle states that as the air velocity increases, the pressure decreases; and as the velocity decreases, the pressure increases. So, the wing is lifted upward as a result of a higher pressure created on the lower surface of the wing compared to the

that on the higher surface of the wing (Figure 1.4). Also, by changing angle of blades by some mechanism of the helicopter, other components of forces are obtained.

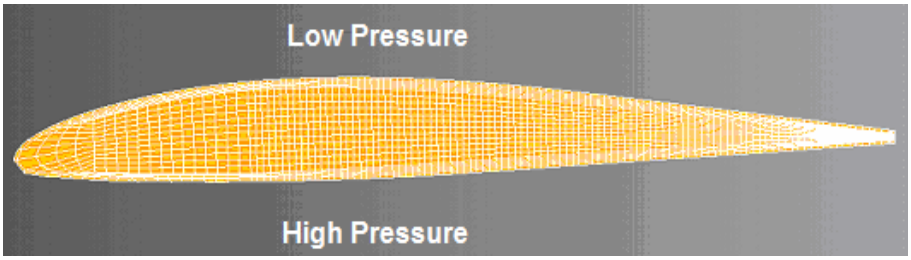

Figure 1.4 : A Typical Airfoil

1.3 Problem

Helicopters operate in difficult environments. Furthermore, emergency conditions (such as emergency landing) are always a possibility. On the other hand, a typical helicopter has many sources of excitations coming from main rotor, mils, tail rotor, rolling bearings, gears, etc. Figure 1.5, shows some possible excitation frequencies up to 1800 Hz though the main excitations can be summarised as in Figure 1.6. A helicopter should survive under all these excitations, dynamic and static loads. Importantly, it should be remembered that these machines are designed to carry people, hence the reliability of these machines are extremely important.

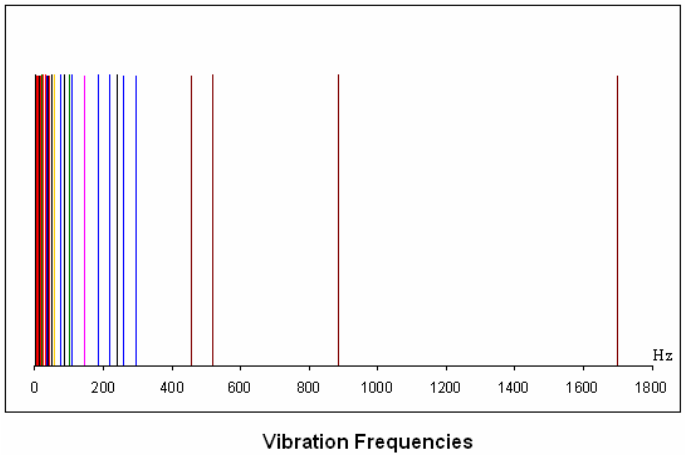

Figure 1.5 : All Excitation Frequencies on a Typical Helicopter Airframe

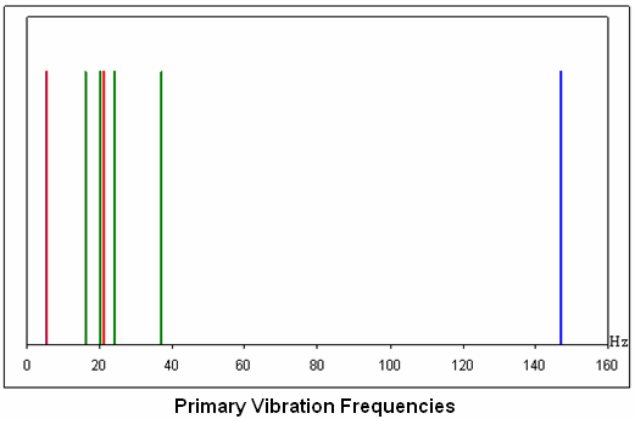

Figure 1.6 : Main Excitation Frequencies on a Typical Helicopter Airframe

Before a helicopter can fly, it should be assured that it will take off and land without encountering any ground resonance, fly safely in the air and survive under all emergency conditions. If there are validated theoretical models available for a helicopter, all these scenarios can be simulated and required design modifications can be made. As it is not possible to make prototypes for every possible design or design changes, it is very beneficial to simulate design changes on the computer using validated models. In most cases, as on this thesis, FE models are used for these purposes.

As mentioned before, helicopter structures are very complicated structures. Their designs are not easy and require years of experience and 'know-how'. A typical helicopter is made of tens of thousands of sub components. The structural components of a typical helicopter are joined using huge number of rivets (see Figure 1.7). Therefore, it should be noted that developing a FE model with so many components and rivets for a helicopter structure is also a very demanding task. Validation process comes after this difficult process.

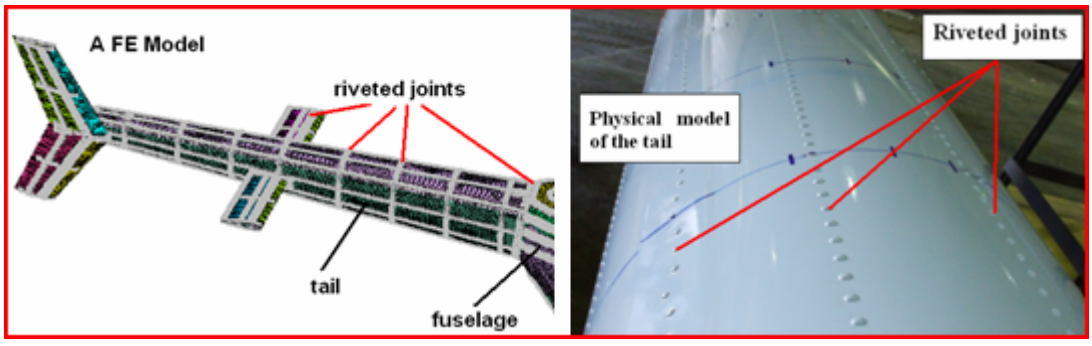

Figure 1.7 : Huge Number of Rivets in the Helicopter Structures (the components of ITU-LCH)

Aforementioned problems are real problems, and there is a serious need of, proper designing and modelling of helicopter structures, validation and improving of these models, performing detailed analyses and determine/optimise design parameters.

1.4 Literature Review

1.4.1 General theory of helicopters

Three are some books on rotary wing aircraft that mostly focus on rotor dynamics. Johnson in his book [3] gives general theory of helicopter structures, but mostly focusing of analytical methods of aerodynamics and rotor dynamics. Leishman in his book gives principles of helicopter aerodynamics with many extended examples [5]. Bielawa deals with structural dynamics and vibration test procedures of helicopters in addition to their aerodynamics in his book. [8]. Coyle deals with aerodynamics of helicopters and some practical issues of the helicopters such as emergency procedures [9]. There are also some other works dealing with flight and performance tests [10], rotorcraft design methodologies [11], design of some special kind of helicopters [7] and design of helicopter rotor systems (hubs) [12].

1.4.2 Theoretical modelling

Obtaining a validated theoretical model of structures is very important for design and optimization purposes. Such models can be used to optimise the structure for maximum efficiency, maximum life, minimum vibration and noise, etc. However, model validation and updating is usually a difficult task, not only due to the cost involved during this process, but also due to the fact that a unique and realistic theoretical model may not be available at the end of the model updating process. The problem is further complicated when the structure has joints and associated nonlinearities.

Helicopters and other types of air vehicles are complex structures and the theoretical methods used to predict helicopter vibrations are mostly based on finite element modelling techniques because of the flexibility of FE approach for modelling structures with any geometry. A helicopter is an assembly of thousands of structural parts connected using huge number of riveted joints. The structural parts can be

modelled using solid, shell, beam and truss, etc. elements, as well as simpler lumped parameters such as point mass, simple spring and dashpot.

There are many resources on FE modelling of practical structures in the literature but less on helicopter structures. Fortunately, building up FE models of all types of the structures follows the same path. Gabel et. al., in their paper, built up a quite simple FE model of a helicopter to calculate static internal loads and vibration of airframe structure [13]. Howland et. al, in their report, modelled a UH-60A helicopter using a commercial FE program [14]. As seen in Figure 1.8a, their FE model has quite a few number of degree of freedoms and it is fairly simple. Using 60, 100 and 150 modes, they made forced vibration analysis by using damping values obtained from vibration tests. Idosor and Seible in their work [15], firstly built a primary FE model of UH-0A helicopter (Figure 1.8b) add then some secondary components to the first model. It was then concluded that secondary components had significant effects on dynamic modal parameters. In another report in 1993, Idosor and Seible built some models of UH-60A to compare the results with air loads test configuration [16].

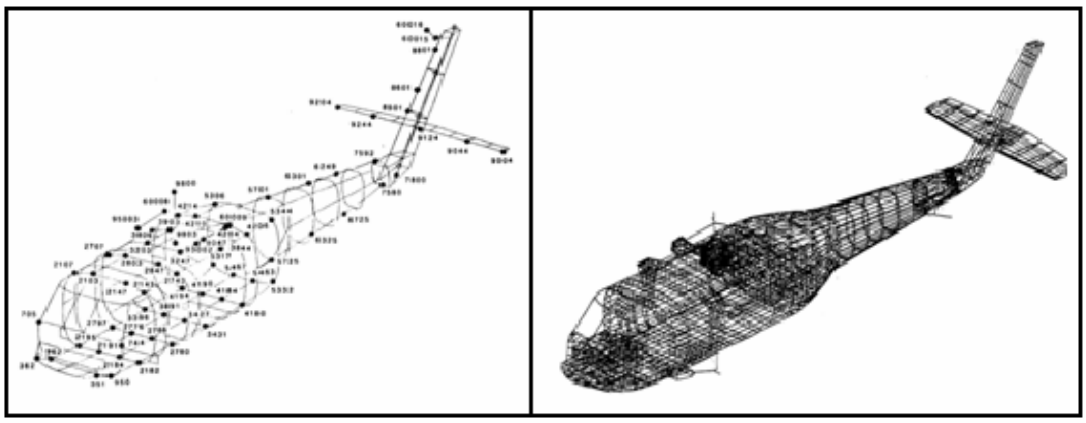

(a) **(b)**

Figure 1.8 : a) UH-60A FE Model [14], b) UH-60A FE Model [15]

Dompka [17] in his article investigated the effects of so-called “difficult components” on FE model vibration prediction for a helicopter airframe, AH-1G. He concluded that engines, fuel, avionics, fairings, canopy, cowlings, covers, doors etc. are “difficult” components and both in ground vibration tests and its FE analysis these components are removed.

Riveted joints are used to assemble sub components of many structures including helicopters, aircrafts, trucks, rails and trailers [18-24]. However, modelling and updating is a difficult problem for riveted structures due to the fact that there may be excessive number of riveted joints in representative models. Furthermore, riveted joints on structures that rely on contact forces to maintain the assembly are not fully modelled yet [18-19]. On the other hand, it is well known that the strong effects of joints and fasteners, on the mechanical assembly of the system, are very strong and therefore the accuracy of the predictions of structural response is strongly based on how accurately these joints are modelled. For this reason, to be able to model the dynamic behaviour of a structure with acceptable accuracy, it is of paramount importance to include models of such joints in theoretical models.

Continuous structures such as beams, plates and solids are generally well defined in FE applications. However, in practice, structures consist of many sub components and interactions between them are not well understood. Especially under dynamic loads, their behaviours are nonlinear (sliding and separation of the contact surfaces, etc.). Jalali et. al. studied bolted joint connecting two beam interfaces and obtained nonlinear SDOF equation representing the first mode of vibration [25]. By using the steady state response of the structure, the joint parameters are identified for different excitation frequencies. They concluded that a cubic stiffness parameter may indeed be identified and the linear damping coefficient depended on the amplitude of response levels. However, the behaviour of joints between sliding surfaces are very complicated hence, the models aim to represent such behaviour usually need parameters obtained from vibration tests [76-78]. But it should be noted that it is not easy to measure exactly the transmitted forces and relative displacements between contact surfaces under operating conditions.

It seems that including nonlinear models for individual riveted joints is still extremely difficult for those structures (most aerospace structures including helicopters) containing huge number of rivets. There are some practical approaches for riveted joints, especially for the purpose of fatigue life and stress analyses [18-23]. Bisagni [18] dealt with experimental and numerical investigations on the energy absorbing mechanism of a structure fastened by rivets. Langrand and others [19-20] dealt with a new numerical methodology to improve the representativeness of the riveted joint modelling for numerical analysis of airframe crashworthiness. Simmons

and Schleyer [21] used FE modelling for prediction of the response of riveted and laser-welded stiffened panels to pulse pressure loading though they did not include nonlinear effects. Karaoğlu and Kuralay [22] performed stress analysis of a truck chassis with riveted joints using Finite Element method. Related to modal analysis of riveted structures, Josh and Hau [24] in their study simulated rivets the same way as welds, in which welds are modelled using Point-to-Point Contact (PCM) and Area Contact Method (ACM) and compared modal frequencies and mode shapes with experimental results. PCM simulates the weld by connecting only one grid point from each side of the welded (riveted) parts with either spring or rigid elements while ACM simulates the weld (rivets) by connecting several grid points from each side of the welded parts with solid, spring or rigid elements. Al-Emrani and Kliger in their paper study the behaviour of stringers-to-floor beam connections for riveted railway bridges using FE analysis [25]. By making some static and fatigue tests, they studied the forces on these connections.

HoYun and Bauchau in their papers, deal with the development of simple but improved numerical models based on a lumped parameter approach which accounts for joint flexibilities by a set of concentrated linear and torsional springs whose parameters are experimentally determined [27-28]. Buehrle et. al., in their paper focused finite element modelling of aircraft fuselage structures, such as tail boom, with different combinations of element types, such as beams, plates, etc. and compared their performances [29].

As it was mentioned before, most of the numerical methods that are used to predict helicopter vibrations are based on finite element modelling techniques. A helicopter is an assembly of thousands of structural sub components connected using tens of thousands of riveted joints. These parts are usually modelled using solid shell, beam and truss types of elements, although lumped masses and simple spring and dashpots are also used. It should be notes however that the details and the complexity needed in a model depend on the objective for which such a model will be used.

1.4.3 Vibration tests and parameter estimation

There are various references on vibration tests and parameter estimation from measured data. Ewins in his book gives both theory and application of vibration tests

of structures and methods of parameter extraction from measured data [30]. By measuring response and excitation by impact hammer or shaker, Frequency Response Functions (FRFs) of the structure are obtained and modal parameters such as natural frequencies, mode shapes and damping values are extracted by using various modal analysis methods. Inman also gives some basics of vibration test methods [31].

Before performing the vibration tests, some pre-tests are suggested to determine the best test parameters, such as the best excitation and suspension points etc. Ewins and Pickrel give details of modal pre-tests in their works [30, 32]. Pavic and Reynolds demonstrated that the development of a relatively crude initial FE model prior to modal testing may be used for test planning and this can provide better quality of the experimental data [33].

There are also some specialised studies on helicopter structures. Bielawa gave some guidelines specifically on vibration tests of helicopters and parameter extraction from measured data [8]. Giansante and Flannelly [34] identify structural parameters, such as mass, damping, stiffness, etc., of a simple mathematical model of a helicopter from its dynamic tests and determine natural frequencies and mode shapes of the structure. In the same year, Kenigsberg et. al. performed some shake tests on a full-scale helicopter in which free vibrations of the structure were measured, and developed a FE model of the structure that was capable of predicting accurately the natural frequencies and mode shapes of the complex helicopter structure [35]. Reed and Gabel in their report reviewed the test plan and presented results for a shake test of the Boing Model 360 helicopter [36]. They obtained detailed frequency response and mode shape data for variety of conditions, such as independent excitation at both rotor hubs. Exciting forces were applied at the rotor hubs which encompass all significant actual hub forces and moments. The airframe was suspended so that free-free conditions were simulated and the structure was excited with electrodynamics shakers which permit vertical, lateral, longitudinal, pitch and roll excitation at the hub. Using some accelerometers attached, vertical, lateral and longitudinal measurements were obtained at different locations. So, they measured accelerations and forces, and determined modal parameters from FRFs.

Howland et. al. made shake tests of Sikorsky UH-60A helicopter by suspending the helicopter at its main and tail rotor tops with chords and wire cables and exciting the structure primarily at the main rotor hub with swept sine force input [14]. Dompka made some ground tests on Bell AH-1G helicopter and its some components to investigate the so called “difficult components” of the structure [17]. For this, he excited the structure from several locations (not simultaneously) and obtained FRFs and forced response and mode shapes from 0 to 35 Hz. He also made some tests on some isolated components. Modal parameters were obtained using SDOF circle fit and MDOF curve fit analysis capability. Idosor and Seible made some similar ground vibration tests on a sikorsky UH-60A Black Hawk helicopter [15]. In their experiment they gathered modal data leading to the extraction of free-response quantities such as mode shapes/frequencies, damping levels and frequency/time domain response functions. Another work on helicopter structure was done by Kenigsberg et. al. where they suspended a full-scale helicopter fuselage so as to provide free-free condition and used a rotor-head mounted unidirectional shaker and some accelerometers to obtain free vibration characteristics of the structure [35]. They specify that ideally one mode of the fuselage could be determined by the peak and corresponding phase in the quadrature response. Once the natural frequency was determined, all the quadrature responses could be used to determine mode shapes.

Determination of damping values is usually not as easy as other modal parameters. From a theoretical point of view there are different methods to measure damping [37]. These methods are divided in two main groups depending on whether the response of the system is expressed as a function of time or as a function of frequency, i.e. time response methods and frequency-response methods. Logarithmic decrement method, step-response method and hysteretic loop method are time-response methods, whereas magnification-factor method and bandwidth method are frequency-response methods. Logarithmic decrement method is effective when damping of the structure is low. In general, frequency response based methods are more common.

Mielczarek et. al. by exciting a single clamped cantilever beam arrangement by a permanent magnet placed at the end of a coil system, measured the logarithmic decrement of the free decaying bending vibrations to find damping of the structure [37]. Li et. al. [38] employed a time series analysis method to obtain the relationship

between damping and vibration amplitude for a tall building based on full scale measurements on the structure. Lamarque et al. [39] introduced a wavelet-based formula similar to the logarithmic decrement formula to estimate damping for multi-degree-of-freedom systems from time-domain responses. Both analytical and numerical approaches were investigated. Huang et al. proposed a new approach for identification of modal damping ratios from free vibration response of a linear structure with viscous damping in their paper [40]. In reference [30], [41] and [42] the use of frequency response function based methods were explained in detail.

1.4.4 Correlation, validation and updating

Once the theoretical and experimental models are obtained, data set from these two models can be compared, validated and if it is required and possible, theoretical model is updated via manual-correction or using mathematical tools so-called automatical updating methods. Ewins in his book widely dealt with tools of correlation of two data sets and gave both theoretical and practical applications [30]. Imamovic dealt with validation of large structural dynamic models using modal test data [43]. Fotsch focused on development of valid FE models for structural dynamic analyses using various mathematical tools [44]. Ewins also studied some updating methods [30]. Visser studied updating structural dynamics using frequency response data [45] and Jung studied the same subject using eigensensitivity analysis [46].

Contrary to civil structural engineering [47], in mechanical and aerospace engineering disciplines, studying of prototype models of the structure and its correlation with corresponding FE model is common. Kaewunruen and Remennikov in their work showed that simple analytic and FE models calibrated with experimental data may predict railway track vibration response [48] and specified that for design purposes, complex models may not be practical in the case of field tests. Buehrle et. al, in their paper, focused on validation of various aircraft fuselage structures, such as tail boom [29]. They concluded that beam element models were sufficient for characterizing the dynamic response of the continuous cross-section longitudinal stringers in their study. However, they stated that the stringers should be modelled with plate elements at higher levels of assembly to incorporate a proper attachment of skins and stringers and validate some models up to relatively high frequencies (up to 1000 Hz).

In earlier studies, model updating was carried out by means of direct intervention and modification of the theoretical model [49]. Model updating or FE computational model updating emerged in the 1990s. Aircraft structure FE models were updated or improved using manual correction approach. Göge [49] in his paper use the inverse sensitivity approach to minimize the differences between theoretical and measured eigenfrequencies and mode shapes of aircraft models. Zivanovic et. al. in their paper, built up a detailed initial FE model of a lively footbridge structure based on available design data and best engineering judgement [47]. In another study on the same structure they stated that for automatical updating, a manual correction was required on the first FE model to obtain a reasonably initial FE model [50]. Kozak et. al used frequency resonse function method and sensitivty method to update some practical models, such as a plane test model [51]. Twomey et. al, in their paper, presented a general method to systematically modify the element properties in a finite element model to improve structural dynamics correlation with modal test results and apply the method to a UH-60A Black Hawk helicopter [52]. But they encountered difficulties in finding a solution due to numerical problems.

1.4.5 Concluding remarks

The scope of the literature survey of this thesis was summarised under different sections, including the modelling of helicopter or similar structures, correlation, validation and updating of these structures. However, it is seen that most of these are not directly related to helicopter structures although most of the methods are general. In general, the studies performed on the measurement, modelling and analyses of helicopter structures have commercial implications, hence it is not possible to find detailed information applicable to helicopters directly. In the literature (books, journal papers, conference papers, and some scientific papers, etc.) mostly general information about these structures are encountered.

1.5 Motivation, Objective and Scope

As it was mentioned before, helicopter structures are very complex structures. Also, it is very difficult to rely on mathematical models of these structures for design purposes. So, there is a serious need of:

- proper modelling of helicopter structures,

- validation and improving of these models using experimental data,

- performing detailed analyses,

- determine/optimise design parameters.

The overall objectives of this thesis are to build up, correlate, validate and improve theoretical models of some helicopter related structures, ranging from the simple ones to the most complicated helicopter fuselage using the results of modal tests, so that these models can be used for design, optimization and certification purposes with higher level of confidence and provide experimental (real) data/knowledge for better designs of helicopter structures. The specific objectives for this research can be listed as:

- define the problem and propose an approach for validation of FE models of helicopter structures with riveted joints,
- obtain a validated FE model for some simple riveted structures using modal test results (build up a simple FE model for riveted joints that yield acceptable accuracy)
- apply validated FE model for riveted structures to more complex helicopter structures, such as tail boom section, etc.,
- perform detailed modal tests on a helicopter tail boom and build up some FE models of the tail boom,
- compare and correlate FE and experimental modal analysis results of the helicopter tail boom and validate its FE model,
- perform modal tests on a helicopter airframe and compare experimental results with those of corresponding FE models,
- improve FE model of the helicopter airframe,
- comment on design considerations of the helicopter tail boom and airframe.

In what follows, main theories on theoretical modelling, experimental modal analysis, comparison and correlation of theoretical and experimental results and model updating are summarised in the second chapter. Third chapter presents case studies, ranging from some simple structures to very complex helicopter structures, such as tail boom. In this section, mainly theoretical (FE) and experimental modal analyses results of some structures are compared and correlated, and validated FE models of the structures with riveted joints are obtained. Fourth chapter is devoted to modal tests and theoretical modelling of a helicopter airframe. In the last chapter, some concluding remarks given and some comments are made on design considerations of the interested helicopter airframe.

2. THEORY

2.1 Finite Element Modelling

2.1.1 Introduction

In theoretical mechanics, there are two methods; synthetic method and analytical method [53, 54]. Synthetic method can also be called Newton approach in which the system is divided into its discrete elements and Second Law of Newton is written for each of these. In this approach, forces and displacements are main definitions. On the other hand, in analytical approach, system is considered as a whole and its main definitions are kinetic energy and work. Analytical method is utilized from d'Alembert principle, virtual work principle, Lagrange equations, Hamilton principle etc.

Examination of real mechanical systems is performed by building up their mathematical models. Mathematical model should be as simple as possible. However, it must have an acceptable level of simulation capability of the real system. Mathematical models of mechanical systems are divided into two groups according to determining their physical characteristics; discrete and continuous.

In discrete systems, physical properties of components of system are discrete values. Behaviours of these systems are represented with finite number of ordinary differential equations. As a simple example, a single degree of freedom system is given in Figure 2.1a and its differential equation in (2.1a). In solution of discrete systems, matrix methods are widely utilized.

$$m\ddot{x}(t) + c\dot{x}(t) + kx(t) = F(t) \qquad \textbf{(2.1a)}$$

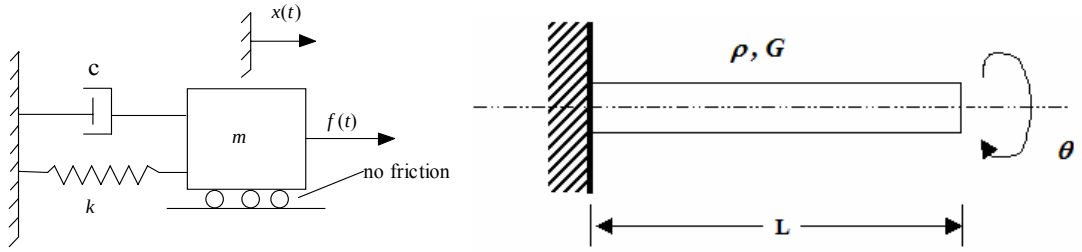

(a) **(b)**

Figure 2.1 : a) A Discrete System, b) A Continuous System – Circular Shaft

Continuous systems are those which have infinite number of DOFs. Their behaviours are represented by partial differential equations or sometimes by integral equations. A circular shaft that makes torsional vibration given Figure 2.1b is an example of a continuous system and its differential equation is given in (2.1b). The differential equations for simple continuous systems can be solved using analytical methods while in practice widely FE method is used for modeling more complex structures.

$$\frac{\partial^2\theta(x,t)}{\partial t^2} = \left(\frac{G}{\rho}\right)\frac{\partial^2\theta(x,t)}{\partial x^2} \qquad \textbf{(2.1b)}$$

Only simple and well-defined systems can be solved with analytical methods with a number of assumptions. However, real systems are complex and analytical methods can very rarely be used to obtain analytical solutions. In practice, FE method is widely used for modeling and solution of real structures. It is simply based on dividing continuous systems into well-defined finite elements. By assembling these elements, a continuous structure is approximated. Before dealing with FE method of real structures, modeling and dynamic analyses of single and multiple degree of freedom systems are presented in the next sections.

Systems are also classified as linear and nonlinear systems. It is well-known that the response of a system is a function of those characteristics of the system. In the case of linear systems, dependent variables which determine the system behaviour are first order and their behaviours are represented with linear differential equations. On the other hand, in the case of nonlinear systems, dependent variables may be available at different orders and their behaviours are represented with nonlinear differential equations [53]. The linearity or nonlinearity of a system can simply be

determined using the rules of the principle of superposition. That is, if the response of the system under two forces is equal to the sum of the responses of the each force, the system is said to be linear, if not the system is nonlinear.

2.1.2 Single degree of freedom systems

All real systems are continuous systems and, in practice they are usually represented as multi degree of freedom systems. However, as MDOF systems are assumed the sum of individual SDOF systems according to superposition principle, understanding of these SDOF systems is important.

2.1.2.1 Undamped SDOF systems

An undamped system is the one whose damping is assumed to be zero. If the viscous damping coefficient, c, in Figure 2.1a is taken zero, this system represents an undamped SDOF system. Equation of motion of such system is as in Eq. (2.2).

$$m\ddot{x}(t) + kx(t) = f(t) \tag{2.2}$$

In the case of free vibration, this equation becomes:

$$m\ddot{x}(t) + kx(t) = 0 \tag{2.3}$$

As the system will make harmonic motion at its natural frequency, ω_r with $x(t) = Xe^{i\omega_r t}$, from Eq. (2.3), Eq. (2.4) can be written and natural frequency of the system is found as in (2.5).

$$k - m\omega_r^{\,2} = 0 \tag{2.4}$$

$$\omega_r = \sqrt{\frac{k}{m}} \tag{2.5}$$

In the case of harmonic excitation with a driving force, $f(t) = Fe^{i\omega t}$ and corresponding response at steady state $x(t) = Xe^{i\omega t}$, from (2.2), the expression in (2.6) can be written.

$$\left(k - m\omega^2\right)Xe^{i\omega t} = Fe^{i\omega t} \tag{2.6}$$

So, the Frequency Response Function (FRF) of the system is found as

$$\alpha(\omega) = \frac{X}{F} = \frac{1}{k - m\omega^2} \tag{2.7}$$

where $\alpha(\omega)$ represents frequency response function in receptance format.

2.1.2.2 Damped SDOF systems

Free vibration of the viscously damped system in Figure 2.1a is given as

$$m\ddot{x}(t) + c\dot{x}(t) + kx(t) = 0 \tag{2.8}$$

As the system is damped, it is assumed that the system makes free vibration with $x(t) = Xe^{st}$, where s is a complex number. If the assumed solution is substituted into Eq. (2.8) and after simplification, this leads to:

$$ms^2 + cs + k = 0 \tag{2.9}$$

The solution of Eq. (2.9) for s yields

$$s = -\omega_r \xi \mp i\omega_d \tag{2.10}$$

where ω_r is undamped natural frequency, ξ is viscous damping ratio and ω_d is damped natural frequency of the system. Their expressions are as follow.

$$\omega_d = \omega\sqrt{1 - \xi^2}\ , \tag{2.11}$$

$$\xi = \frac{c}{c_{cr}} = \frac{c}{2\sqrt{km}} \tag{2.12}$$

where c_{cr} is critical damping. So, free vibration expression can be written as follows.

$$x(t) = Xe^{(-\omega\xi+\omega_d)t} \tag{2.13}$$

$$x(t) = Xe^{-\omega\xi t}e^{\omega_d t} \tag{2.14}$$

where $Xe^{-\omega\xi t}$ shows exponential decay.

In the case of harmonic excitation of damped system with driving force, $f(t) = Fe^{i\omega t}$ and corresponding response at steady state $x(t) = Xe^{i\omega t}$, from (2.1), the expression in (2.15) can be written.

$$\left(k + i\omega c - m\omega^2\right)Xe^{i\omega t} = Fe^{i\omega t} \tag{2.15}$$

So, FRF is determined as follows:

$$\alpha(\omega) = \frac{X}{F} = \frac{1}{\left(k - m\omega^2\right) + i(\omega c)} \tag{2.16}$$

From (2.16), the amplitude and the phase of the FRF can be written as:

$$\left|\alpha(\omega)\right| = \frac{|X|}{|F|} = \frac{1}{\sqrt{\left(k - m\omega^2\right)^2 + (\omega c)^2}} \tag{2.17}$$

$$\angle\alpha(\omega) = \angle X - \angle F = \arctan\left(\frac{-\omega c}{k - m\omega^2}\right) \tag{2.18}$$

2.1.3 Multiple degree of freedom systems

An example of a MDOF viscously damped system with N degree of freedom is shown in Figure 2.2.

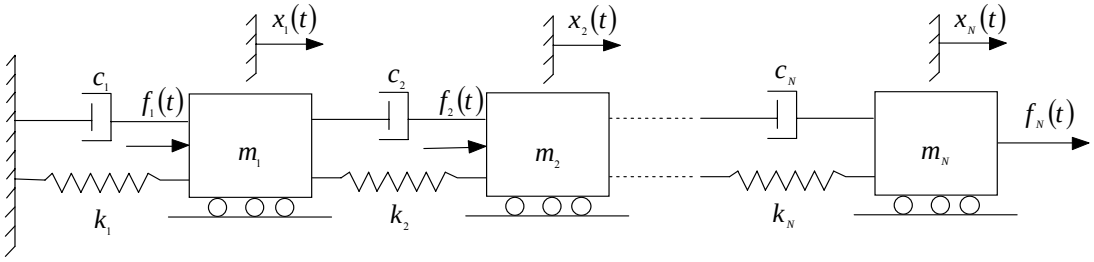

Figure 2.2 : A MDOF System

Equation of motion of MDOF system with N degrees of freedom is given in (2.19).

$$[M]\{\ddot{x}(t)\}+[C]\{\dot{x}(t)\}+[K]\{x(t)\}=\{f(t)\} \quad \textbf{(2.19)}$$

where $[M]$, $[C]$ and $[K]$ are respectively mass, damping and stiffness matrices of this system, and $\{\ddot{x}(t)\}$, $\{\dot{x}(t)\}$ and $\{x(t)\}$ are acceleration, velocity and displacement vectors of the system, respectively.

Damping level for most structures is such that the damped natural frequencies are very nearly equal to the undamped natural frequencies. Thus, if only the natural frequencies of the structure are required, damping can usually be neglected in the modal analysis as this offers a significant simplification. Additionally, "if the harmonic response of a structure at a frequency well away from a resonance is required, a similar simplification can also be made in the analysis. However, if the response of a structure at a frequency in the region of the resonance is required, which would be the case if the amplitude or dynamic stress levels at the resonance were required; damping effects must be included in the analysis. Coulomb and hysteretic damping can be difficult to analyze exactly, particularly in multi-degree of freedom systems, but approximations can be made to linearize the equations of motion. For example, an equivalent viscous damping coefficient for equal energy dissipation may be assumed or alternatively the nonlinear damping force may be replaced by an equivalent harmonic force or series of forces" [41].

By taking viscous damping coefficient in Figure 2.2 as zero, the equation of motion and free vibration equation are as in (2.20) and (2.21) respectively.

$$[M]\{\ddot{x}(t)\}+[K]\{x(t)\}=\{f(t)\} \quad \textbf{(2.20)}$$

$$[M]\{\ddot{x}(t)\}+[K]\{x(t)\}=0 \quad \textbf{(2.21)}$$

Assuming that system makes free vibration with, $\{x(t)\}=\{X\}e^{i\omega_r t}$ where $\{X\}$ is amplitude vector of dimensions Nx1; the expression in (2.22) is obtained.

$$([K]-\omega^2[M])\{X\}e^{i\omega_r t}=\{0\} \quad \textbf{(2.22)}$$

Accordingly to have non-singular solutions, the expression (2.23) should satisfy.

$$\det([K]-\omega_r^2[M])=0 \quad \textbf{(2.23)}$$

Solution of (2.23) gives natural frequencies $\omega_{r1}, \omega_{r2}, \omega_{r3}, ..., \omega_{rN}$. By inserting these values one by one into (2.22), corresponding amplitude vectors that are mode shapes, $\{\Psi_1\}, \{\Psi_2\}, \{\Psi_3\}, ..., \{\Psi_N\}$ can be found.

Mostly numerical methods have to be used for the solution of multi degree of freedom systems. These methods can be used with a computer to solve the frequency equation in (2.23) and to determine the mode shapes.

2.1.4 Finite Element Modelling

2.1.4.1 Introduction

FE method is based on dividing a continuous structure into sufficiently small and simple pieces called elements whose connections are defined using nodes, so that it is possible to calculate their individual behaviors reasonably accurately (55). Thus, a complicated structure is modelled as an assembly of large number of simple pieces or elements. Figure 2.3 shows approximation of an arbitrarily shaped structure by idealized elements.

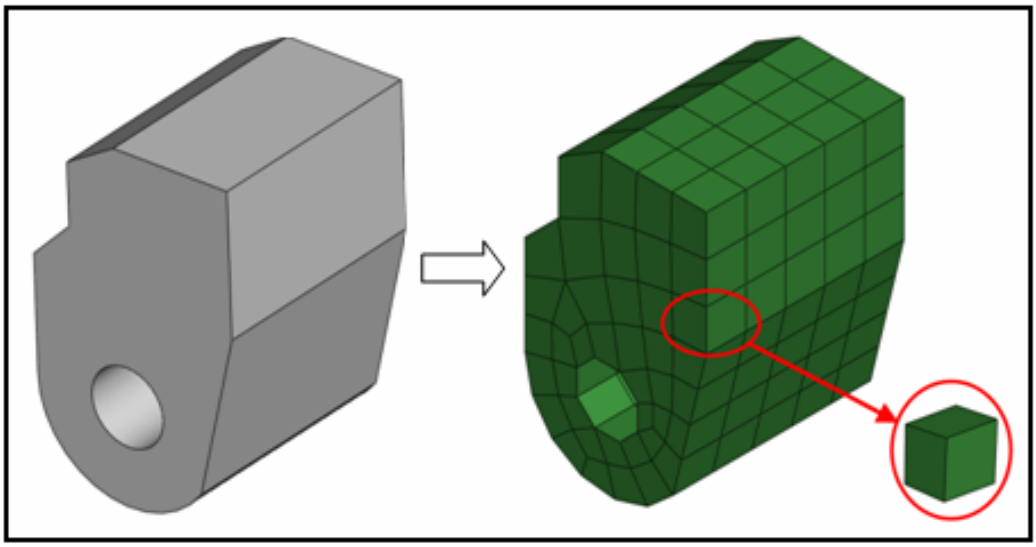

Figure 2.3 : Approximation of an Arbitrarily Shaped Structure by Idealized Elements

Although the theory of elasticity gives exact solution procedure, it is very difficult to obtain related solutions for most of real structures and im practice FE method is widely used. FE method is based on finding approximate solutions of partial differential equations as well as of integral equations. The solution approach is based either on eliminating the differential equation, or rendering the partial differential equations into an approximating system of ordinary differential equations, which are then solved using standard solution techniques.

The development of the FE method in structural mechanics is often based on energy principles, e.g., the virtual work principle or the minimum total potential energy principle.

2.1.4.2 FE formulation

In FE procedure, it is mainly aimed to determine the distribution of displacements and stresses under the loading and boundary conditions in structural mechanics. To develop a mathematical model using FE, it is essential to understand the basic equations of structural mechanics.

Let's consider the arbitrarily shaped 3-D solid body in Figure 2.4.

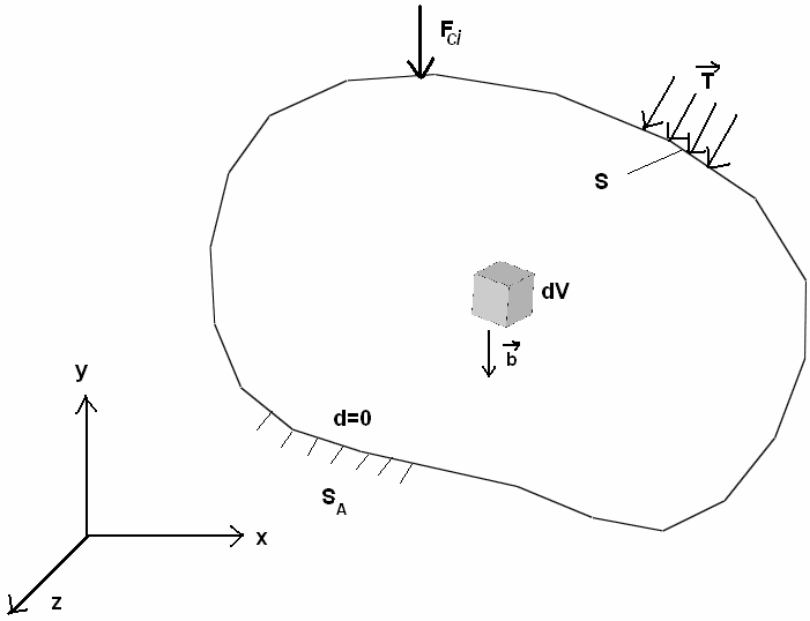

Figure 2.4 : A General Solid Body under Loads

The body is supported and under loads such as body forces per unit volume $\vec{b}$, surface loads per unit area $\vec{T}$ and, concentrated forces $\vec{F}_{ci}$, the body deforms and strains and stresses are developed in the body. The relation between strains and displacements is as in (2.24)

$$\{\varepsilon\} = \begin{Bmatrix} \varepsilon_{xx} \\ \varepsilon_{yy} \\ \varepsilon_{zz} \\ \varepsilon_{xy} \\ \varepsilon_{yz} \\ \varepsilon_{zx} \end{Bmatrix} = \begin{bmatrix} \frac{\partial}{\partial x} & 0 & 0 \\ 0 & \frac{\partial}{\partial y} & 0 \\ 0 & 0 & \frac{\partial}{\partial z} \\ \frac{\partial}{\partial y} & \frac{\partial}{\partial x} & 0 \\ 0 & \frac{\partial}{\partial z} & \frac{\partial}{\partial y} \\ \frac{\partial}{\partial z} & 0 & \frac{\partial}{\partial x} \end{bmatrix} \begin{Bmatrix} u(x,y,z) \\ v(x,y,z) \\ w(x,y,z) \end{Bmatrix} = [\partial]\{d\} \qquad \textbf{(2.24)}$$

where $\{\varepsilon\}$, $[\partial]$ and $\{d\}$ are strain vector, derivative matrix and displacement vector, respectively. Stress-strain relations for linearly elastic isotropic 3-D solid can be written as

$$\{\sigma\}=\begin{Bmatrix}\sigma_{xx}\\ \sigma_{yy}\\ \sigma_{zz}\\ \sigma_{xy}\\ \sigma_{yz}\\ \sigma_{zx}\end{Bmatrix}=\frac{E}{(1+\nu)(1-2\nu)}\begin{bmatrix}1-\nu & \nu & \nu & 0 & 0 & 0\\ \nu & 1-\nu & \nu & 0 & 0 & 0\\ \nu & \nu & 1-\nu & 0 & 0 & 0\\ 0 & 0 & 0 & \frac{1}{2}(1-2\nu) & 0 & 0\\ 0 & 0 & 0 & 0 & \frac{1}{2}(1-2\nu) & 0\\ 0 & 0 & 0 & 0 & 0 & \frac{1}{2}(1-2\nu)\end{bmatrix}\begin{Bmatrix}\varepsilon_{xx}\\ \varepsilon_{yy}\\ \varepsilon_{zz}\\ \varepsilon_{xy}\\ \varepsilon_{yz}\\ \varepsilon_{zx}\end{Bmatrix}=[D]\{\varepsilon\} \quad \textbf{(2.25)}$$

where $[D]$ and $\{\sigma\}$ are respectively matrix of elastic coefficients and stress vector.

In FE formulation, the essential thing is the approximation of the displacement field of an element by using interpolation functions and nodal displacements as given below

$$\{d\}=\begin{Bmatrix}u(x,y,z)\\ v(x,y,z)\\ w(x,y,z)\end{Bmatrix}=[N]\{q\} \quad \textbf{(2.26)}$$

where $[N]$ and $\{q\}$ are shape function matrix and the nodal displacement vector, respectively. So, strain and stress vectors can be rearranged as in (2.27) and (2.28) using (2.26)

$$\{\varepsilon\}=[\partial]\{d\}=[\partial][N]\{q\}=[B]\{q\} \quad \textbf{(2.27)}$$

$$\{\sigma\}=[D]\{\varepsilon\}=[D][B]\{q\} \quad \textbf{(2.28)}$$

where $[B]$ is the transformation matrix from displacements to strains .

To establish equilibrium equations, various methods such as, principle of minimum potential energy, principle of virtual work etc. can be used [55-57]. Here, principle of minimum potential energy is utilized. However, firstly potential energy expression for an element, which is the sum of its strain energy and work done on it by external forces, should be developed. Strain energy, U_e, for an element can be developed as follow.

$$U_e = \frac{1}{2}\int_{V_e} \{\varepsilon\}^T [D]\{\varepsilon\} dV$$

$$U_e = \frac{1}{2}\int_{V_e} \{q\}^T [B]^T [D][B]\{q\} dV$$

$$U_e = \frac{1}{2}\{q\}^T \int_{V_e} [B]^T [D][B] dV \{q\}$$

$$U_e = \frac{1}{2}\{q\}^T [k]\{q\} \qquad \textbf{(2.29)}$$

where $[k]$ is element stiffness matrix and it is definition is as in (2.30).

$$[k] = \int_{V_e} [B]^T [D][B] dV \qquad \textbf{(2.30)}$$

The work done by applied external forces, W_e, can also be written in a similar way as:

$$W_e = -\int_{V_e} \{d\}^T \{b\} dV - \int_S \{d\}^T \{T\} dS$$

$$W_e = -\int_{V_e} \{q\}^T [N]^T \{b\} dV - \int_S \{q\}^T [N]^T \{T\} dS$$

$$W_e = -\{q\}^T \int_{V_e} [N]^T \{b\} dV - \{q\}^T \int_S [N]^T \{T\} dS$$

$$W_e = -\{q\}^T \{f_B\} - \{q\}^T \{f_S\} \qquad \textbf{(2.31)}$$

where $\{f_B\}$ is element body force vector and $\{f_S\}$ is element surface load vector, and their expression are respectively as in (2.32) and (2.33).

$$\{f_B\} = \int_{V_e} [N]^T \{b\} dV \qquad \textbf{(2.32)}$$

$$\{f_S\} = \int_S [N]^T \{T\} dS \tag{2.33}$$

Then, the potential energy of an element can be written as in (2.34).

$$\Pi_e = U_e + W_e = \frac{1}{2}\{q\}^T [k]\{q\} - \{q\}^T \{f_B\} - \{q\}^T \{f_S\} \tag{2.34}$$

where Π_e is potential energy of an element. It should be noted that, a FE model may contain many individual elements; hence potential energy of the entire model is the sum of the potential energy of all the individuals. Hence, potential energy of the entire model can be written as

$$\Pi = \sum_{e=1}^{E} \Pi_e - \{Q\}^T \{F_c\} \tag{2.35}$$

where Π is potential energy of the entire model and $\{Q\}$ is the vector of nodal displacements of the entire model as given in (2.36).

$$\{Q\}^T = \{Q_1 \quad Q_2 \quad . \quad . \quad Q_N\} \tag{2.36}$$

So, the potential energy of the entire model can be written as follow.

$$\Pi = \frac{1}{2}\sum_{e=1}^{E} \{q\}^T [k]\{q\} - \sum_{e=1}^{E} \{q\}^T \{f_B\} - \sum_{e=1}^{E} \{q\}^T \{f_S\} - \{Q\}^T \{F_c\}$$

$$\Pi = \frac{1}{2}\{Q\}^T [K]\{Q\} - \{Q\}^T (\{F_B\} + \{F_S\} + \{F_c\})$$

$$\Pi = \frac{1}{2}\{Q\}^T [K]\{Q\} - \{Q\}^T \{F\} \tag{2.37}$$

where $[K]$ is the global stiffness matrix and $\{F\}$ is the global load vector. These are obtained by assembly of individual elements as in (2.38) and (2.39)

$$[K] = \sum_{e=1}^{E} k_e \tag{2.38}$$

$$\{F\} = \sum_{e=1}^{E} \left(\{f_B\} + \{f_S\} \right) + \{F_c\} \tag{2.39}$$

The sum operator in (2.38) and (2.39) denotes assembly procedure. Finally, the static equilibrium equations of the entire model can be obtained using principle of minimum potential energy as in (2.40)

$$\frac{\partial \Pi}{\partial Q_i} = 0 \qquad i = 1,2,3,...N \tag{2.40}$$

Hence, by inserting (2.37) into (2.40), the equation of the entire model is obtained and the static solution can be obtained as:

$$\{Q\} = [K]^{-1} \{F\} \tag{2.41}$$

2.1.4.3 Dynamic analysis of FE models

In global view, analyses performed on structures can be divided into two groups: static and dynamic analysis. Static analyses hold when loads are time independent (or, applied so slowly). In the case of the loads are time-dependent, the mass and acceleration effects become important [56-57]. In dynamic analysis, to take into account mass and acceleration effect, mass matrices of finite elements are needed. In the scope of this thesis it is mainly dealt with modal analysis. So in the next section, how to obtain the mass matrices of finite elements and mass matrix of an entire structure is described, the equations of motion of a general FE model are derived and generalized eigenvalue problem is introduced.

Hamilton's principle may be used for formulation of mechanical problems. It states that, in conservative systems, for an arbitrary time interval from t_1 to t_2, the state of motion of a body extremizes the time integral of Lagrangean function, L, in t_1 to t_2 [53-58] as in (2.42).

$$I = \int_{t_1}^{t_2} L dt : Extremum \tag{2.42}$$

The variation of expression above is also zero [53] as:

$$I = \delta \int_{t_1}^{t_2} L dt = 0 \tag{2.43}$$

The Lagrangean is defined as

$$L = T - \Pi \tag{2.44}$$

where T is kinetic energy and Π is potential energy. The Lagrangean can be expressed in terms of the generalized variables, $q_1, q_2, ..., q_n, \dot{q}_1, \dot{q}_2, ..., \dot{q}_n$, and then from (2.43), (2.45) can be written for a n degrees of freedom discrete system [56]

$$\frac{d}{dt}\left(\frac{\partial L}{\partial \dot{q}_i}\right) - \frac{\partial L}{\partial q_i} = 0 \qquad i = 1 \text{ to } n \tag{2.45}$$

where $\dot{q}_i = dq/dt$.

For a solid element of volume V and density ρ kinetic energy may be written as

$$T = \frac{1}{2}\int_v \left\{\dot{d}\right\}^T \left\{\dot{d}\right\} \rho dV \tag{2.46}$$

where $\left\{\dot{d}\right\}$ is velocity vector of the mass distributed point and given by the expression:

$$\left\{\dot{d}\right\} = \left\{\dot{u} \quad \dot{v} \quad \dot{w}\right\}^T \tag{2.47}$$

In the case of FE method, the structure is divided into finite elements and similar to the procedure in section 2.1.4.2, $\{d\}$ is expressed for each element in terms of nodal displacements and shape functions as in (2.48).

$$\{d\} = [N]\{q\} \tag{2.48}$$

In dynamic analysis, q is time-dependent and by inserting (2.48) into (2.46), the kinetic energy of a finite element can be written as

$$T^e = \frac{1}{2}\{\dot{q}\}^T [m]^e \{\dot{q}\} \tag{2.49}$$

where $[m]^e$ is element mass matrix which is be obtained as

$$[m]^e = \int_{V^e} \rho \{N\}^T \{N\} dV \tag{2.50}$$

Summation of kinetic energies of all the individual elements gives entire kinetic energy of the structure as in (2.51)

$$T = \sum_e^E T^e = \sum_e^E \frac{1}{2}\{\dot{q}\}^T [m]^e \{\dot{q}\} = \frac{1}{2}\{\dot{Q}\}^T [M]\{\dot{Q}\} \tag{2.51}$$

Once kinetic energy and potential energy are found, Lagrangean can be written, and using the expression (2.45), the equation of motion can be written as

$$[M]\{\ddot{Q}\} + [K]\{Q\} = \{F\} \tag{2.52}$$

In the case of free vibration $\{F\} = \{0\}$, thus, the expression in (2.53) is obtained.

$$[M]\{\ddot{Q}\} + [K]\{Q\} = \{0\} \tag{2.53}$$

As Chandrupatla states for steady-state condition and starting from the equilibrium state [56], it is assumed that

$$\{Q\} = \{X\} \sin \omega t \tag{2.54}$$

where $\{X\}$ is the vector of the nodal amplitudes of the vibration and ω is the circular natural frequency known as eigen frequency. Inserting (2.54) into (2.53) yields

$$[K]\{X\} = \omega^2 [M]\{X\} \tag{2.55}$$

where $\omega^2 = \lambda$, eigenvalue. This is the general eigenvalue problem expression and it is solved so that eigenvalues λ and the vector $\{X\}$ which corresponds to vibrating mode of the related eigenvalue are found.

As stated in [56], the previous equations can also be obtained by using D'Alembert's principle and the principle of virtual work. Galerkin's approach applied to equations of motion of an elastic body also yields this set of equations.

In the FE formulation above, damping is not taken into consideration, although all materials have some damping. However, mostly used materials such as, steel, aluminum have very little internal damping. In practice, mostly modal analysis is performed by assuming zero damping and it provides important simplifications. However, in some applications such as free and constrained viscoelastic composites, damping level is high. In such cases, it is essential to model damping anyway [59].

2.1.4.4 Solution methods

There are various methods including sub space iteration and Lanczos methods [60-62] for the solution of eigenvalue problem given in Section 2.1.4.3. In the scope of this thesis, mostly, Lanczos method is used. Lanczos method is widely used in the structural vibration applications for solution of eigenvalue problem. It can determine the required number of eigenvalues and corresponding eigenvectors with minimum number of iterations [60-61]. This method is a type of the power methods in which iteration begins with an initial vector.

2.1.4.5 Properties of mode shapes

The mass matrix obtained in the previous section is symmetric and positive definite in the problems of interest here [61]. A matrix is positive definite if the expression (2.56) holds for every nonzero choice of the vector $\{x\}$ [31].

$$\{x\}^T [M]\{x\} > 0 \quad \textbf{(2.56)}$$

The stiffness matrix which may include large-displacement effects, such as "stress stiffening", and, therefore, may not be positive definite or symmetric. But eigenvalue problem may be symmetrized by assuming that stiffness matrix is symmetric. Also, in the problems of interest here, for symmetric eigenproblems, stiffness matrix is assumed to be positive semi definite [61]. As a result, the solution of the eigenvalue problem gives natural frequencies $\omega_{r1}, \omega_{r2}, \omega_{r3}, ..., \omega_{rN}$ and mode shapes $\{\Psi_1\}, \{\Psi_2\}, \{\Psi_3\}, ..., \{\Psi_N\}$. These mode shapes have some important properties.

Let say eigenvalue problem given by (2.55) have two solutions ω_r, $\{\Psi\}^r$ and ω_s, $\{\Psi\}^s$, That is,

$$([K] - \omega_r^2 [M])\{\Psi\}_r = \{0\} \quad \textbf{(2.57)}$$

$$([K] - \omega_s^2 [M])\{\Psi\}_s = \{0\} \quad \textbf{(2.58)}$$

Let us premultiply the first equation with $\{\Psi\}_s^T$ and transpose the second equation and postmultiply the second equation with $\{\Psi\}_r$ as in (2.59) and (2.60).

$$\{\Psi\}_s^T ([K] - \omega_r^2 [M])\{\Psi\}_r = \{0\} \quad \textbf{(2.59)}$$

$$\{\Psi\}_s^T ([K]^T - \omega_s^2 [M]^T)\{\Psi\}_r = \{0\} \quad \textbf{(2.60)}$$

Remembering that $[K]$ and $[M]$ matrices are symmetric and they are identical to their transposes, by subtracting (2.59) from (2.60), following equation is obtained.

$$\left(\omega_r^2 - \omega_s^2\right)\{\Psi\}_s^T[M]\{\Psi\}_r = \{0\} \tag{2.61}$$

Let's now assume that eigenfrequencies ω_r and ω_s are different from each other. In this case

$$\{\Psi\}_s^T[M]\{\Psi\}_r = \{0\}; \quad r \neq s \tag{2.62}$$

This is the expression for the so-called ***orthogonality property***. (2.59) and (2.60) orthogonality property also can be written as

$$\{\Psi\}_s^T[K]\{\Psi\}_r = \{0\}; \quad r \neq s \tag{2.63}$$

when $r = s$, it means $\omega_r = \omega_s$, equations (2.62) and (2.63) do not apply, but from (2.59) the expression in (2.64) can be written.

$$\{\Psi\}_r^T[K]\{\Psi\}_r = \omega_r^2\left(\{\Psi\}_r^T[M]\{\Psi\}_r\right) \tag{2.64}$$

with $\left[\omega_r^2\right] = [m_r]^{-1}[k_r]$, the expression (2.65) and (2.66) are obtained.

$$[\Psi]^T[M][\Psi] = [m_r] \tag{2.65}$$

$$[\Psi]^T[K][\Psi] = [k_r] \tag{2.66}$$

Here $[m_r]$ and $[k_r]$ are called respectively modal mass and modal stiffness matrices and they are diagonal matrices [30]. These have no unique values, but the ratio between any modal mass and its corresponding modal stiffness is the same, and this ratio gives eigenvalue or squared natural frequency. Mostly, mode shapes are normalized so that normalized mode shapes satisfy expression (2.67) and thereby (2.68).

$$[\phi]^T [M][\phi] = [I] \quad \textbf{(2.67)}$$

$$[\phi]^T [K][\phi] = [\omega^2] \quad \textbf{(2.68)}$$

So, normalized mode shape can be written in terms of arbitrarily scaled mode shape and modal mass as in (2.69).

$$[\phi] = [\Psi]\left[m_r^{-1/2}\right] \quad \textbf{(2.69)}$$

where $[\phi]$ is the normalized mode shape matrix.

2.2 Experimental Modal Analysis Approach

2.2.1 Introduction

Regardless of the physical details of a system, it is important to know [63]:

- response of the system with respect to time under any special disturbance,
- damping characteristic of the system when a disturbance is given for a time and then removed this disturbance,
- the system becomes stable or unstable when the disturbance removed
- which modifications for some practical applications result in better dynamic characteristics.

Frequency Response Functions (FRFs) are widely used to model mechanical vibrational systems in frequency domain [64]. Presentation of a vibrational system in frequecy domain is useful, especially in the case of analysis, design, control and tests. Furthermore, it is possible to obtain modal parameters of a structure by analysing FRFs measured on the structure, which is known as the modal testing procedure.

In modal analysis it is aimed to find modal parameters, in other words, natural (modal) frequencies, mode shapes and modal damping values using various parameter estimation methods which are widely explained by Ewins in his book [30]. In this procedure, responses of the structure under some special excitations are measured in time domain. Using Fourier transformation analyses, time domain data are transformed into frequency domain, that is, spectrums of the signals are obtained. If the excitation force is also measured, FRFs are calculated. In structural response measurements, Fast Fourier Transformation (FFT) analysis is mostly used, because of its high effectiveness.

2.2.2 Experimental modal analysis

Experimental modal analysis or modal testing can be defined as "derivation of a mathematical model from measured data to describe the dynamic properties of a structure" [30, 65]. Modal analysis method can be classified into different categories. According to data domain used to extract parameters, they divided into two groups:

- Frequency Domain Methods
- Time Domain Methods

Frequency domain methods are based on extracting modal parameters from FRFs while time domain methods are based on extracting parameters from Impulse Response Functions (IRFs). On the other hand, according to dealing with only one mode or all modes in the related frequency range, modal analysis methods are divided into two groups:

- Single Degree Of Freedom (SDOF) Methods
- Multi Degree of Fredom (MDOF) Methods.

In the case of SDOF methods, modal properties of one of the system's modes are extracted at a time by dealing with that resonance and all the modes in the frequency range are analyses one by one. On the other hand, in the case of MDOF methods, parameters of several modes can be extracted at a time. These methods are more practical, and have many advantages on SDOF methods, such as being able to analyse more accurately closely-coupled modes [30-Ewins].

Another classification is related to the number of FRFs which are used in a single analysis.

- Single FRF Methods
- Multi FRF Methods

As their names specify, in the case of single FRF methods only a single FRF is utilized, while many FRFs are used in the case of multi FRF methods to extract parameters. Multi FRF Methods also are divided into further two groups: Single Input Multi Output (SIMO) methods and Multi Input Multi Output (MIMO) methods. Responses are measured on the structure with exciting the structure at single point in the case of SIMO methods and at more than one point in the case of MIMO methods.

2.2.3 Peak-Peacking method

The peak-peacking method is the simplest modal analysis method of frequency domain which is used to obtain resonant frequencies, mode shapes and damping values from FRFs measured on the structure whose modes are relatively well-separated [79].

In this method, individual resonance peaks are detected firstly on the FRF plot. The frequency of one of the maximum responses corresponds to the modal frequency of that individual mode [30]. The half power method may be used to determine damping. Half power points are defined as the two frequencies where the response is $1/\sqrt{2}$ of the resonance [79]. By remembering the receptance equation for a SDOF model, the maximum response at the undamped natural frequency, ω_r, is given as in (2.70).

$$|\alpha| = 1/c\omega_r = 1/2\zeta k \qquad \textbf{(2.70)}$$

Remembering the definition of the half power points, the frequencies correspond to half power points (ω_a, ω_b) are in relation with η_r and ω_r as in (2.71)

$$\eta_r = 2\zeta_r = \frac{\omega_a^2 - \omega_b^2}{2\omega_r^2} \tag{2.71}$$

For small η_r (<0.2), damping is approximated as in (2.72)

$$\eta_r \cong \frac{\omega_a - \omega_b}{\omega_r} = \frac{\Delta\omega}{\omega_r} \tag{2.72}$$

Lastly, by assuming that the overall response in the resonant of the interest is attributed to a single term in the general FRF series in the equation (2.73) [30], modal constant is found as in (2.74).

$$\alpha_{jk}(\omega) = \frac{{}_rA_{jk}}{\omega_r^2 - \omega^2 + i\eta_r\omega_r^2} + \sum_{s=1}^{N} \frac{{}_sA_{jk}}{\omega_s^2 - \omega^2 + i\eta_s\omega_s^2} \tag{2.73}$$

$$A_r = \left|\hat{\alpha}\right| \eta_r \omega_r^2 \tag{2.74}$$

2.2.4 Circle-Fit method

The basic function of a system which has structural damping is as in (2.75).

$$\alpha(\omega) = \frac{1}{\omega_r^2 - \omega^2 + i\eta_r\omega_r^2} \tag{2.75}$$

The effect of consideration of modal constant, ${}_rA_{jk}$, scale the size of the circle by $\left|{}_rA_{jk}\right|$ and rotate it by $\angle {}_rA_{jk}$ [30]. For any frequency, ω the following expressions may be written.

$$\tan\gamma = \frac{\eta_r}{1 - (\omega/\omega_r)^2} \tag{2.76}$$

$$\tan\left(\frac{\pi}{2} - \gamma\right) = \tan\left(\frac{\theta}{2}\right) = \frac{1 - (\omega/\omega_r)^2}{\eta_r} \tag{2.77}$$

from which, the expressions in (2.78) and (2.79) can be written.

$$\omega^2 = \omega_r^2\left(1-\eta_r \tan\left(\theta/2\right)\right) \tag{2.78}$$

$$\eta_r = \frac{\omega_a^2 - \omega_b^2}{\omega_r^2\left(\tan\left(\theta_a/2\right)+\tan\left(\theta_b/2\right)\right)} \tag{2.79}$$

For small η_r (<0.2), damping is approximated as in (2.80)

$$\eta_r \cong \frac{2\left(\omega_a - \omega_b\right)}{\omega_r\left(\tan\left(\theta_a/2\right)+\tan\left(\theta_b/2\right)\right)} \tag{2.80}$$

If ω_a and ω_b are the half power points for which $\theta_a = \theta_b = 90^0$, the expressions simplify to:

$$\eta_r = \frac{\omega_a^2 - \omega_b^2}{2\omega_r^2} \tag{2.81}$$

And if the damping is low:

$$\eta_r \cong \frac{\omega_a - \omega_b}{\omega_r} \tag{2.82}$$

The diameter of the circle is:

$${}_rD_{jk} = \frac{1}{\eta_r \omega_r^2} \tag{2.83}$$

By scaling the size of the circle by $\left|{}_rA_{jk}\right|$, from the diameter modal constant is found as in (2.84).

$$\left|{}_rA_{jk}\right| = \eta_r \omega_r^2\ {}_rD_{jk} \tag{2.84}$$

In the case of the system with viscous damping, mobility is used. Mobility expression for a SDOF system is given in (2.85).

$$V(\omega) = \frac{\dot{x}}{F} = \frac{i\omega}{k - m\omega^2 + ic\omega} \tag{2.85}$$

This expression may be divided into the real and imaginary parts as in the following expressions.

$$\mathrm{Re}(V) = \frac{\omega^2 c}{\left(k - m\omega^2\right)^2 + (c\omega)^2} = X \tag{2.86}$$

$$\mathrm{Im}(V) = \frac{\left(k - m\omega^2\right)}{\left(k - m\omega^2\right)^2 + (c\omega)^2} = Y \tag{2.87}$$

Plotting X against Y results in a circle of radius 1/2c, with its centre at the point (1/2c, 0).

From above expressions, the expressions in (2.88) and (2.89) can be written.

$$\left(X - \frac{1}{2c}\right)^2 + Y^2 = \frac{1}{(2c)^2} \tag{2.88}$$

$$\tan\left(\frac{\theta}{2}\right) = \frac{\omega\left(k - m\omega^2\right)}{c\omega^2} = \frac{1 - (\omega/\omega_r)^2}{(2\zeta\,\omega/\omega_r)} \tag{2.89}$$

Inserting ω_a and ω_b into the expression above, (2.90) can be written

$$\tan\left(\frac{\theta_a}{2}\right) = \frac{1 - (\omega_a/\omega_r)^2}{(2\zeta\,\omega_a/\omega_r)}, \qquad \tan\left(\frac{\theta_b}{2}\right) = \frac{1 - (\omega_b/\omega_r)^2}{(2\zeta\,\omega_b/\omega_r)} \tag{2.90}$$

from which, the expression (2.91) is obtained

$$\zeta = \tan\left(\frac{\theta_b}{2}\right) = \frac{\omega_a^2 - \omega_b^2}{2\omega_r\left(\omega_a \tan\left(\theta_a/2\right) + \omega_b \tan\left(\theta_b/2\right)\right)} \tag{2.91}$$

For light damping, the expression in (2.92) is obtained.

$$\zeta \cong \frac{\left(\omega_a - \omega_b\right)}{\omega_r\left(\tan\left(\theta_a/2\right) + \tan\left(\theta_b/2\right)\right)} \tag{2.92}$$

If ω_a and ω_b are the half power points for which $\theta_a = \theta_b = 90^0$, the expressions simplify to:

$$\zeta \cong \frac{\omega_a - \omega_b}{2\omega_r} \tag{2.93}$$

A typical Circle-Fit analysis procedure performed on a FRF measured on the one of the clamped blade of the ITU-LCH is given in Figure 2.5.

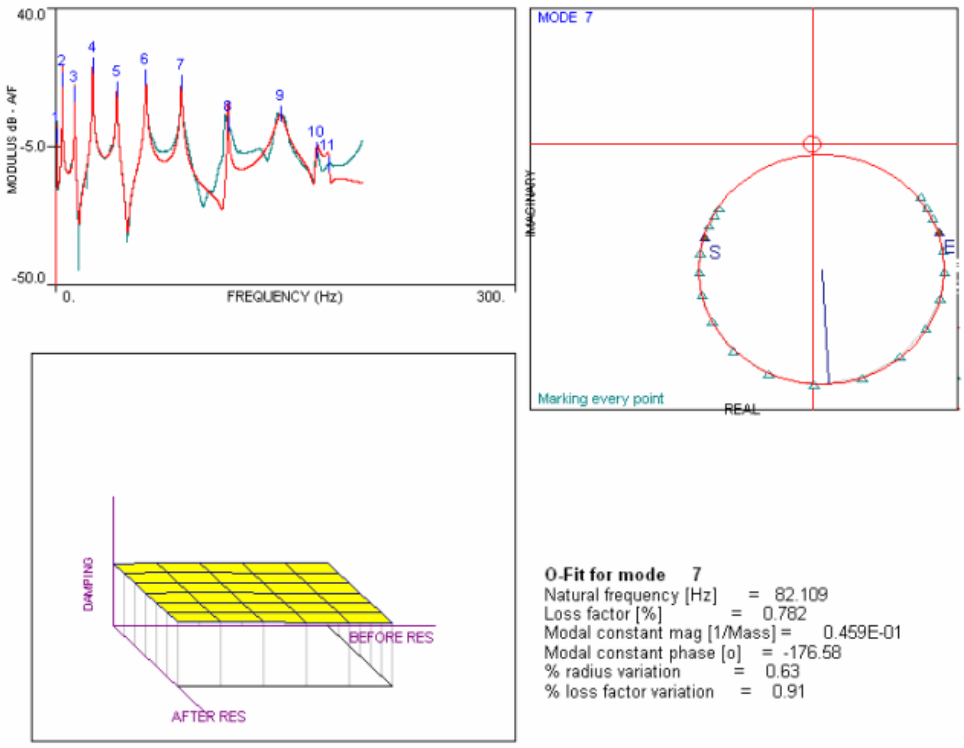

Figure 2.5 : A Typical Circle-Fit Analysis Procedure

2.2.5 Line-Fit method

Line-Fit procedure is outlined as follow [30, 79].

The normal receptance equation and its inverse for a truly SDOF model are given in (2.94) and (2.95), respectively.

$$\alpha(\omega)=\frac{1}{k-m\omega^2+i(c\omega)} \tag{2.94}$$

$$\alpha^{-1}(\omega)=k-m\omega^2+i(c\omega) \tag{2.95}$$

The modal constant A (=1/m) for a SDOF system can be determined from the slope of the real part of the $\alpha^{-1}(\omega)$ plotted against ω^2. This is not possible for a MDOF system [79]. In other words, the corresponding inverse in the case of more than one mode presents is not similarly convenient which means that in reciprocal form the modal series does not apply [30].

The Line-Fit analysis procedure for a MDOF system assumes that around a particular resonance ω_r, with modal constant ${}_rA$ and damping η_r, the response includes a constant residual term R_r which represents the contribution of the modes other than the one of the interest [30, 79] as given in (2.96).

$$\alpha_{jk}(\omega)_{\omega=\omega_r}\cong\frac{{}_rA_{jk}}{\omega_r^2-\omega^2+i\eta_r\omega_r^2}+R_r \tag{2.96}$$

The method define a new FRF term, $\alpha'_{jk}(\omega)$, which is the difference between the actual FRF and the value of the FRF at one fixed frequency in the range of interest ($\alpha_{jk}(\Omega)$) to remove the residual effect [30] as in (2.97).

$$\alpha'_{jk}(\omega)=\alpha_{jk}(\omega)-\alpha_{jk}(\Omega) \tag{2.97}$$

The inverse FRF parameter that will be used for the modal analysis is defined as in (2.98) and for each value of ω near the resonance the expression in (2.99) can be written [30, 79].

$$\Delta(\omega) = \frac{\left(\omega^2 - \Omega^2\right)}{\alpha'_{jk}(\omega)} \tag{2.98}$$

$$\Delta(\omega) = \left(\omega_r^2 - \omega^2 + i\eta_r\omega_r^2\right)\left(\omega_r^2 - \Omega^2 + i\eta_r\omega_r^2\right)\Big/ A_r \tag{2.99}$$

The difference are divided into the real and imaginary parts which are mainly related to the variable frequency, ω, as in (2.100).

$$\mathrm{Re}(\Delta) = m_R\omega^2 + C_R, \qquad \mathrm{Im}(\Delta) = m_I\omega^2 + C_I \tag{2.100}$$

where

$$m_R = a_r\left(\Omega^2 - \omega_r^2\right) - b_r\left(\eta_r\omega_r^2\right), \qquad m_I = -b_r\left(\Omega^2 - \omega_r^2\right) - a_r\left(\eta_r\omega_r^2\right) \tag{2.101}$$

and

$${}_rA_{jk} = a_r + ib_r \tag{2.102}$$

By selecting a fixed frequency Ω_j in the vicinity of the resonance ω_r and then calculate the possible $\Delta(\omega)$ using the remaining measured data points, real and imaginary values are plotted against ω^2. Using least squares fit to compute the best-fit straight line in each case to determine $m_R\left(\Omega_j\right)$ and $m_I\left(\Omega_j\right)$ for the selected fixing frequency, Ω_j. These m_R and m_I parameters are also linear functions of Ω^2 as in (2.103).

$$m_R = n_R\Omega^2 + d_R, \qquad m_I = n_I\Omega^2 + d_I \tag{2.103}$$

where

$$n_R = a_r \qquad \text{and} \qquad n_I = -b_r \tag{2.104}$$

$$d_R = -b_r\left(\eta_r\omega_r^2\right) - a_r\left(\omega_r^2\right) \qquad \text{and} \qquad d_I = -b_r\left(\omega_r^2\right) - a_r\left(\eta_r\omega_r^2\right) \tag{2.105}$$

With $p = n_I / n_R$ and $q = d_I / d_R$, the expressions below can be written.

$$\eta_r = \frac{(q-p)}{1+pq}; \quad \omega_r^2 = \frac{d_R}{(p\eta_r - 1)n_R}; \quad a_r = \frac{\omega_r^2(p\eta_r - 1)}{(1+p^2)d_R}; \quad b_r = -a_r p \tag{2.106}$$

The set of plots of the parameters $m_R(\Omega)$ and $m_I(\Omega)$ against Ω^2 will also result in straight lines. By determining the slopes of the best-fit straight lines through these two set of plots, the best values of n_R and n_I, and their intercepts with the vertical axis, d_R and d_I are found. And finally, using the expression in (1), modal parameters are found [30, 79].

In Figure 2.6, a typical display for determination of modal parameters with Line-Fit procedure is shown.

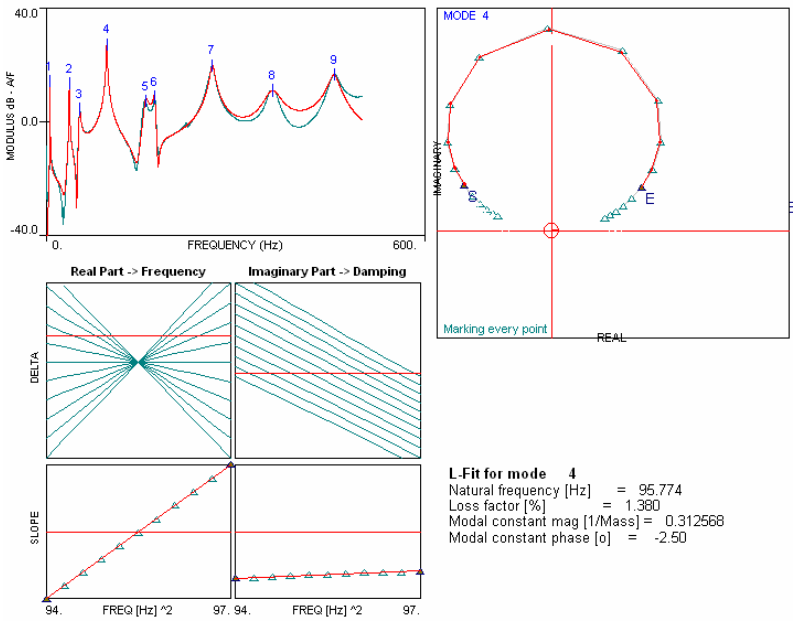

Figure 2.6 : A Typical Line-Fit Analysis Procedure

2.3 Comparison and Correlation

2.3.1 Introduction

Experimental data are utilized in many ways. If a theoretical model for a particular problem is not available, experimental data can be used directly for design and analyses purposes. But, mostly, especially in the field of structural analyses, experimental data are also used for many other purposes including correlation, validation and updating of theoretical models.

It should be noted that, in order to improve or update a theoretical model, it is essential to have theoretical basis for the correlation of the experimental and theoretical models. It should also be noted that comparison and correlation of experimental and theoretical models are also required for model updating purposes.

Comparison and correlation of experimental and theoretical data sets are performed in terms of natural frequencies, mode shapes and FRFs. In literature, there are different approaches and methods for comparison and correlation of different data sets using natural frequencies, mode shapes and FRFs [30, 43, 44]. Some of these are based on visual comparison of two data sets, such as comparison of mode shapes visually and overlying of individual FRFs while some others are more sophisticated methods that compare data sets mathematically, such as the method of modal assurance criteria which aims to establish a degree of coherence of two vibration modes.

In the following sections, various approaches and methods for comparison and correlation of experimental and theoretical data sets are given in a hierarchical order. It should be noted that all these comparison and correlation methods are not necessarily used at the same time in all practical cases. The selection of the use of these depends on the structure and the purpose of the experiment.

Although it is not given below as a method of comparison of theoretical and experimental method, it is very important that the total mass of the real structure and that of the theoretical model should be compared before going through further comparison and correlations.

2.3.2 Comparison of natural frequencies

The basic and easiest method for correlation of experimental and theoretical models is the comparison of natural frequencies from two models. In most cases, comparison is made by plotting experimental natural frequencies against theoretical natural frequencies with the same mode order. A straight line with a slope of 1 is obtained in the case of exact correlation of experimental and theoretical natural frequencies. The differences between two corresponding frequencies give information about the degree of matching of experimental and theoretical models. A systematic deviation of this slope from unity is usually a result of a common error, such as wrong inputting material properties, units etc. whereas a random scatter of points means weak correlation between two models. In this simple comparison method, it is important that the correlated frequencies should be the corresponding frequencies of the same vibration mode

2.3.3 Comparison of mode shapes

A further step for comparison of experimental and theoretical models is based on comparison of mode shapes of two models. Mode shapes can be compared visually by means of mode shape animations and/or by using improved mathematical tools such as Modal Scale Factor (MSF) and Modal Assurance Criteria (MAC).

2.3.3.1 Visual comparison of mode shapes

Visual comparison of mode shapes is fast and relatively easy. Also, when a quick comparison of natural frequencies of experimental and theoretical models is needed, mode shapes may be compared visually to match corresponding modes. However, if quantitative values for the level of correlation of mode shapes are of interest, the correlation methods such as MSF, MAC etc. need to be used. MSF, MAC and similar approaches and methods are used for the comparison and correlation of two vectors.

2.3.3.2 Modal Scale Factor (MSF)

Modal Scale Factor (MSF) can be defined as the slope of the best straight line through the existing points of the compared modes and it is expression is given as

$$MSF(E/N) = \frac{\sum_{r=1}^{n} \{\Psi_E\}_r \{\Psi_N\}_r^*}{\sum_{r=1}^{n} \{\Psi_N\}_r \{\Psi_N\}_r^*} \quad \textbf{(2.107)}$$

where $\{\Psi_E\}_r$ and $\{\Psi_N\}_r$ are experimental and numerical eigenvectors of rth mode respectively, and n is the number of DOFs [30]. It should be noted that MSF is a slope value hence it gives no information about the quality of the fit of the points to the straight line. Therefore, some other methods of correlation are needed to overcome this problem. Modal Assurance Criterion is one of these methods as explained in the next section.

2.3.3.3 Modal Assurance Criteria (MAC)

Modal Assurance Criterion (MAC), also known as the "Mode Shape Correlation Coefficient", compares two vectors in the space and it is "the coherence of two vectors" or "a measure of the least-squares deviation or scatter of the points from the straight line correlation" [30, 44, 66]. It is defined as follows:

$$MAC(E/N) = \frac{\left|\{\Psi_E\}^T \{\Psi_N\}\right|^2}{\left(\{\Psi_E\}^T \{\Psi_E\}\right)\left(\{\Psi_N\}^T \{\Psi_N\}\right)} \quad \textbf{(2.108)}$$

MAC simply calculates the projection of a vector on another vector. All vectors in one set (e.g. experimental modes) are compared with all the vectors in another set (e.g. theoretical modes) one by one. The resulting matrix gives indication about degree of relation of the vectors of two sets. MAC value varies between unity and zero. If correlated modes or vectors are too close to each other, MAC value is close to 1, whereas, if they are considerably different, it is value is close to zero. Sometimes, theoretical and experimental modes are not in the same order. In those cases, the vectors need to be sorted and made compatible before the MAC calculations are to be done.

When MSF and MAC are to be used, the formulations assume that eigenvectors have the same dimensions. If the dimensions of the eigenvectors from two sets are different, either the big model is to be reduced or small model is to be expanded.

There are some features and extended representations of MAC, which are used for some other purposes and for better correlation of mode shapes. AutoMAC is important feature of MAC, while Improved MAC (IMAC) and Frequency Scaled MAC (FMAC) are extended representation of MAC. Normalised Cross Orthogonality (NCO) and SEREP-Cross-Orthogonality (SCO), which are known as normalized form of MAC, are also extended representation of MAC, but they are given in detail in the section of orthogonality check (Section 2.3.4) as orthogonality property is included in them.

AutoMAC is the use of MAC to check whether the chosen DOFs as measurement points are adequate/sufficient or not. This is performed by correlating mode shape vectors with themselves. In practice, to able to determine the modes in the interested frequency range correctly, that is to avoid spatial aliasing, AutoMAC is used to decide how many, or which measurement points are needed.

2.3.3.4 Coordinate Modal Assurance Criteria (COMAC)

In the calculation of the MAC between two vectors, all the DOFs are included by a summation process which results in a single numerical value for the correlated modes [30]. To include the effect of individual DOFs in calculations, Coordinate Modal Assurance Criteria (COMAC) is used. Simply, COMAC is similar to MAC, but former gives a correlation between two models for a specific chosen coordinate. For a particular DOF, say i, COMAC is expresses as.

$$COMAC(i) = \frac{\sum_{i=1}^{L} \left| (\Psi_E)_{il} (\Psi_N)_{il} \right|^2}{\sum_{i=1}^{L} ((\Psi_E)_{il})^2 \sum_{i=1}^{L} ((\Psi_N)_{il})^2} \quad \textbf{(2.109)}$$

2.3.4 Comparison of Frequency Response Functions (FRFs)

Similar to comparison and correlation of mode shapes, frequency response functions (FRFs) are also compared and correlated both visually and using some mathematical tools. As FRFs contain the knowledge of natural frequencies, amplitudes and damping at the same time, their comparison is very important. Mostly, it is compared

simply by overlying individual FRFs on the same graph. On the other hand, there are also some tools for comparison and correlation of FRFs numerically.

2.3.4.1 Overlaying individual FRFs

As it is well-known, the first step in modal testing is the measurement of some FRFs. Therefore, without any further processing of FRFs, they can be compared directly with the theoretical ones by simply overlying FRFs of two data sets. This type of comparison immediately highlights the differences of the FRFs in terms of natural frequencies, damping and amplitudes. Effect of not including residual modes can also be apparent in such comparison. In practice, taking at least three times of the interested frequency range for theoretically generation of FRFs can provide a good comparison.

2.3.4.2 Frequency Domain Assurance Criterion (FDAC)

In experimental modal analysis, some set of FRFs are measured, and in a typical SIMO analysis only one column or one row of FTF matrix is available while the number of rows or columns is more than one in the case of MIMO analysis. To utilize all the information contained in these FRFs, similar comparison tools used for MAC and COMAC are also derived for FRF comparisons. Using such an approach, individual elements of the FRF matrix of one set is compared with that of the other set. The so-called Frequency Domain Assurance Criterion (FDAC) is derived from this view of point, and its definition is given as [30].

$$FDAC\left(E\left(\omega_j\right),N\left(\omega_i\right)\right)_k=\frac{\left|\left\{H_E\left(\omega_i\right)\right\}_k^T\left\{H_N\left(\omega_j\right)\right\}_k\right|^2}{\left(\left\{H_E\left(\omega_i\right)\right\}_k^T\left\{H_E\left(\omega_i\right)\right\}_k\right)\left(\left\{H_N\left(\omega_j\right)\right\}_k^T\left\{H_N\left(\omega_j\right)\right\}_k\right)} \qquad \textbf{(2.110)}$$

In (2.4) $H_E\left(\omega_i\right)$ and $H_N\left(\omega_j\right)$ are the theoretical and experimental FRFs at the frequency ω_i and ω_j, respectively and k is the suffix of reference points for both experimental and theoretical data set. Values of FDAC vary between zero and one and like MAC, value of 1 means good correlation and value of 0 means poor correlation. FDAC results are highly dense because the dimensions of FDAC matrix are as much as the number of FRFs and every discrete point in FRFs.

2.3.4.3 Frequency Response Scale Factor (FRSF)

Frequency Response Sale Factor (FRSF) is analogous to MSF and it can be defined as

$$FRSF\left(E\left(\omega_j\right),N\left(\omega_i\right)\right)_k=\frac{\left\{H_N\left(\omega_i\right)\right\}^T\left[W\right]\left\{H_E\left(\omega_j\right)\right\}}{\left\{H_N\left(\omega_i\right)\right\}^T\left[W\right]\left\{H_N\left(\omega_i\right)\right\}} \tag{2.111}$$

where $\left[W\right]$ is the weighting matrix [44-Fotsch]. While FDAC gives a quantitative comparison of two FRFs, FRSF gives a qualitative comparison in the domain of FRFs, so it is not proper for assessment of the degree of correlation. Similar to MSF, FRSF gives values between 1 and -1.

2.3.4.4 Frequency Response Assurance Criterion (FRAC)

Frequency Response Assurance Criterion (FRAC) is analogous to COMAC, so FRAC is used to make comparison of FRFs according to related DOFs and it can be defined as in (2.112)

$$FRAC\left(j\right)_k=\frac{\sum_{i=1}^{L}\left|\left({}_EH_{jk}\left(\omega_i\right)\right)\left({}_NH_{jk}^{*}\left(\omega_i\right)\right)\right|^2}{\sum_{i=1}^{L}\left|{}_EH_{jk}\left(\omega_i\right)\right|^2\cdot\sum_{i=1}^{L}\left|{}_NH_{jk}\left(\omega_i\right)\right|^2} \tag{2.112}$$

In (2.6) $i=1$ to L represents the number of the both experimental and theoretical discrete frequency points and k represents the excitation DOF [30]. Similar to COMAC, FRAC values varies between one (perfect correlation) and zero (no correlation). It is claimed that interpretation of the results FRAC gives may be difficult [67]. For example, in the case of lightly damped structures, which have big differences between their maximum and minimum amplitudes, FRAC value may result in relatively low values while the FRFs appear to have good correlation if they are simply overlaid.

2.3.5 Orthogonality based comparisons

Orthogonality property is normally checked to estimate correlation between experimental and theoretical eigenvectors.

2.3.5.1 Normalised Cross Orthogonality (NCO)

Although, MAC is sufficient in most cases for the correlation of mode shapes, in some special cases, especially in the case of automatically correlation processes, it may be desired to make control of orthogonality property of modes in calculation of MAC [Gürbüzer]. The control of orthogonality property is managed by inserting matrices of the system into MAC equation . The new MAC formulation is called Normalised Cross Orthogonality (NCO) and it is definition is given in (2.113) [30].

$$NCO(N,E)=\frac{\left|\{\Psi_E\}^T[W]\{\Psi_N\}\right|^2}{\left(\{\Psi_E\}^T[W]\{\Psi_E\}\right)\left(\{\Psi_N\}^T[W]\{\Psi_N\}\right)} \tag{2.113}$$

In (2.113), $[W]$ is the weighting matrix and it can be obtained using the mass or stiffness matrices of the system.

Mostly, because of experimentally derived system matrices are incomplete; it is difficult to make the control of orthogonality property. Even if, mass or stiffness matrix is complete, reducing the DOFs of theoretical model to ones of experimental data set is the main difficulty, a Guyan-type or equivalent reduction methods must be used to achieve this [30]. So these results in the need of derivation of a new cross orthogonality method, which is given in the following section.

2.3.5.2 SEREP-Based Normalised Cross Orthogonality (SCO)

Apart from using system mass matrix explicitly, "System Equivalent Reduction Expansion Process (SEREP)" based approaches are more practical. Using (2.114) "a pseudo-mass matrix is computed" from the measured eigenvectors or corresponding theoretical ones using in this approach [30].

$$\left[M^R\right]=[\psi]^{+T}[\psi]^{+} \tag{2.114}$$

Afterwards this new mass matrix is used in the calculation of NCO as a weighting matrix and this resulted definition is called SEREP-Based Normalised Cross Orthogonality (SCO) as given in (2.115).

$$SCO(N,E)=\frac{\left|\{\Psi_E\}^T[\psi]^{+T}[\psi]^{+}\{\Psi_N\}\right|^2}{\left(\{\Psi_E\}^T[\psi]^{+T}[\psi]^{+}\{\Psi_E\}\right)\left(\{\Psi_N\}^T[\psi]^{+T}[\psi]^{+}\{\Psi_N\}\right)} \quad \textbf{(2.115)}$$

As only the eigenvectors are utilized in the calculation of SCO like in the case of MAC, implementation of SCO is easier than NCO and other orthogonality methods which are given in the following sections. Fotsch pointed out that although experimental mode shapes also may also be used for obtaining pseudo-mass matrix, the theoretical mode shapes are usually chosen to avoid available noise and test uncertainties into calculations [44]. It is claimed that the SCO gives higher values in correlation of two similar mode shapes while it gives lower values the in correlation of two dissimilar mode shapes. Therefore, SCO is more sensitive than the MAC to actual differences in mode shapes [44].

Similar to AutoMAC, there is AutoSCO with the same logic.

2.3.5.3 Pseudo Orthogonality Check (POC)

Pseudo orthogonality check is defined as in (2.116) [44, 68-69].

$$POC_{ij}=\sum_{k=1}^{n}\sum_{l=1}^{n}\left(\Psi_E\right)_{ki}\left(m_N\right)_{kl}\left(\Psi_N\right)_{lj} \quad \textbf{(2.116)}$$

POC uses the theoretical mass m_N and it can be done at the experimental or theoretical DOFs. A reduction or expansion process such as SEREP [30] must be utilized for either set of DOFs, for the proper reduction of the mass matrix or expansion of the eigenvectors. Ideally, all off-diagonal terms of mass matrix must be zero or close to zero for perfect correlation, while for some applications values as much as 10 percent of unity are acceptable. On the other hand in some applications

in practice, although off-diagonal terms are very near to zero, such as 5 percent of unity, the vectors may be relatively uncorrelated [44].

2.3.5.4 Coordinate Orthogonality Check (CORTHOG)

By performing conventional orthogonality checks, contribution of individual physical DOFs of modal vectors can not be identified. To identify how each physical DOF contributes to the orthogonality check produced by the POC, Coordinate Orthogonality Check (CORTHOG) is proposed [68]. The CORTHOG identifies where differences exist between the two vector sets with a reference degree of freedom. It is defined as

$$CORTHOG_{ij}^{kl} = \frac{\left(\Psi_E\right)_{ki}\left(m_N\right)_{kl}\left(\Psi_N\right)_{lj} - \left(\Psi_N\right)_{ki}\left(m_N\right)_{kl}\left(\Psi_N\right)_{lj}}{\sum_{k=1}^{n}\sum_{l=1}^{n}\left(\left(\Psi_E\right)_{ki}\left(m_N\right)_{kl}\left(\Psi_N\right)_{lj} - \left(\Psi_N\right)_{ki}\left(m_N\right)_{kl}\left(\Psi_N\right)_{lj}\right)} \quad \textbf{(2.117)}$$

where kl is the DOF pair and ij is the mode pair [44, 68]. The CORTHOG identifies which DOFs are the best and least correlated between two mode sets.

2.4 Model Updating

Model updating can be defined as the adjustment of a theoretical model that simulates the structure under study by means of experimental data, so that it more accurately reflects dynamic behaviour of the structure [45]. To update theoretical models and to obtain more accurate ones, many researchers have dealt with model updating. However, model updating techniques can not successfully be applied to practical structures today. Insufficient experimental modes and coordinates, size and mesh incompatibility of the experimental and FE models, experimental and other random and systematic errors are some difficulties encountered during model updating [45]. Still, mostly theoretical models are updated manually using experimental data.

Model updating methods are generally divided into two groups [66]: Direct Methods, such as, Berman method, error matrix method, eigendynamic constraint method, etc., and Iterative Methods, such as ones based on orthogonality property, sensitivity

methods, etc. Direct methods mostly require low computational effort; however, the updated models do not always constitute physically meaningful models. These kinds of methods transform the physically meaningful models into-representative models. On the other hand, iterative methods require larger computational effort because of repeated solution of the eigendynamic problem and the pseudo-inversion of large matrices, though only some of these will always constitute physically meaningful models if they converge [46, 52].

In the following, some of the model updating methods will be summarised briefly for the sake of completeness.

2.4.1 Direct Methods

In the direct updating methods, theoretical mass matrix $[M_T]$ and/or stiffness matrix $[K_T]$ are updated using measured eigenvalues $[\omega_E^2]$ and eigenvectors $[\phi_E]$ with constrained such as eigendynamic and orthogonality properties [46].

Berman Method

In this method, it is assumed that mass, $[M_T]$ and stiffness, $[K_T]$ matrices of the theoretical model are wrong or incomplete and mass and stiffness matrices of the theoretical model are changed directly. Firstly mass matrix is updated, and then using this updated mass matrix, stiffness matrix is updated [45, 66]. Error function which wanted to be minimized and related constrained equations are given in (2.117) and (2.118) respectively.

$$\varepsilon = \left\| [M_T]^{-1/2} \left([M_U] - [M_T] \right) [M_T]^{-1/2} \right\| \tag{2.117}$$

$$[M_U] = [M_U]^T, \qquad [\phi_E]^E [M_U] [\phi_E] = [I] \tag{2.118}$$

This is an extremum (minimum) problem and can be solved using Lagrange Multipliers method [66]. As a result, expression for the updated mass matrix can be written as in (2.119).

$$[M_U]=[M_T]+[M_T][\phi_E]\left[m^*\right]^{-1}\left([I]-\left[m^*\right]\right)\left[m^*\right]^{-1}[\phi_E]^T[M_T] \quad \textbf{(2.119)}$$

where, $\left[m^*\right]=[\phi_E]^T[M_T][\phi_E]$. Similar to for the mass matrix, the error function and related constrained equations can be written for stiffness matrix as in (2.120) and (2.121) respectively.

$$\varepsilon=\left\|[K_T]^{-1/2}\left([K_U]-[K_T]\right)[K_T]^{-1/2}\right\| \quad \textbf{(2.120)}$$

$$[K_U]=[K_U]^T, \quad [K_U][\phi_E]=[M_U][\phi_E]\left\lfloor\omega_E^2\right\rfloor, \quad [\phi_E]^T[K_U][\phi_E]=\left\lfloor\omega_E^2\right\rfloor \quad \textbf{(2.121)}$$

After all of this, updated stiffness matrix is found as follow.

$$[K_U]=[K_T]+\left([\Delta K]+[\Delta K]^T\right) \quad \textbf{(2.122)}$$

where

$$[\Delta K]=\frac{1}{2}[M_U][\phi_E]\left([\phi_E]^T[K_E][\phi_E]+\left[\omega_E^2\right][\phi_E]^T[M_E]-[K_T][\phi_E][\phi_E]^T[K_U]\right) \quad \textbf{(2.123)}$$

As correct eigenvalues and eigenvectors are already available, this method does not require any iteration and eigenvalue analysis. Also, as the stiffness matrix is updated with updated mass matrix which also contains some errors, the errors in mass matrix are also included into the stiffness matrix. At the end of the updating stage, a model which represents the real structure but physically meaningless may be obtained.

Error Matrix Method

In this method it is aimed to update the incomplete or wrong regions of the theoretical model using experimental data. As it is well known, with limited experimental data, at the end of the updating stage, updated model may not represent real structure physically. Locating errors and updating regions with errors may prevent the problem mentioned [66]. To locate the main errors in the theoretical

model, difference between real stiffness matrix and theoretical stiffness matrix is utilized [45, 66]. This stiffness error matrix is given in (2.124).

$$[\Delta K] = [K_E] - [K_T] \tag{2.124}$$

There are some various formulations of error matrices as mentioned by Gürbüzer and Visser [45, 66]. However, these assume that the error matrix is first-order approximation and is only valid for small errors. One of these formulations [45] that including the orthogonality condition is given in (2.125) and (2.126).

$$[\Delta K] = \left[[I] - [K_T] \sum_{r=1}^{n} \left(\{\phi_E\}_r (\omega_E)_r^2 \{\phi_E\}_r^T - \{\phi_T\}_r (\omega_T)_r^2 \{\phi_T\}_r^T \right) \right]^{-1} [K_T] - [K_T] \tag{2.125}$$

$$[\Delta M] = \left[[I] - [M_T] \sum_{r=1}^{n} \left(\{\phi_E\}_r \{\phi_E\}_r^T - \{\phi_T\}_r \{\phi_T\}_r^T \right) \right]^{-1} [M_T] - [M_T] \tag{2.126}$$

The formulations given in (2.125) and (2.126) are quite complex in practical applications. This method is useful to determine the regions of the theoretical model which are modelled incomplete or wrong.

2.4.2 Iterative Methods

Iterative model updating methods solve the eigendynamic problem iteratively. As mentioned before, they require larger computational effort compared to direct methods because of repeated solution of the eigendynamic problem and the pseudo-inversion of large matrices [46].

Methods based on orthogonality

The methods based on the orthogonality property are developed with consideration of orthogonality of eigenvectors. By arranging orthogonality property [66], it is desired to reach (2.127).

$$[A]\{b\} = \{B\} \tag{2.127}$$

where the unknown $\{b\}$ contains the elements of the updated mass and stiffness matrices, and $\{B\}$ contains values of 0 and 1 [45]. The matrix $[A]$ given in (2.128) is defined in terms of the experimental eigenvector elements.

$$[A]=\begin{bmatrix} \phi_{11}^2 & 2\phi_{11}\phi_{21} & 2\phi_{11}\phi_{31} & \dots & \phi_{n1}^2 \\ \phi_{11}\phi_{12} & \phi_{11}\phi_{21}+\phi_{22}\phi_{11} & \phi_{12}\phi_{31}+\phi_{22}\phi_{11} & \dots & \phi_{n1}\phi_{n2} \\ . & . & . & . & . \\ . & . & . & . & . \\ \phi_{1m}^2 & 2\phi_{1m}\phi_{2m} & \dots & \dots & \phi_{nm}^2 \end{bmatrix} \quad \textbf{(2.128)}$$

Using a least squares approximation method, solution vector $\{b\}$ is obtained. Method requires incomplete eigenvectors, and as the DOFs of the theoretical and experimental models are usually different, method is not practical.

Sensitivity Methods

Nearly, all sensitivity based methods compute a sensitivity matrix $[S]$. Sensitivity values can be defined according to eigenvectors, eigenvalues or FRF. These sensitivity values can be any property of the theoretical model, such as elements of the stiffness or mass matrices, geometrical dimensions of the theoretical model, material properties, etc. $[S]$ is computed considering the partial derivatives of modal parameters with respect to structural parameters via a truncated Taylor's expansion [45]. The mentioned matrix equation is given in (2.129).

$$\{\Delta w\}=[S]\{\Delta p\} \quad \textbf{(2.129)}$$

where elements of $\{\Delta p\}$ are the unknown changes in structural elements and $\{\Delta w\}$ shows the changes in modal data required, for example as in (2.130) [45].

$$\{\Delta w\}=\left\{\{\Delta\phi_1\}^T,\{\Delta\phi_2\}^T,\{\Delta\phi_3\}^T,...,\{\Delta\phi_m\}^T,\left\{\omega_1^2,\omega_2^2,...,\omega_m^2\right\}^T\right\}^T \quad \textbf{(2.130)}$$

The matrix equation in (2.129) is solved so that the unknown vector $\{\Delta p\}$ is found, and then this new $\{\Delta p\}$ is used to update the theoretical mass and stiffness matrices [45, 51, 66]. Then, a new eigensolution analysis is performed and the process is repeated until the desired modal properties are obtained.

2.4.3 Improving theoretical models using manual correction method

In earlier studies, model updating was carried out by means of direct intervention and modification of the theoretical model [49]. Model updating or FE computational model updating emerged in the 1990s. Göge stated that "model updating has not yet become the state of the art in aeronautical applications, and the aeronautical industry used to validate their large aircraft FE models using a so-called manual correction approach [49]". In other words, huge complex models, such as helicopter FE models may not be appropriate to be updated using mathematical tools. Although the updating process can be turned into minimising the difference between the theoretical and experimental models by adjusting some (usually a few) parameters, this approach is not followed in this thesis due to the lack of reliable model updating software that will provide unique and physical answers at the end of the this updating process.

As result, in this thesis, it has been decided that some of the input parameters of the theoretical models, such as material properties, etc. are to be changed manually to match the theoretical and experimental results. In the scope of this thesis, the theoretical models are improved by this methodology. Also, starting from simple structures, step by step, very complex structures are managed to be modelled and validated. As a result, improved FE models of very complex structures, such as, helicopter tail boom, helicopter airframe, etc. are obtained.

3. MODAL ANALYSES OF HELICOPTER STRUCTURES

3.1 Introduction

A theoretical model should represent the real structure with acceptable accuracy. This requires validating the model which leads to manufacturing prototype of the structure and performing experiments for correlation and updating purposes. If it is not possible to manufacture a prototype due to time and economical constraints or if it is difficult to build, correlate and update theoretical model of the entire structure, it is possible to perform similar works on a simplified but representative - in terms structural members and manufacturing processes – prototype.

In this thesis, a finite element model for a helicopter tail boom is developed first. Then a simplified but representative - in terms of structural members and manufacturing processes - prototype is manufactured and its numerical model is developed. In the next step, an experimental set-up is prepared and the accuracy and the reliability of the measured data are established using some preliminary tests. This is followed by measurements of Frequency Response Functions at many locations on the test structure. Then, the natural frequencies, damping factors and mode shapes are obtained by analysing the measured data. When the measured behaviour of the test structure is compared with that of the first FE model predictions, it was found that there were large differences between the experimental and theoretical (FE) results of the tail boom section and the theoretical model could not represent the structure with an acceptable accuracy. Difference even at first natural frequency was about 25 %. To identify the errors in modelling such structures it was concluded that new experimental and theoretical studies especially on relatively simpler parts, should be performed.

3.2 Validation of FE Models of Simple Structures with Riveted Joints

3.2.1 Introduction

Rivets are used as fasteners for joining metal parts together in many industrial applications, especially those in aerospace industry. They are particularly useful for joining sheet metals. However, modelling structures assembled using such joints is still quite difficult due to the fact that riveted joints rely on contact forces to maintain the joints and this, in general, causes non-linear behaviour. Furthermore, a typical structure may contain excessive number of riveted joints and this may well prohibit including realistic non-linear contact forces in theoretical models.

In this section, linear FE models of relatively simple structures with rivets are built and in those models so-called using "effective clamping diameter" is used in rivet models so as to reflect the stiffening effects of such joints. Then appropriate size of this clamping diameter is determined by correlating predicted modal data corresponding to various clamping diameters with the measured modal data [8, 9]. This is done by first validating the material properties of a structure without any riveted joints. Then, some structures with riveted joints are manufactured and their FE models are developed by assuming that a rivet is effectively clamping the matching surfaces around it within a specified diameter. Then experimental modal analyses are performed to obtain the natural frequencies and mode shapes. The experimentally determined modal data are then used to adjust the effective clamping diameter of the rivets in order to minimize the error between the predicted and the measured natural frequencies and mode shapes. Results show that the procedure explained here can be used to obtain quite representative linear FE models for riveted structures.

3.2.2 Definition of the problem and the proposed approach

For structures that may contain excessive number of rivets, there is a real need to model the rivets in the structure in an effective way, especially for the determination of the natural frequencies and mode shapes with acceptable accuracy and also to see the effects of the design modifications immediately. However, riveted joints rely on contact forces and in general exhibit non-linear behaviours; hence the "correct"

riveted joint model may require complicated non-linear models. However, this is in contrast with the real need in industry due to the serious difficulty of incorporating excessive number of non-linear joint models in those structures such as aircrafts and helicopters.

The proposed approach in this study for modelling structures with riveted joints is based on an assumption that each rivet is effectively clamping the matching surfaces within a certain diameter around the attachment centre. This diameter is also called as "Effective Clamping Diameter" which is illustrated in Figure 3.1a. In Finite Element (FE) modelling, this assumption can be realized by constraining (joining together) the nodes on matching surfaces of the joint within this diameter [70] as illustrated in Figure 3.1b.

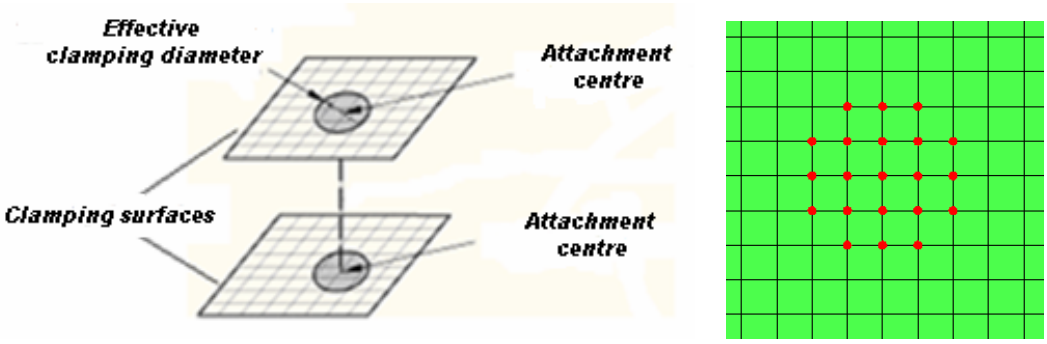

a) **b)**

Figure 3.1 : a) FE Model of a Rivet, b) Joining Nodes within the Effective Clamping Diameter

Once the problem is defined as in Figure 3.1, then the determination of the Effective Clamping Diameter (ECD) for a given rivet configuration becomes the main task. The proposed approach in this study is to determine the ECD indirectly by utilizing the predicted and measured modal properties of some sample structures assembled using appropriate rivets. The proposed approach is given in Figure 3.2 as a flow chart. Note that initial validation of the material properties may be necessary if those properties are not known with acceptable accuracy.

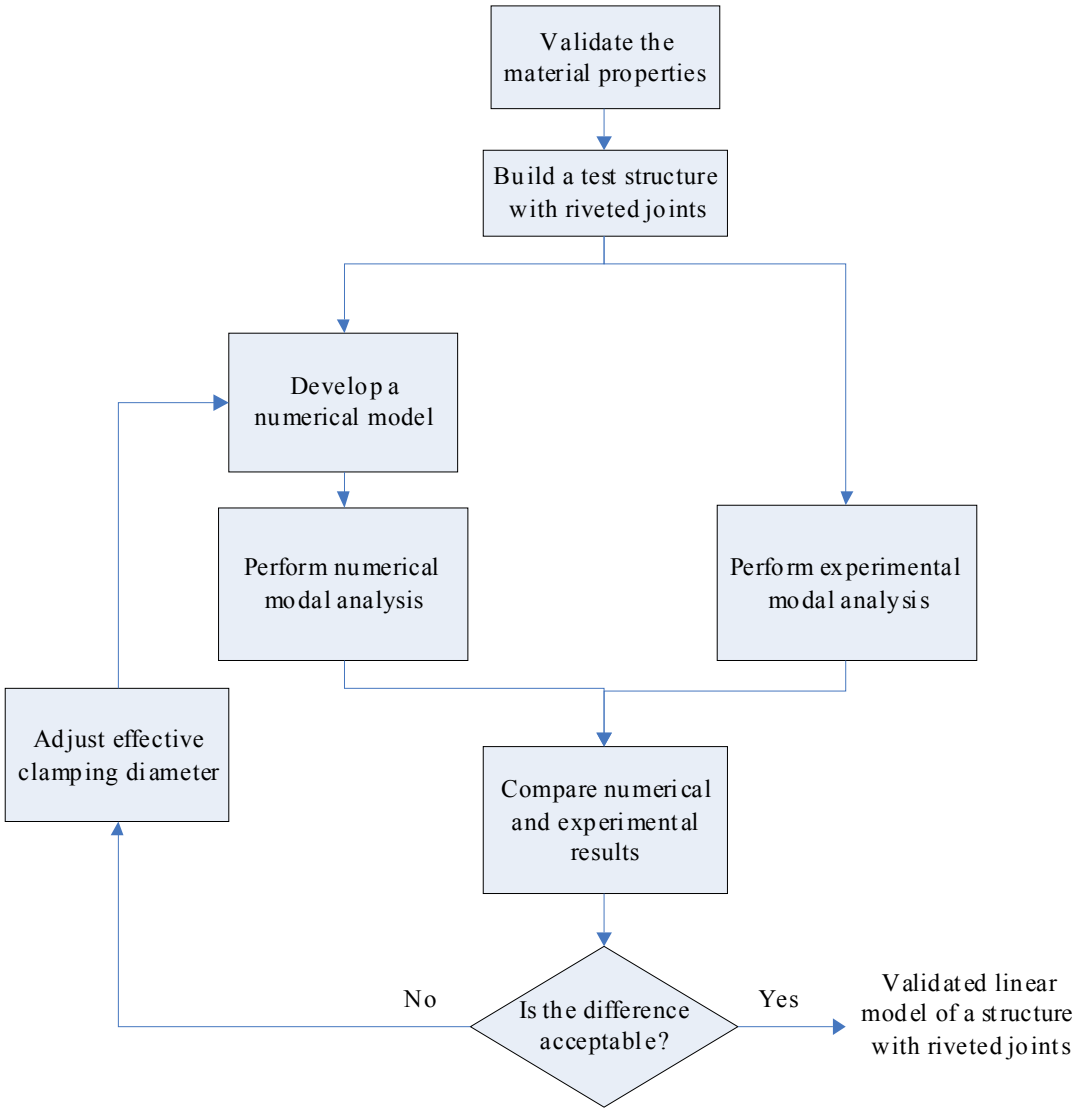

Figure 3.2 : Flowchart for Obtaining a Validated Linear Model of a Structure with Riveted Joints

3.2.3 Model validation of a riveted L-plate

3.2.3.1 Introduction

For the validation of the rivet model summarized above, two L-shaped plates were manufactured. The plates had identical dimensions and were made of the same material (ALCLAD 2024-T3). However, as can be seen in Figure 3.3, one of the plates had no rivets at all while the other was made of two parts joined by two rows of rivets.

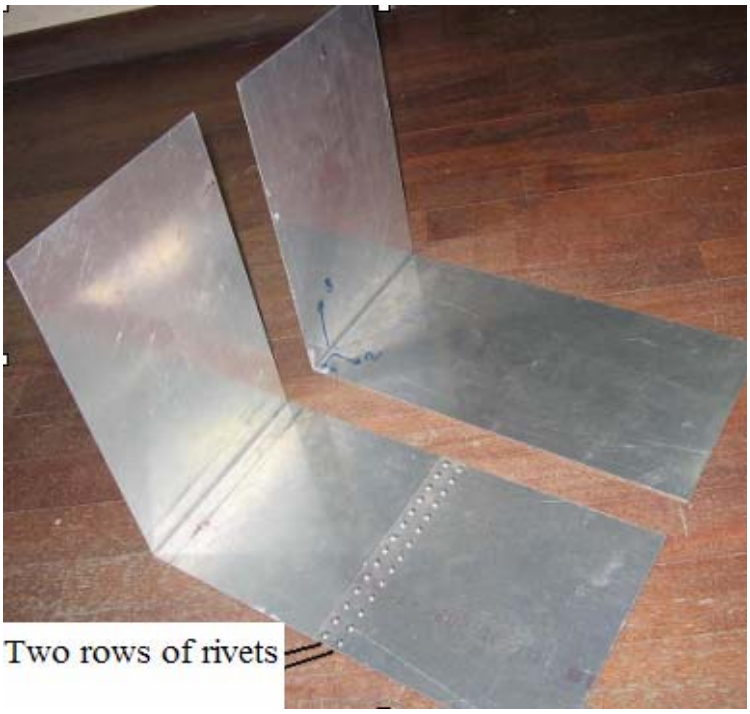

Figure 3.3 : The Riveted Plate and the Plate without Rivets

The mass of the plate without any rivets is 459.8 g and the riveted plate is 499.7 g, the difference being due to the 28 rivets and the additional material due to overlapping over the riveted region. Here, one of the rivets is 0.8 g and its diameter is 3.3 mm and its head diameter is 6.4 mm.

3.2.3.2 Modal tests of L-plates

Experimental modal analysis was performed on the two plates in free-free conditions using the Frequency Response Functions (FRFs) measured at the nodes depicted in Figure 3.4.

The FRFs were measured using impact excitation with an instrumented hammer while the responses were recorded using accelerometers. Excitation point was carefully selected not to miss any mode within the frequency of interest and about 90 FRFs were measured on individual plates. All measured FRFs for the two plates are plotted in Figure 3.5a and 3.5b.

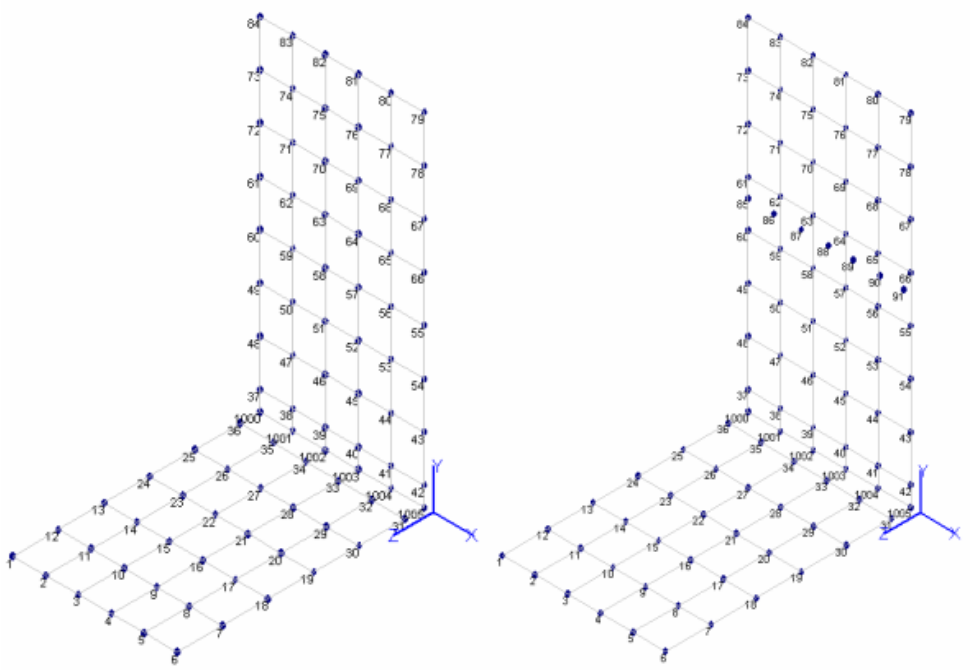

Figure 3.4 : Experimental Meshes for Plates with and without Rivets

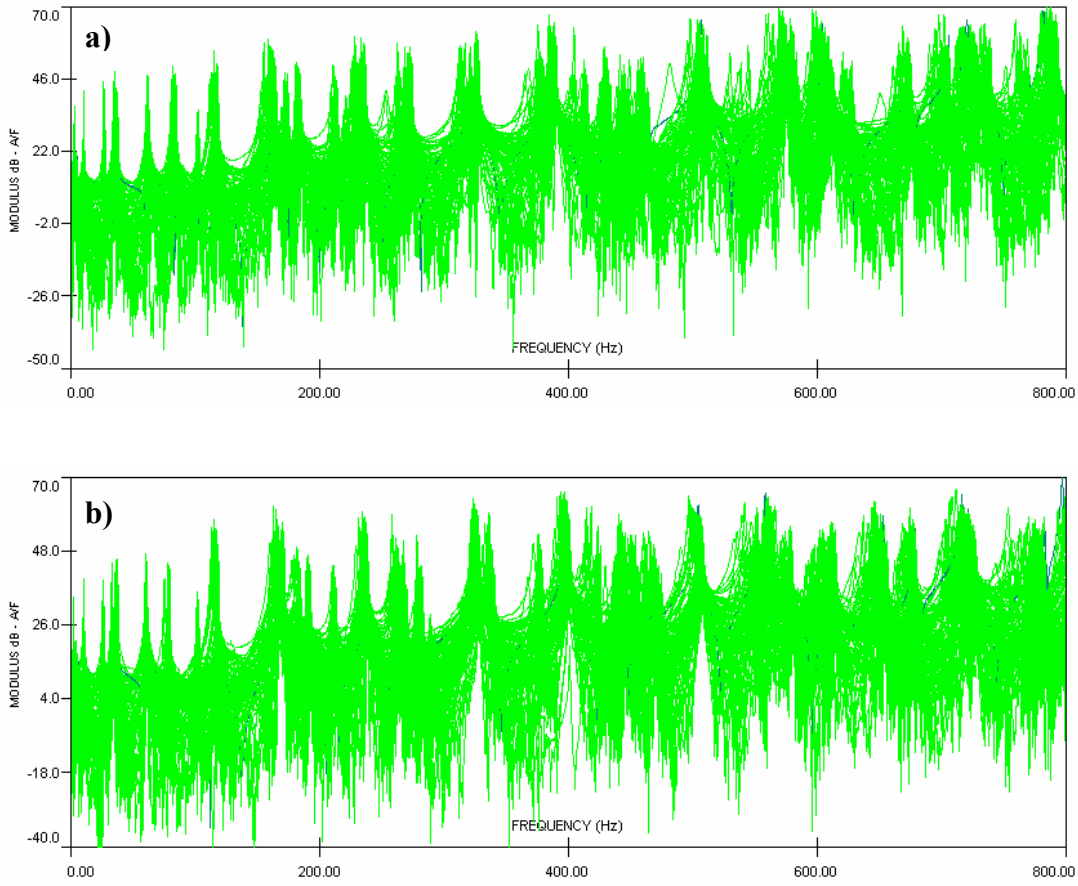

Figure 3.5 : a) Measured 84 FRFs on the Plate without Rivets b) Measured 91 FRFs on the Riveted Plate

The measured FRFs were processed by ICATS program [71] so as to obtain the modal properties of the plates.

3.2.3.3 FE models of L-plates

FE models for individual plates were developed in commercial program ABAQUS [62, 70] as shown in Figure 3.6. After determining mid-surfaces of the structures, quadrilateral shell elements were used for this purpose and sufficient numbers of elements were included in the model to avoid any significant discretization errors within the frequency range of interest.

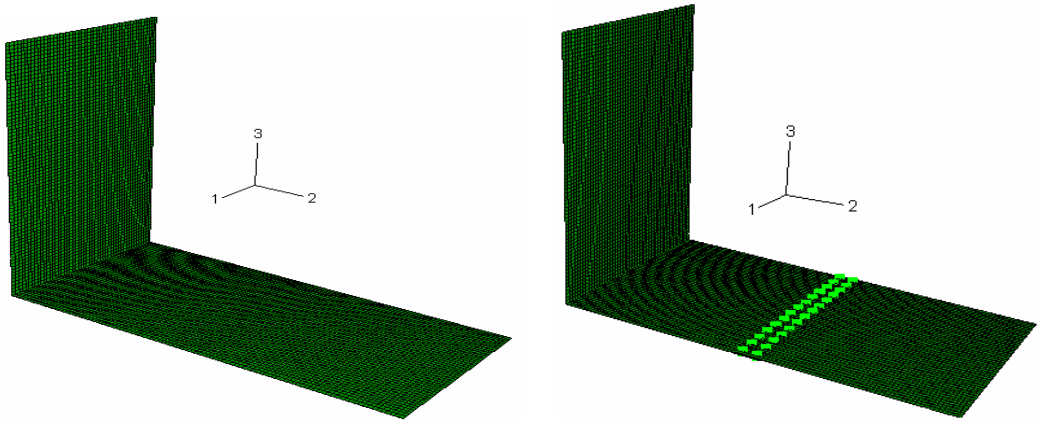

(a) **(b)**

Figure 3.6 : a) FE Model of the Plate without Rivets, b) FE Model of the Riveted Plate

Rivets are modelled using the proposed approach given in Section 3.2.2. The mass of each rivet is also included in the model.

3.2.3.4 Validation of material properties

The reason for studying the plate without any rivet in this study is to validate the material properties used in the FE model and to be sure that everything except rivets is modelled properly in riveted plate. This is done by comparing the measured and the predicted natural frequencies and FRFs of the plate without rivets. Modal Assurance Criteria (MAC) is utilized during the comparisons. The initial material properties used in the FE model are taken from reference [72]. At the end of this exercise, the density and the elastic properties of the material were slightly adjusted so as to match the measured modal properties of the plate. After this adjustment, the

predicted and the measured natural frequencies for more than 20 modes agreed very well (see Table 3.1). These frequencies are also compared as in Figure 3.7. The measured and the predicted FRFs are also compared. A typical example corresponding to point FRF is illustrated in Figure 3.8. As can be seen, the FRFs are very close to each other. Small differences in natural frequencies are believed to be due to the mass loading effect [30, 73] of the transducer. Predicted and experimental mode shapes are also compared using Modal Assurance Criteria (MAC) in Figure 3.9. It is found that the measured and the predicted mode shapes correlate with each other well too. Visual comparison of these first three mode shapes is also given in Figure 3.10.

Table 3.1 : Theoretical and Experimental Natural Frequencies of the Plate without Rivets

Mode No	*Theo. Nat. Freq. [Hz]*	*Exp. Nat. Freq. [Hz]*	*Difference [%]*
1	10.4	10.3	0.8
2	26.6	26.9	-1.1
3	34.7	34.5	0.5
4	37.1	37.2	-0.4
5	63.0	62.5	0.9
6	83.2	84.4	-1.2
7	104.3	102.5	1.7
8	119.9	117.8	1.8
9	162.1	162.5	-0.3
10	167.9	165.2	1.6
11	173.2	175.3	-1.2
12	185.5	184.1	0.8
13	216.5	214.7	0.8
14	230.9	230.5	0.2
15	240.2	236.6	1.5
16	273.4	268.2	2.0
17	275.6	273.5	0.8
18	322.1	319.7	0.7
19	334.4	327.2	2.2
20	387.1	379.8	1.9
21	394.7	390.1	1.2
22	421.2	414.7	1.6

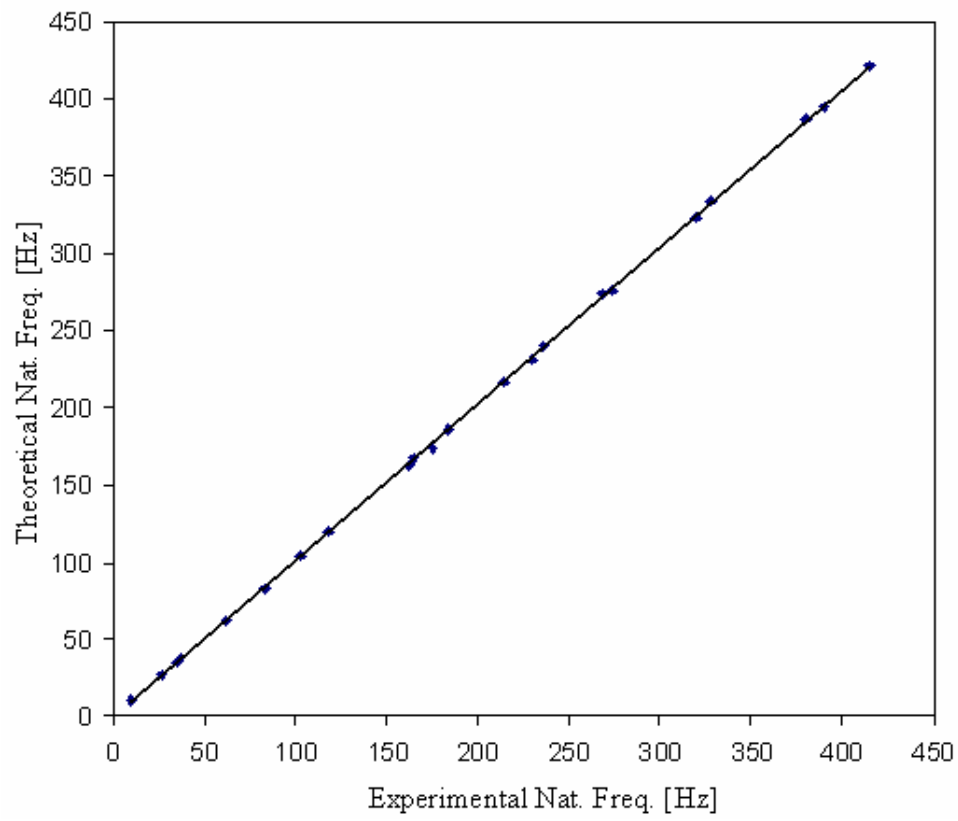

Figure 3.7 : Comparison of Predicted and Measured Natural Frequencies

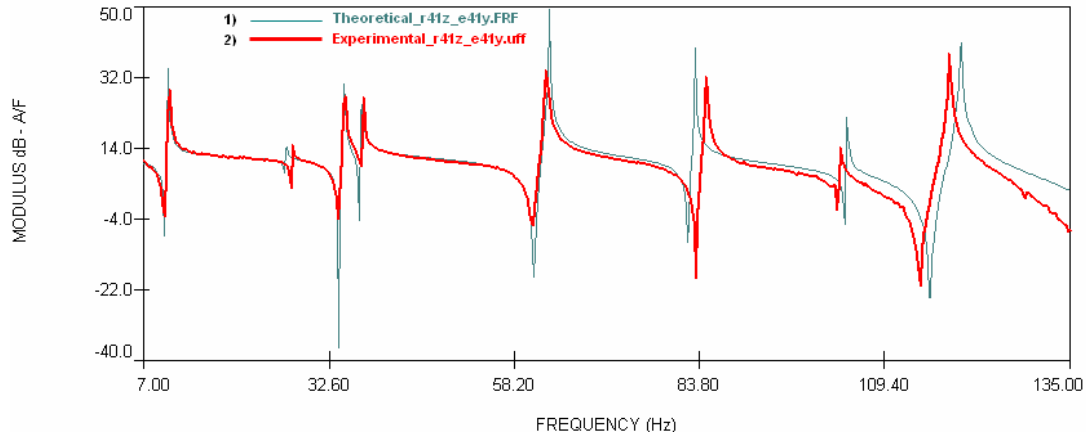

Figure 3.8 : Comparison of Theoretically Generated and Measured Point FRF

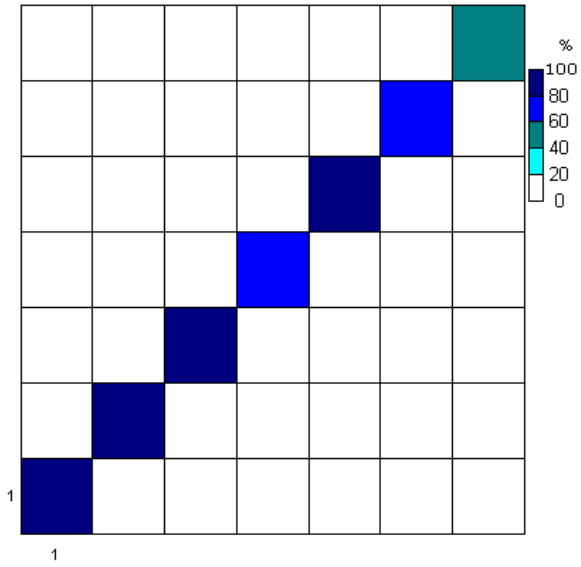

Figure 3.9 : MAC for the Plate without Rivets

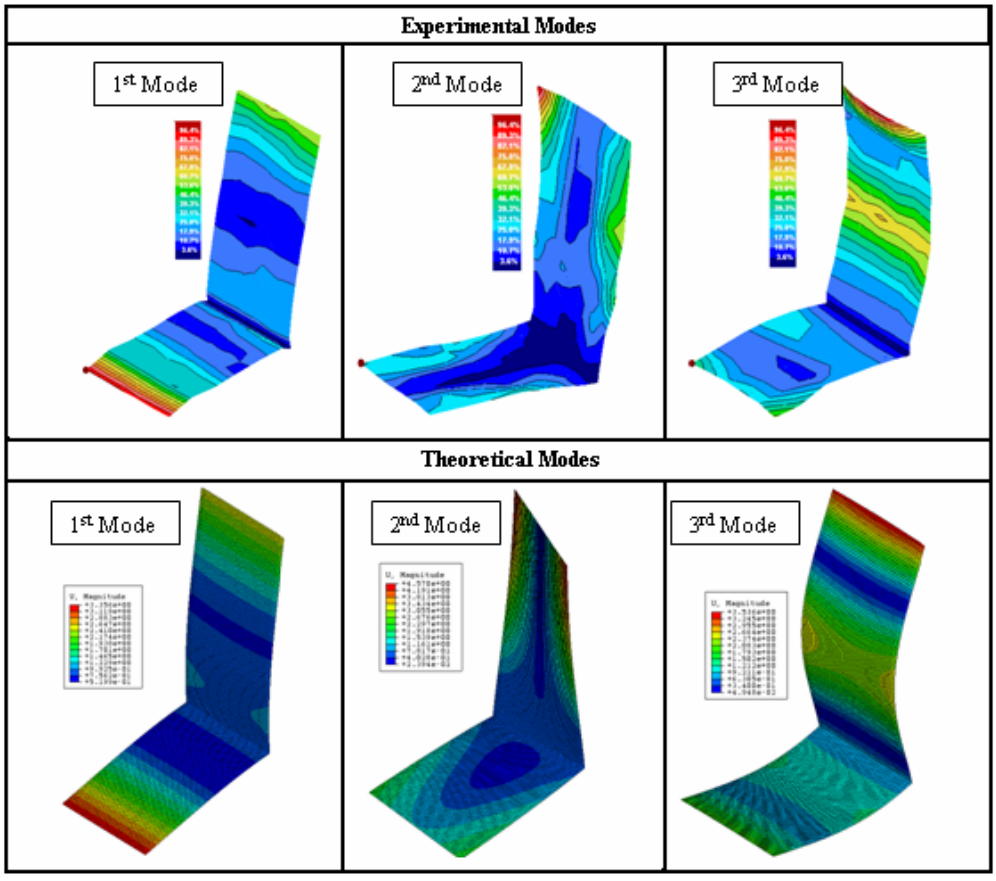

Figure 3.10 : Comparison of Experimental and Theoretical Mode Shapes of the L-Plate without Riveted Joints

At the end of this validation process, Elasticity modulus, Poisson rate and density of the related material are determined as 72.4×10^9, 0.33 and 2750 kg/m^3, respectively.

3.2.3.5 FE model validation of the riveted L-plate

As mentioned before, the riveted plate was made of the same material as the plate without rivets. Therefore, the validated material properties were also used in the FE model of the riveted plate. As a result, it was appropriate to assume that any discrepancy between the measured and the predicted behaviour of the riveted plate would be due to the errors in the models of the riveted joints. Furthermore, it is aimed in this study to minimize this error by adjusting the Effective Clamping Diameter (ECD) described in Figure 3.1 according to the approach summarized in Figure 3.2. To achieve this objective, fully-welded (or fully-clamped) condition across the riveted joints was simulated first, i.e., all the nodes on the matching (overlapping) surfaces of the riveted plate were tied to each other. Then, the analyses were repeated for various values of the effective clamping diameter (D) and the results were compared with measured modal data. The results are summarized in Table 3.2. It should be noted that the fully-welded condition sets the upper limit for the predicted natural frequencies. It is also noted that the predicted natural frequencies decrease as the ECD decreases.

Table 3.2 : Theoretical and Experimental Natural Frequencies of the Riveted Plate

	D=3 mm	D=6 mm	D=20 mm	Fully Clamped	Experimental
Mode No	Natural Frequency [Hz]				
1	10.5	10.5	10.6	10.7	10.4
2	27.4	27.8	29.3	29.1	26.6
3	33.9	34.3	35.1	36.9	33.3
4	37.9	38.1	38.8	38.5	37.4
5	62.8	62.9	63.1	64.0	61.3
6	81.5	82.3	85.0	87.8	79.8
7	107.1	107.3	107.4	107.9	102.9
8	120.4	120.7	121.0	121.3	118.5
9	169.5	170.2	171.1	172.1	167.0
10	174.2	177.3	185.2	183.5	171.4
11	183.2	184.0	194.5	186.9	185.6
12	193.1	193.6	195.1	196.3	192.9
13	216.0	218.3	222.9	231.0	213.0
14	242.6	244.1	250.4	247.8	238.4
15	256.2	258.3	260.6	268.9	262.6
16	269.2	271.7	277.7	281.5	270.1
17	277.6	278.1	278.2	286.6	282.6
18	338.1	339.0	340.0	344.4	328.4
19	346.0	349.8	357.7	364.4	340.2
20	389.5	390.6	390.9	393.1	377.3

The results in Table 3.2 are processed so as to obtain the percentage difference of the natural frequencies between the measured and the predicted values as a function of ECD and the results are plotted in Figure 3.11.

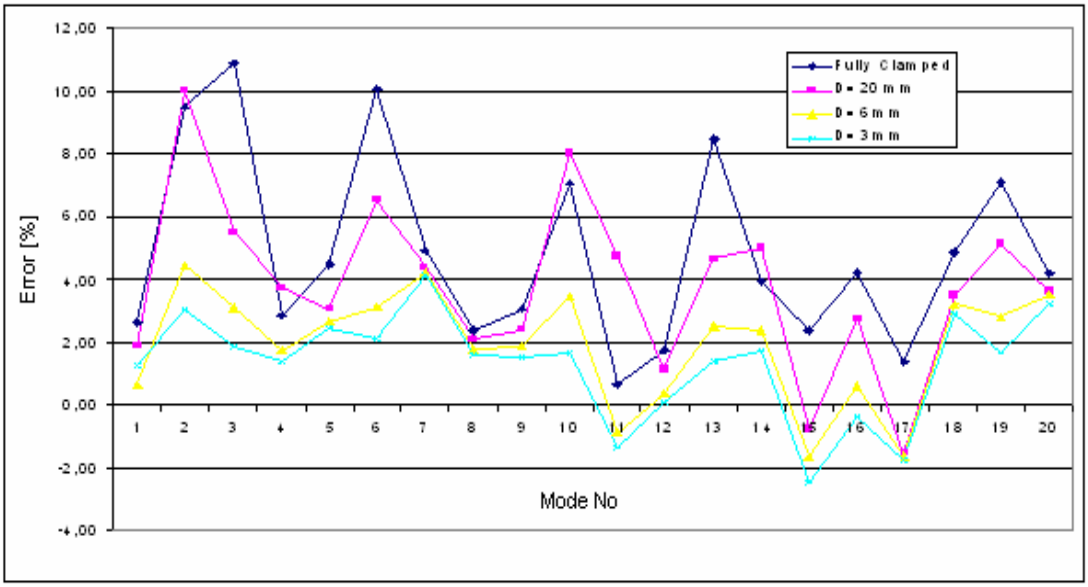

Figure 3.11 : Difference between Theoretical and Experimental Natural Frequencies of the Riveted Plate

Referring to Figure 3.11 it is seen that in the case of fully-clamped condition the error is the highest, exceeding 10 % for some modes. In the case of the largest ECD (20 mm) the error is also high. It appears that the structure is stiffer than reality in those cases. However, when ECD is low (e.g., 3mm or 6 mm) the FE model represents the real structure very successfully. It should be noted, however, that choosing ECD lower than 3 mm will make the riveted joints over flexible. Therefore, for the particular riveted joints, the optimum ECD was determined to be about 4 mm. Then the modal properties corresponding to this value of ECD were computed and the results are compared to the measured values. Measured and predicted natural frequencies for 4 mm diameter are also compared in Figure 3.12.

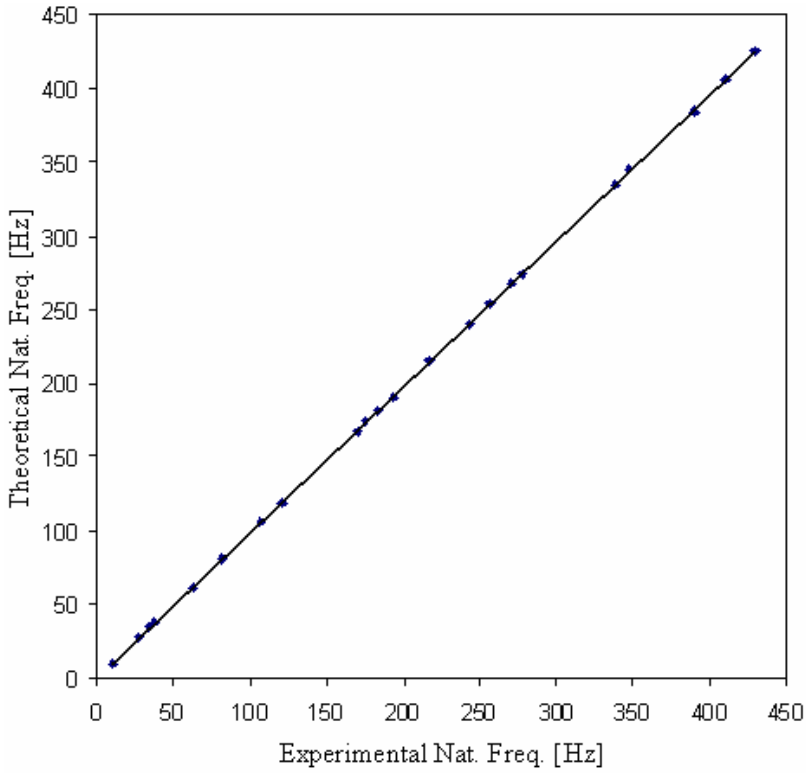

Figure 3.12 : Comparison of Theoretically Generated and Measured Natural Frequencies

It is shown in Figure 3.13 that the theoretical and experimental point FRFs agree quite well although the mass loading effect of the transducer is noticeable. The predicted and experimentally identified mode shapes correlate well too as indicated by Modal Assurance Criteria (MAC) in Figure 3.14 and the visual displays of the first 3 mode shapes in Figure 3.15.

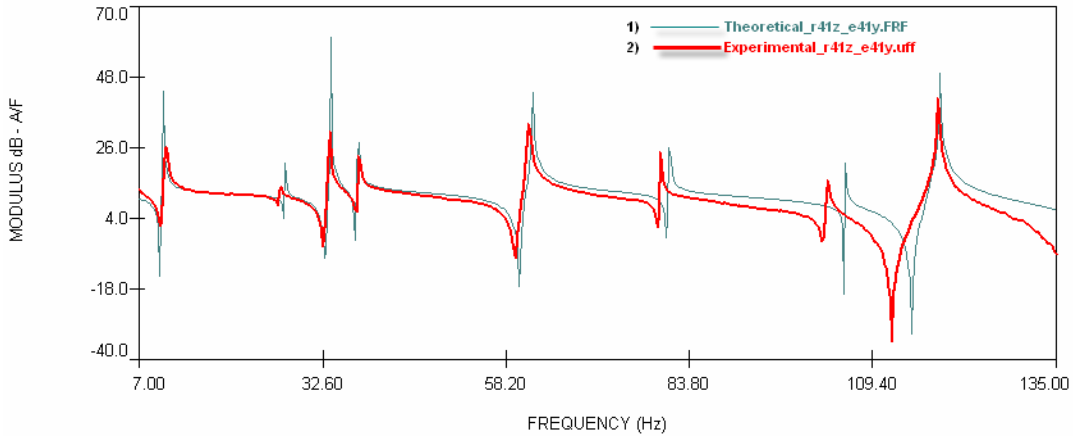

Figure 3.13 : Comparison of Theoretically Generated and Measured Point FRF

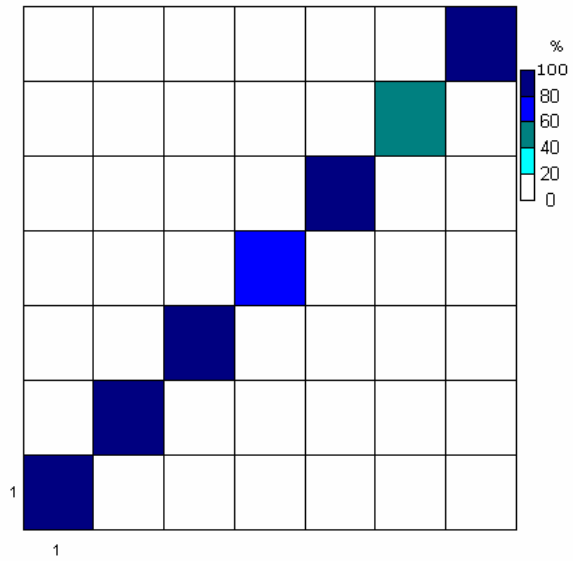

Figure 3.14 : MAC for the Riveted Plate

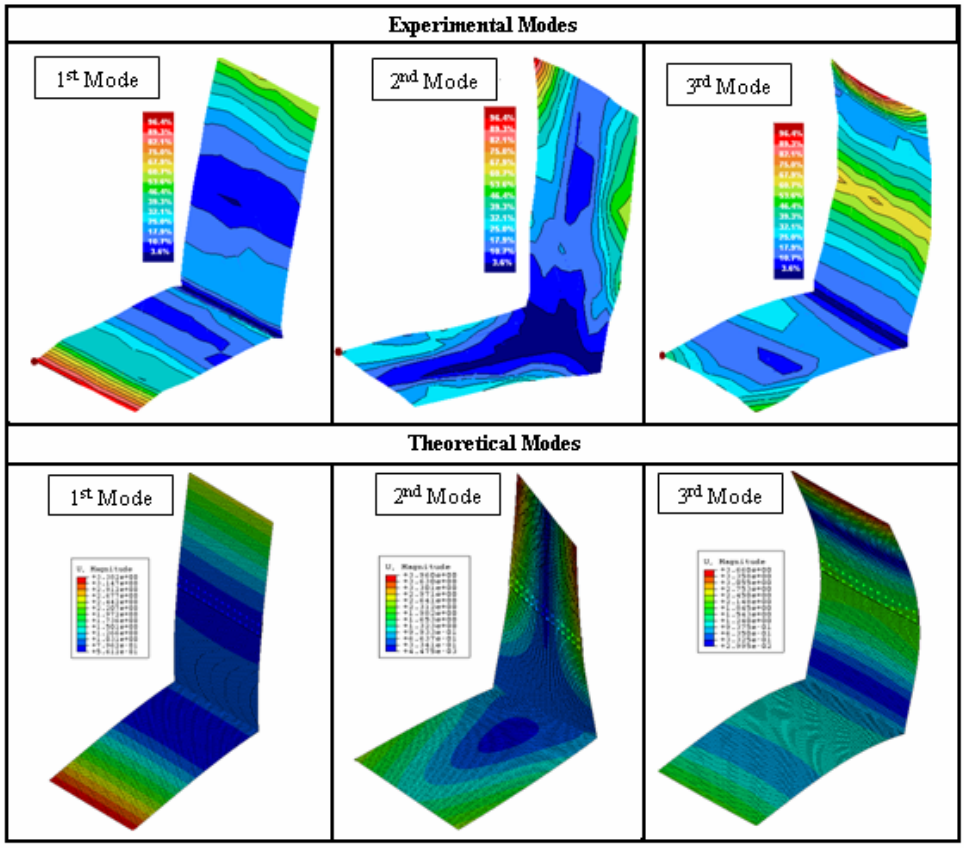

Figure 3.15 : Comparison of Experimental and Theoretical Mode Shapes of the Riveted Plate

It is worth restating here that the diameter of the rivets used in the test cases was 3.3 mm and the head diameter was 6.4 mm.

3.2.4 Model validation of a riveted beam

3.2.4.1 Introduction

The riveted plate used above was fairly simple in terms of its construction and had only 28 rivets in two rows in a narrow region. It was therefore decided to test the model validation approach using a more complex structure with more riveted regions and a lot of rivets. For this purpose a structure which has many rivets distributed in various regions is intentionally designed so that the effects of riveted joints on the dynamics of the structure will be strong. This was achieved after modelling and analysing a few possibilities and finally the structure given in Figure 3.16 is decided. First modes of this structure are mainly bending and torsional modes on which the effects of riveted joints are dominant.

The structure designed is manufactured and is called in this thesis the "riveted beam". Its picture and magnified FE model are given in Figure 3.17. Riveted beam is 1.345 kg and comprises 172 rivets in four rows and it is also made of the material (ALCLAD 2024-T3) as L-plates in the previous section. The dimensions of the rivets used in the construction of this beam were somewhat different than those used in L-plates: the cross sectional and the head diameters were 4.3 mm and 6.4 mm, respectively. Length, width and height of the beam are 128 cm, 10 cm and 2.5 cm, respectively.

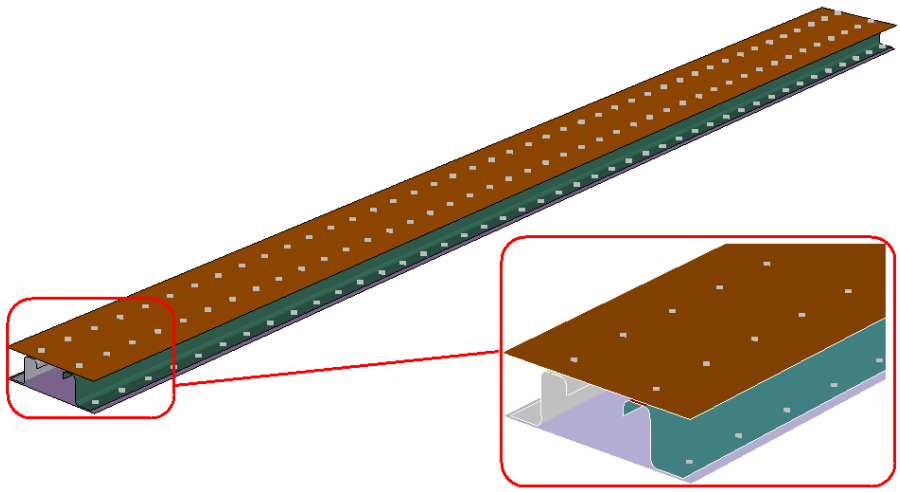

Figure 3.16 : Designed Riveted Beam

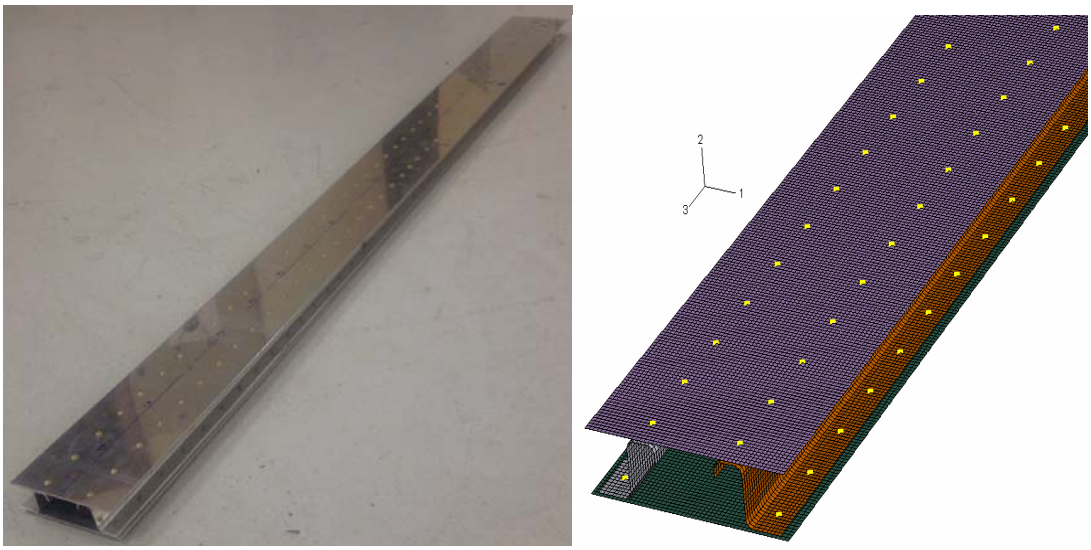

(a) **(b)**

Figure 3.17 : a) Picture of the Riveted Beam and b) Magnified FE Model of the Riveted Beam

The same approach as in the previous sections was followed to model this structure. However, on this relatively more complicated structure some further modelling parameters are investigated. Let's remember the proposed approach for modelling riveted structures mentioned before to explain some new definitions (see Figure 3.18). In this model, the motion of the two attachment points in the matching surfaces is coupled to the rigid body motion of a reference node [70]. The displacement and rotation of each of the attachment point are defined in an average sense by weighting the displacements and rotations of the nodes in the related matching surface. There are various weighting methods or functions which will be explained later.

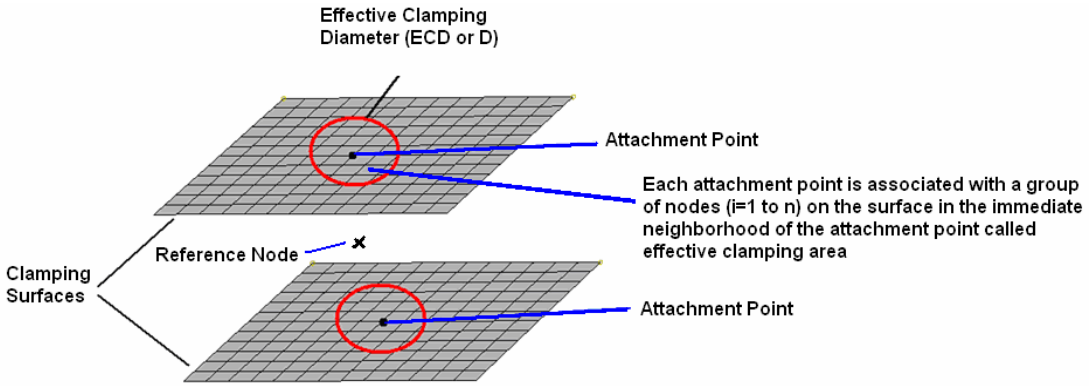

Figure 3.18 : FE Modelling Parameters of a Riveted Joint

In modelling the riveted L-plate, although it was not mentioned, uniform weighting function was used to associate the motion of a group of nodes in the effective clamping area to the motion of the attachment point. In other words, the motion of the attachment point is the uniformly the average of the motions of the nodes in the effective clamping area. In the following section various weighting methods will be explained.

3.2.4.2 Weighting methods

There are different kinds of weighting methods or functions, such as uniform, linear, quadratic and cubic. Weighting function constraints the motion of the attachment point to the motions of the coupling nodes in the clamping area. The contribution of the displacement and rotation of each coupling node to the displacement and rotation of the attachment point, so that to reference point, is as much as weight factor (w_i) of the weighting function at that node.

Uniform weight distribution

In this method, the weight factors of all the coupling nodes in the clamping area are equal to 1. In other words, all the coupling nodes in the clamping area affect the motion of the attachment point at same rate. Weighting scheme for this type of weighting function for coupling nodes from i to n is [70]

$$w_i = 1, \qquad \text{i=1, n} \tag{3.1}$$

Linear weight distribution

In this method, a linearly decreasing weighting scheme is the case as in (3.2)

$$w_i = 1 - \frac{r_i}{r_0} \tag{3.2}$$

where r_i is the coupling radial distance from the reference node and r_0 is the distance to the furthest coupling node or the value of the effective clamping radius [70].

Quadratic polynomial weight distribution

In this method, weighting scheme is such that the weight factor decreases as a quadratic polynomial as in (3.3)

$$w_i = 1 - \left(\frac{r_i}{r_0} \right)^2 \quad \textbf{(3.3)}$$

Cubic weight distribution

In this method, a monotically decreasing weight distribution according to the cubic polynomial is the case as in (3.4)

$$w_i = 1 - 3\left(\frac{r_i}{r_0} \right)^2 + 2\left(\frac{r_i}{r_0} \right)^3 \quad \textbf{(3.4)}$$

3.2.4.3 Numerical applications

In this section, riveted joints are modelled using various weighting functions while joining the selected degrees of freedom within a so-called effective area of the matching surfaces. Effects of the various parameters, including the types of weighting functions, the rotational degree of freedom of the reference point, the size of the effective clamping area and mesh density are investigated using FE program ABAQUS [70].

Effect of the rotational DOF of the reference point

In this section, the effect of the rotational Degree of Freedom (DOF) perpendicular to the surface of the reference point is investigated. For this, first, the rotational DOF of this point is allowed to be free, that is, all the DOFs except rotational DOF of this point are restricted (DOF: 1-5) and modal analyses are performed. Then, all the DOFs of this point are restricted (DOF: 1-6) and the same analyses are repeated. For these two cases, using uniform, quadratic and cubic weighting functions modal analyses are performed and predicted natural frequencies are given in Table 3.3. As the rivet cross sectional diameter is 4.3 mm and the rivet head diameter is 6.4 mm, according to results obtained for the riveted L-plate, an appropriate clamping diameter was chosen.

Table 3.3 : Theoretical Natural Frequencies of the Riveted Beam for Various Weighting Methods and Clamping Cases [Hz]

	Uniform		Quadratic		Cubic	
Mode No	*DOF:1-5*	*DOF:1-6*	*DOF:1-5*	*DOF:1-6*	*DOF:1-5*	*DOF:1-6*
1	129,06	129,08	128,90	128,91	128,73	128,73
2	310,94	310,98	310,84	310,86	310,71	310,73
3	335,49	335,70	333,92	334,03	332,32	332,35
4	378,07	378,79	369,40	369,73	359,58	359,66
5	509,01	509,51	498,01	498,26	485,94	486,03
6	591,36	592,14	585,04	585,46	576,33	576,51
7	601,73	602,52	589,72	590,15	579,46	579,62
8	682,22	682,22	669,19	669,19	655,22	655,23
9	776,74	778,18	760,23	761,02	741,40	741,75
10	796,19	796,60	780,72	780,89	764,59	764,62
11	798,86	801,41	784,33	785,73	774,90	775,59
12	817,52	817,66	816,31	816,42	815,05	815,16
13	857,37	857,41	846,89	847,00	841,71	841,78
14	858,77	859,00	851,48	851,57	847,16	847,24
15	865,78	866,53	857,04	857,72	850,42	851,35
16	875,67	879,69	860,87	863,00	854,49	855,25
17	880,02	881,50	871,92	872,85	867,28	867,93

To see the effect of the rotational DOF of the reference point, for each weighting function, the differences of the natural frequencies of two cases are plotted in Figure 3.19.

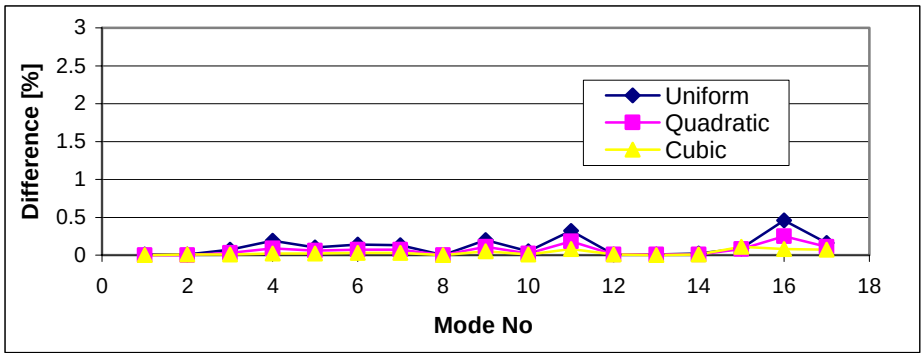

Figure 3.19 : Effect of Rotational DOF of the Reference Point for Various Weighting Cases

As seen in Figure 3.19, the differences between the cases (DOF:1-5) and (DOF:1-6) are minimum in the case of cubic weighting function while they are maximum in the case of uniform weighting function. On the other hand, for all the cases the differences are less than 0.5 %. Although this result is depend on the structure, the

number of rivets and distribution of rivets, in such structures the rotational DOF of the reference point has nearly very little effect on the results.

Effect of weighting methods

In the previous section it was concluded that there was very little effect of the rotational DOF of the reference point on the results. Therefore, in the following analyses, the rotational DOF of the reference point is constrained. In Figure 3.20, the results of the analyses of the riveted beam with 6 mm clamping diameter are summarized. Here, the natural frequencies of the cubic case are taken as reference and the differences between the natural frequencies of quadratic and uniform cases from the cubic case are plotted with respect to the mode number.

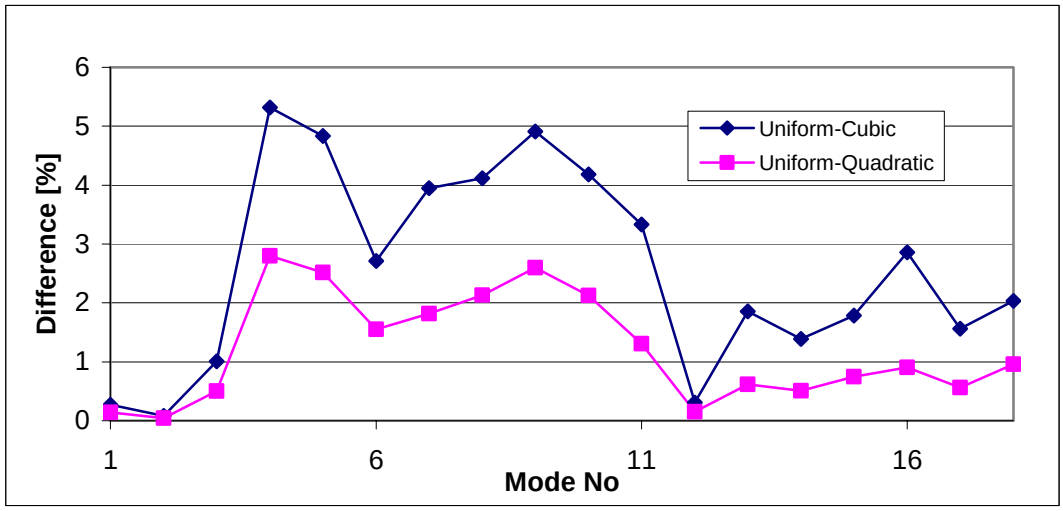

Figure 3.20 : Effect of Weighting Methods (cubic weighting case is taken as reference and Effective Clamping Diameter is 6 mm)

As seen in Figure 3.20, in the case of uniform case, the differences are quite high and the natural frequencies are highest while the natural frequencies are smallest in the case of cubic case. This means that going from the cubic case to the uniform case, the structure behaves more rigid as expected. Also, using the effective clamping diameter 10 mm the same analyses are performed and the natural frequencies are given in Table 3.4 and the differences are summarized in Figure 3.21. Similar observations to the 6 mm case are valid for the results of this diameter.

Table 3.4 : Theoretical Natural Frequencies of the Riveted Beam for Various Weighting Methods (10 mm Clamping Diameter) [Hz]

Mode	Uniform	Quadratic	Cubic
1	129,26	129,15	129,06
2	311,17	311,08	311,01
3	337,59	336,44	335,48
4	393,26	386,39	380,23
5	531,1	521,74	513,52
6	600,29	595,13	591,18
7	623,11	613,51	605,18
8	713,98	701,56	690,59
9	797,78	785,88	775,83
10	818,53	809,22	799,39
11	823,87	813,45	802,76
12	830,89	820,78	818,34
13	866,59	859,08	854,68
14	868,49	861,03	856,69
15	876,81	869,19	864,39
16	892,42	884,37	878,17
17	904,99	889,11	879,6

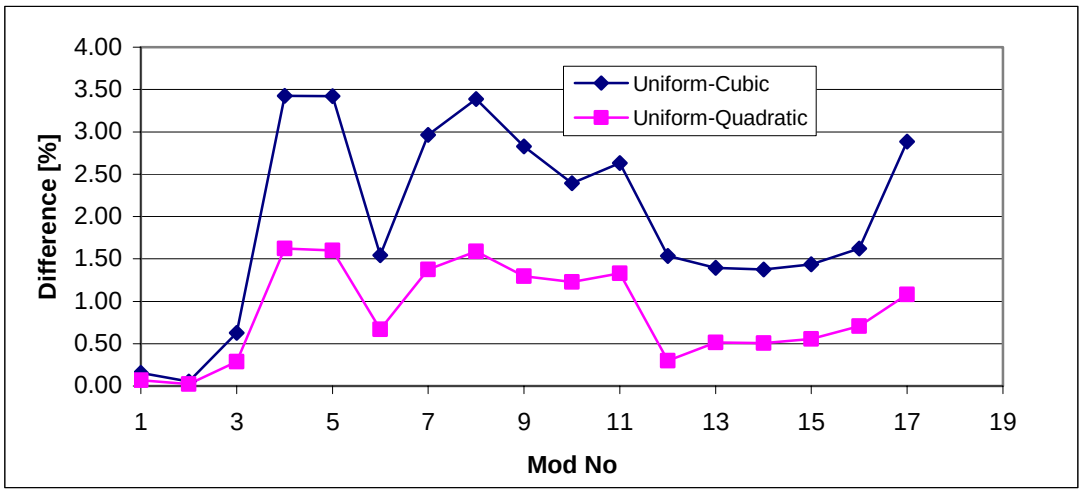

Figure 3.21 : Effect of Weighting Methods (cubic weighting case is taken as reference and Effective Clamping Diameter is 10 mm)

Effect of mesh density

For two mess density values (3 mm and 5 mm) modal analyses are performed for both cubic and uniform weighting and the natural frequencies obtained from these analyses are given in Table 3.5. As a very small mesh density is meaningless and there is a restriction of taken high mesh density values due to dimensions of dimensions of the subparts of the structure, only the analyses are performed for the given mesh densities. Also, to be able to define enough nodes in the clamping area,

10 mm effective clamping diameter is chosen as clamping diameter. In Figure 3.22, the differences between the natural frequencies obtained from the FE models with 3 and 5 mm mesh sizes are given for two different weighting methods.

Table 3.5 : Mesh Density Effect (Effective Clamping Diameter is 10 mm)

Mode	Uniform		Cubic	
	3 mm	5 mm	3 mm	5 mm
1	129,26	129,42	129,06	129,05
2	311,17	311,15	311,01	310,85
3	337,59	339,72	335,48	336,14
4	393,26	408,88	380,23	385,67
5	531,1	556,33	513,52	530,04
6	600,29	610,36	591,18	596,44
7	623,11	648,57	605,18	622,28
8	713,98	748,34	690,59	718,17
9	797,78	821,54	775,83	794,15
10	818,53	828,55	799,39	816,97
11	823,87	855,41	802,76	823,17
12	830,89	863,25	818,34	825,97
13	866,59	883,26	854,68	872,84
14	868,49	885,43	856,69	877,64
15	876,81	893,93	864,39	884,29
16	892,42	909,67	878,17	898,88
17	904,99	930,55	879,6	910,97

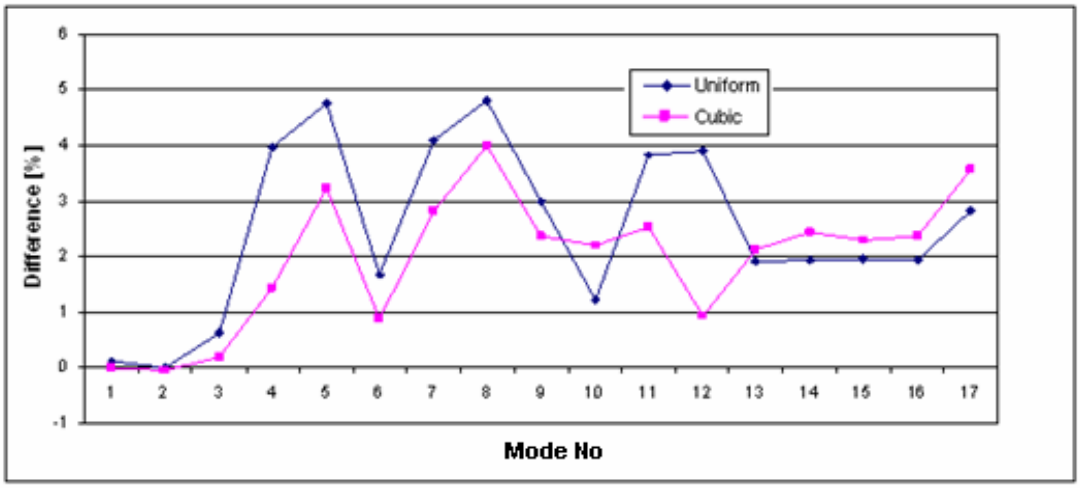

Figure 3.22 : Mesh Density Effect (Effective Clamping Diameter is 10 mm)

As seen in Figure 3.22, for the two mesh densities there are some differences in the results. In the case of 5 mm mesh density as expected the natural frequencies are a little bit higher. In addition, the differences are generally higher in the uniform case. It should be noted that with 10 mm clamping diameter, there are 19 nodes within the clamping area in the case of 3 mm mesh density while there are 9 nodes within the clamping area in the case of 5 mm mesh density. Here, this should be noted also. That is, what is resulted is not exactly as a result of mesh density.

Here it can be said that if it is not possible to have a fine mesh due to geometry of the structure etc., it is better to use cubic weighting method with appropriate clamping diameter.

Effect of Effective Clamping Diameter (ECD)

Differences between the natural frequencies of the FE models with 10 mm and 6 mm effective clamping diameters for the three different weighting functions are given in Figure 3.23.

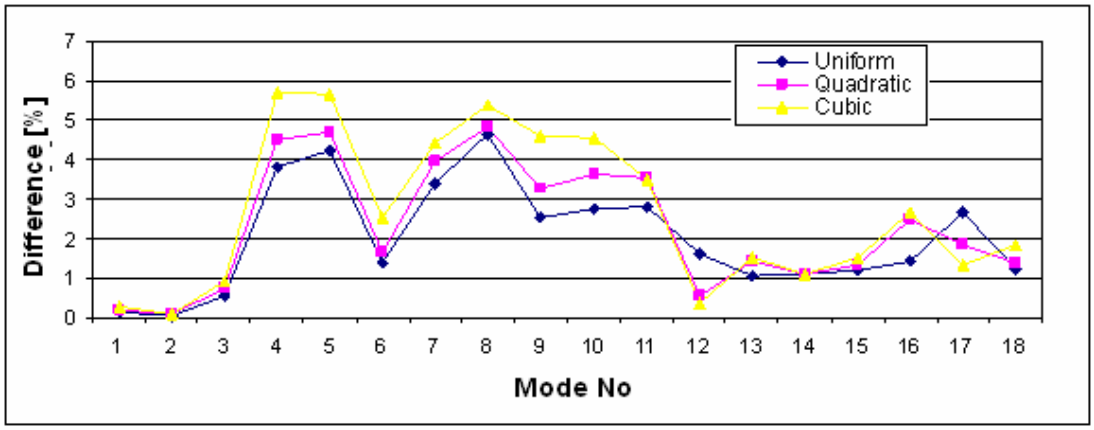

Figure 3.23 : Effect of Effective Clamping Diameter for Different Weighting Functions (6 mm Effective Clamping Diameter is taken as reference)

As seen in Figure 3.22, the natural frequencies are higher in the case of 10 mm for both weighting functions. The differences are higher especially in the middle frequencies.

3.2.4.4 Experimental applications and comparisons

In this section, the modal parameters of the riveted beam are determined and results of the modal analyses of the riveted beam with these determined parameters are compared with experimental results.

Test planning

Using the FE model of the riveted beam developed in the previous section, analyses for the best suspension, impact excitation and accelerometer locations [71] for 20 modes are determined and shown in Figure 3.24.

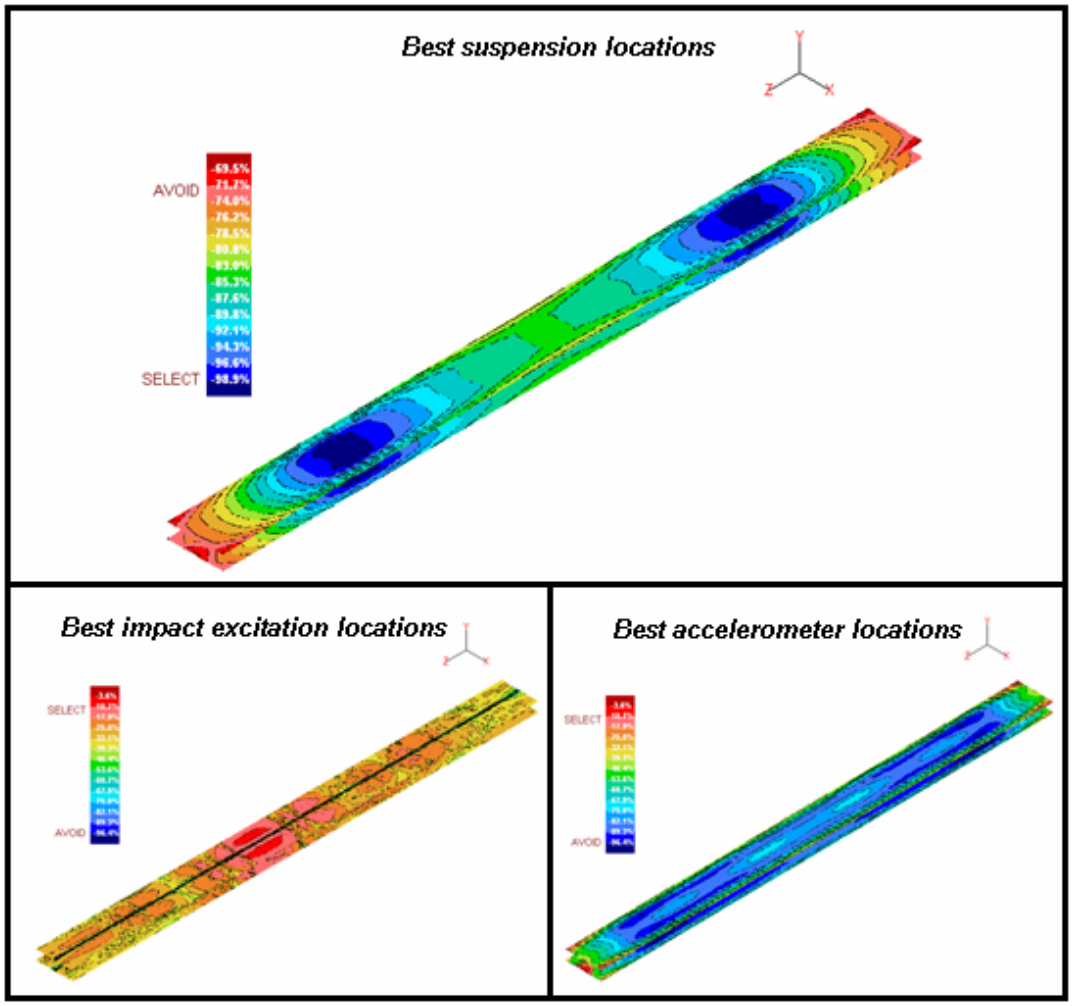

Figure 3.24 : Best Suspension, Impact Excitation and Accelerometer Locations

Experimental modal analysis and comparisons

FRFs are measured on the structure at 110 points using a 3-D accelerometer by exciting the structure at a fixed point. Those measured 330 FRFs are given in Figure 3.25.

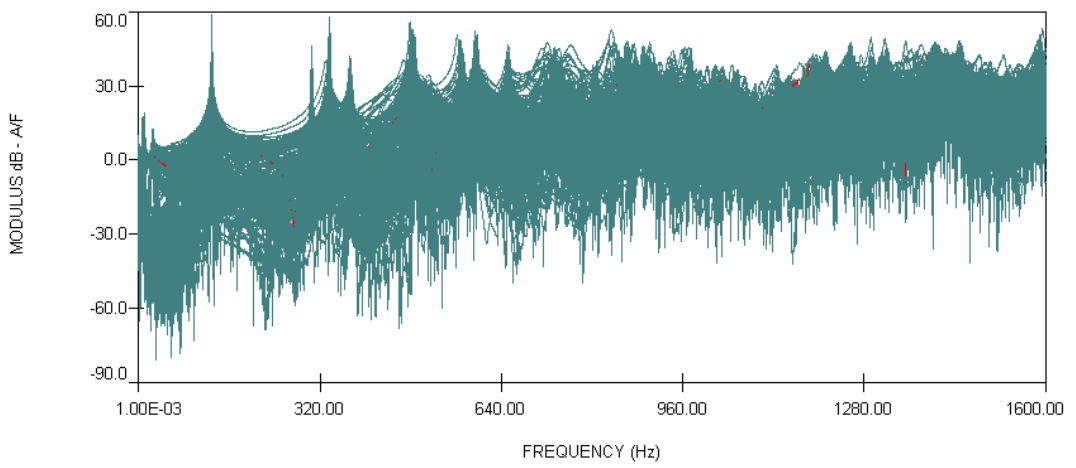

Figure 3.25 : All Measured FRFs on the Structure

However, as the mass of the structure is relatively small, there is mass effect of the accelerometer, so at some modes it is difficult to determine the modal parameters. To overcome this problem, by selecting a fixed measurement point, the structure is excited at 110 points, and 330 FRFs are measured (see Figure 3.26).

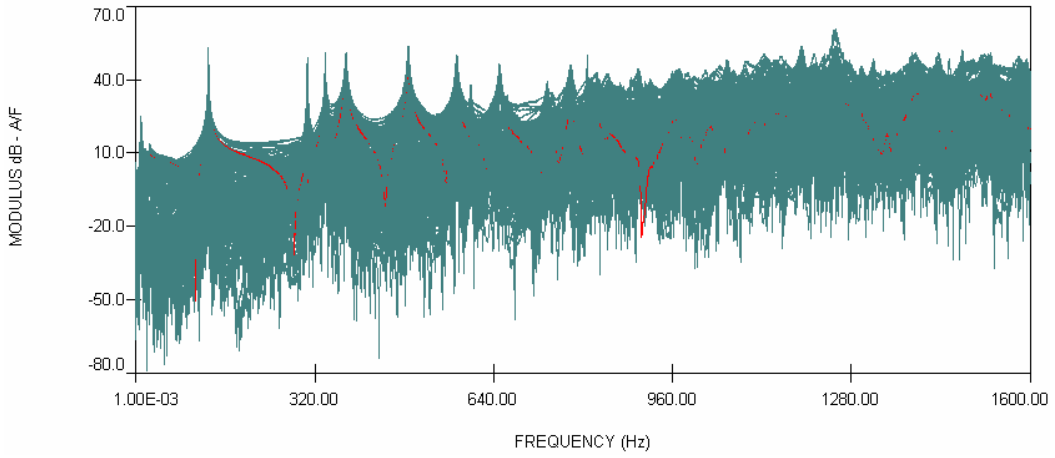

Figure 3.26 : All the Measured FRFs on the Structure (exciting the structure at 110 nodes)

The obtained two set of FRFs are analysed [71] using SIMO methods and modal parameters of the structure are obtained. Some experimentally obtained and theoretical mode shapes are given in Figure 3.27.

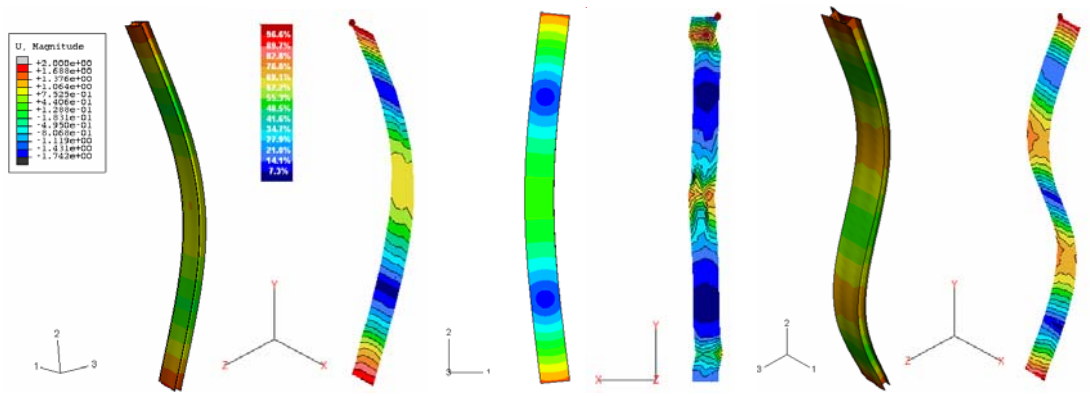

1st Mode Shapes 2nd Mode Shapes 3rd Mode Shapes

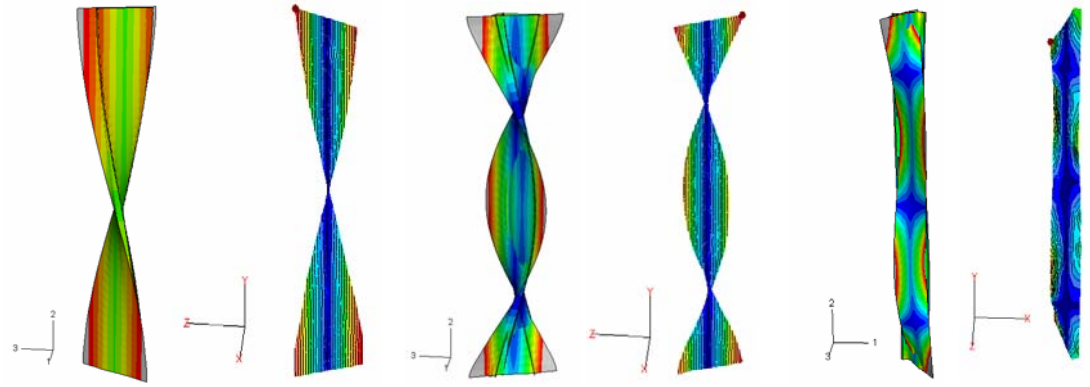

4th Mode Shapes 5th Mode Shapes 6th Mode Shapes

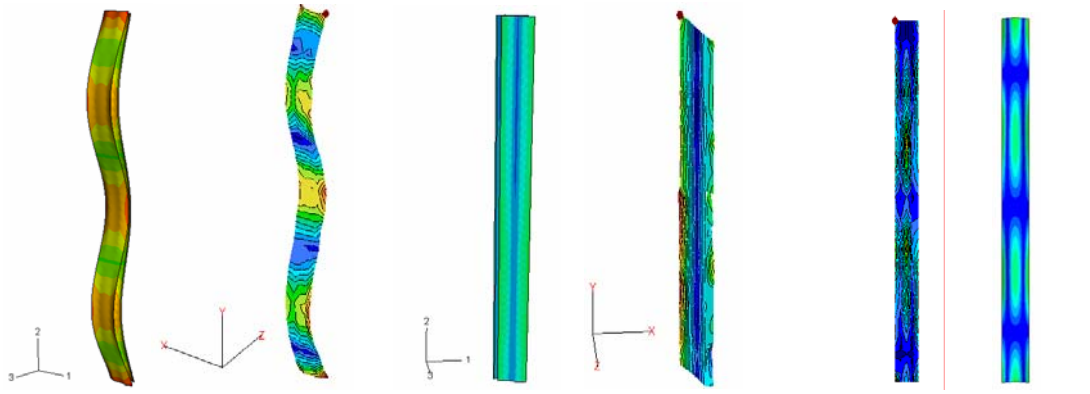

7th Mode Shapes 8th Mode Shapes 17th Mode Shapes

Figure 3.27 : The First 8th and 17th Theoretical and Experimental Mode Shapes (first pictures are the theoretical ones and second ones are the experimental ones)

Natural frequencies of these experimental modes are given in Table 3.6.

Table 3.6 : Experimentally Obtained Natural Frequencies

Mode	Experimental Natural Frequency [Hz]
1	129,7
2	308,2
3	338,8
4	376,1
5	487,4
6	573,9
7	599,1
8	651,4
9	735,7
10	778,1
11	807,5
12	825,3
13	842,0
14	843,9
15	857,8
16	867,7
17	885,0

Theoretical modal analyses of the FE model of the riveted beam with the 6 mm effective clamping diameter for three weighting functions are performed, and their results are compared with experimental natural frequencies in Figure 3.28.

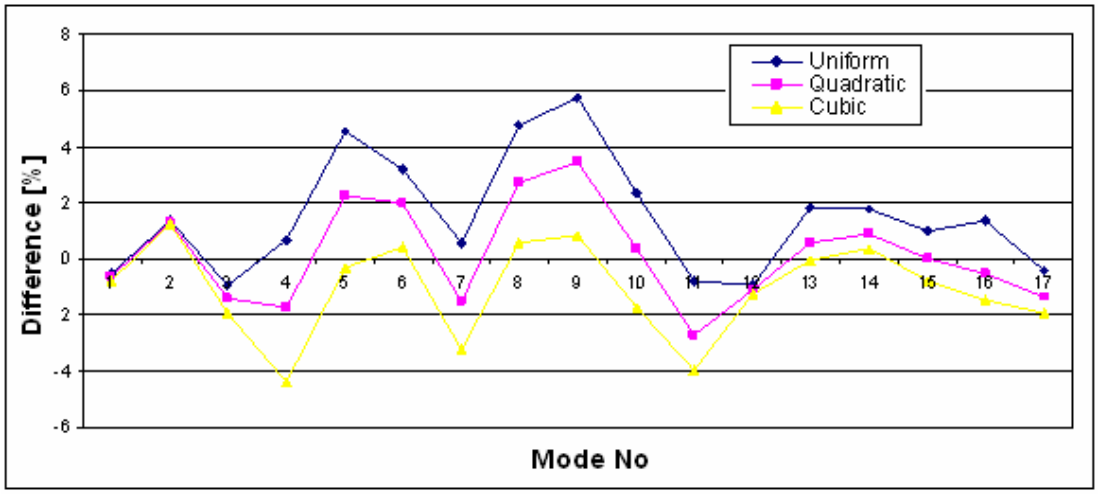

Figure 3.28 : Difference between Experimental and Theoretical Natural Frequencies Obtained for Different Weighting Functions (Effective Clamping Diameter is 6 mm)

As seen in Figure 3.28, the structure is modelled most rigid in the case of uniform weighting method and the most flexible in the case of cubic weighting. Here, for the

6 mm effective clamping diameter at three weighting functions, the errors are under % 6 and the experimental and theoretical results are close to each other. However, for this specific effective clamping diameter (6 mm), the best similarity in terms of natural frequencies results in the case of quadratic weighting function.

Sometimes, due to the geometry of the structure, FE mesh of the structure can not be fine and it is not possible to define a small effective clamping diameter for the given FE mesh. So, a bigger effective clamping diameter should be used. In Figure 3.29, the natural frequencies of the FE model with 10 mm effective clamping diameter are compared with experimental ones.

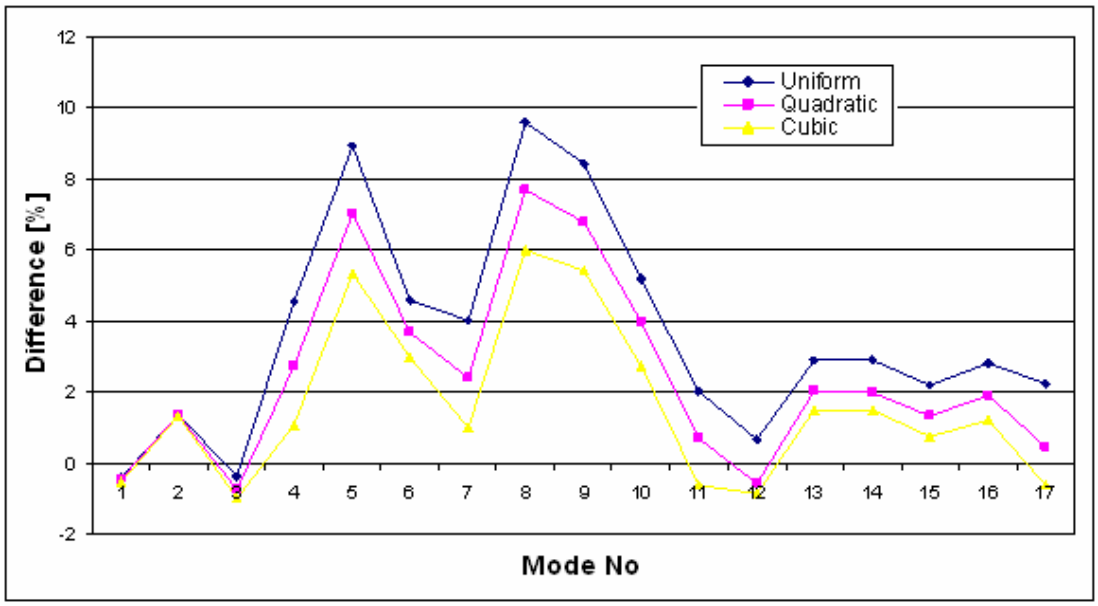

Figure 3.29 : Difference between Experimental and Theoretical Natural Frequencies Obtained for Different Weighting Functions (Effective Clamping Diameter is 10 mm)

For 6 mm effective clamping diameter with quadratic weighting function, the theoretical (FE) and experimental results are best agreed with each other resulting in errors less than a few percent. For a bigger effective clamping diameter, 10 mm, theoretical (FE) and experimental results are best agreed with each other at cubic weighting function. This is an important result. For instance, in the case of a huge helicopter structure, it may not possible to define small effective clamping diameters due to its relatively coarse mesh. For such cases, it is better to define larger effective clamping diameters and use cubic weighting function. It is interesting to note that the optimum value of the ECD, 6 mm, is found to be about the average of the rivet's

cross sectional diameter and rivet head diameter, or it is between the rivet's cross sectional diameter and rivet head diameter. On the other hand, the bigger ECD value, 10 mm, is between two times of the rivet's cross sectional diameter and two times of the rivet head diameter. Therefore, for an ECD value between the rivet's cross sectional diameter and rivet head diameter, it is better to use quadratic weighting function while it is better to use cubic weighting function for higher ECD values.

MAC table which compares the experimental and theoretical (6 mm effective clamping diameter, quadratic weighting) natural frequencies and mode shapes is given in Table 3.7. As seen, high MAC values and low errors between the experimental and theoretical natural frequencies determines that the theoretical model represents the real structure well.

Table 3.7 : MAC Table (Riveted Beam)

Exp. Mode No	**Exp. Nat. Freq. [Hz]**	**Theo. Mode No**	**Theo. Nat. Freq. [Hz]**	**Nat. Freq. Error [%]**	**MAC**
1	129.7	***1***	128.9	1.	***97.8***
2	308.2	***2***	310.9	1.	***77.6***
3	338.8	***3***	334.0	1.	***81.6***
4	376.1	***4***	369.7	2.	***89.6***
5	487.4	***5***	498.3	2.	***96.1***
6	573.9	***6***	585.5	2.	***68.4***
17	885.0	***17***	872.9	1.	***45.4***

A typical measured FRF and theoretically generated FRF for the case of 6 mm ECD with cubic weighting function are also compared in Figure 3.30. It is seen that the correlation is quite good although there are still some differences between the theoretical and experimental natural frequencies. It should also be noted that the FE models did not include any damping, hence the amplitudes of measured and predicted FRFs around natural frequencies are quite different in Figure 3.30. The modal damping values for the individual modes were determined experimentally and, if required, they can be used directly in an FE model described in terms of modal model. Further research seems to be necessary for the damping mechanism if it is to be incorporated in a rivet model.

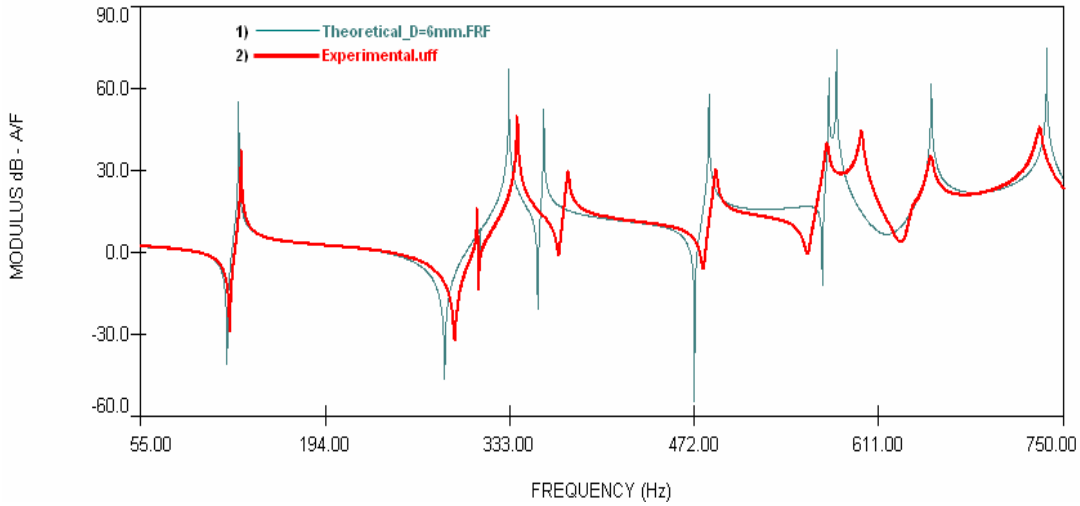

Figure 3.30 : Comparison of Measured and Theoretically Generated FRFs for ECD=6 mm and Cubic Weighting Function

3.3 Tail Boom Section

3.3.1 Introduction

In this section, a finite element model for a helicopter tail boom section is developed first. Then a simplified but representative - in terms structural members and manufacturing processes - prototype is manufactured and its numerical model is developed (see Figure 3.31). In the next step, an experimental set-up is prepared and the accuracy and the reliability of the measured data are established using some preliminary tests. This is followed by measurements of Frequency Response Functions at many locations on the test structure. Then, the natural frequencies, damping factors and mode shapes are obtained by analysing the measured data. Finally, the measured behaviour of the test structure is compared with that of the predictions.

3.3.2 Experimental study

3.3.2.1 Experimental setup and preliminary tests

For the tail boom section 11 measurement stations are selected along the axial direction and at each station, 11 points in circumferential directions are selected for FRFs measurement. The structure is suspended with flexible rubber as seen in Figure

3.32, so that free-free boundary conditions are provided. Structure is excited with a modal hammer and responses are measured in radial directions with one dimensional accelerometers. In Figure 3.33, the measurement points on the test structure are seen.

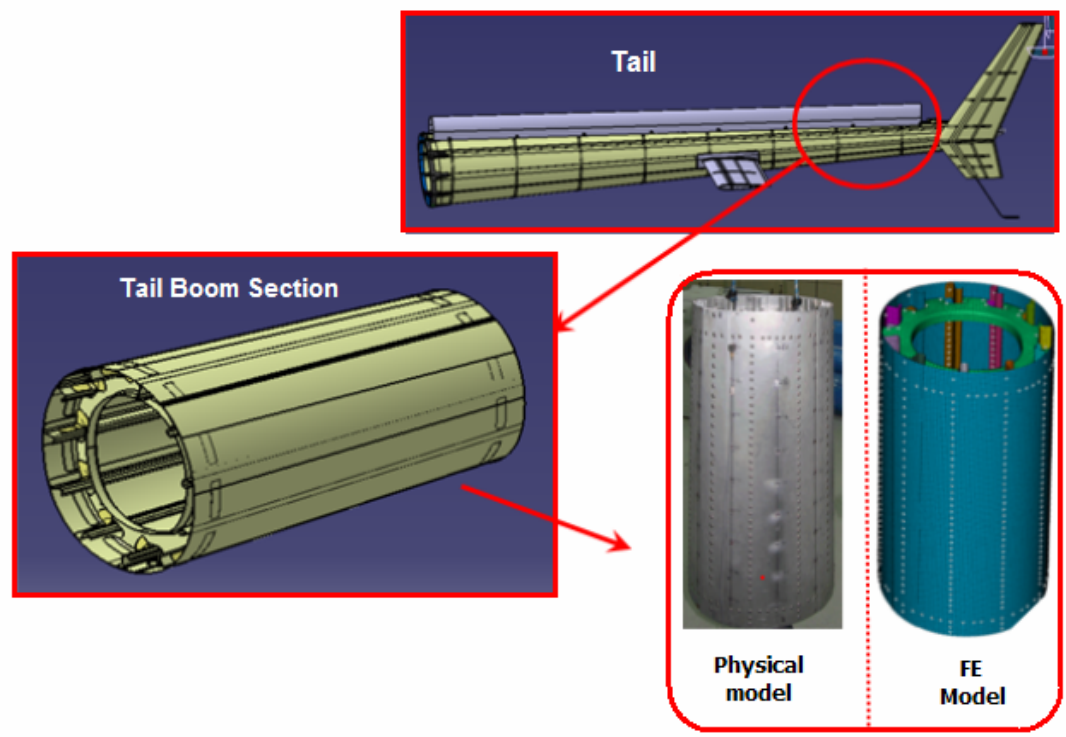

Figure 3.31 : Tail Boom Section

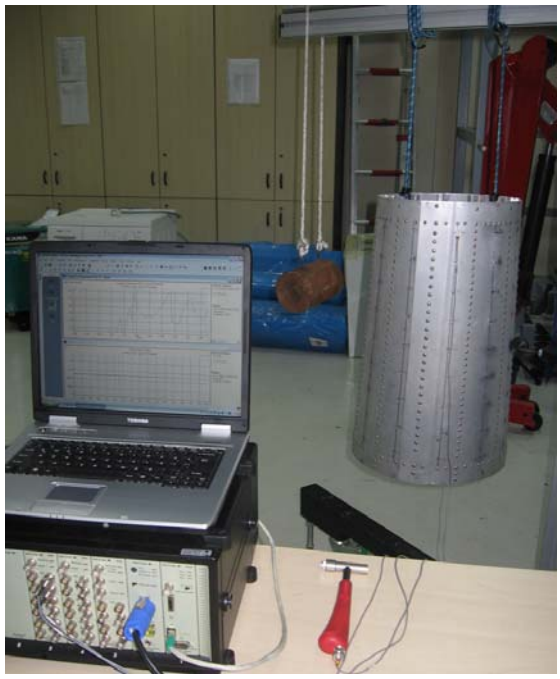

Figure 3.32 : Experimental Setup

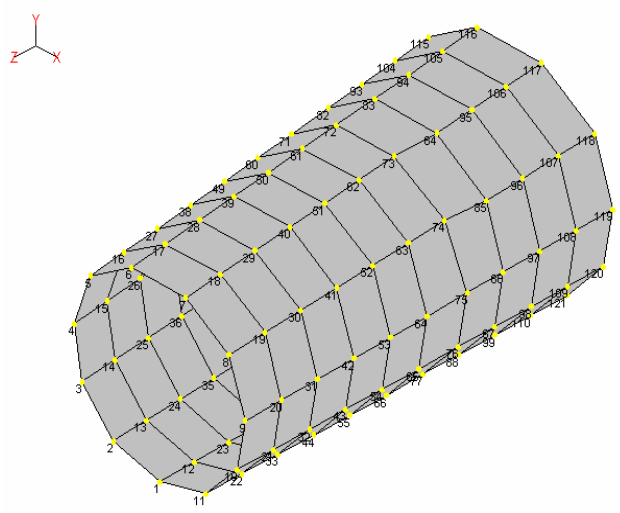

Figure 3.33 : Measurement Points

To identify a proper excitation point, some pre-tests are performed and the proper excitation is determined so that all the vibration modes can be excited in the interested frequency range.

Calibration

The calibration of the equipments used in the experiments should be known and they should be calibrated if their calibrations are not proper. For this, using a structure whose response is theoretically known, calibration of the system is controlled. In this study, a 10 kg cylinder which is assumed to be rigid is used for calibration. In a pendulum obtained using this cylinder (see Figure 3.34), acceleration of this mass can be written as

$$A = \frac{F}{m} \tag{3.5}$$

where m is the mass of the cylinder, A is the acceleration amplitude of the rigid mass and F is the force amplitude applied to cylinder. FRF also can be written as in (3.6) and the amplitude of the FRF is as in (3.7) with reference 1 $\left[kg^{-1}\right]$.

$$\frac{A}{F} = \frac{1}{m} \tag{3.6}$$

$$\frac{A}{F} = -20 \quad \text{dB} \tag{3.7}$$

Using the pendulum explained above the measurements are performed, and as seen in Figure 3.35,

$$\frac{A}{F} \cong -20 \pm 0.5 \text{ dB}$$

in the worst case. It means that calibration of the system is appropriate.

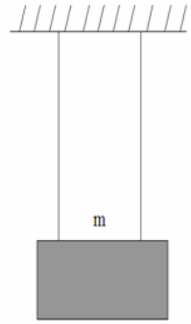

Figure 3.34 : Calibration Cylinder

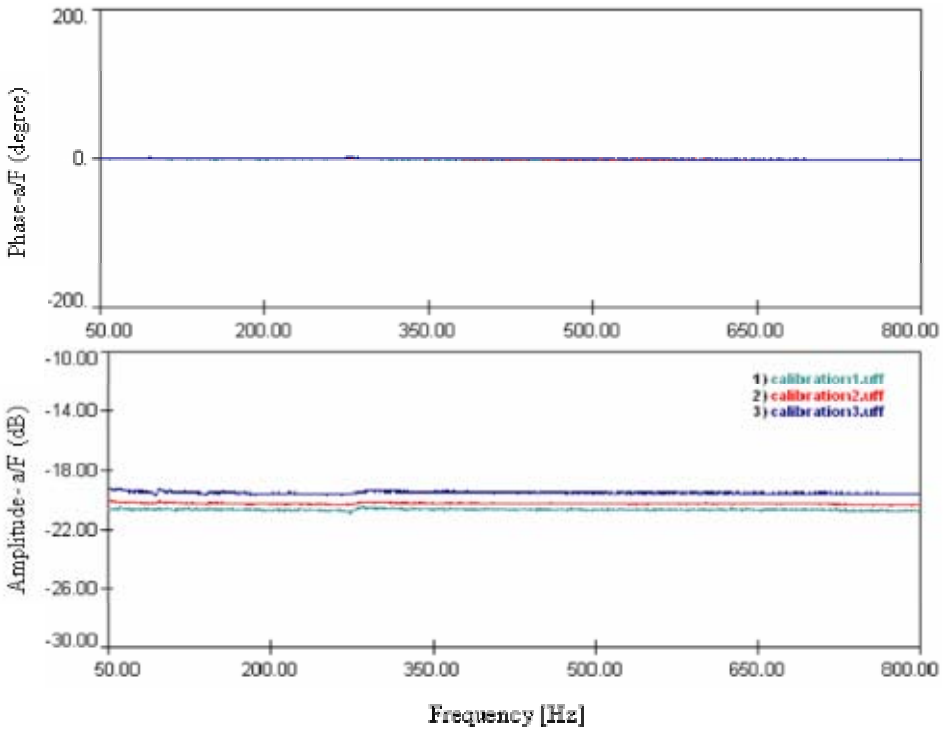

Figure 3.35 : Calibration Results

Selection of measurement parameters

In this study, measurements are performed in the frequency range of 7-800 Hz, the measurement period being $T = 2$ s. While calculating FRFs, to prevent leakage in the spectrum of acceleration, proper windowing should be applied to the signals. But, before that, it should be decided whether application of the windowing is needed. Because, although with suitable windowing function leakage can be prevented, it may also cause some loss of data. In Figure 3.36, a typical acceleration time signal without applying windowing is seen.

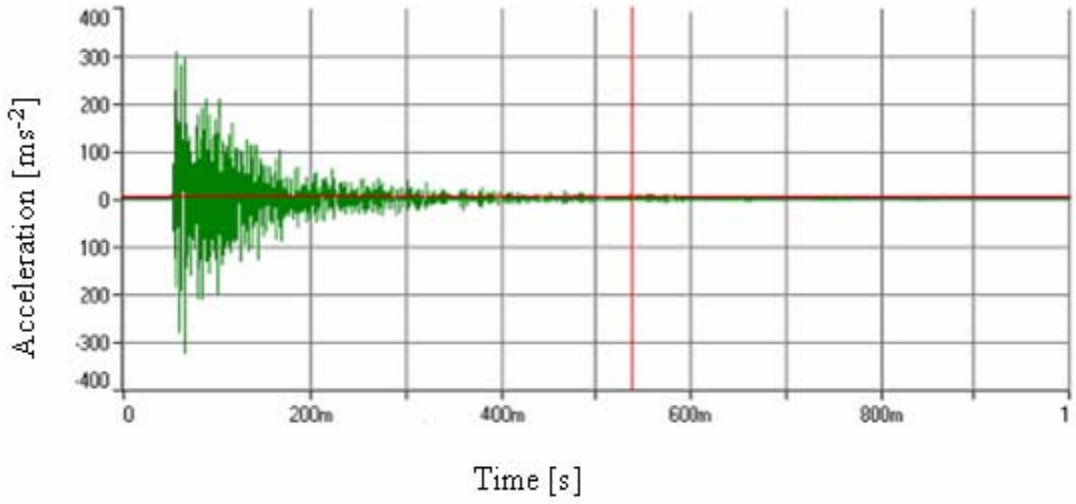

Figure 3.36 : Time Signal

Applying a windowing function is not recommended when it is not needed. To demonstrate this, an exponential window is applied to the acceleration signal shown in Figure 3.36 [74], and the FRFs in the cases with and without windowing are compared as in Figure 3.37. As seen in Figure 3.37, in the case of applying windowing to the acceleration signal, the form of the FRF is not changed, only amplitudes are decreasing a bit. As a result, as seen in Figure 3.36, because at the end of at $T = 2$ s the acceleration signal decays to zero, in the calculation of the spectrum there will not be any leakage, so it is not needed to apply windowing to the signal. Hence, it is prevented being added a numerical damping.

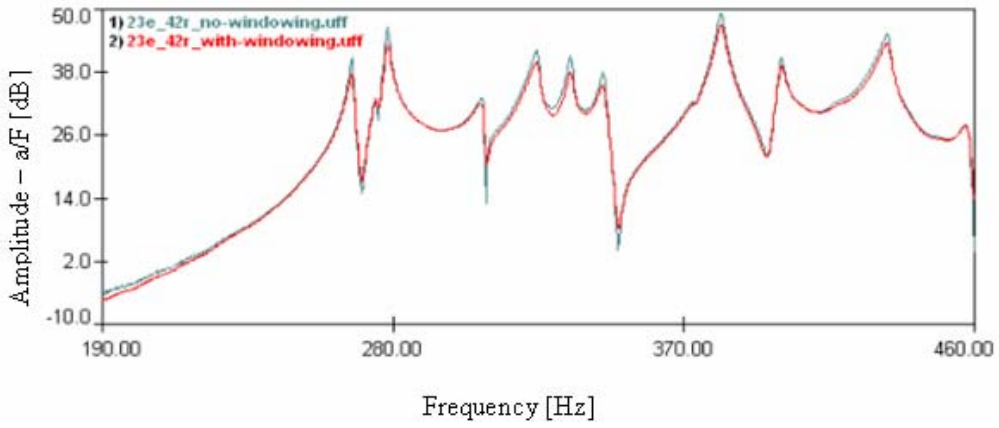

Figure 3.37 : Effect of Application of Windowing to the Acceleration Signal on FRF (excitation at 23rd point, response at 42nd point)

Repeatability and reciprocity tests

For repeatability behaviour control, the structure is excited at a coordinate (63rd point) and response is measured at another coordinate (22nd point) at different times and measured FRFs are given in Figure 3.38. As seen, at three different cases, nearly the same results are obtained. This shows that the measurements are very repeatable.

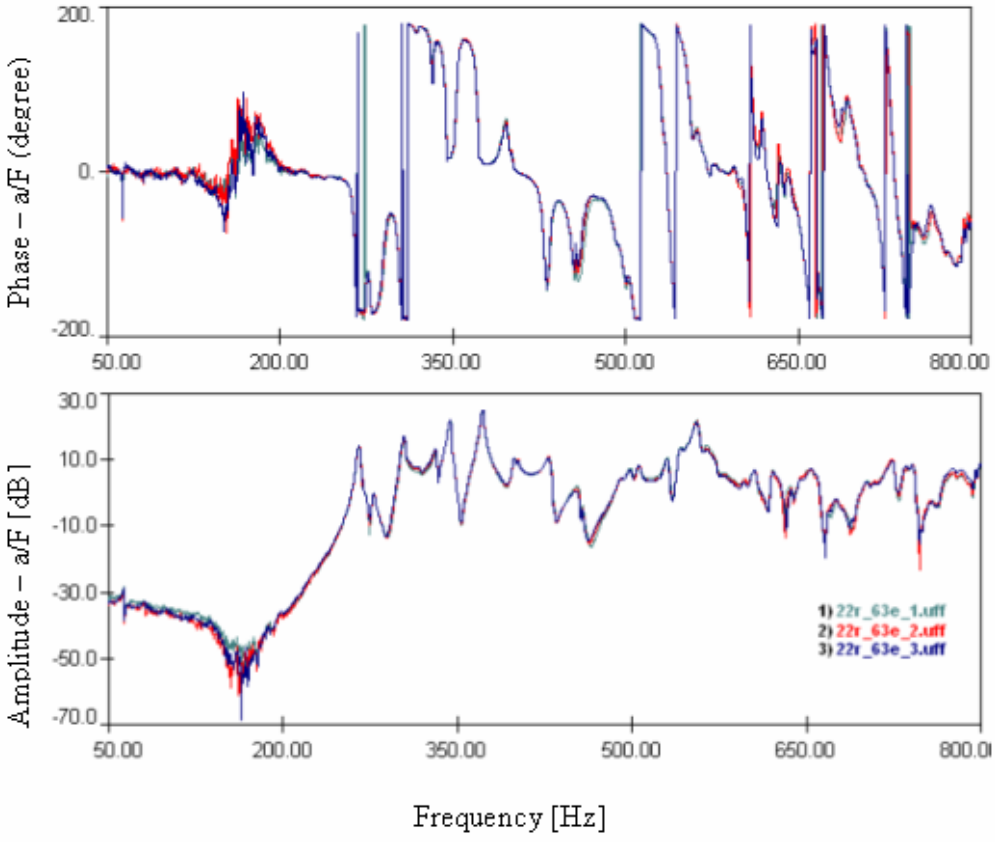

Figure 3.38 : Repeatability Tests

For reciprocity behaviour control, the structure is excited at one of the coordinates (36th point) and response is measured at some other coordinate (72nd point). Then the measurements are repeated by swapping the excitation and response coordinates. The corresponding FRFs are compared in Figure 3.39. As seen, the measured FRFs are nearly the same and this shows that the measurements are properly done.

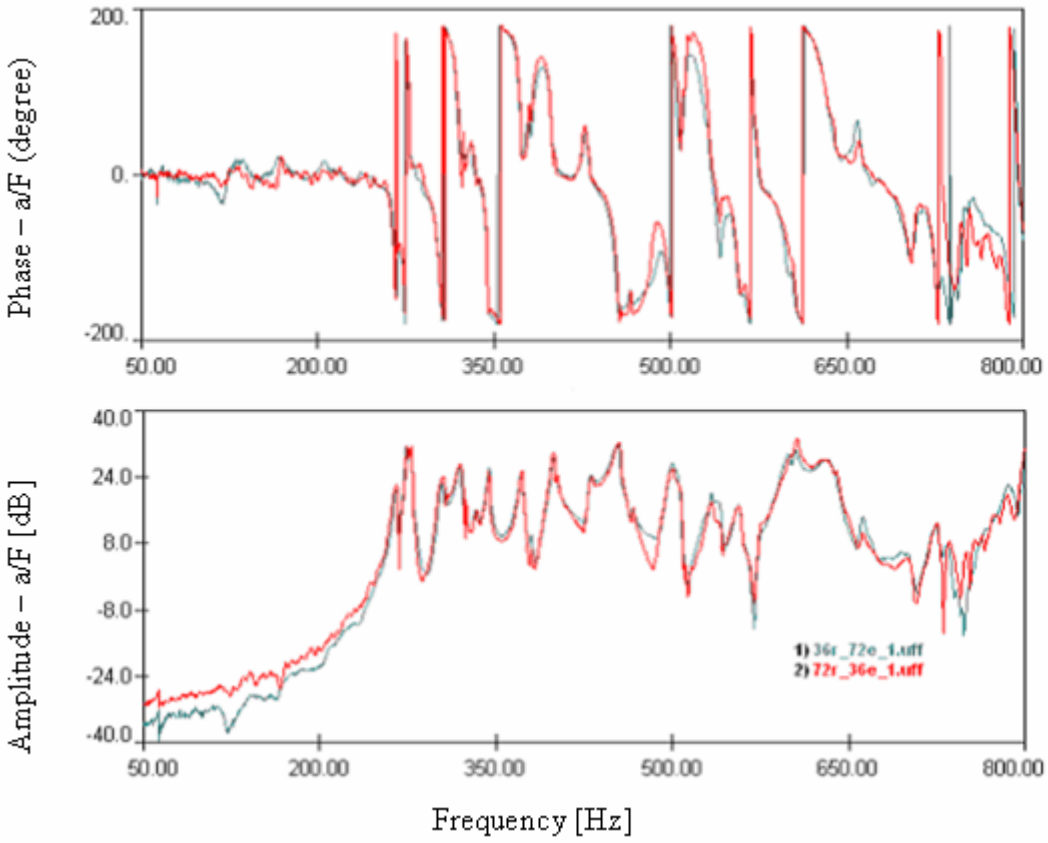

Figure 3.39 : Reciprocity Control

Nonlinearity control

As seen in Figure 3.40, although the FRFs obtained by changing the amplitude of the force level (low, high) results show negligible differences. It can be said that nonlinearity behaviour of the structure is not dominant.

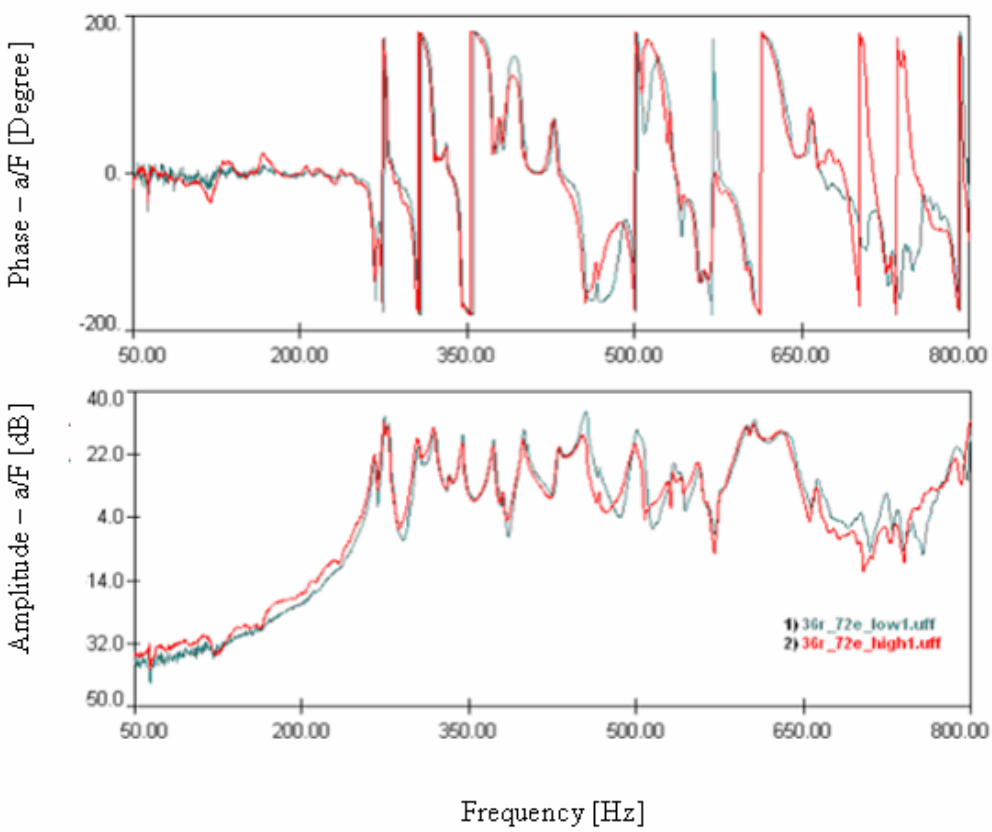

Figure 3.40 : Nonlinearity Control (excitation at 72nd point, response at 36th point)

3.3.2.2 Experimental modal analysis

Following experimental controls, test structure is excited at its 72nd node and FRFs are measured at 121 nodes (see Figure 3.41). The measured FRFs are analysed [71] using SIMO methods and modal parameters of the structure are obtained. Because of the complexity of both geometry and the joints the structure contains, it may not be possible to excite all interested modes by exciting it at a single coordinate. Hence, the structure is also excited at another node (23rd) and responses are measured again at 121 nodes (see Figure 3.42).

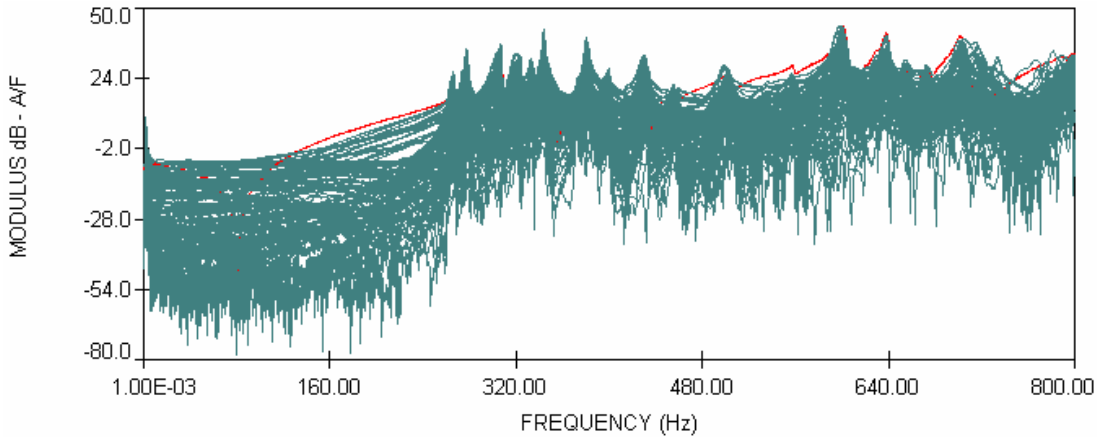

Figure 3.41 : All Measured FRFs on the Structure (Point FRF 23)

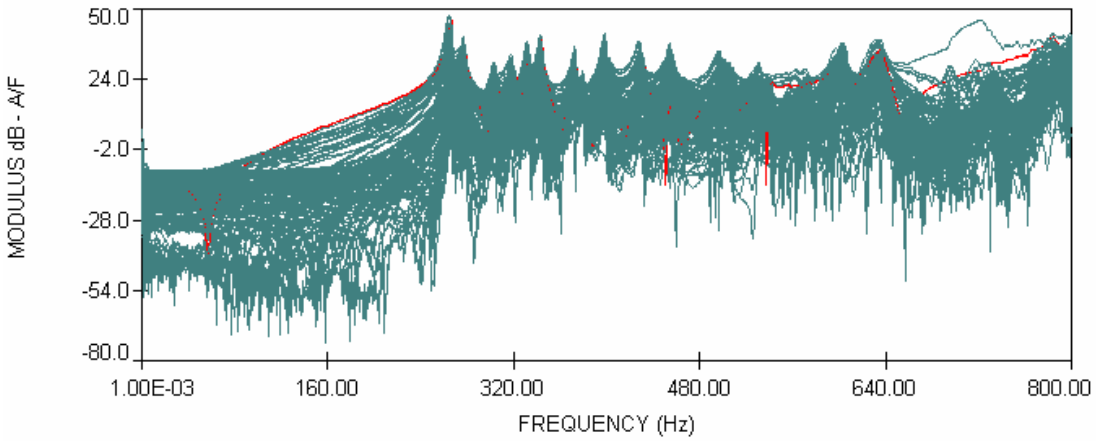

Figure 3.42 : All Measured FRFs on the Structure (Point FRF 72)

These two measurement data sets obtained are analysed using MIMO to extract modal parameters. For example, in Figure 3.43, a typical experimental SIMO modal analysis procedure to estimate natural frequencies, modal damping values and mode shapes by using all measured FRFs in the range of 270-285 Hz (the range including 2nd and 3rd modes) is demonstrated.

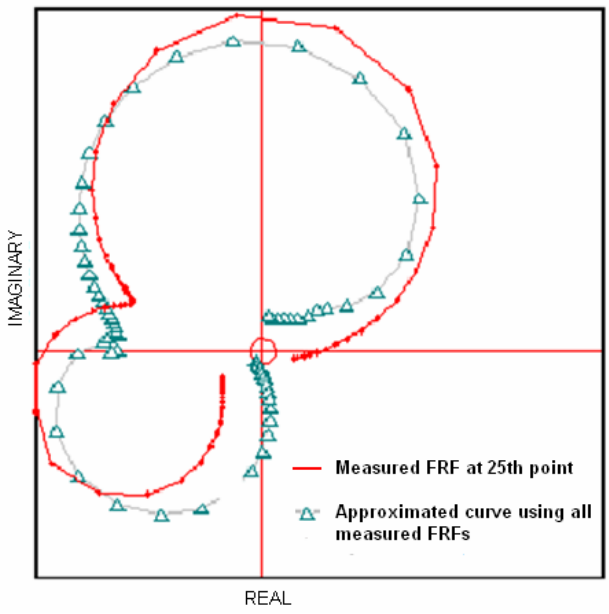

Figure 3.43 : A Typical Experimental Modal Analysis Procedure

Similarly, using frequency ranges including one or two modes at a time, all the modal parameters are estimated using both SIMO and MIMO options in ICATS [71]. MIMO Multivariate Mode Indicator Function (MIF), in which the lowest local values give the natural frequencies, predicted using both of the FRF data sets at the beginning of the analyses is given in Figure 3.44. The measured natural frequencies, modal damping values and some mode shapes via SIMO and MIMO options are given in Table 3.8 and Figure 3.45.

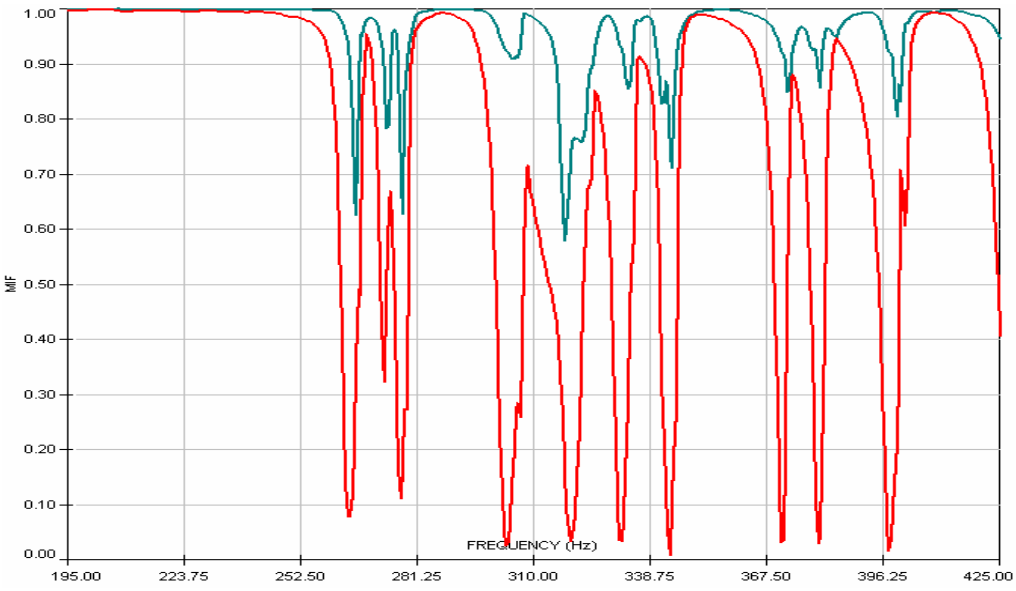

Figure 3.44 : MIMO Multivariate MIF

Table 3.8 : Experimental Obtained Natural Frequencies

Mode No	Experimental Nat. Freq. [Hz]	Loss Factor [%]
1	265.9	0.7
2	273.3	0.3
3	277.4	0.6
4	305.6	0.9
5	318.9	1.0
6	332.5	0.8
7	344.2	0.9
8	371.3	0.6
9	380.7	0.9
10	397.9	0.7

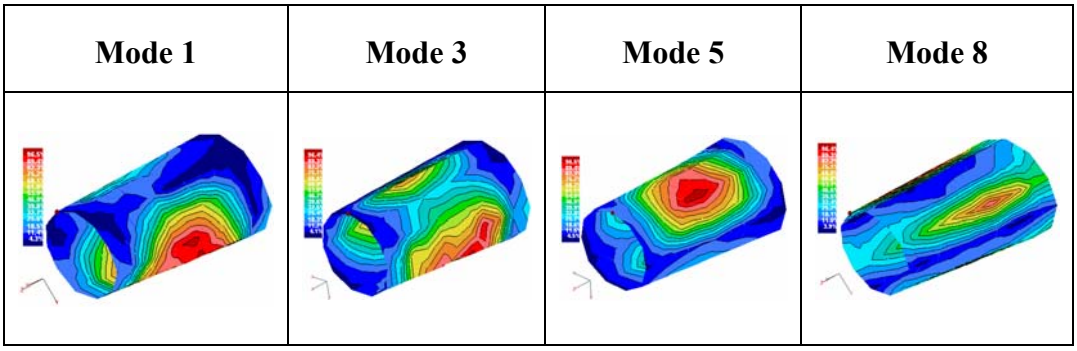

Figure 3.45: Some Experimentally Obtained Mode Shapes of the Tail Boom Section

3.3.3 Corralation, validation and updating

3.3.3.1 Preliminary FE models

A FE model of the tail boom section is built up [70] by using reference surfaces (mid-surfaces) of the parts of the structure (see Figure 3.46).

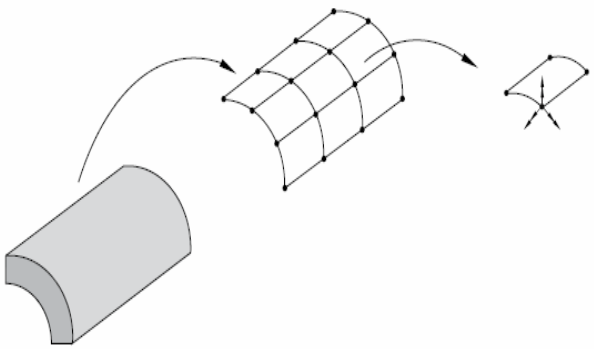

Figure 3.46 : Approach in Building up FE Model of Structures

Mesh of the parts is generated using a four node linear element (S4R). Assembling of the parts is performed firstly by assuming that the overlapping sections are fully constrained, i.e., fully-welded assumption (1st FE model-see Figure 3.47). Also, the geometrical details of the structure were not modelled and masses of about 580 rivets were not included in this first model. Global mesh size is 6.5 mm. Mesh of the resulted model is quite fine, which has 27646 elements, 31091 nodes and 186546 DOFs in total. Mass of the model was about 4000 g while the measured mass of the test structure was 4505 g.

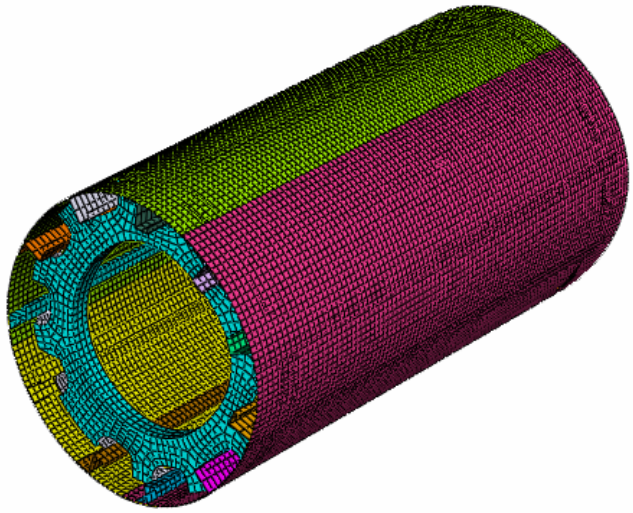

Figure 3.47 : First FE Model of the Tail Boom Section

Using the first FE model built up in ABAQUS program, modal analysis performed using Lanczos solver for the first 35 modes. Comparison of the first eight natural frequencies with their corresponding experimental ones is given in Table 3.9.

Table 3.9 : Theoretical Natural Frequencies (1st FE Model) and Differences from Experimental Ones

Mod No.	Theoretical Nat. Freq. [Hz]	Difference [%]
1	333,3	25,3
2	342,8	25,4
3	344,3	24,1
4	346.0	13,2
5	394,4	23,7
6	398,9	20,0
7	483,8	40,6
8	498,1	34,1

The first observation is that there are big differences between theoretical and experimental results. Also, in Figure 3.48, the measured and the predicted FRFs (excitation at 75th point in x direction and measuring response at 31st point in x direction) are compared. Although there seems to be some shifts in natural frequencies, FRFs do not match.

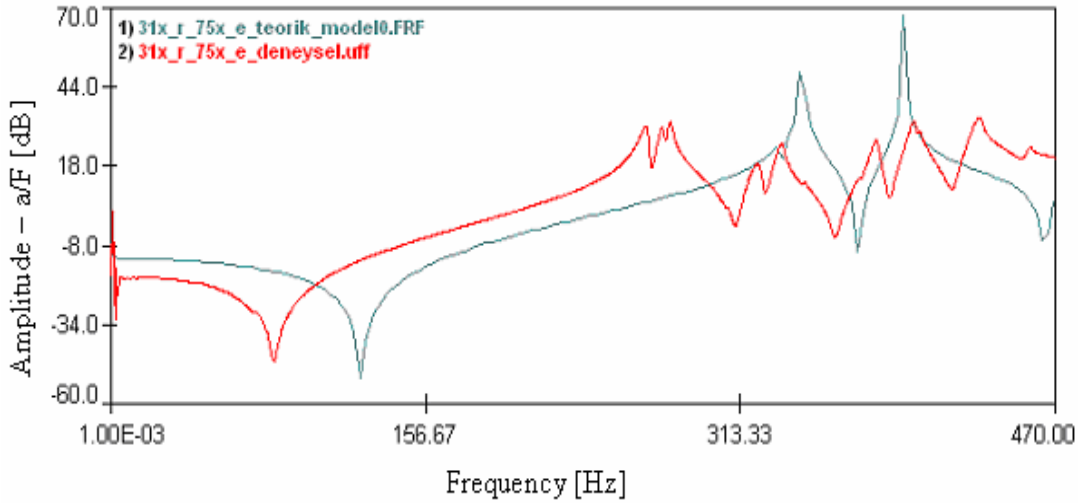

Figure 3.48 : Comparison of Measured and Theoretically Generated (1st FE Model) FRFs (Excitation at 75th Point in x Direction, Response at 31st Point in x Direction)

As seen in Table 3.9, the differences between the theoretical and experimental frequencies are large, even at first natural frequency difference is about %25. In Figure 3.49, these two sets of frequencies are compared graphically where SET1 shows experimental natural frequencies and SET2 shows theoretical natural frequencies. As seen in Figure 3.49, there are big differences between theoretical and measured natural frequencies.

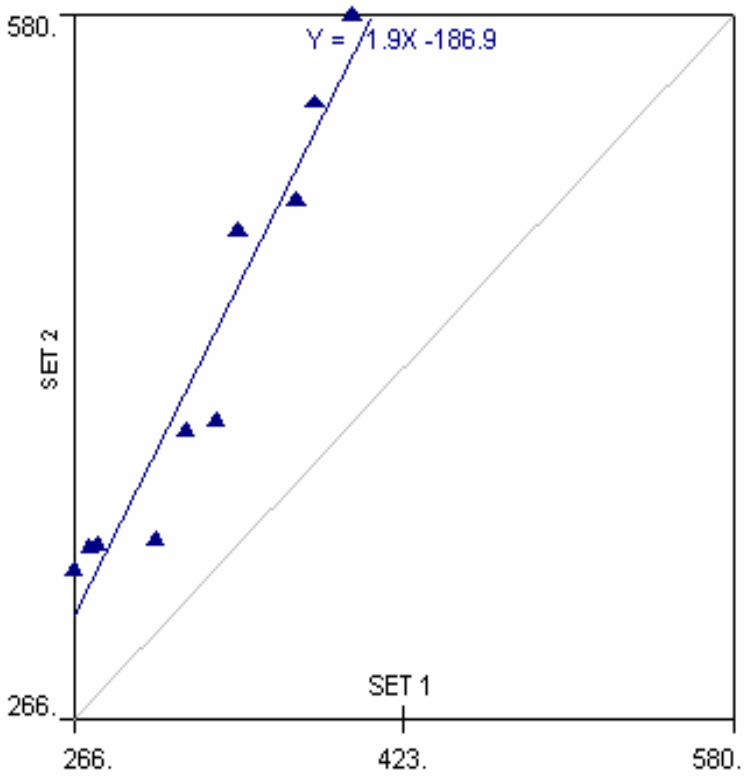

Figure 3.49 : Comparison of Theoretically Generated (1st FE Model) and Measured Natural Frequencies

Following the comparisons summarized above, the mass and some important geometrical details of the structure were examined carefully and the theoretical model is revised in order to minimize the error in the FE model. Then the FE model of the tail boom section is built up based on the assumption that each rivet is effectively clamping the matching surfaces within a specified clamping diameter around the attachment centre [70]. As the model of the boom section was built, rivet parameters were not clear, hence an arbitrarily diameter was assumed. The mass of the each rivet is included in the FE model as point mass. There were about 580 rivets, there being two types of rivets; the mass of one type is 1.3 g, that of other 0.8 g. Mesh size is 6.5 mm. Mass of this new model is 4500 g. This model shown in Figure 3.50 is so-called 2nd FE model of the tail boom section.

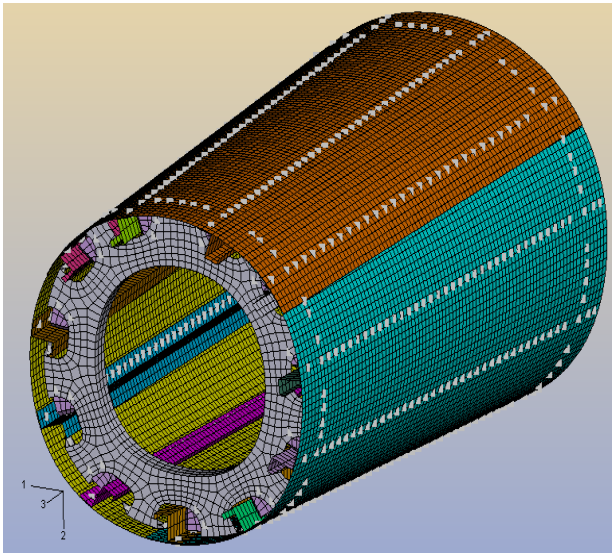

Figure 3.50 : 2nd FE Model of the Tail Boom Section

Modal analysis is performed with this new FE model (2nd model) and its modal parameters are compared with experimental results. As seen in Table 3.10, the differences in natural frequencies are slightly decreased compared to those in Table 3.9. For example, the difference between the first natural frequencies is about %18 instead of 25 % in Table 3.9. Also, the measured and predicted natural frequencies are graphically compared in Figure 3.51, and it is seen that the matching is better than before although the differences are still very high.

Table 3.10 : Theoretical Natural Frequencies (2nd FE Model) and Differences from Experimental Ones

Mod No.	Theoretical Nat. Freq. [Hz]	Difference [%]
1	312,9	17,7
2	322,8	18,1
3	326.0	17,5
4	329,9	8,0
5	368,6	15,6
6	375,6	13,0
7	439,6	27,7
8	452,1	21,8
9	557,8	46,5
10	561,0	41,0

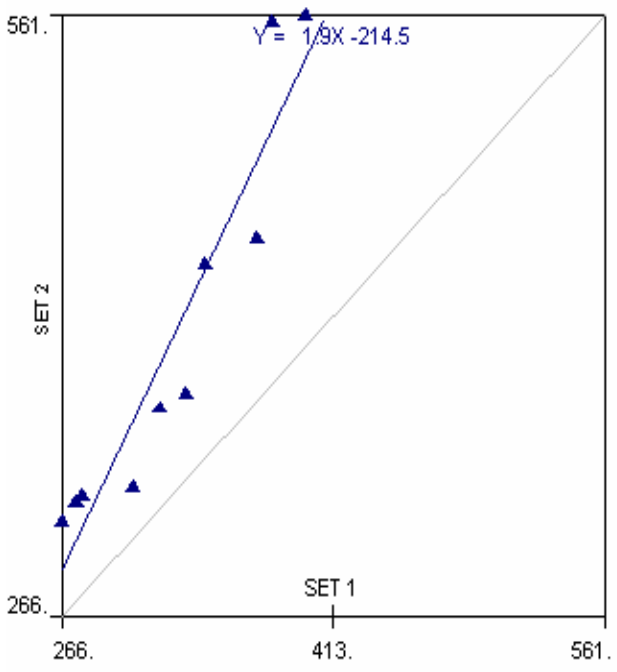

Figure 3.51 : Comparison of Predicted (2nd FE Model) and Measured Natural Frequencies

In Figure 3.52, a typical comparison of the measured and the predicted FRFs is given. Looking at the peaks of FRFs and their general forms, it is seen that there is a similarity between them. However differences are still too high.

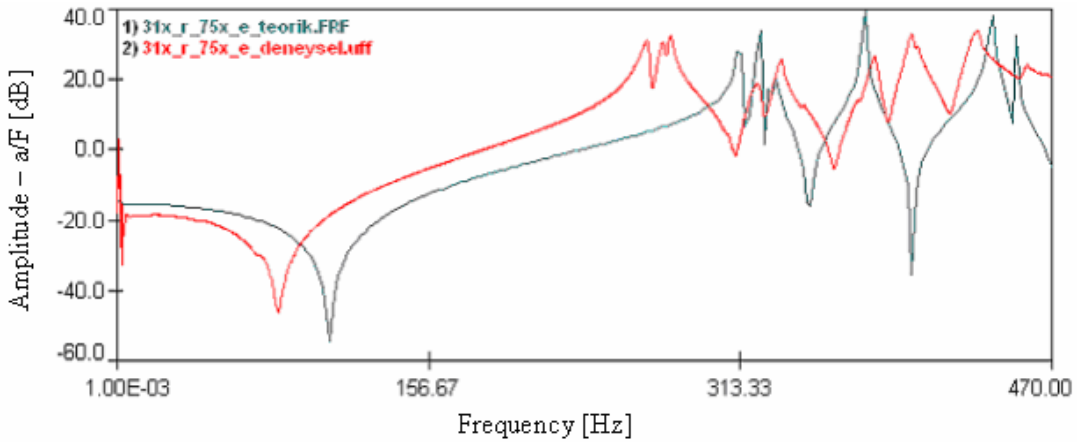

Figure 3.52 : Comparison of the Measured and Theoretically Generated (2nd FE Model) FRFs (Excitation at 75th Point in x Direction, Response at 31st Point in x Direction)

In Figure 3.53, another comparison of the measured and the predicted FRFs is given. There is a similar situation as in Figure 3.52.

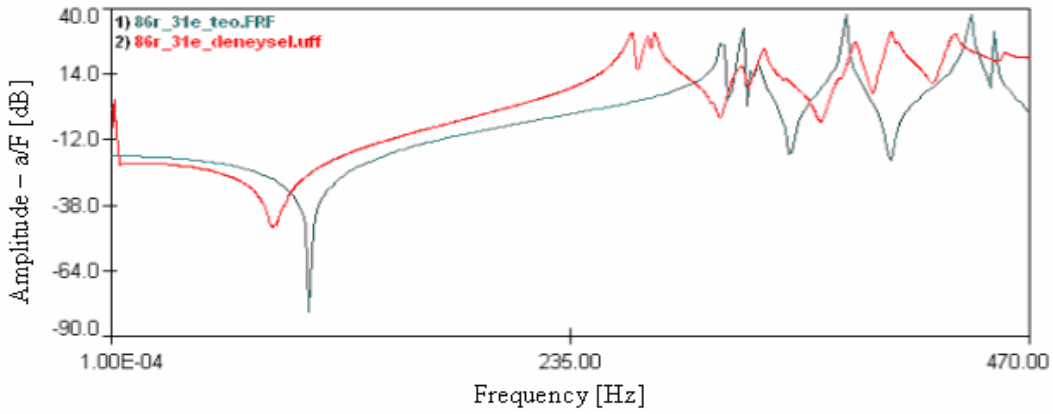

Figure 3.53 : Comparison of the Measured and Theoretically Generated (2nd FE Model) FRFs (Excitation at 31st Point in x Direction, Response at 86th Point in y Direction)

3.3.3.2 Improved FE model

Utilizing the approach proposed in Section 3.2.2, with parameters defined according to procedure described in Sections 3.2.3 and 3.3.4, new FE models of the tail boom section are built up. That is, it is assumed that each rivet is effectively clamping the matching surfaces within a clamping diameter around the attachment centre. This diameter is selected according to the suggestions in Section 3.2. The tail boom section comprises of 3 skins and at the end of skins (both at inner and outer surfaces) these are glued to each other. Without modelling this material, analyses are performed and first natural frequency is found to be about 260 Hz, which is lower than experimental one. So, glued surfaces (6 regions) are modelled in a way that they are fully clamped as seen in Figure 3.54. Resulting model is called the improved (3rd) FE model of the tail boom section.

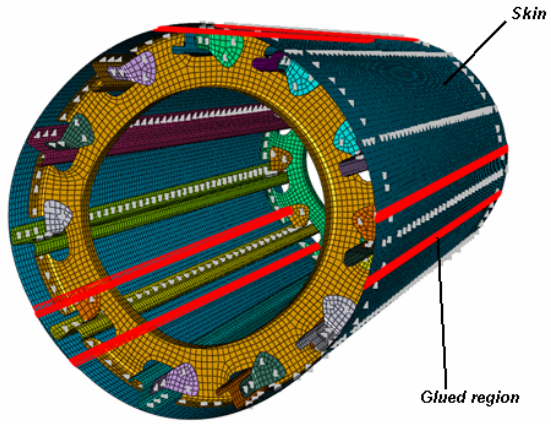

Figure 3.54 : Improved FE Model (3rd) of the Tail Boom Section

Also analyses are performed for two different mesh sizes. As seen in Figure 3.55 converge is achieved at about 5 mm.

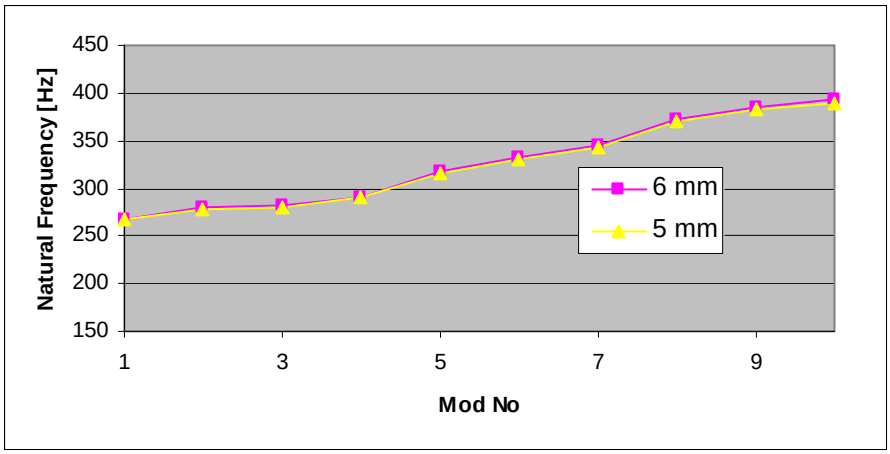

Figure 3.55 : Natural Frequencies of 10 Modes of the Improved (3rd) FE Model of the Tail Boom Section for Different Mesh Sizes

The resulted FE model with 5 mm global mesh size is shown in Figure 3.54. The model has 54815 nodes, 59029 elements, and total 353493 DOFs. Mass of the theoretical model is 4502.4 g, remembering that measured mass of the test structure is 4505 g. As seen in Table 3.11, the results show that the final FE model can predict the natural frequencies with acceptable accuracy. Also some mode shapes of the improved FE model of the tail boom section are given in Figure 3.56. Comparing those theoretical mode shapes with experimental ones in Figure 3.45, it is seen that mode matching mode shapes are similar to each other.

Table 3.11 : Theoretical Natural Frequencies of the Improved FE Model (3rd) and Differences from Experimental Ones

Mode No.	Theoretical Nat. Freq. [Hz]	Difference [%]
1	271.7	2.2
2	275.3	0.7
3	278.6	0.4
4	307.4	0.6
5	329.5	3.3
6	333.7	0.4
7	345.9	0.5
8	376.9	1.5
9	385.2	1.2
10	392.4	-1.4

Mode 1	Mode 3	Mode 5	Mode 8
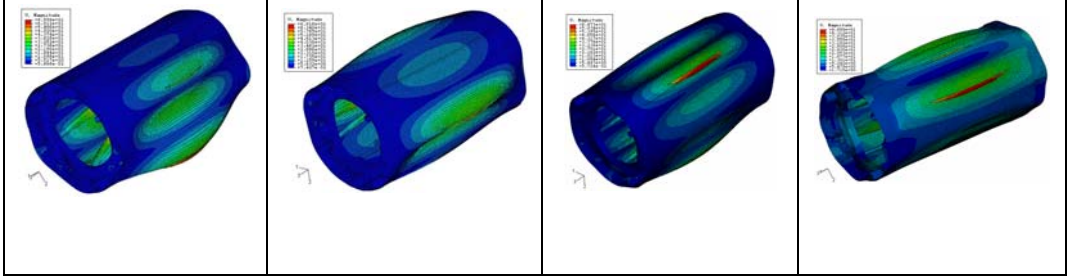			

Figure 3.56 : Some Theoretical Mode Shapes of the Tail Boom Section

3.4 Tail Boom

3.4.1 Introduction

The tail boom is one of the most important components of the helicopter structures. All the helicopter structures, such as fuselage, tail boom, vertical and horizontal stabilizers have similar structural elements.

The helicopter tail boom mainly consists of stringers, frames, skins and brackets and all these parts are joined by rivets (see Figure 3.57). In the manufacturing of the tail boom, firstly, the frames are located to fixtures and later stringers are included to the assembly. Brackets are used for riveting stringers to frames. Lastly, skins are riveted to the structure and assemble process is completed. In Figure 3.58, the manufactured helicopter tail boom of ITU-LCH is seen.

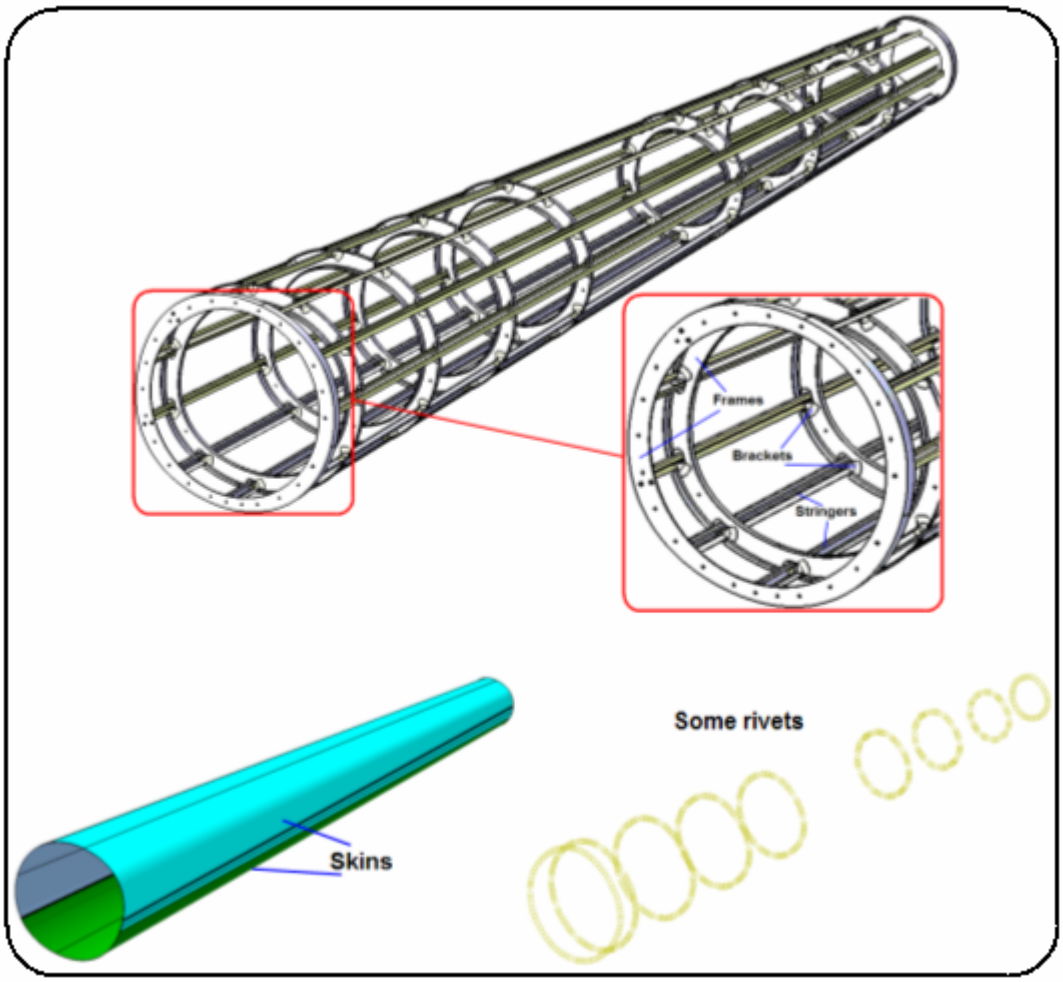

Figure 3.57 : Helicopter Tail Boom Components

Figure 3.58 : Manufactured Tail Boom of ITU-LCH

3.4.2 Preliminary Tests

As the helicopter tail boom has similar components with almost all other helicopter structures and it is quite complex, obtaining a validated FE model of this structure is important. If this structure can be modelled successfully, all the capabilities obtained from modelling this structure will be applied to FE models of all other helicopter structures including fuselage and full-scale airframe. For this reason, very detailed tests are performed on this structure. For this reason large set of FRFs are measured for test planning purposes before final detailed modal tests are carried out.

Using the experience gained so far, preliminary modal tests of the tail boom are performed. Structure is tested in free-free conditions (see Figure 3.59). As before, some quality checks are performed including calibration before measuring the FRFs. Structure is excited from a coordinate and responses are measured by some 3-D accelerometers. In Figure 3.60, the results for calibration checks on 10 kg cylinder as explained in Section 3.3 are given for all three measurement directions (x, y and z) of a typical 3-D accelerometer used in the measurements.

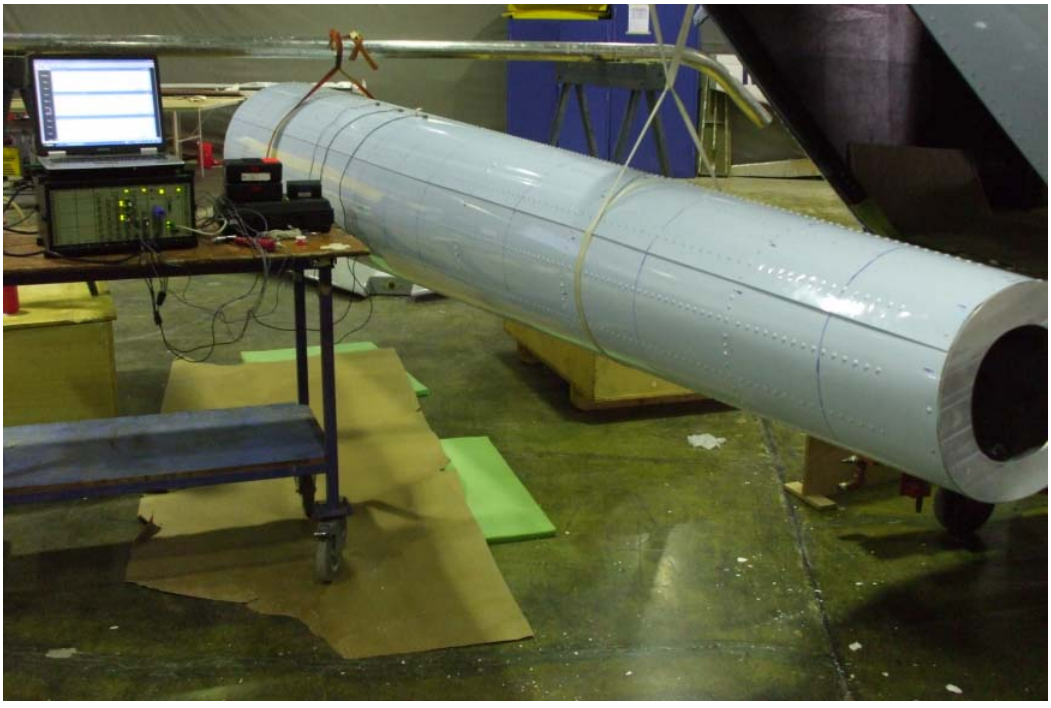

Figure 3.59 : Experimental Setup for the First Modal Tests of the Tail Boom

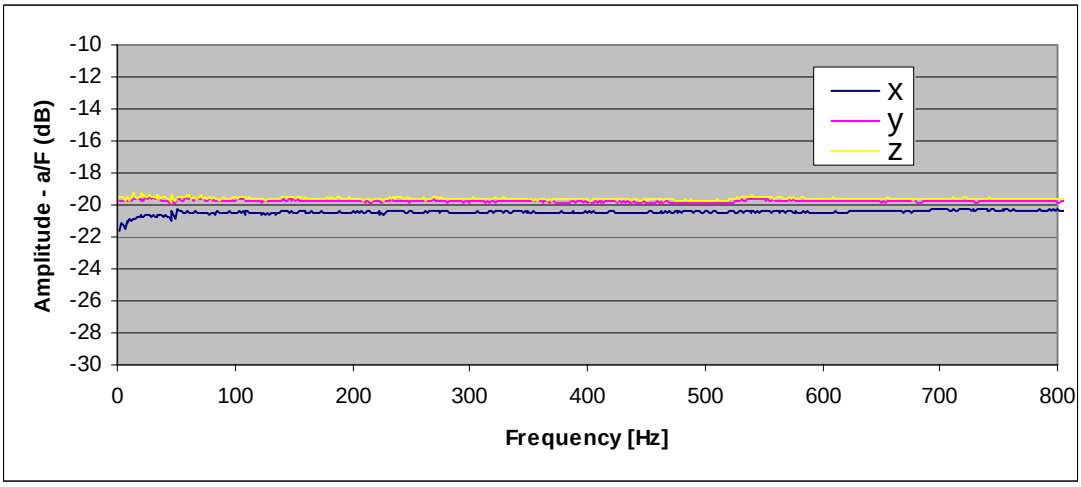

Figure 3.60 : Calibration Results of a Typical 3-D Accelerometer

Time acceleration signals for three directions of a typical response measurement and the impact force signal applied at one coordinate are shown in Figure 3.61. From these, it is seen that there is no need to apply windowing.

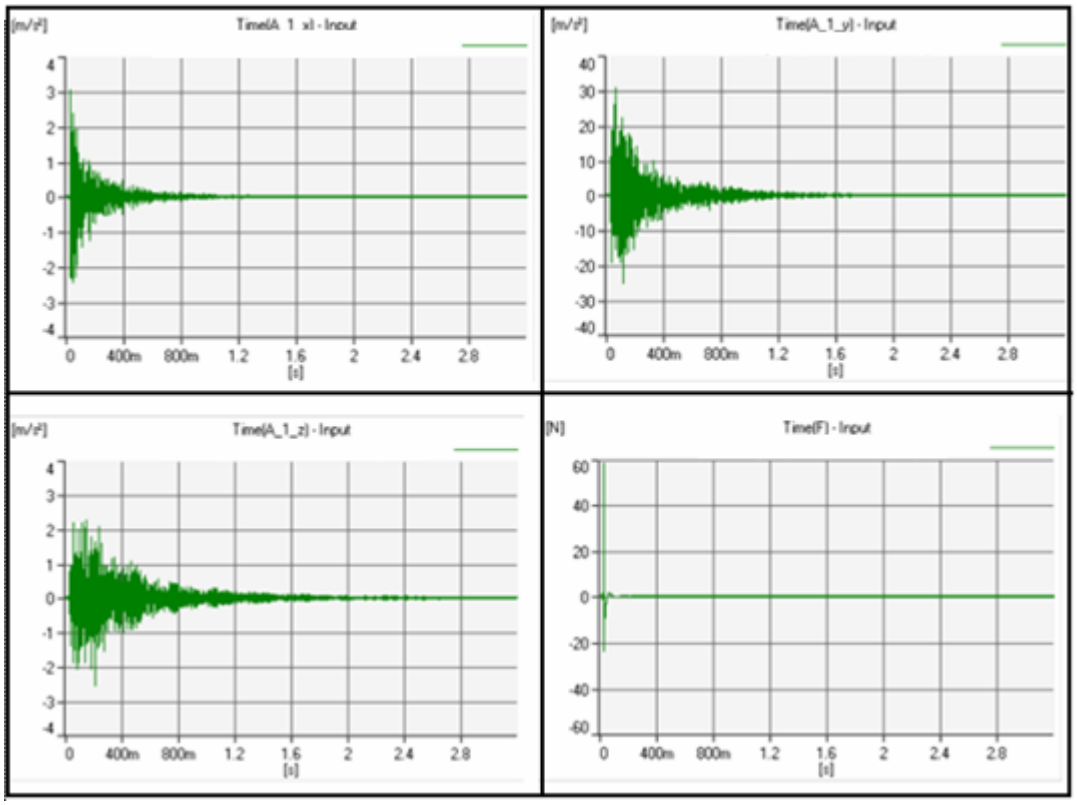

Figure 3.61 : Time Signals of Accelerations in Three Response Directions and Force

Also, by inspecting autospectrum of the force signal (Figure 3.62), it is ensured that the structure is excited properly within the frequency range of interest. In Figure 3.63, the coherence of a typical FRF measurement shows that the measurement quality is quite high.

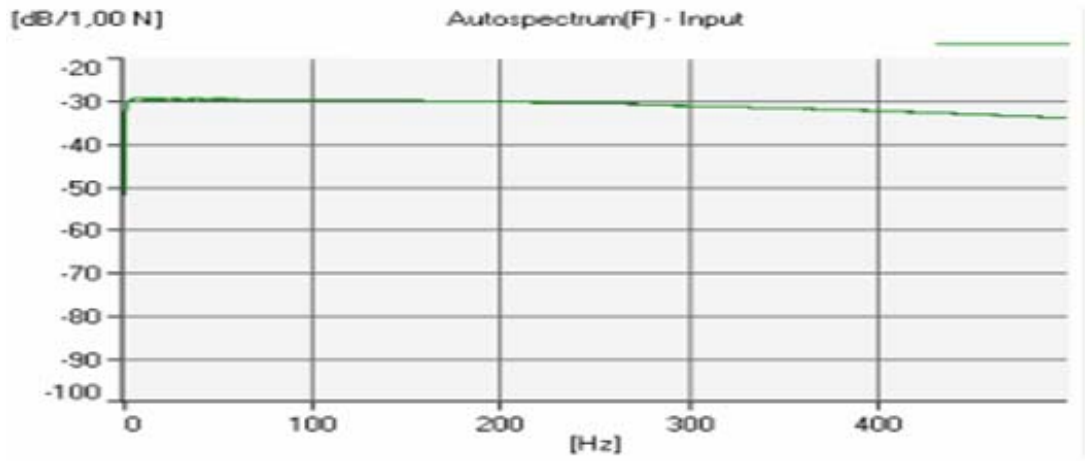

Figure 3.62 : Autospectrum of the Force Signal

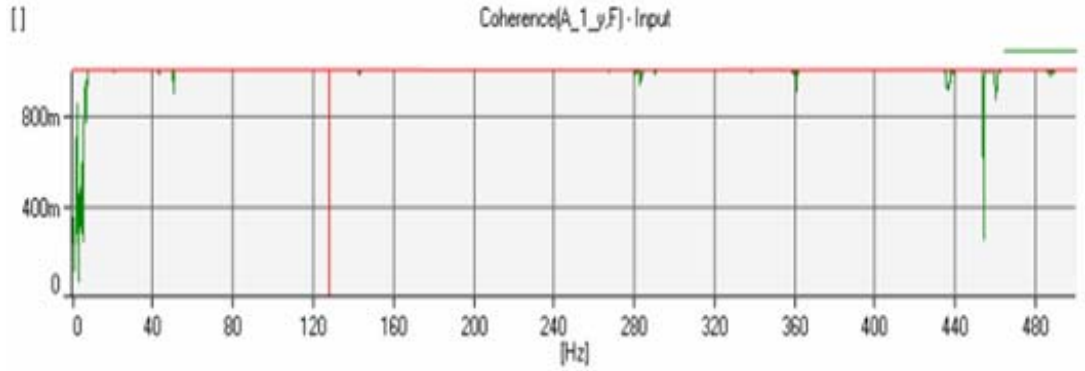

Figure 3.63 : A Typical Coherence Example

After all of these, a set of FRFs are measured by choosing a proper excitation point after some initial measurements. The structure is excited at its 133rd point and responses are taken at 114 points with 3-D accelerometers. Measurement points are given Figure 3.64.

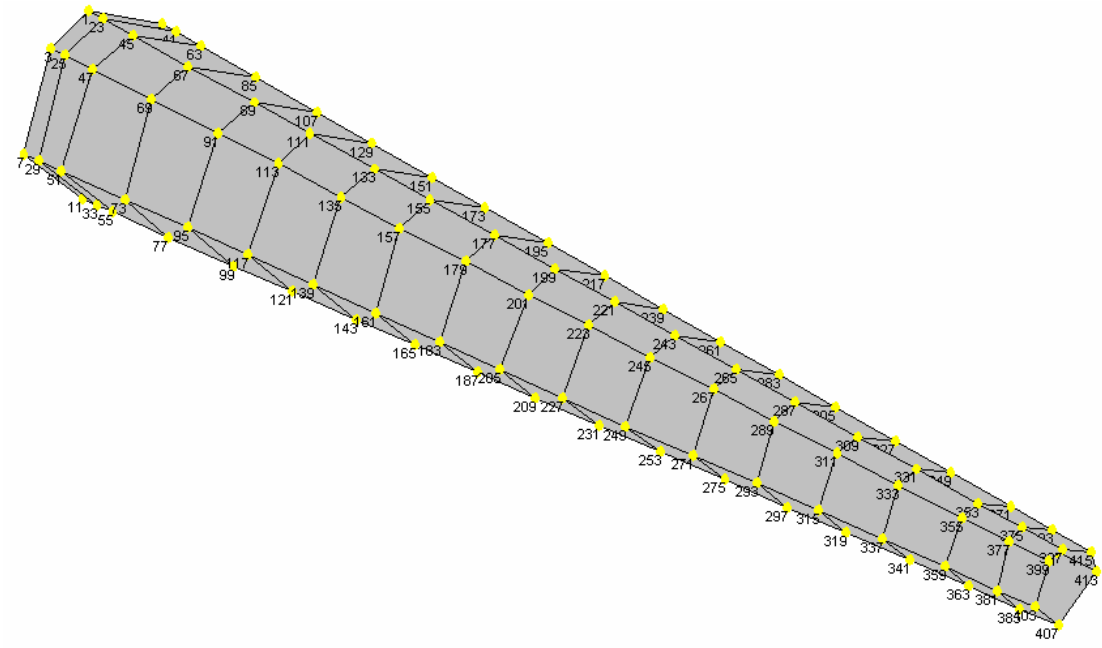

Figure 3.64 : Measurement Points of the Tail Boom

All measured 342 FRFs on the structure are given in Figure 3.65.

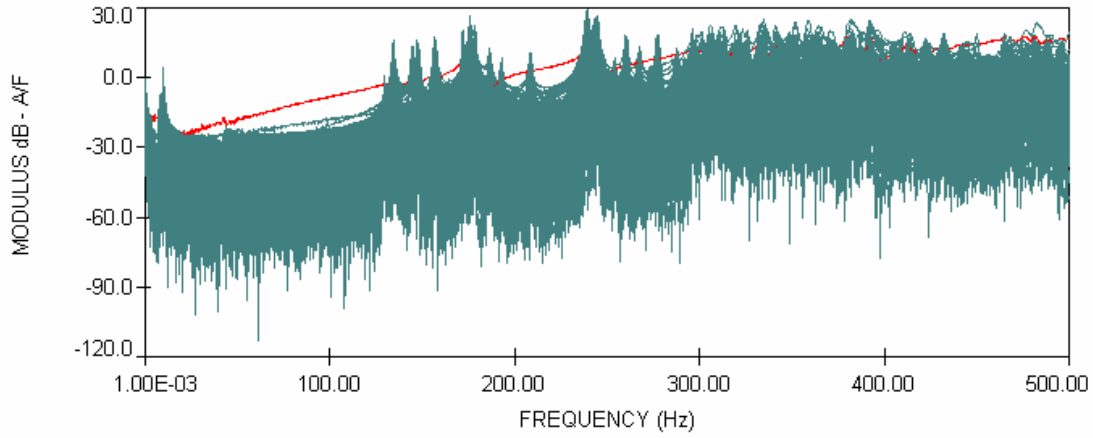

Figure 3.65 : All Measured FRFs on the Structure

Using these measured 342 FRFs, modal analyses are performed. Hybrid Mode Indicator Function (MIF) shows that there are too many modes in the measurement frequency range (up to 500 Hz). So, Hybrid MIF up to 280 Hz is given in Figure3.66.

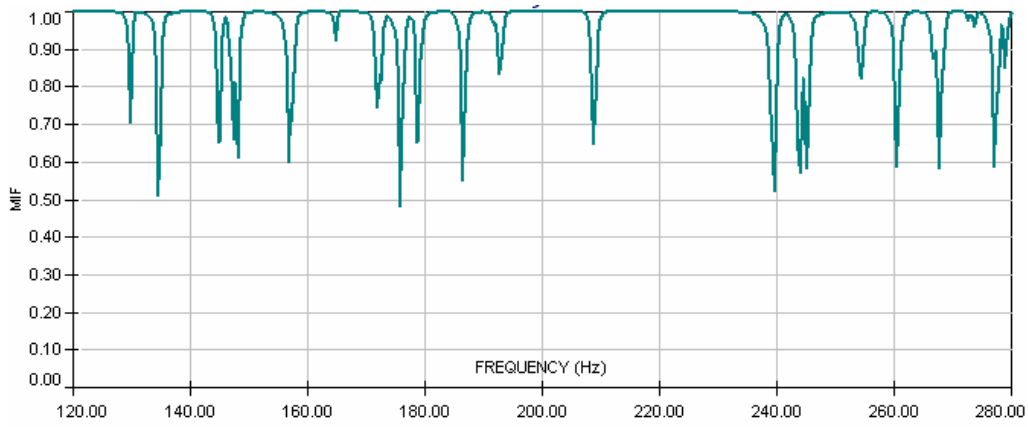

Figure 3.66 : Hybrid MIF up to 280 Hz

The validation of the tail boom is aimed to perform for 15-20 modes. In the frequency range in Figure 3.66, there are 15-20 modes. It is founded that the first two modes are about 130 Hz and 135 Hz.

3.4.3 Initial FE models

After building up an experimental mesh of the tail boom, it was decided to develop very simple FE models first in order to predict the global behaviour of the structure. For this, step by step, 5 different FE models of the structure were developed starting from the simple one to the more complex ones using FINES FE program [75]. These models were just an extension of the experimental mesh.

These FE models are very practical and functional while their solution times are very short. These models may be used effectively for design modifications. For example, changing area and area moment of inertia or positions of frames or stringers by simply writing new values in the input file, desired model is obtained. Also as the solution time is very short, any design sceneries may be tried in a short time effectively.

In the first FE model (TB MODEL 1) all skins are modelled by 3-noded shell elements and constant thickness is assigned to all these elements. Stringers, frames and end parts of the tail boom, -201 and -210, shown in Figure 3.67, are modelled by 2-noded 3D beams.

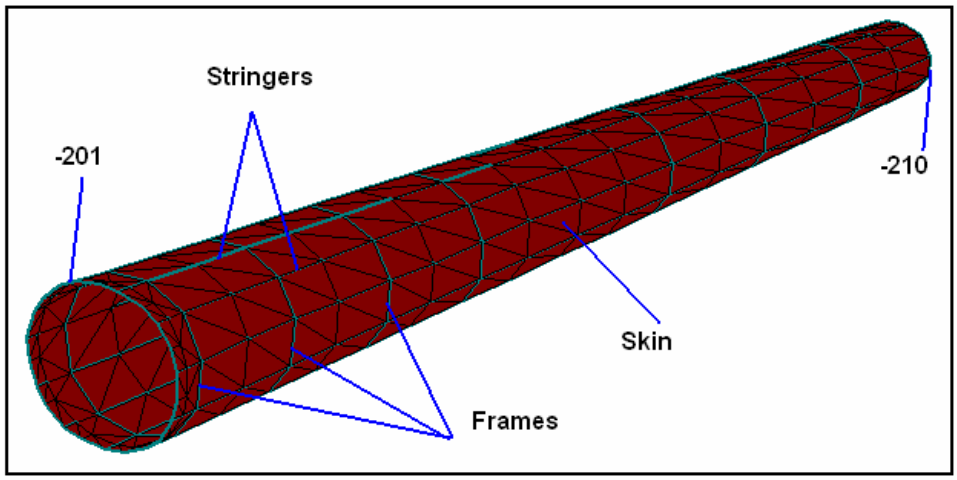

Figure 3.67 : Initial FE Model of the Tail Boom (TB MODEL 1)

Frames and stringers are modelled as beams as mentioned before. Their equivalent moment of inertias and cross sectional areas are calculated and assigned in the model. This model has 429 shell and 308 beam elements, and 1386 DOFs. Modal analysis is performed on this model for 35 modes using sub-space solution method [75]. The mass of this model is 32.30 kg while measured mass of the real structure is about 36.36 kg, and solution for 35 modes takes 23.1 s.

Once an initial FE model is developed, using this reference model, 4 more FE models are developed, Figure 3.68. The first model in Figure 3.67 had very few DOFs, so a new model with more DOFs is developed (TB MODEL 2). In the third model of the tail boom, material overlapping of skins is also taken into account by assigning two times of the thickness of skins to these regions (TB MODEL 3). The fourth model of the tail boom includes more details than the third model, e.g., circumferences of the tail boom end parts (-201 and -210) are modelled by 3-noded shell elements while inner rings are modelled by beam elements (TB MODEL 4). In the fifth model of the tail boom, the tail boom end parts -201 and -210 are fully modelled by 3-noded shell elements (TB MODEL 5). By comparing results of the fourth and fifth models with experimental results, the effects of modelling some structural parts with shells or beams can be examined.

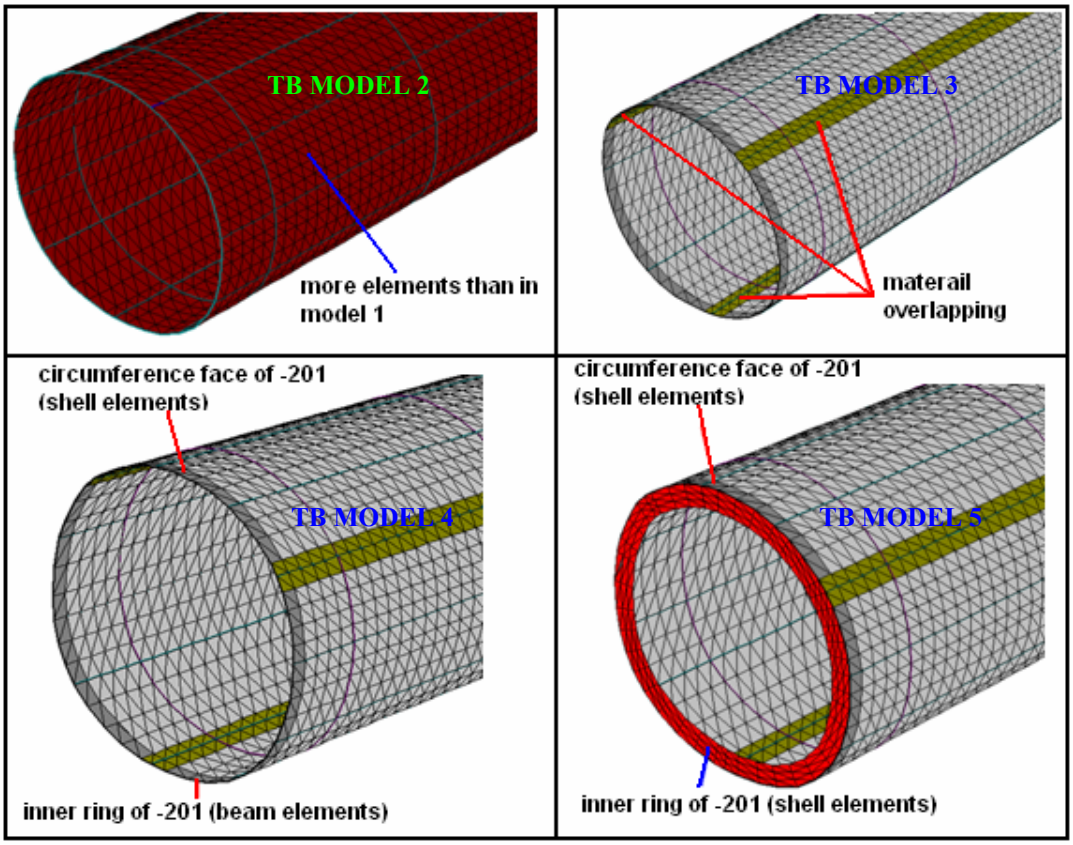

Figure 3.68 : Magnified Picture of Improved FE Models of the Tail Boom

Results of these five models will be given later (in Section 3.4.6) with comparison to experimental results.

3.4.4 Detailed tests and experimental modal analysis

3.4.4.1 Test planning

Some important measurement parameters of the tail boom can be determined using information in Sections 3.4.2 and 3.4.3. FE models created in Section 3.4.3 can be used to determine the best suspension and excitation points. Also the measured FRFs given in Section 3.4.2 can be used to make test plan for detailed modal tests of tail boom. In Figure 3.69, analyses for the best suspension and best excitation locations are shown. The results of the modal analysis of fifth model and modal data obtained from preliminary FRFs are used for performing these analyses.

From FE model data

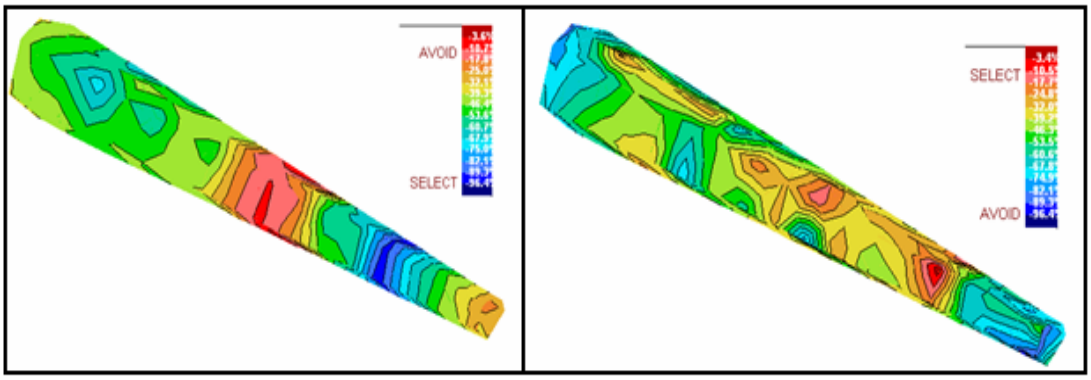

From experimental data

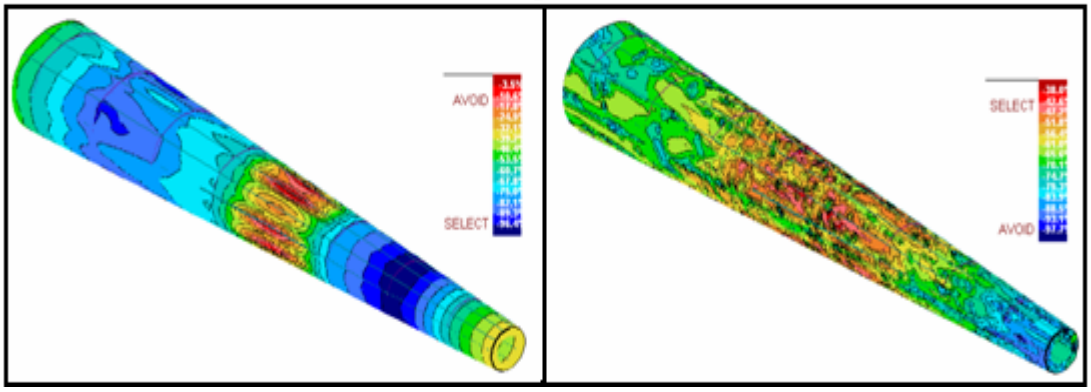

(a) **(b)**

Figure 3.69 : a) Best Suspension and b) Best Excitation locations

Using the knowledge obtained the best suspension and excitation points are selected in detailed tests. It should be noted that similar results are obtained from FE model and preliminary experimental modal data.

In Figure 3.70, AutoMAC for experimentally determined 18 modes is given. As seen measurement points are shown to be sufficient, however more measurement points will be choosen in the detailed tests.

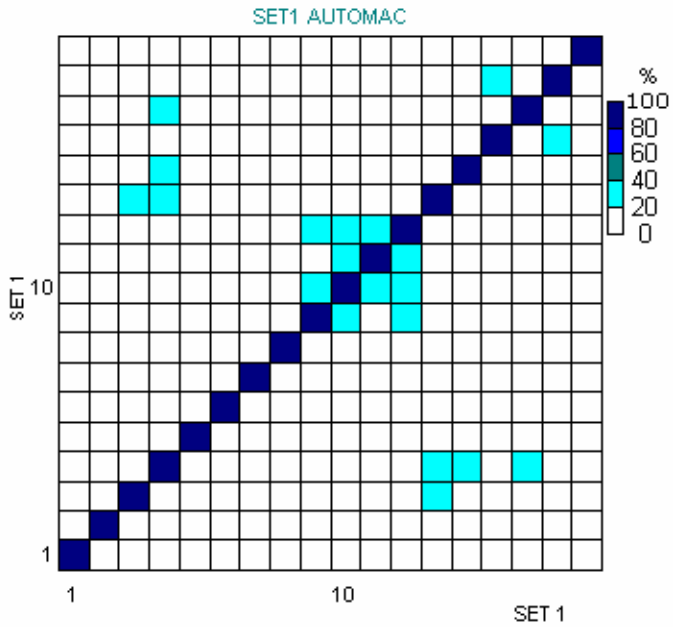

Figure 3.70 : AutoMAC (Tail Boom)

So, detailed experiments on the tail boom may be performed anymore.

3.4.4.2 Detailed modal tests and analysis

In the detailed modal tests, measurement parameters are selected based on the test planning given in the previous section. By exciting the structure at a single point measurements are taken at 220 points as shown in Figure 3.71.

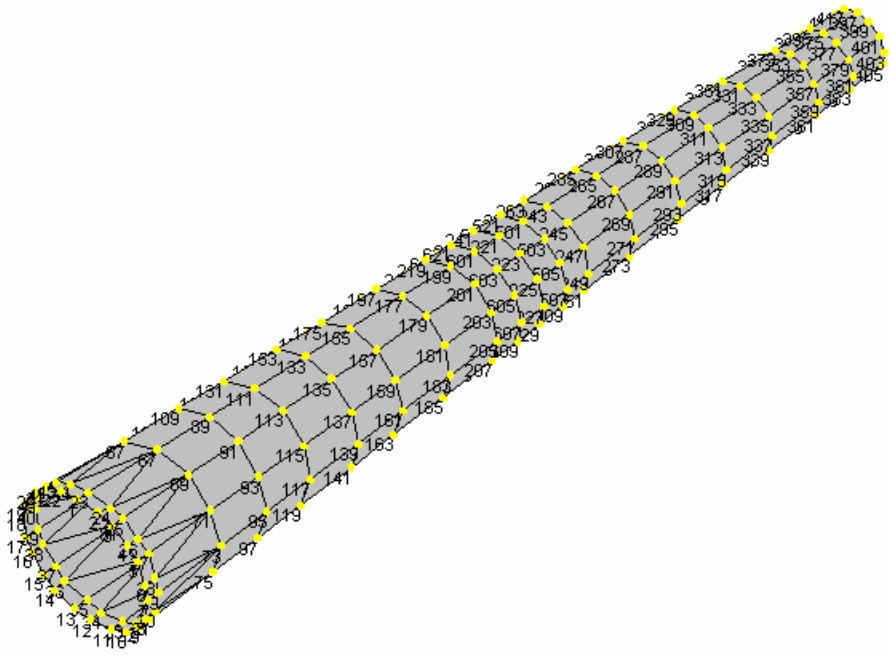

Figure 3.71 : Measurement Points

All the measured 660 FRFs are overlaid in Figure 3.72.

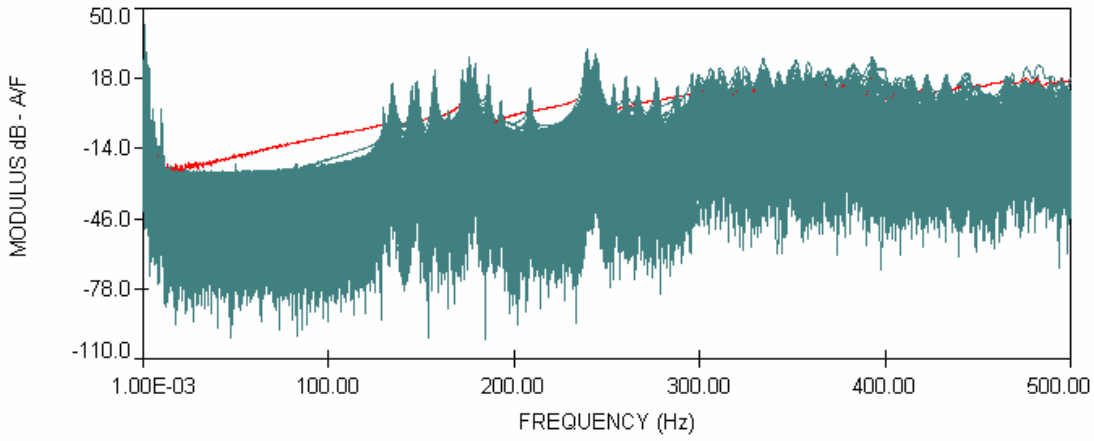

Figure 3.72 : All Measured FRFs

The measured FRFs are analysed [71] using SIMO methods and modal parameters of the structure are obtained. In Figure 3.73, a step in a sample analysis including the 1st and 2nd modes is shown.

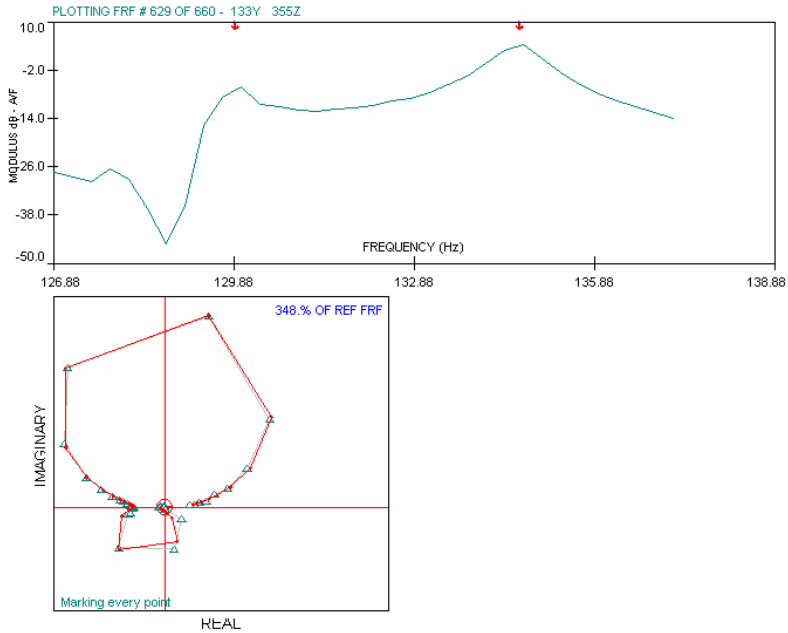

Figure 3.73 : A Step in a Typical Experimental Modal Analysis Procedure

Experimentally obtained 15 natural frequencies and some of the mode shapes of the tail boom are given in Table 3.12 and Figure 3.74, respectively.

Table 3.12 : Experimentally Obtained Natural Frequencies of the Tail Boom

Mode	Nat. Freq. [Hz]
1	129.7
2	134.6
3	144.8
4	147.1
5	148.3
6	157.2
7	164.9
8	169.7
9	175.8
10	179.1
11	184.9
12	186.4
13	193.8
14	208.8
15	239.6

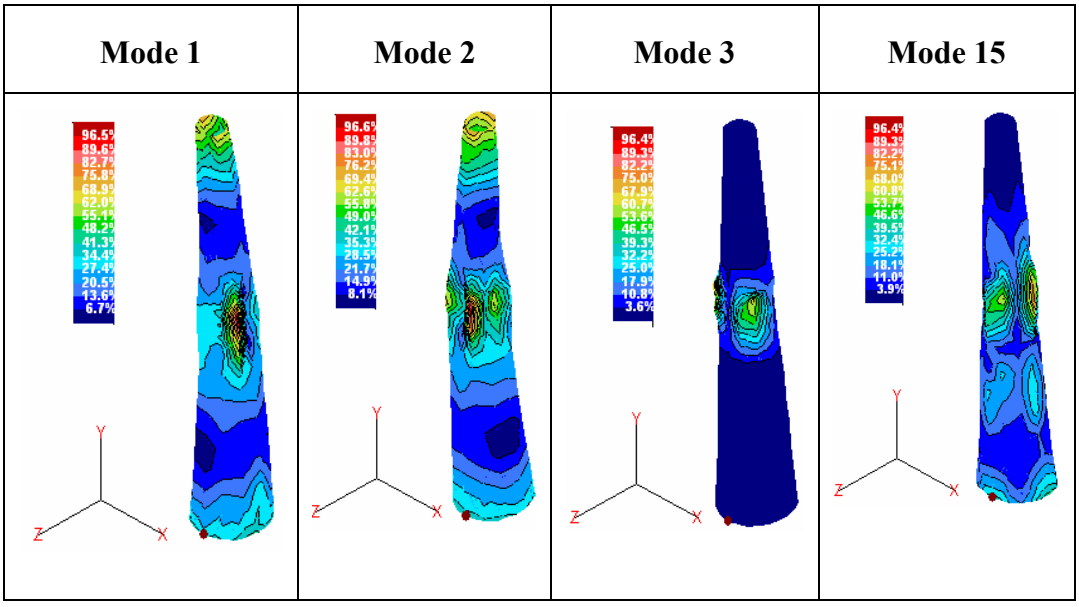

Figure 3.74 : Experimentally Obtained Some Mode Shapes of the Tail Boom

3.4.5 Improved FE model

Based on the proposed approach in Section 3.2.2, with defined parameters according to validated parameters in Sections 3.2.3 and 3.3.4 and 3.4.5, improved FE models of the tail boom are built up [70]. That is, it is assumed that each rivet is effectively

clamping the matching surfaces within a clamping diameter around the attachment centre. This diameter is selected according to the suggestions in previous studies. Again parts are modelled by identifying their mid-surfaces from their solid models.

First, a suitable converged mesh is searched. For this, FE models with three different global mesh sizes (6 mm, 12 mm and 36 mm) are developed. The FE model meshed with mesh sizes 6 mm 12 mm and 36 mm are given in Figure 3.75. But, it should be noted that as some parts has smaller dimensions than defined global mesh sizes, they are meshed with proper smaller mesh sizes.

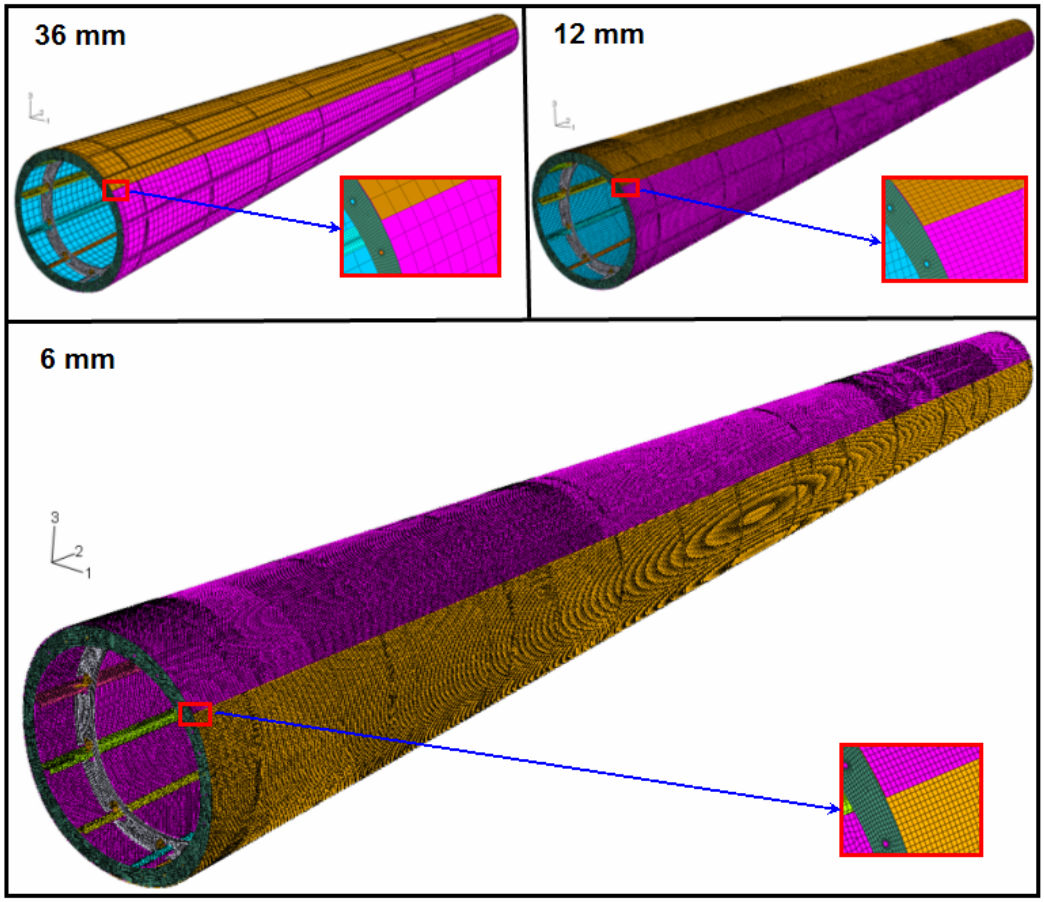

Figure 3.75 : FE Models of the Tail Boom with Various Mesh Sizes

Using these three FE models with different mesh sizes, modal analyses are performed for 300 modes using Lanczos solution method [70]. As seen in Figure 3.76, the results obtained using 6 and 12 mm mesh sizes are very close and an indication that meshes size less than 12 mm is appropriate.

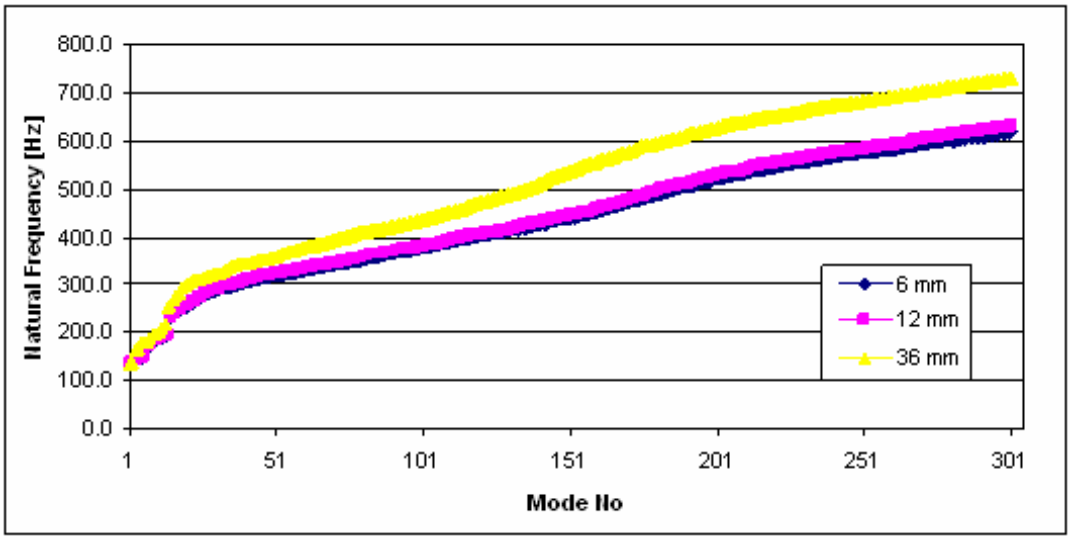

Figure 3.76 : Natural Frequencies of Three Different Mesh Sized FE Models

CPU solution times (for 8 CPUs of 2.6 GHz and 2048 Mb RAM) and masses of these three models with 36 mm, 12 mm and 6 mm mesh sizes are given in Table 3.13. It should be remembered that the measured mass of the tail boom is about 36.36 kg, and difference between the mass of the FE model and measured mass is less than 0.5%.

Table 3.13 : Comparison of Three Different Mesh-sized FE Models of the Tail Boom

FE Model	1	2	3
Global Mesh Size [mm]	36	12	6
CPU Solution Time [h]	1.32	2.88	3.89
Model Mass [kg]	36.21	36.15	36.13

As a result, a FE model of mesh size between 6mm and 12 mm is developed for the purpose of the correlation and comparison with experimental data. This FE model with included rivets is given in Figure 3.77. Results of this model will be given later with comparison to experimental results.

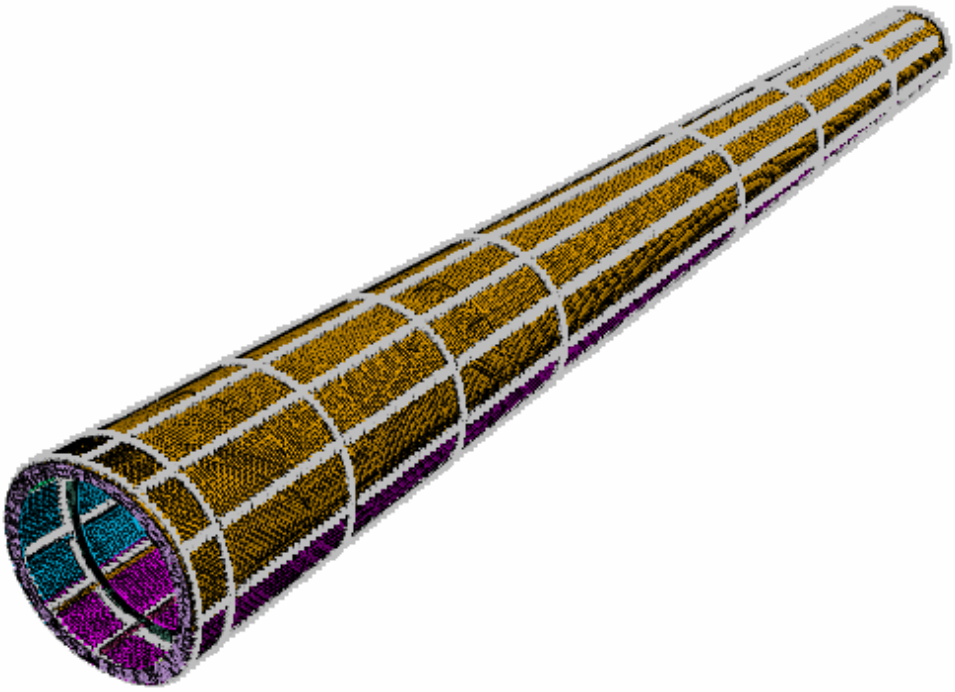

Figure 3.77 : Improved FE Model of the Tail Boom

Theoretical 15 natural frequencies and some of the mode shapes of the tail boom obtained by modal analysis of the improved FE model of the tail boom are given in Table 3.14 and Figure 3.78, respectively.

Table 3.14 : Experimentally Obtained Natural Frequencies of the Tail Boom

Mode	Nat. Freq. [Hz]
1	132.8
2	137.1
3	141.9
4	144.5
5	146.5
6	151.0
7	170.6
8	172.1
9	181.0
10	184.3
11	187.9
12	189.3
13	192.1
14	198.2
15	232.1

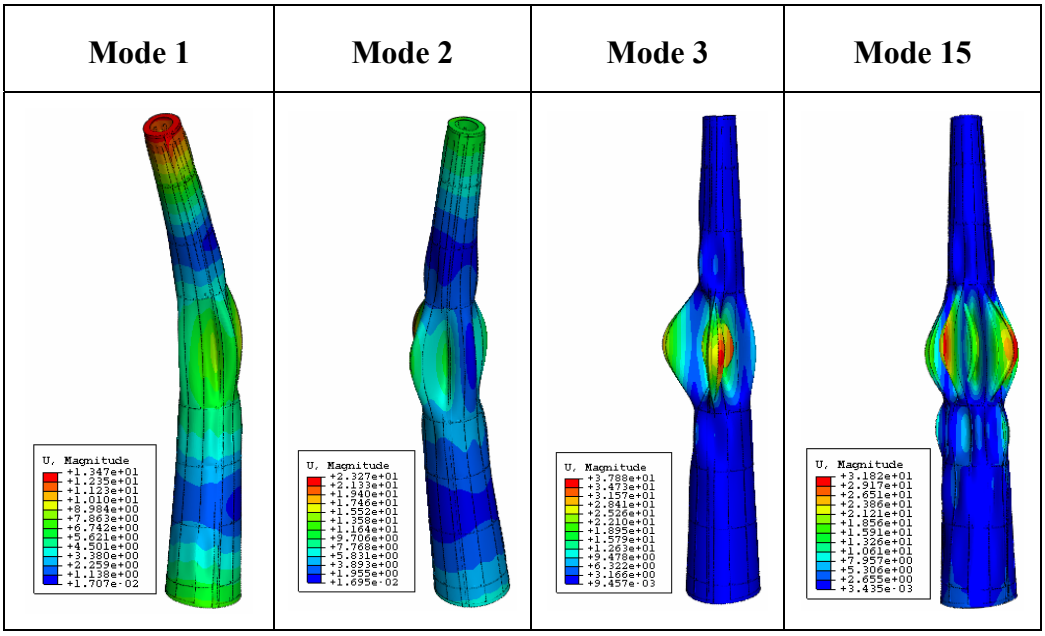

Figure 3.78 : Theoretical Mode Shapes of the Tail Boom

3.4.6 Comparison and correlation

Initial FE Models

Some properties of the initial FE models (those in Section 3.4.3) and CPU times for computing 35 modes are given in Table 3.15.

Table 3.15 : Some Properties of Five FE Models of the Tail Boom

	MODEL 1	MODEL 2	MODEL 3	MODEL 4	MODEL 5
Node	253	5339	5339	5339	5467
Element	737	12027	12027	12491	12543
DOFs	1386	31218	31218	31100	32766
Mass [kg]	32.30	32.9	35.4	34.9	35.5
CPU Time[s]	23.1	304.4	317.1	424.4	402.4

Table 3.16 lists the differences between the natural frequencies of the initial FE models and experimentally obtained ones. As seen, the first two modes are being predicted with a reasonable accuracy although the errors in the following modes are large. It should be noted that the first two modes of the tail boom are global modes while following many modes can be classified as local ones. Also, corresponding first eight mode shapes obtained from these initial models are given in Figure 3.79.

In the case of TB MODEL 5, the results are better than others. Also, it should be noted that the modes higher than the third mode predicted by TB MODEL 1 are incorrect modes as can be seen in Figure 3.79. That's why the corresponding error values are not listed in Table 3.16.

Table 3.16 : Differences between the Natural Frequencies of the First FE Models and Experimental Ones [%]

Mode No	TB MODEL 1	TB MODEL 2	TB MODEL 3	TB MODEL 4	TB MODEL 5
1	5.7	4.6	4.3	5.7	4.3
2	4.5	3.2	4.2	5.6	4.2
3	76.0	47.9	48.3	48.3	48.3
4	X	46.6	47.6	47.6	47.6
5	X	48.5	49.5	49.5	49.5
6	X	42.6	44.5	44.5	44.5
7	X	48.3	46.1	40.3	42.2
8	X	45.3	42.9	42.9	42.9

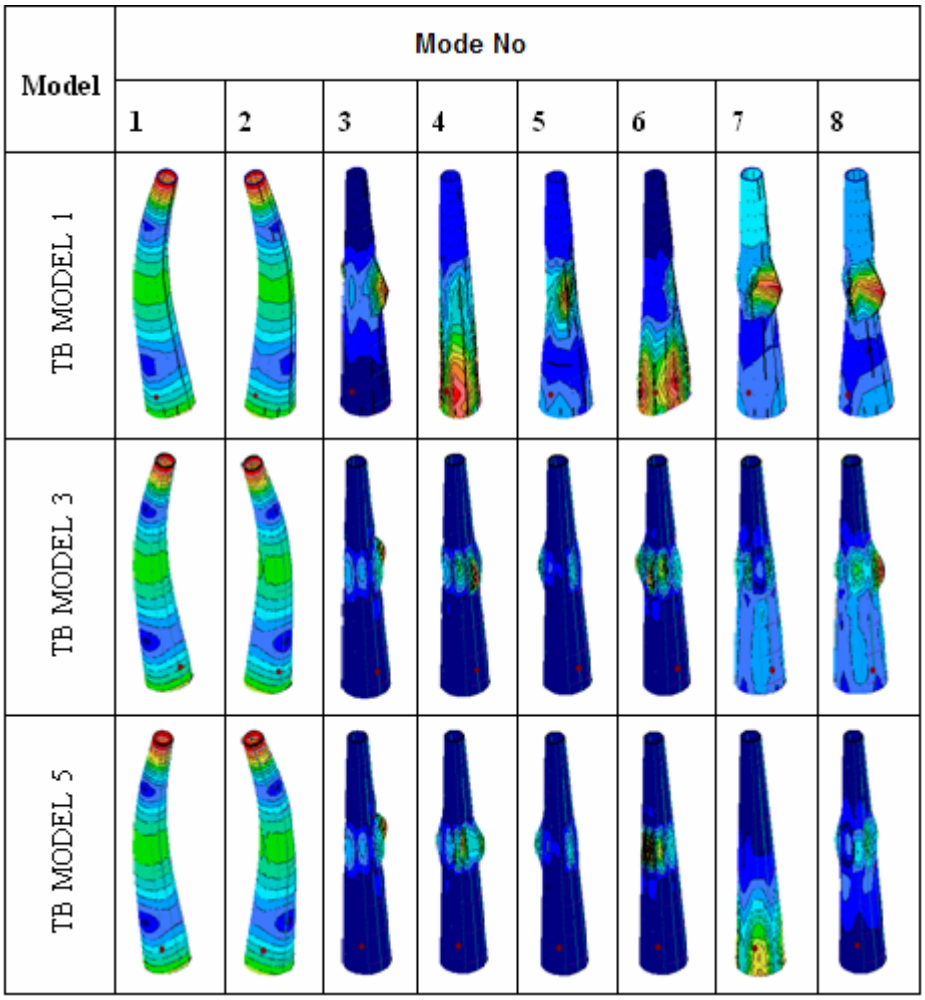

Figure 3.79 : First Eight Modes of Some Initial FE Models of the Tail Boom

It should be noted that with these initial FE models, global behaviour of the tail boom can be examined. Also it should be remembered that the local modes resulting in the tail boom are because of the incomplete structural parts in the tail boom which is intentionally manufactured for the validation purposes. Therefore, in the real tail boom, there will not be such local modes, at least among the lower modes, and by including incomplete parts to these models, the global behaviour of the structure can be predicted with acceptable accuracy. Also it should be remembered that these initial models are built up in a very efficient way while many details are ignored, and their solution times are very low.

The initial FE models given in this section are relatively simple ones, and they cannot predict the behaviour of the real structure with required accuracy, especially for higher modes, although these models may be used for test planning and some sensitivity analyses. Therefore, more detailed and validated FE model of the tail boom was developed (in Section 3.4.5) based on the proposed approach in Section 3.2.2, and the results obtained are given in the next section.

Improved FE Model

Experimentally obtained modal data of the tail boom are compared to the modal analysis results of the improved FE model of the tail boom (global mesh size 6-12 mm) using a mathematical tool, MAC. In Figure 3.80, the experimental and theoretical mode shapes are compared using MAC plot where SET1 and SET2 indicate experimental and theoretical modes, respectively. This plot in general indicates a good correlation between the two data sets. In Table 3.17, MAC values of the correlated mode shapes and difference between the natural frequencies of the correlated modes are given. As seen, the differences between the natural frequencies are very small and MAC values are considerably high. Therefore, it is concluded that a validated and representative FE model of the tail boom that can provide results with good accuracy is obtained.

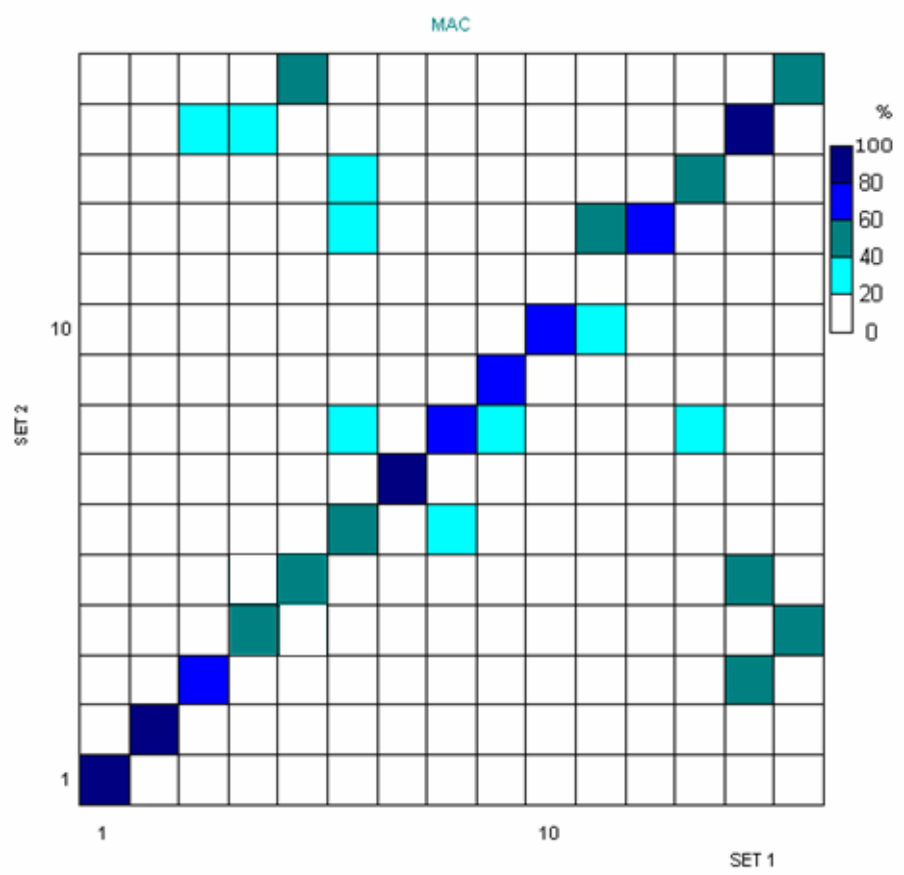

Figure 3.80 : MAC for 15 Modes (Tail Boom)

Table 3.17 : Differences between the Natural Frequencies of the Improved FE Model and Experimental ones [%]

Exp. Mode	Exp. Nat. Freq. [Hz]	Theo. Mode	Theo. Nat. Freq. [Hz]	Nat. Freq. Error [%]	MAC
1	129.7	***1***	132.8	2.4	***92.5***
2	134.6	***2***	137.1	1.9	***89.7***
3	144.8	***3***	141.9	-2.0	***70.4***
4	147.1	***4***	144.5	-2.5	***56.8***
5	148.3	***5***	146.5	-1.2	***45.6***
6	157.0	***6***	151.0	-3.8	***48.4***
7	164.9	***7***	170.6	3.5	***88.2***
8	169.7	***8***	172.1	1.4	***71.1***
9	175.8	***9***	181.0	3.0	***63.2***
10	179.1	***10***	184.3	2.9	***60.3***
11	184.9	***11***	187.9	1.6	***<20***
12	186.4	***12***	189.3	1.5	***77.7***
13	193.8	***13***	192.1	-1.0	***59.3***
14	208.3	***14***	198.2	-4.9	***83.7***
15	239.6	***15***	232.1	-3.2	***53.9***

4. MODAL ANALYSES OF HELICOPTER AIRFRAME

4.1 Introduction

Up to here, various structures including the tail boom are modelled using FE method and their FE models are validated using experimental data. Based on the experiences gained from both theoretical modelling and vibrations tests on some helicopter structures, modal tests on a full-scale helicopter airframe are performed and some FE models of this structure are developed. The results are summarised in this chapter.

As schematically illustrated in Figure 4.1, the helicopter airframe (ITU-LCH) on which FRFs are measured comprises mainly a fuselage, tail boom, skid, nose and an engine. The physical helicopter airframe and the test setup are shown in Figure 4.2. All the FRFs are measured on the airframe when it is on its skid on the ground.

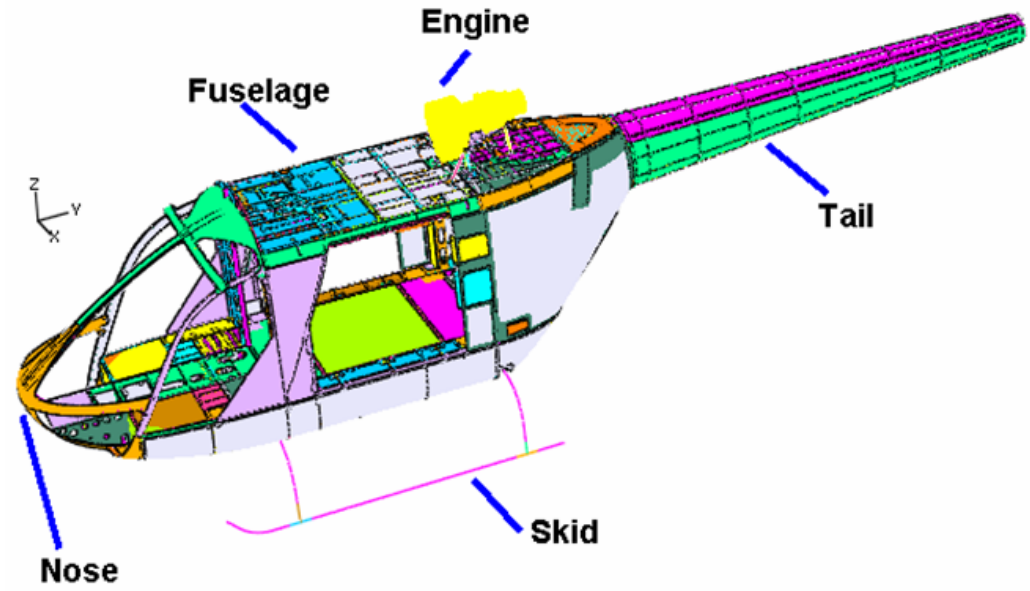

Figure 4.1 : Main Components of the Helicopter Airframe Tested

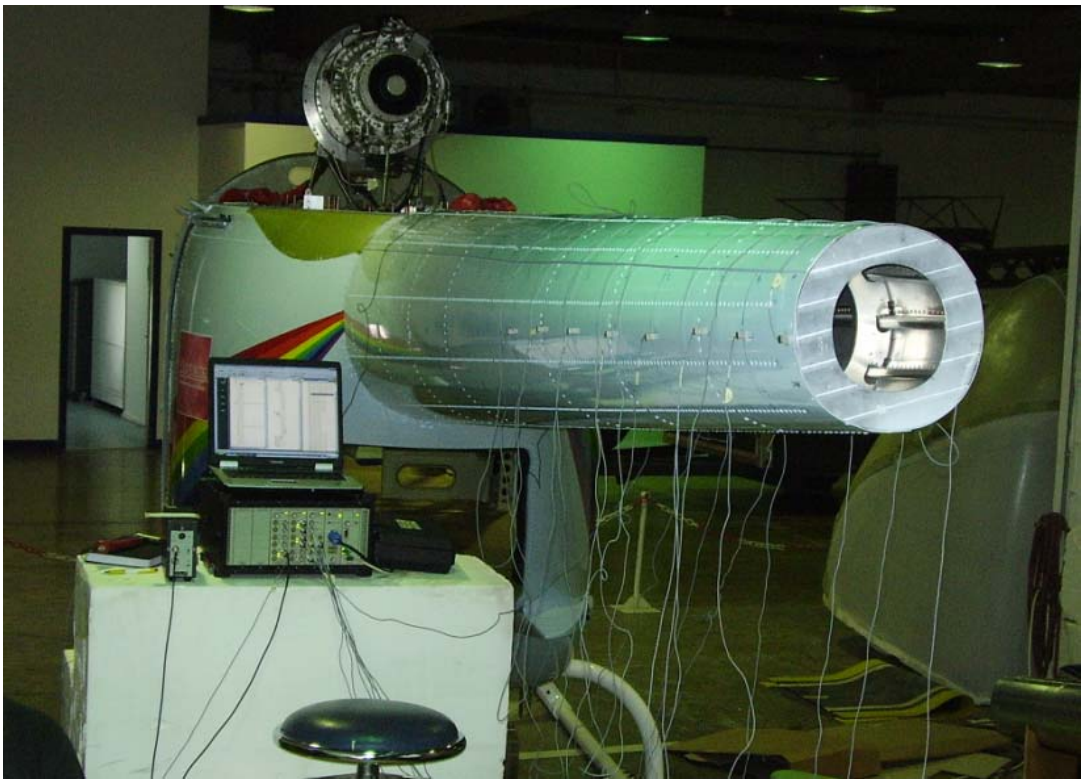

Figure 4.2 : Helicopter Airframe and the Experimental Setup

4.2 Modelling Helicopter Airframe

The FE model of the helicopter airframe on which the FRFs are measured is built up using FE program ABAQUS [61]. As it is well-known, most of the helicopter structures are built using thin composites or metal sheets. These parts are mostly modelled using shell elements. Parts of the skids are modelled using beam and shell elements. In this thesis, the helicopter engine is modelled as a discrete rigid part, but its mass and mass moment of inertias are included. Also, the details of the engine attachments to the fuselage are defined in the model. Individual attachment parts of the engine to the fuselage are modelled using beam elements. A typical FE model of the helicopter airframe with these features is shown in Figure 4.3.

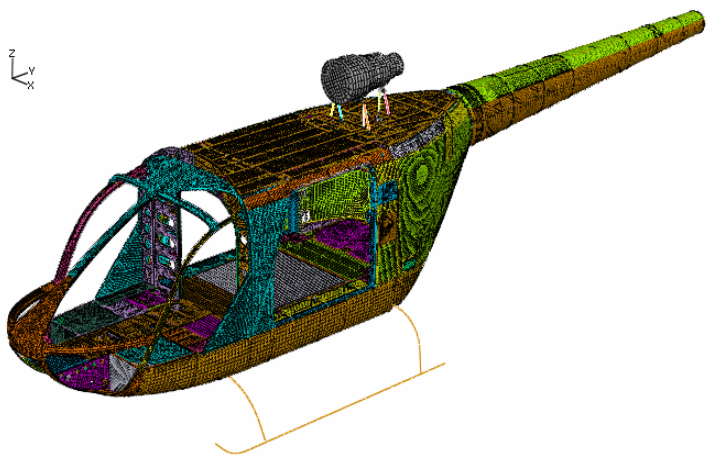

Figure 4.3 : FE Model of the Helicopter Airframe

Helicopter boom is assembled to the fuselage using some bolts. Nearly all other parts of the helicopter airframe are joined together using rivets. The FE model of the fuselage that also includes the rivets is shown in Figure 4.4.

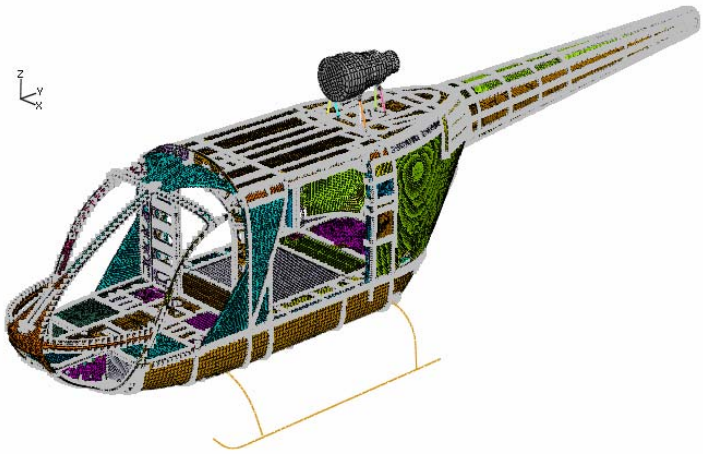

Figure 4.4 : FE Model of the Airframe Including Rivets

4.3 Measurement of FRFs on Helicopter Airframe

4.3.1 Experimental setup and preliminary tests

Experimental setup of the structure on which FRFs are measured is shown in Figure 4.2. An impact hammer and eight accelerometers are used to excite the structure and to measure responses, respectively. Similar to previous tests, calibration of the system is cheeked both at the beginning and at end of the measurements. Calibration

results performed with rigid cylinder given in Section 3.3.2 are shown in Figure 4.5. In the worst case, modulus of the FRF is in the range of -20 ± 0.5 dB. This means that calibration of the system is quite appropriate.

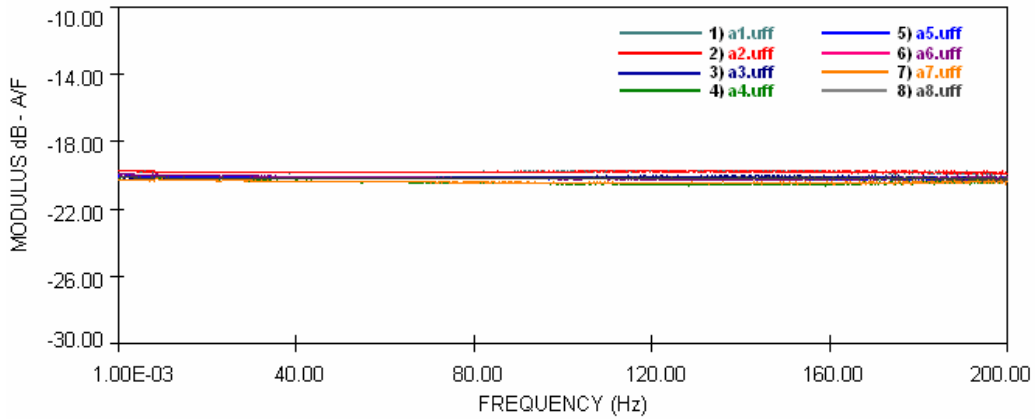

Figure 4.5 : Calibration Results

During FRF measurements, it is essential that the structure is excited properly. By inspecting the autospectrum of the force signal, it is concluded that the structure is excited well as the autospectrum of the force signal given in Figure 4.6 is nearly flat in the interested frequency range.

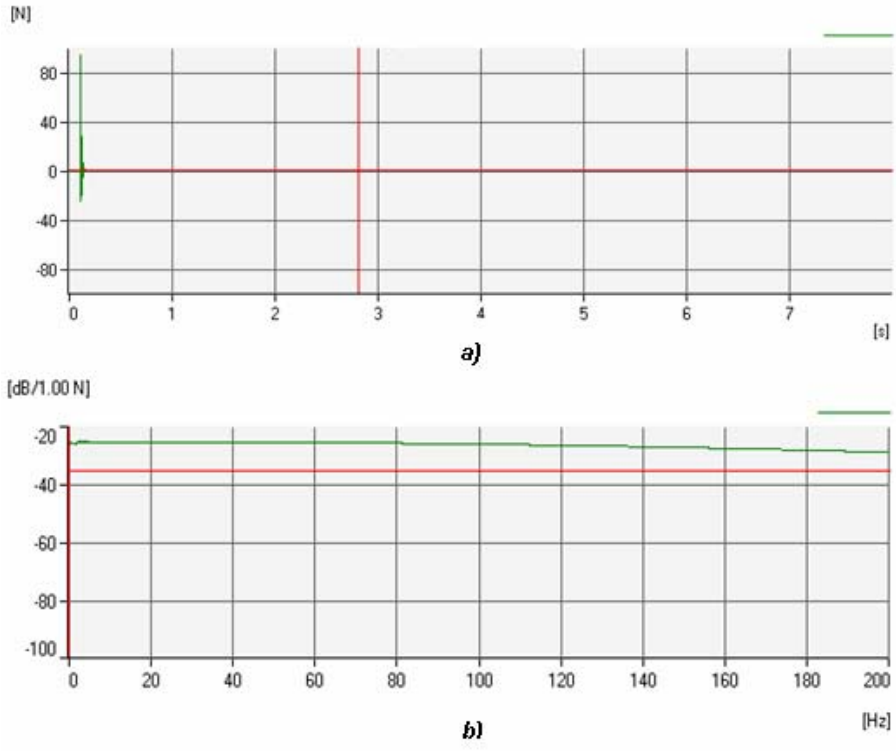

Figure 4.6 : a) Time and b) Autospectrum of the Force Signal

As the time signal of the acceleration measured on the structure decays to nearly zero at the end of the measurement period (see Figure 4.7), there is no need to apply any windowing to the acceleration signals.

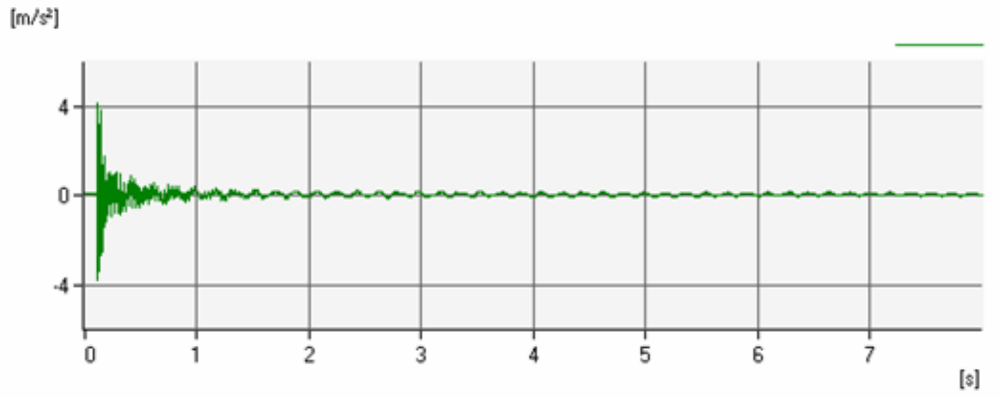

Figure 4.7 : Time Signal of the Response

An FRF measured on the structure and the coherence - after three averages - are shown in Figure 4.8. This typical measurement shows that the measurement procedure is appropriate.

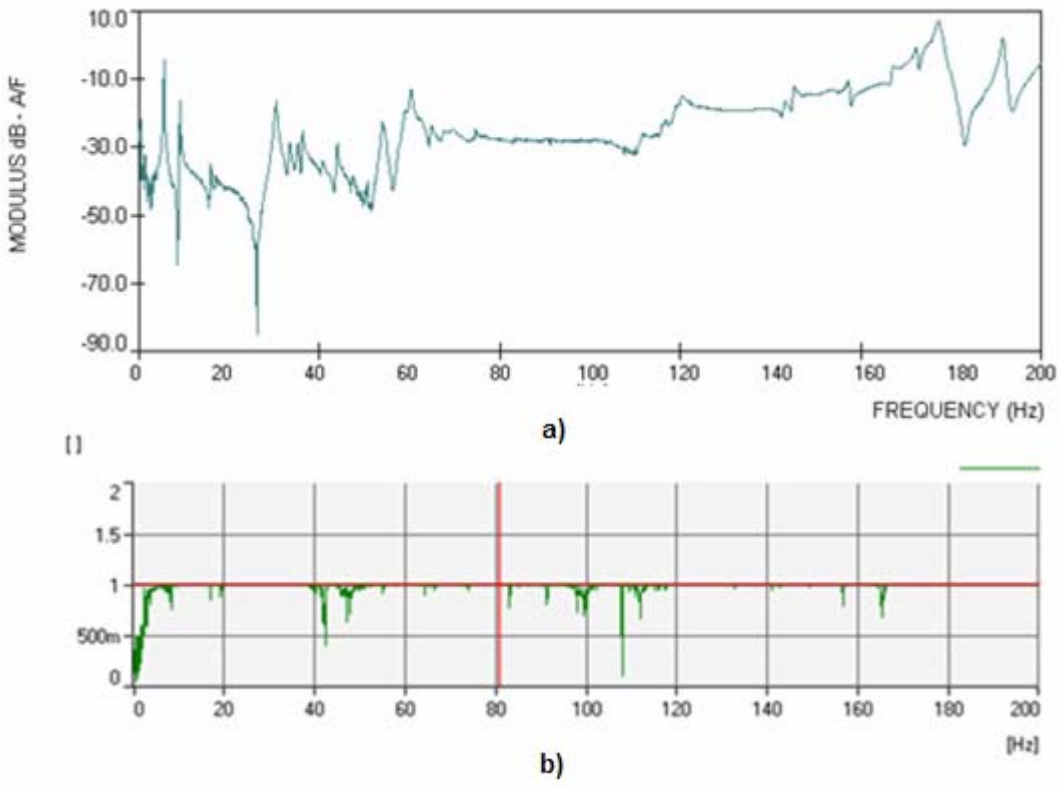

Figure 4.8 : a) FRF and b) Related Coherence of a Typical Signal

Also, the repeatability of the measurements is checked. Two measured point FRFs in the x direction at different times implies that repeatability is quite good, Figure 4.9.

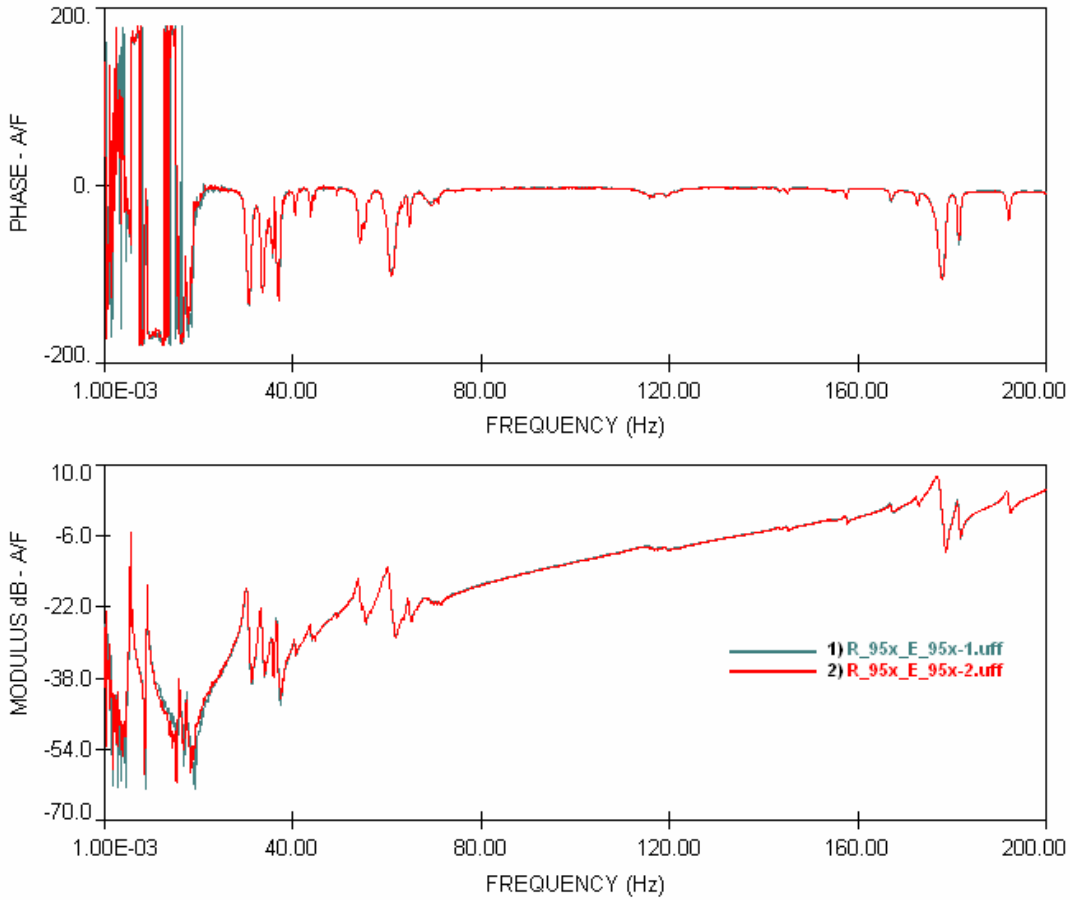

Figure 4.9 : Repeatability Tests

Repeatability is also checked using other FRFs measured at some points on the helicopter engine. The results given in Figure 4.10 and Figure 4.11 indicate that the repeatability of the measurements is good for those measurements as well.

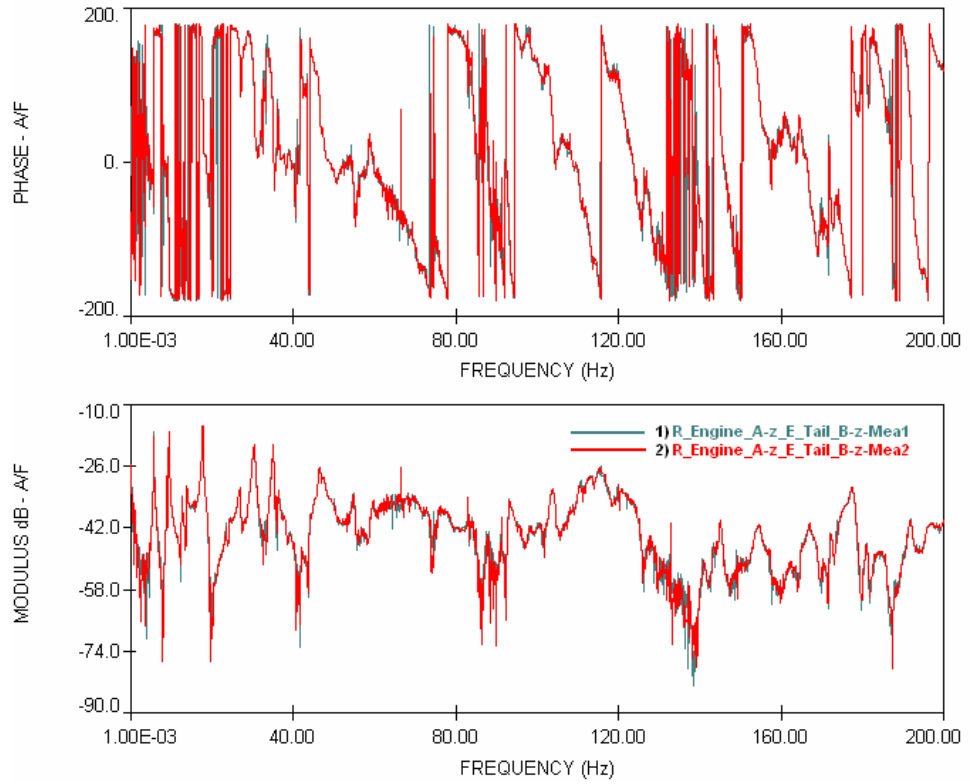

Figure 4.10 : Repeatability Tests (on the Engine in the z Direction)

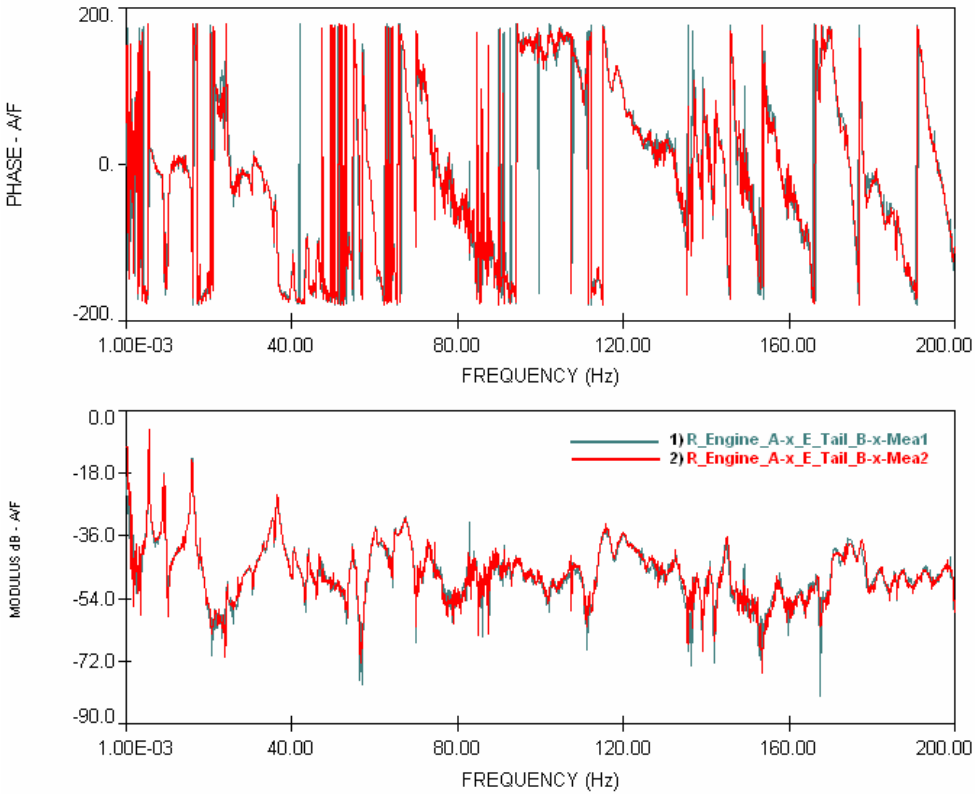

Figure 4.11 : Repeatability Tests (on the Engine in the x Direction)

4.3.2 Measurements

4.3.2.1 Complete airframe

The structure is excited in horizontal and vertical directions with respect to the ground, from the nodes shown in Figure 4.12, but not simultaneously. That is, the structure is first excited at node number 95 in the x-direction and at 185 nodes responses are measured in the x-direction. Then, the structure is excited at node number 89 in the z-direction and at 185 points the responses are measured in the z-direction. These two excitation points are selected after some trial measurements so that in the frequency range of interest maximum number of modes can be excited.

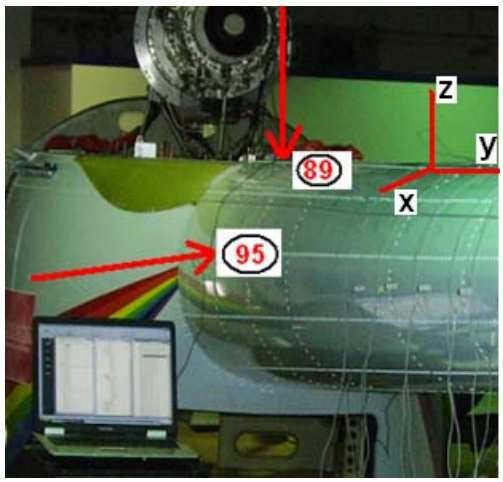

Figure 4.12 : Excitation Points

The response locations used for FRF measurements are shown Figure 4.13.

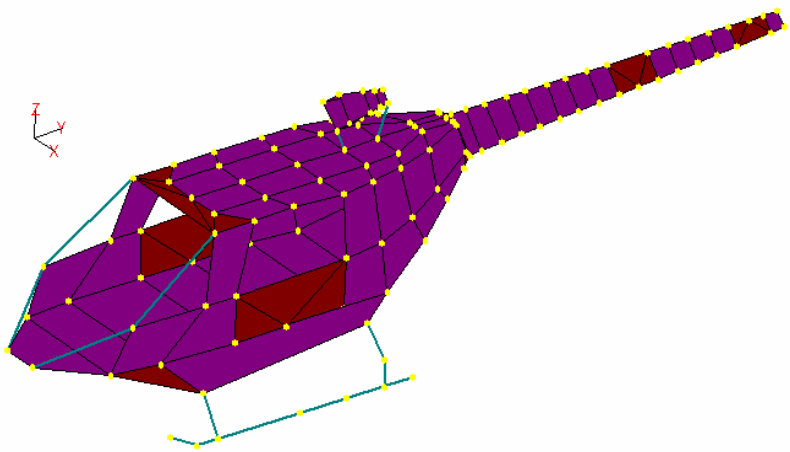

Figure 4.13 : Measurement Points

Measured FRFs in the x and z directions are given in Figure 4.14 and Figure 4.15, respectively.

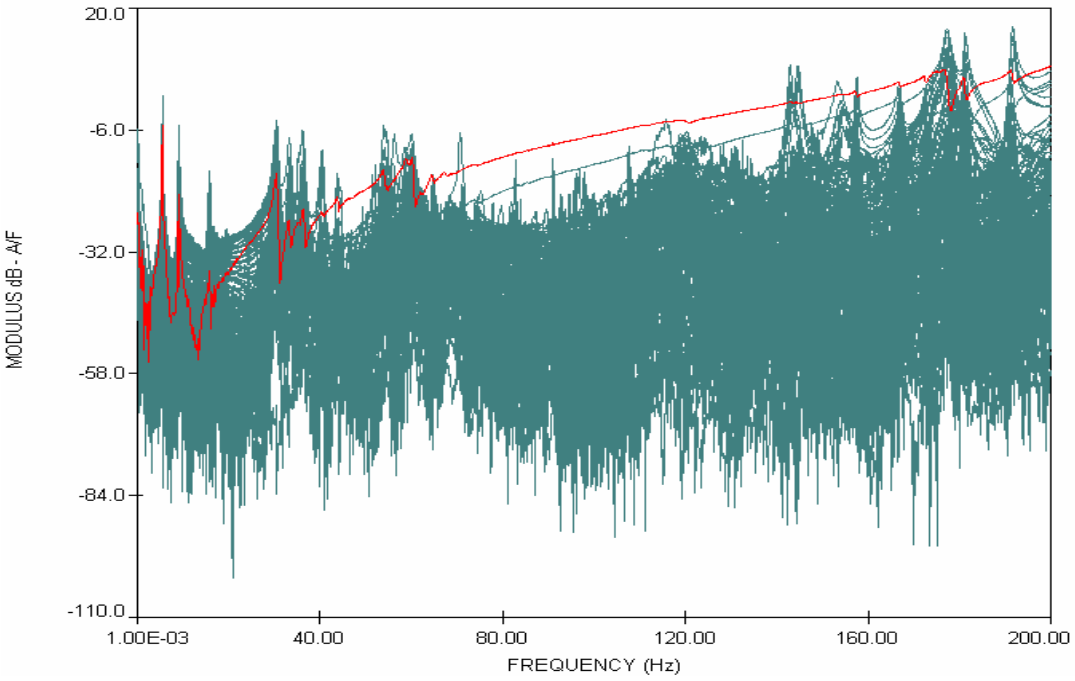

Figure 4.14 : Measured FRFs in the x Direction

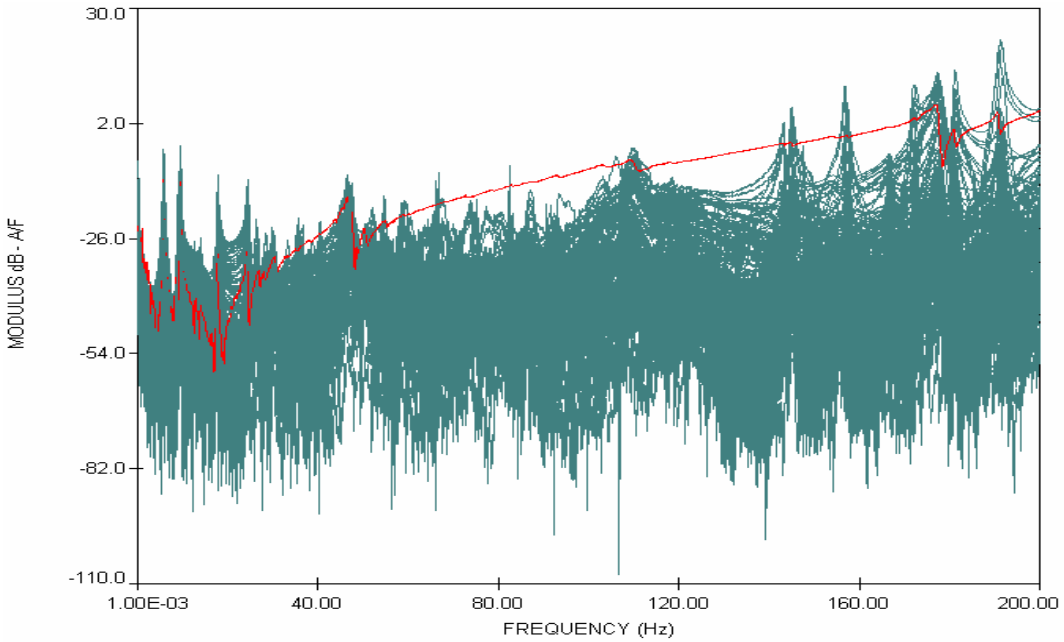

Figure 4.15 : Measured FRFs in the z Direction

4.3.2.2 Isolated engine

Independent from the measurements on the complete helicopter airframe, three set of FRFs are measured on the engine and on the roof of the helicopter by exciting the engine at three different directions. By means of these measurements, engine dominated modes are expected to be identified easily. Experimental setup and the measurement points of the isolated engine are shown in Figure 4.16a and 4.16b, respectively.

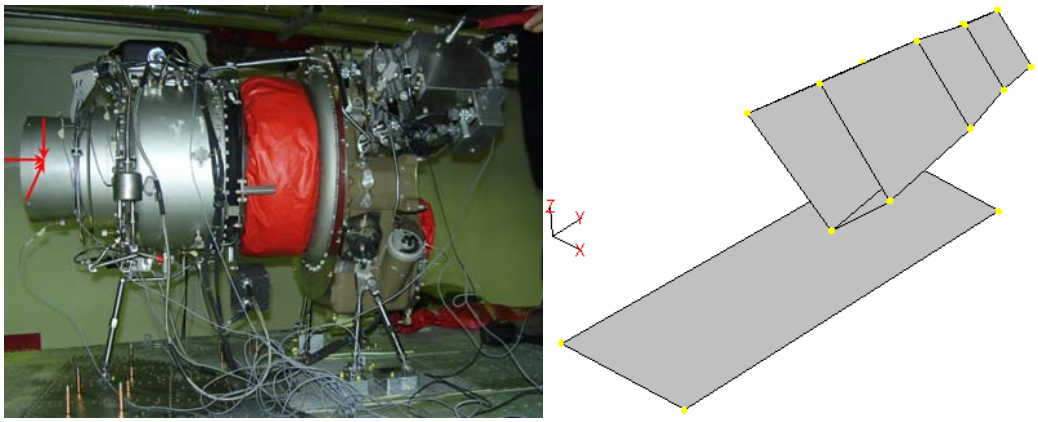

a) **b)**

Figure 4.16 : a) Experimental Setup and b) Measurement Points of the Isolated Engine

Measured FRFs in the x, y and z directions on the helicopter engine are given in Figure 4.17, 4.18 and 4.19, respectively.

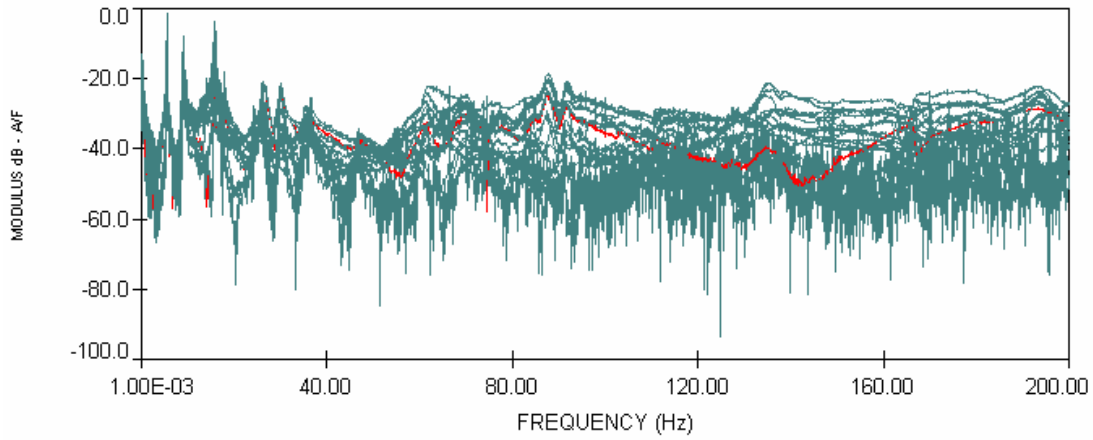

Figure 4.17 : Measured FRFs on the Engine in the x Direction

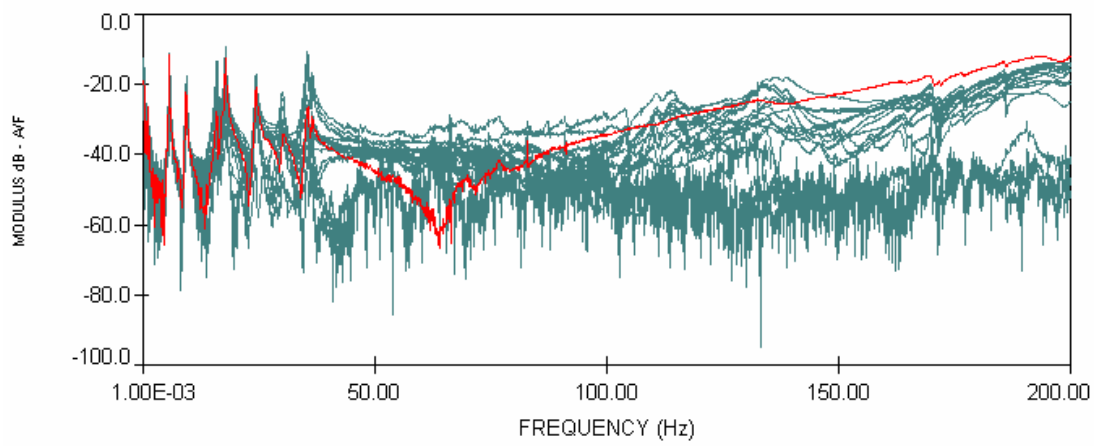

Figure 4.18 : Measured FRFs on the Engine in the y Direction

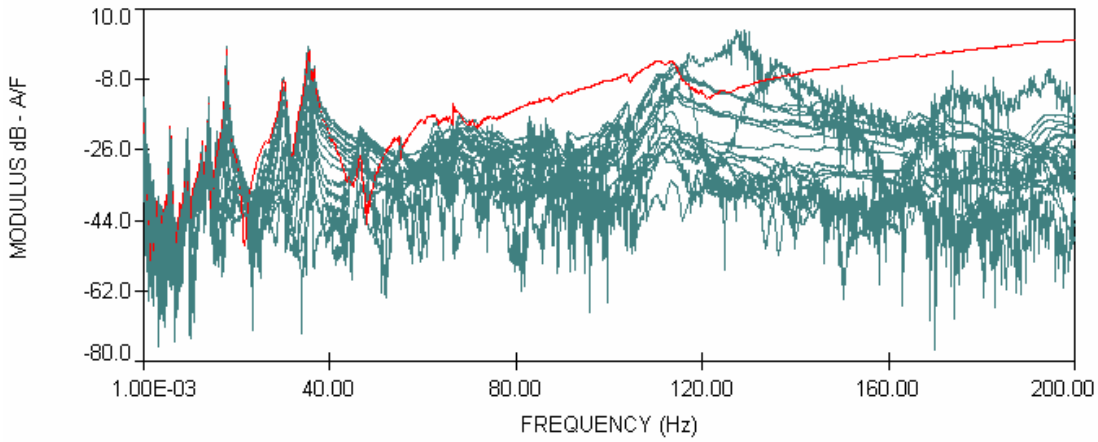

Figure 4.19 : Measured FRFs on the Engine in the z Direction

4.4 Experimental Modal Analysis

Two sets of FRFs measured on the complete airframe (of x and z directions) and three sets of FRFs measured on the isolated engine (of x, y and z directions) are analysed using SIMO analysis methods [71] separately for each set. In Figure 4.20, a step in a modal analysis procedure including the 1st mode is shown.

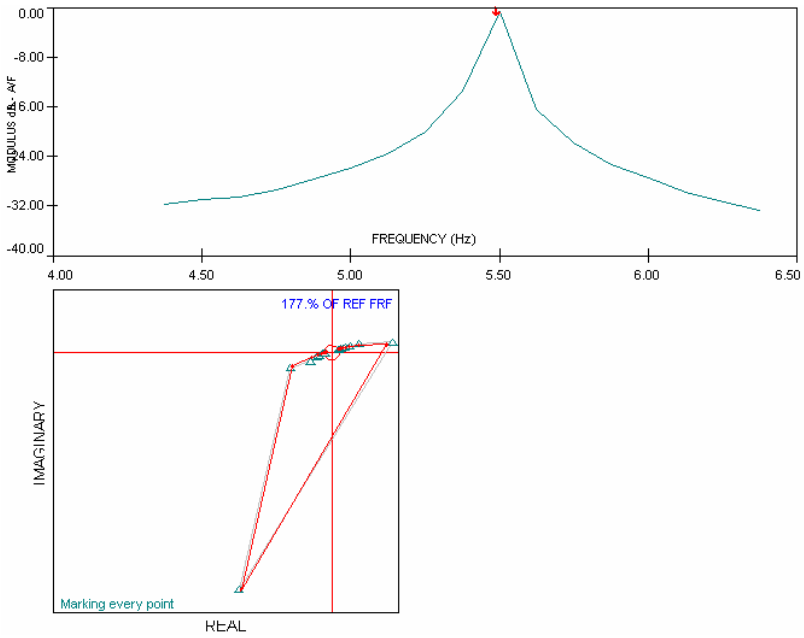

Figure 4.20 : A Typical Experimental Modal Analysis Step

Via experimental modal analysis, some modes are identified using measured FRFs on the complete airframe in both the x and z directions and on the isolated engine in three directions. The 1st mode identified using the measured FRFs on the complete airframe in the x direction, is illustrated in Figure 4.21. It is worth stating here that the same mode shape is shown in Figure 4.21 using two different display types in order to help the reader visualise the mode shape easily. These double display formats are also used in other figures.

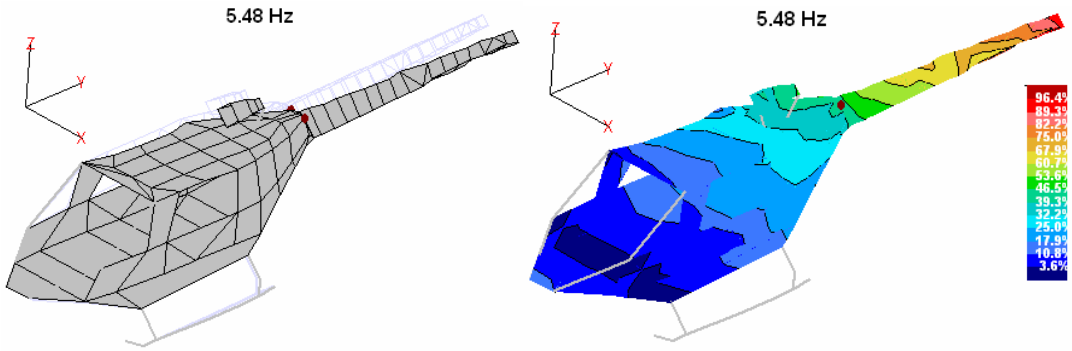

Figure 4.21 : Tail Boom Rolling (Left-and-Right) Mode

As expected the rolling mode shown in Figure 4.22 is not very visible in the FRFs measured in the z directions. On the other hand, tail boom rocking (up-and-down) mode (in y-z plane) is not clear in the FRFs measured in the x direction. However,

this ‘tail boom rocking’ mode can easily be found using the FRFs measured in the z direction (see Figure 4.22).

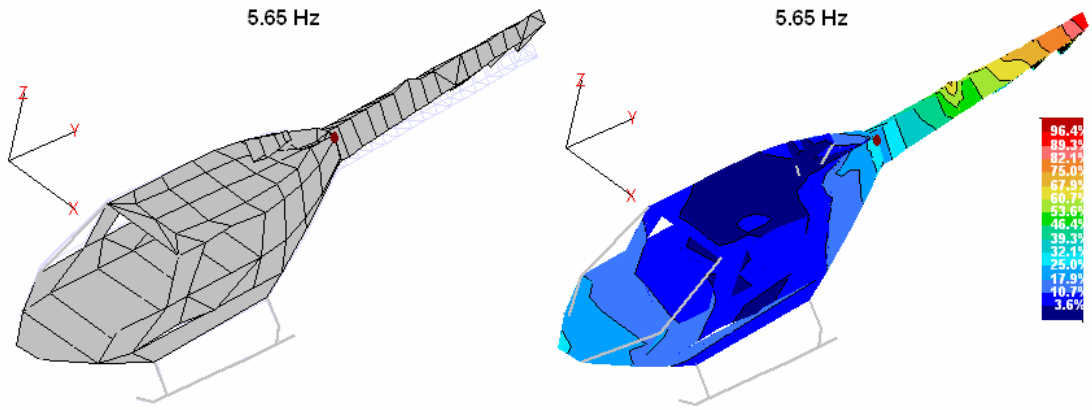

Figure 4.22 : Tail Boom Rocking (Up-and-Down) Mode

Determination of natural frequencies is important. In Figure 4.23, four FRFs, where two of them are measured in the x direction (61-x and 73-x) and the other two in the z direction (61-z and 73-z), are overlaid. As seen in this Figure, these two closely-spaced modes can be identified easily by exciting the structure in different directions at appropriate locations.

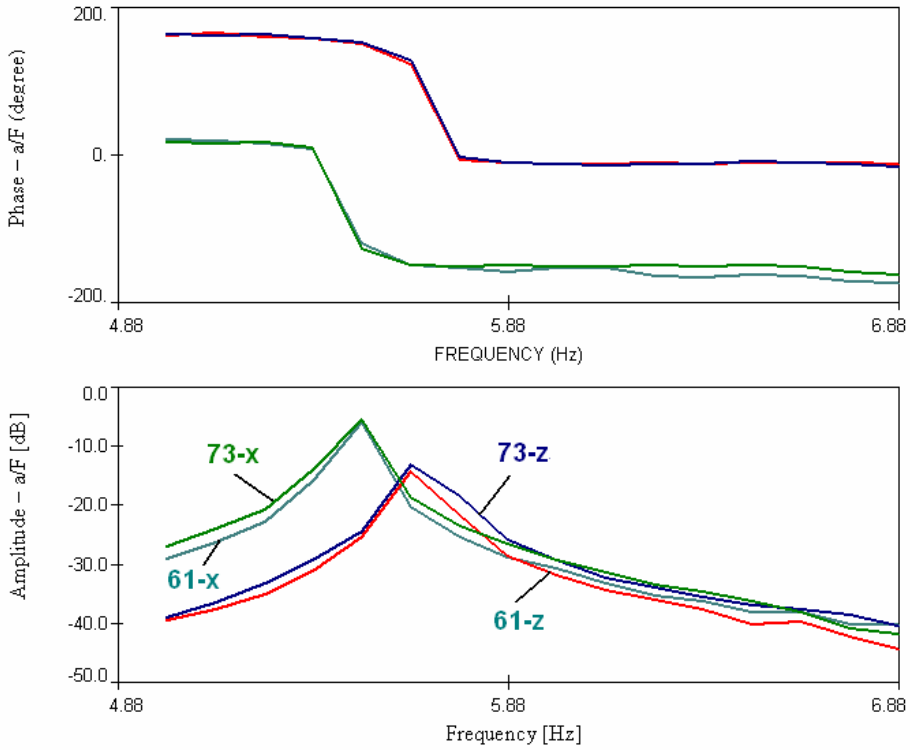

Figure 4.23 : Measured FRFs in the x and z Directions

In the frequency range between 9 and 10 Hz, at first it seems that there are two close modes. These two modes are clearly seen when the FRFs measured in both directions (x and z) are plotted as in Figure 4.24.

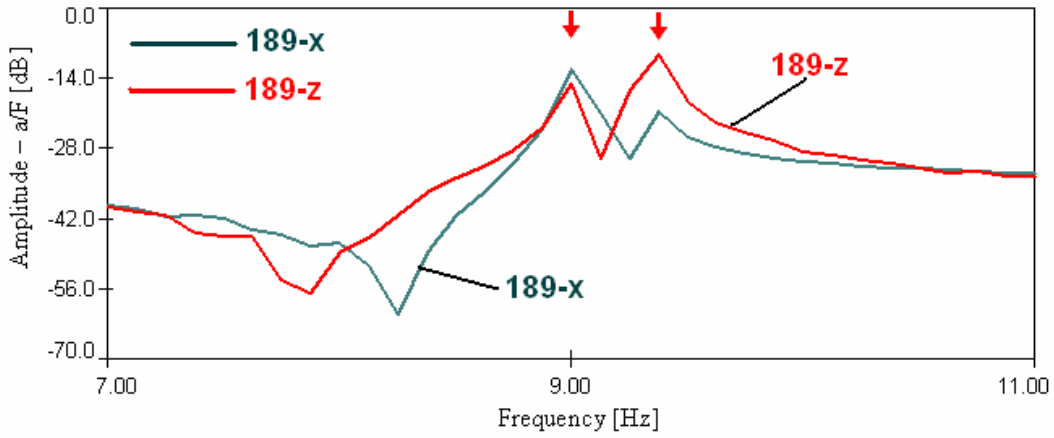

Figure 4.24 : Measured FRFs in the x and z Directions at the Point 189

The two modes seen in Figure 4.24 can be determined using both sets of FRFs. These two modes are also global modes of the helicopter airframe. The frequency of the first of these modes is found to be 9.03 Hz as a result of the modal analysis using FRFs measured in the x direction, and 9.00 Hz from modal analysis of measured data in the z directions. The mode shape for this mode obtained using FRFs measured in the x direction is shown in Figure 4.25.

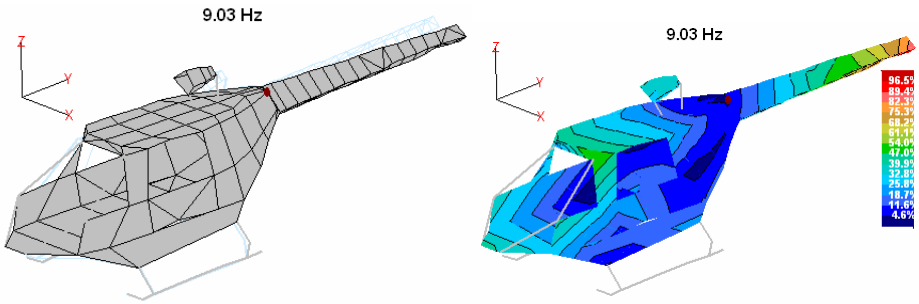

Figure 4.25 : First Rolling Mode (Using Measurements in the x Direction)

From both of the data sets, nearly the same natural frequencies are found. This also confirms that the measurements performed are very consistent and suitable. Similar to the first of these modes, other mode is found using both data sets. The frequency of the second of these modes is found to be 9.34 Hz as a result of modal analysis

using FRFs measured in the x direction and 9.39 Hz from modal analysis of measured data in the z directions (Figure 4.26).

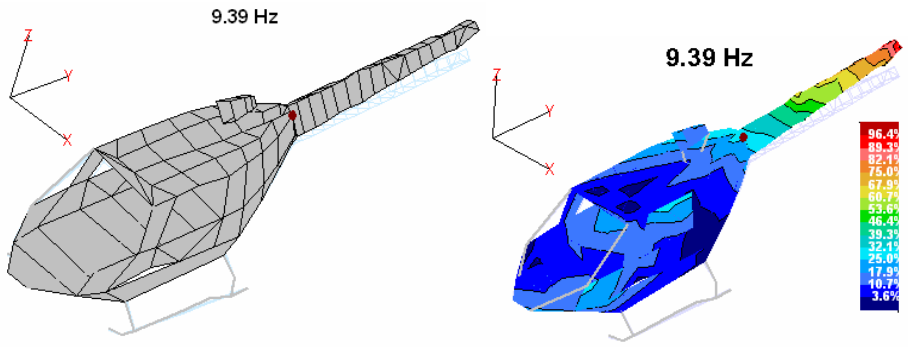

Figure 4.26 : Second Rolling Mode (Using Measurements in the z Direction)

As mentioned before, FRFs are measured on the complete airframe in the x and z directions. On the other hand, some FRFs are measured in the y direction only on the helicopter engine. Examining the FRFs measured in the y direction on the engine itself, it is seen that there are 3 modes in the frequency range between 9 and 10 Hz (see Figure 4.27). Two of these modes are the modes displayed in Figure 4.25 and 4.26. The other mode (at 9.27 Hz) is found to be a forward-backward mode of the fuselage on the skid (see Figure 4.28). Also by examining all the measured FRFs on the complete airframe, it is found that there are some small peaks in the frequency range between 9-10 Hz in addition to peaks at 9.0 Hz and 9.4 Hz.

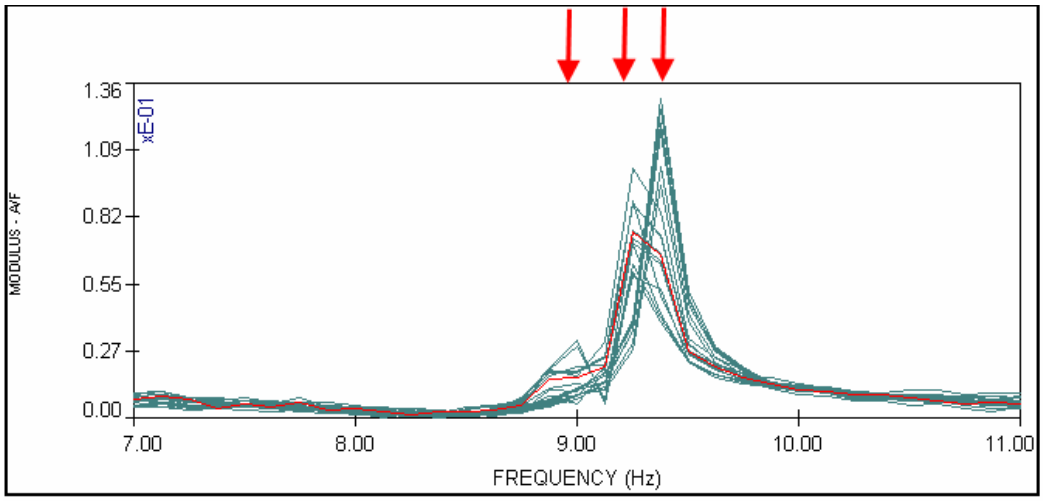

Figure 4.27 : Measured FRFs on the Engine in the y Direction

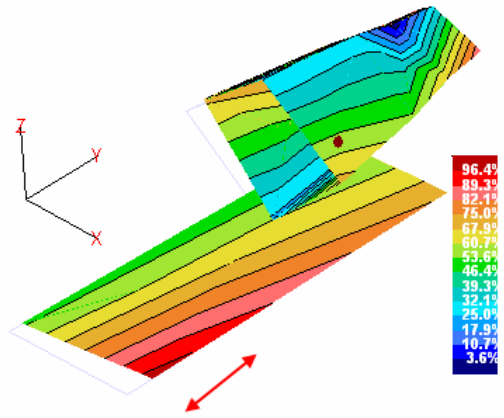

Figure 4.28 : A Forward-Backward Mode (Using the Measurements in the y Direction)

Analysing the FRFs measured on the complete airframe in the z direction, the mode mainly related to the engine is found and it is shown in Figure 4.29a. By also analysing the measured FRFs on the isolated engine in the z direction, the same mode is found nearly at the same frequency as given in Figure 4.29b.

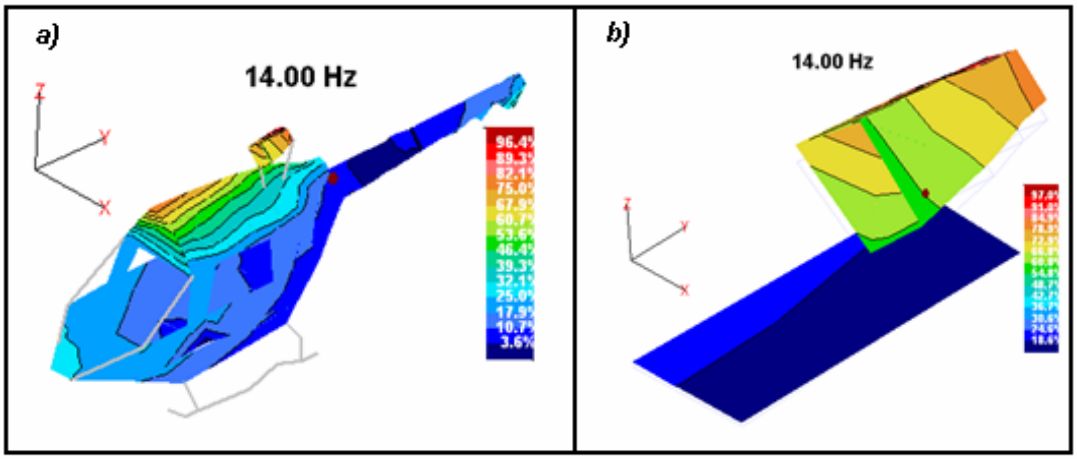

Figure 4.29 : An Engine Dominated Mode (Up-and-Down) in y-z plane: Using the Measurements on the a) Complete Airframe, b) Isolated Engine

Analysing the FRFs measured on the complete airframe in the x direction, another mode mainly related to the engine is found. This mode is displayed in Figure 4.30a. As shown in Figure 4.30b, the same mode is also found by analysing the measured FRFs on the isolated engine in the x direction .

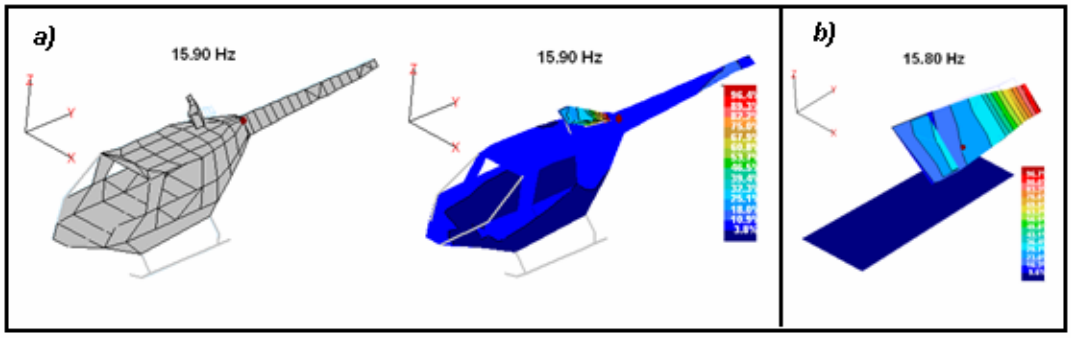

Figure 4.30 : An Engine Dominated Mode (Left-and-Right) in x-y plane: Using the Measurements on the a) Complete Airframe, b) Isolated Engine

Analysing FRFs measured on the complete airframe in the z direction, the mode mainly related to the engine and the tail is found and it is shown in Figure 4.31a. The same mode is found by analysing the measured FRFs on the isolated engine, as given in Figure 4.31b.

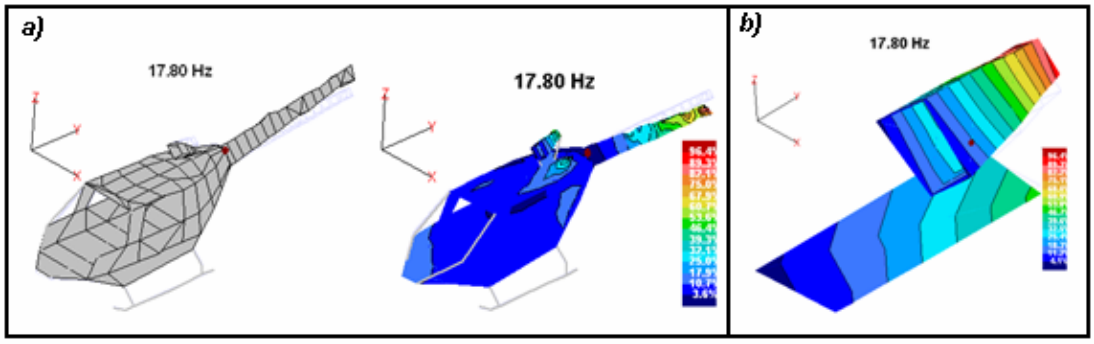

Figure 4.31 : An Engine and Tail Dominated Mode in y-z plane: Using the Measurements on the a) Complete Airframe, b) Isolated Engine

Also, at 24.35 Hz, a global bending mode in y-z plane is identified using the FRFs measured in the z direction (see Figure 4.32).

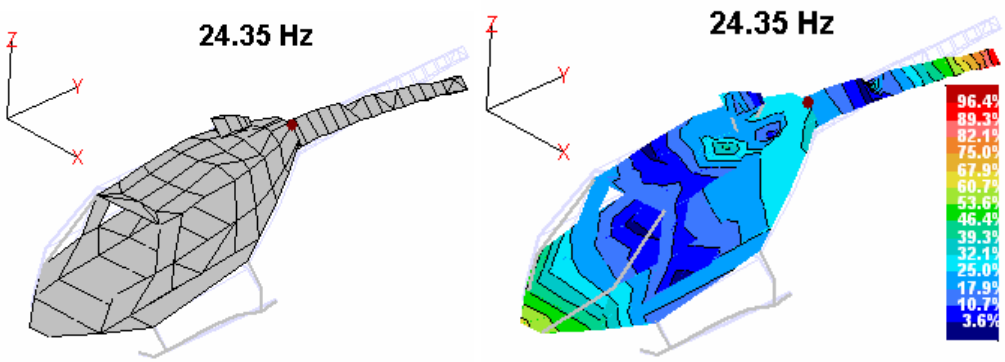

Figure 4.32 : A Global Bending Mode in y-z Plane

Analysing FRFs measured on the complete airframe in the z direction, the two modes mainly related to motion of the nose are found and given in Figure 4.33a and 4.33b

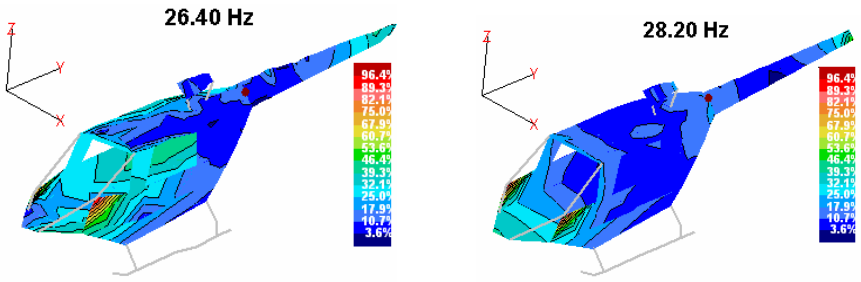

a) b)

Figure 4.33 : Nose Dominated Modes a) in x-y Plane b) in y-z Plane

When analysing the measured FRFs in the x and z direction, an important global mode at 30.33 Hz is identified (see Figure 4.34). This mode is mainly a bending mode.

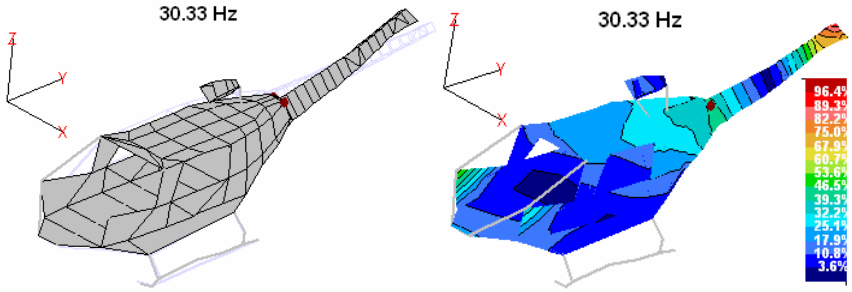

Figure 4.34 : An Important Global Bending Mode of the Helicopter Airframe

Also there are some other modes: at 33.3 Hz (nose dominated), 35.4 Hz (engine, upper deck and nose dominated) 36.3 Hz (skid and fuselage dominated). FRFs measured on the engine also indicated the existence of the mode at 36.3 Hz.

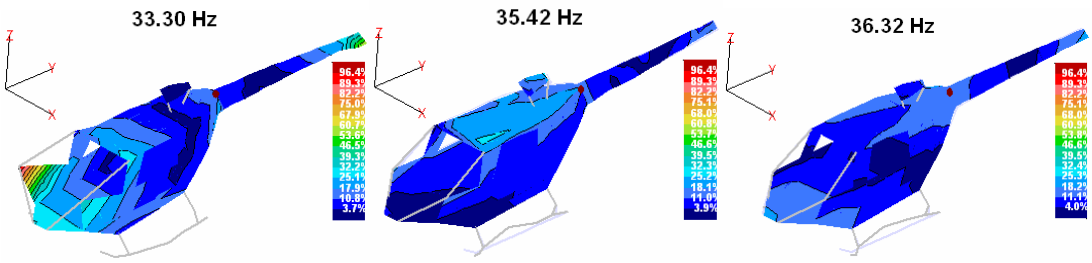

Figure 4.35 : Some other Modes of the Helicopter Airframe

It is also possible to determine the modal parameters of the helicopter airframe at higher frequencies. For example, two local mode shapes of the helicopter obtained using the measured FRFs on the complete airframe in the x and z directions are given in Figure 4.36.

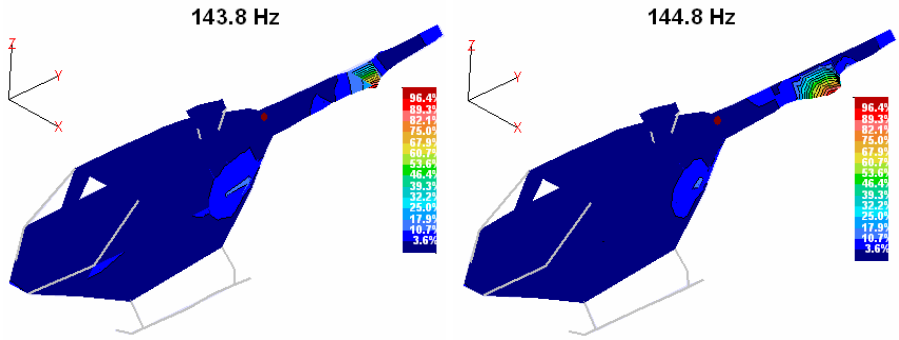

Figure 4.36 : Two Local Modes of the Helicopter Airframe

Also, the damping values of the related modes can be identified by analysing the measured FRFs. In Table 4.1, the damping values of some important modes are listed.

Table 4.1 : Experimentally Obtained Damping Values

Experimental Nat. Freq. [Hz]	Loss Factor [%]
5.48	0.8
5.65	0.9
9.03	0.8
9.34	0.7
14.00	1.3
15.90	1.4
24.35	1.3

4.5 Comparison and Correlation of Theoretical and Experimental Results

4.5.1 Initial FE models

The approach followed during the development of the FE model of the airframe is based on modelling the subcomponents first and then assembling them. Although the division of substructures into finite elements is based on the same common logic, joining the substructures requires engineering judgement. Experimental data provide important guidance for assigning the most appropriate joints between the parts. Before the modal tests were performed on the helicopter airframe, some FE models

of the airframe were developed by assembling the subcomponents. It is worth examining these models in order to highlight some missing features of these models and the associated errors.

The first few natural frequencies and mode shapes obtained from an initial crude FE model of the helicopter airframe are shown in Figure 4.37. It should be noted that this model has vertical and horizontal stabilizers. Also, the engine is not included in this model.

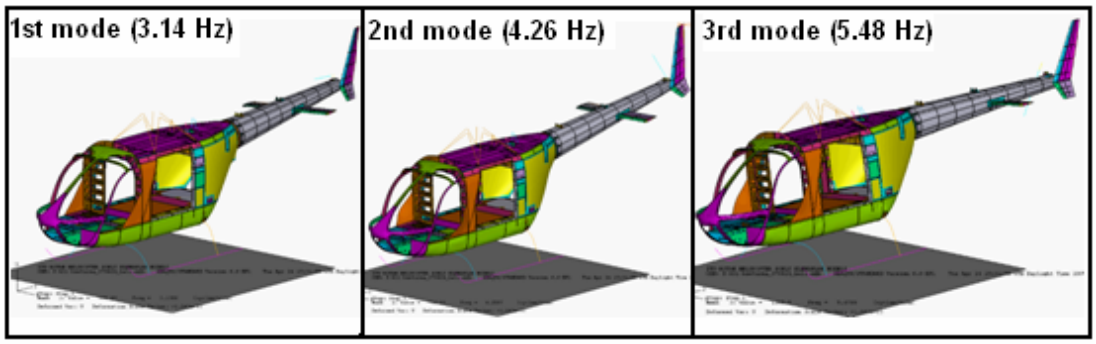

Figure 4.37 : First Three Mode Shapes of the Initial FE Model of the Helicopter Airframe

In this so-called initial FE model of the airframe, the skid is clamped to the ground at the contact regions. This FE model and the physical structure tested are not exactly the same; however, they are somewhat similar and the first global modes of this FE model are expected to yield results closer to the experimental ones. However, in general, the modes shown in Figure 4.37 are tail boom-fuselage connection dominated modes and they are not the same modes obtained from measured data (Figure 4.21, 4.22 and 4.25). It should be noted that the subcomponents are assembled using a very crude approximation and also some incomplete parts not included in this FE model. For example, the tail and the fuselage are joined together using some (not all) of the bolted connections and there are also some missing parts at the back of the fuselage. As a result, this FE model turned out to be more flexible, hence yielding lower natural frequencies than measured values. Consequently, this FE model can be improved by including the missing parts at the back of the fuselage into the model and assembling (joining) the tail to the fuselage by considering all the fasteners at this region. Also, in the FE model above, the engine is not included.

However the structure tested had an engine installed. Therefore, the engine should be included in the improved model.

Results of another FE model of the helicopter airframe, in which the engine is included, are given in Figure 4.38. In this FE model of the airframe the skids are clamped to the ground at the contact regions by constraining all the translations in all directions. The first three vibration modes predicted by this FE model (Figure 4.38) are tail boom-fuselage and engine dominated modes and they are almost completely different modes compared to those obtained experimentally. These results obtained so far suggest that the assembly of the tail and the engine to the fuselage should be improved.

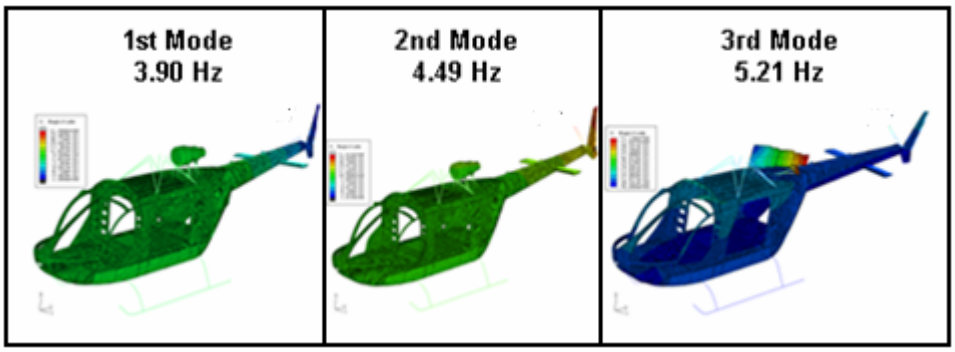

Figure 4.38 : The First Three Mode Shapes of the Initial FE Model of the Helicopter Airframe

4.5.2 Improved FE model

After some analyses using the initial FE models of the helicopter airframe described in the previous section, an improved FE model representing the airframe on which modal tests were performed is built up. This model comprises the fuselage, the tail, the skids and the engine. The tail boom assembled to the fuselage is the validated FE model of the tail boom given in Section 3.4.5. The engine is included in the model by approximating the engine as a discrete rigid part while its connections to the fuselage are modelled using beam elements. However, in the roof and back regions of the fuselage, there were still some incomplete structural parts (parts that are not included in the model).

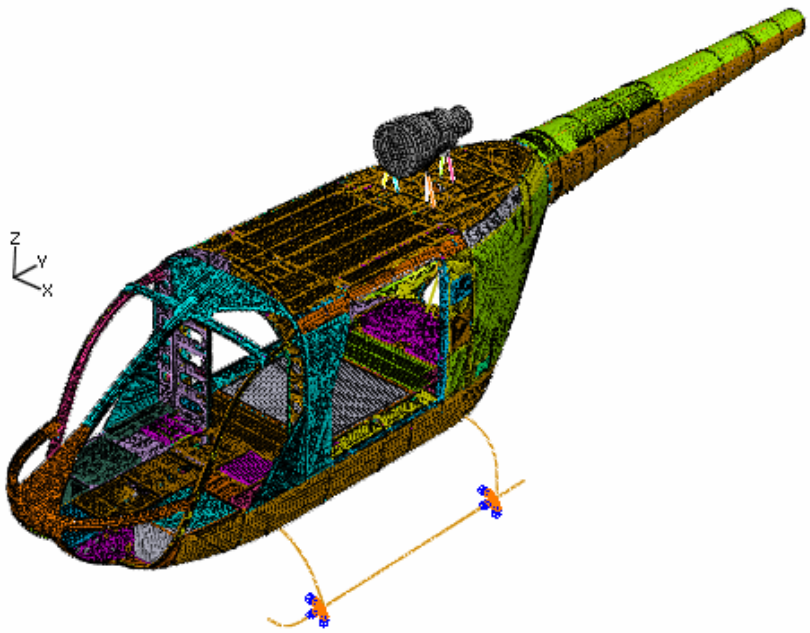

Figure 4.39 : Improved FE model of the Helicopter Airframe

Unlike the initial models in the previous section, this new model contains a validated tail boom. Also, the connections of the tail boom to the fuselage are made properly, and the engine, which was already installed to the airframe when FRFs were measured, is included in the new model (see Figure 4.39). Some properties of this FE model are summarised in Table 4.2.

Table 4.2 : Some Properties of the Improved FE Model of the Airframe

Mass [kg]	***Number of Elements***	***Number of Nodes***	***Number of DOFs***
377.4	446523	525134 + 485911	3114624

As it was mentioned before, the modal tests of the structure were performed when the structure was on its skid on the ground. In this FE model, the structure is clamped at four points of the skids to the ground by constraining translational degrees of freedoms in all directions. Some of the vibration modes predicted using this model are shown in Figure 4.40.

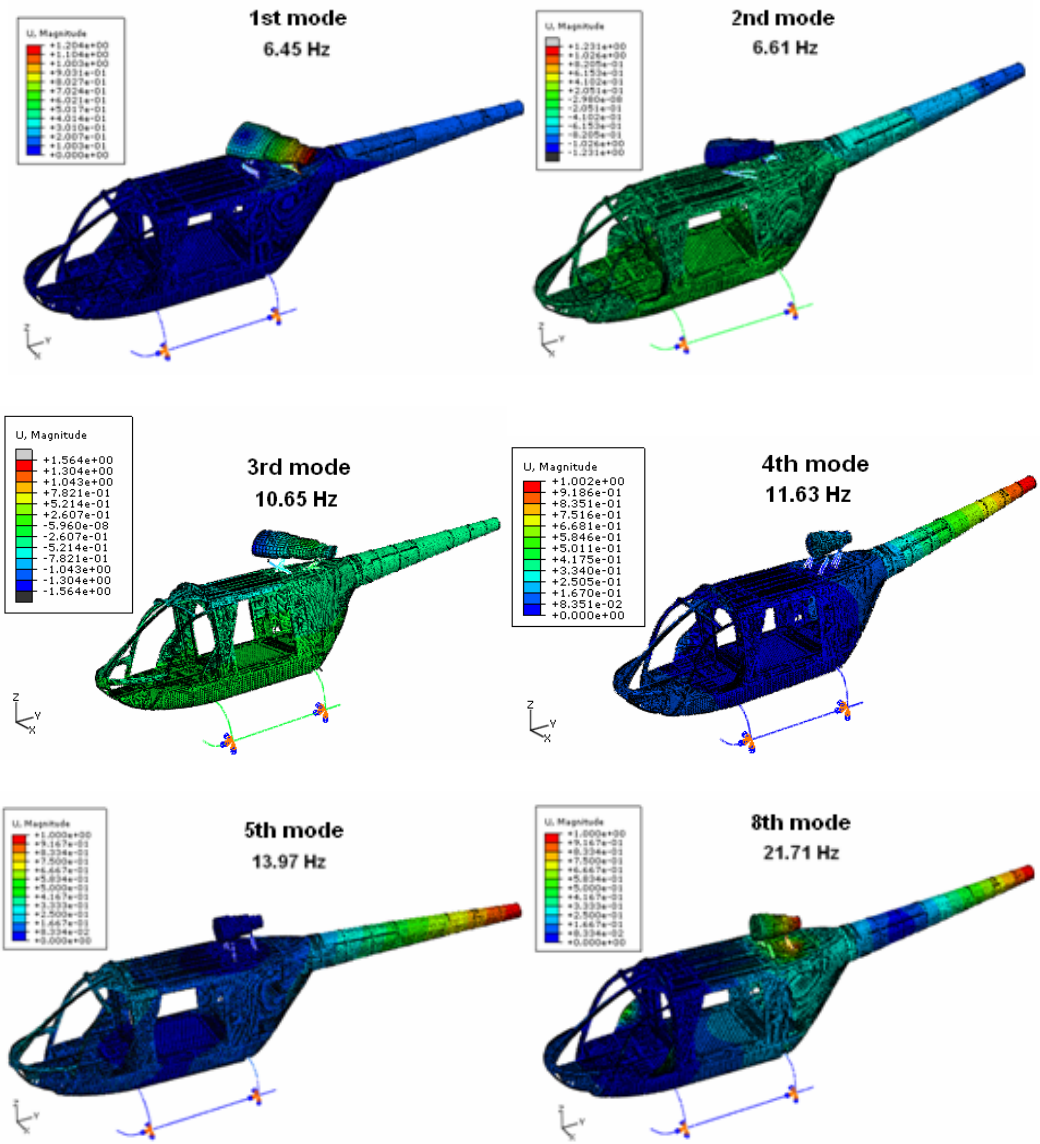

Figure 4.40 : Some Modes of the Improved FE Model of the Helicopter Airframe

As seen in the Figure 4.40, the FE model predicts the first mode at 6.45 Hz, and it is an engine dominated mode although the first mode determined experimentally is a global mode of the airframe at 5.48 Hz. The corresponding engine mode determined experimentally is at 15.90 Hz. This indicates that the engine instalment to the fuselage is yet not appropriate and it should be improved. The second and the third predicted modes are also engine dominated modes. Predicted modal frequencies 11.43 Hz, 13.97 Hz and 21.71 Hz correspond to experimentally determined 5.65 Hz, 5.48 Hz and 24.35 Hz, respectively. It is obvious that differences between the

predicted and measured natural frequencies are too large especially for the first two modes. The modes at 5.65 Hz and 5.48 Hz are mainly related to the skid modelling and the skid connection to the fuselage. However, the mode at 24.35 Hz is an elastic mode of the fuselage in which mainly the motion of the tail is dominated. All these results indicate that the engine and the skid connections to the fuselage should be revised and improved.

4.5.3 Latest FE model

To obtain a representative FE model of the helicopter airframe, the connection of the engine to the fuselage is improved and incomplete parts are included into the FE model as much as possible. Also, many incomplete rivets which were not included in the initial and improved FE model are included in the latest FE model of the helicopter airframe. To improve the connection of the engine to the fuselage, the brackets of the engine are meshed with acceptable mesh size, and its connections to the fuselage are revised. Also, some incomplete parts at the roof are included and meshed with finer mesh sizes.

The mass of this latest FE model is quite close to the mass of the tested structure although there is still a mass difference of about %5. By including the incomplete parts and rivets, and more correct material properties in the future FE models, this difference can be eliminated. Some properties of this model are given in Table 4.3.

Table 4.3 : Some Properties of the Latest FE Model of the Airframe

Mass [kg]	***Number of Elements***	***Number of Nodes***	***Number of DOFs***
391.4	667480	766864 + 720863	4576486

After clamping the structure at four points of the skids to the ground by constraining all the translations in all directions, modal analysis is performed and results are given in Figure 4.41. At first sight, it can be said that this latest FE model gives similar modes to the experimental ones given in Section 4.4.

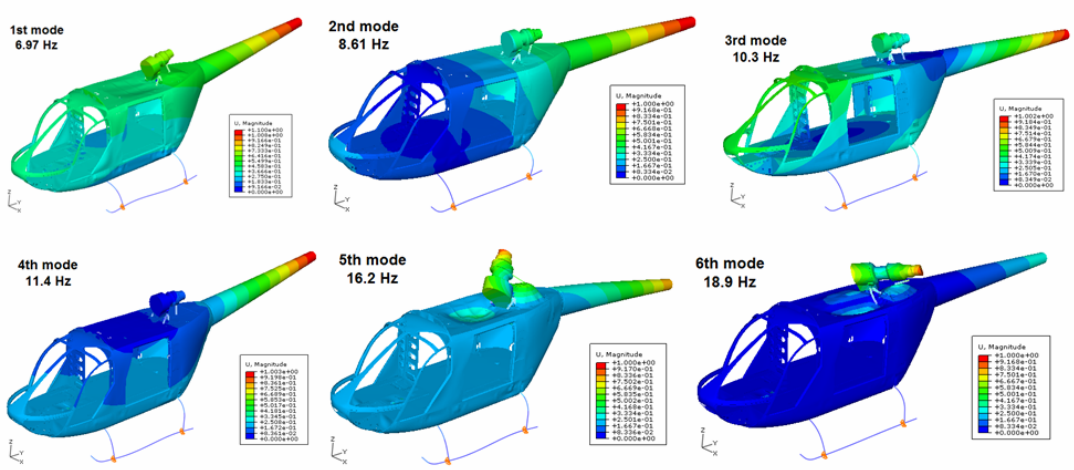

Figure 4.41 : Some Modes of the Latest FE Model of the Helicopter Airframe

The first 6 theoretical modes of this latest FE model are compared in Table 4.4. Although there are still some differences between the theoretical and experimental natural frequencies and some modes are "missing", it can be said that this model is much better than all the previous models. As can be seen from Table 4.4, the first theoretical mode corresponds to the second experimental mode while second theoretical mode corresponds to the first experimental mode. Also, there is no theoretical mode corresponding to the experimental fourth mode.

Table 4.4 : Comparison of the Experimental and Theoretical Results [%]

Exp. Mode No	Exp. Nat. Freq. [Hz]	Theo. Mode No	Theo. Nat. Freq. [Hz]
1	5.48	***2***	8.61
2	5.65	***1***	6.97
3	9.03	***3***	10.3
4	9.27	**-**	-
5	9.39	***4***	11.4
6	14.00	***5***	16.2
7	15.90	***6***	18.9

4.5.4 Determination of the appropriate Boundary Conditions (BCs)

In the analysis performed with the FE model above, the skids were clamped to the ground with idealized Boundary Conditions (BCs). Boundary conditions have huge effect on the theoretical predictions. On the other hand, including the real BCs in the

FE model is not easy. In this section, the effects of the BCs on the results of the FE model are discussed and the best choice of BCs is determined for the helicopter airframe on its skid on the ground. For this purpose, modal analyses are performed using various BCs. Firstly, FE modal analysis is performed assuming that the helicopter airframe is in free-free conditions. However, such BCs resulted in very different results from those of the experiments. Therefore, vertical translations at four points of the skids to the ground are constrained and FE modal analysis is performed (Vertical-Constrained). In the third case, all the translational DOFs are constrained at four points of the skids to the ground (Half-Clamped). In fourth case, all the translational and rotational DOFs are constrained at four points of the skids to the ground (Fully-Clamped). The skids of the helicopter with related DOFs and the four connection points are shown in Figure 4.42. The BCs described and the related free and constrained DOFs are given in Table 4.5. Here (+) and (-) signs mean constrained and free boundary conditions, respectively.

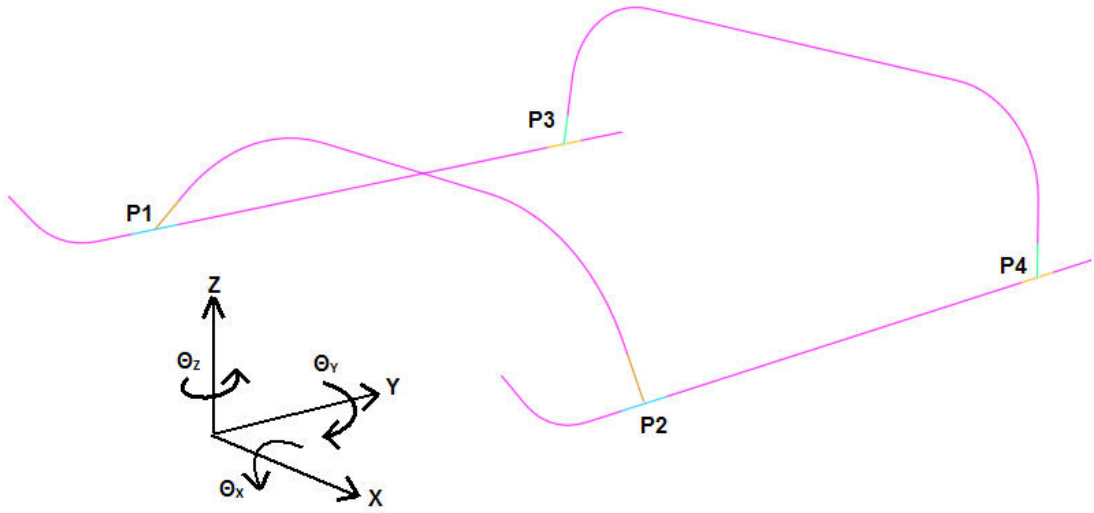

Figure 4.42 : Skid of the Helicopter

Table 4.5 : Boundary Condition Types and Their Settings

	BC Type and Setting			
DOF	**Free-Free**	**Vertical-Constrained**	**Half-Clamped**	**Fully-Clamped**
X	P1 P2 P3 P4 - - - -	P1 P2 P3 P4 - - - -	P1 P2 P3 P4 + + + +	P1 P2 P3 P4 + + + +
Y	P1 P2 P3 P4 - - - -	P1 P2 P3 P4 - - - -	P1 P2 P3 P4 + + + +	P1 P2 P3 P4 + + + +
Z	P1 P2 P3 P4 - - - -	P1 P2 P3 P4 + + + +	P1 P2 P3 P4 + + + +	P1 P2 P3 P4 + + + +
Θ_X	P1 P2 P3 P4 - - - -	P1 P2 P3 P4 - - - -	P1 P2 P3 P4 - - - -	P1 P2 P3 P4 + + + +
Θ_Y	P1 P2 P3 P4 - - - -	P1 P2 P3 P4 - - - -	P1 P2 P3 P4 - - - -	P1 P2 P3 P4 + + + +
Θ_Z	P1 P2 P3 P4 - - - -	P1 P2 P3 P4 - - - -	P1 P2 P3 P4 - - - -	P1 P2 P3 P4 + + + +

Results of the FE model using the BCs summarised in Table 4.5 and comparison of these results with experimental results are given in Table 4.6, 4.7 and 4.8. As expected, in the case of "Free-Free" boundary conditions, theoretical results are very different from experimental results. Therefore, these results are not included here. In the case of "Vertical-Constrained" (see Table 4.6), although some modes could be predicted (1st, 6th, 7th, 8th and 9th modes), some modes have no corresponding theoretical modes (2nd, 3rd, 4th, and 5th modes).

Table 4.6 : Comparison of the Experimental and Theoretical Results (Vertical-Constrained)

Exp. Mode No	**Exp. Nat. Freq. [Hz]**	**Theo. Mode No**	**Theo. Nat. Freq. [Hz]**
1	5.48	***4***	2.82
2	5.65	**-**	**-**
3	9.03	**-**	**-**
4	9.27	**-**	**-**
5	9.39	**-**	**-**
6	14.00	***7***	15.67
7	15.90	***8***	18.72
8	17.80	***9***	23.07
9	24.35	***10***	25.95

In the case of "Half-Clamped" (see Table 4.7), more modes are correlated (1st, 2nd, 3rd, 5th, 6th and 7th modes), although some modes still do not have corresponding theoretical modes (4th, 8th, and 9th modes).

Table 4.7 : Comparison of the Experimental and Theoretical Results (Half-Clamped)

Exp. Mode No	Exp. Nat. Freq. [Hz]	Theo. Mode No	Theo. Nat. Freq. [Hz]
1	5.48	***2***	8.61
2	5.65	***1***	6.98
3	9.03	***3***	10.30
4	9.27	***-***	-
5	9.39	***4***	11.39
6	14.00	***5***	16.22
7	15.90	***6***	18.93
8	17.80	***-***	-
9	24.35	***-***	-

In the case of "Fully-Clamped" (see Table 4.8), a few number of modes (1st, 2nd, 5th and 7th) are correlated. Furthermore, the natural frequency differences between theoretical and experimental values are very large.

Table 4.8 : Comparison of the Experimental and Theoretical Results (Fully-Clamped)

Exp. Mode No	Exp. Nat. Freq.[Hz]	Theo. Mode No	Theo. Nat. Freq.[Hz]
1	5.48	***4***	15.19
2	5.65	***1***	7.99
3	9.03	***-***	-
4	9.27	***-***	-
5	9.39	***-***	-
6	14.00	***5***	17.10
7	15.90	***6***	19.60
8	17.80	***-***	-
9	24.35	***-***	-

In all the cases presented above, the results of the "Vertical-Constrained" and "Fully-Clamped" are very different than the experimental results while "Half-Clamped" case is providing better results. Utilizing the experimental data, inspection of the results obtained under various BCs summarised above and using engineering observations/judgements, some optimum BCs listed in Table 4.9 are selected. In this

case, it is aimed that the minimum level of BCs compatible with engineering observations should be imposed. For example, as the helicopter is standing on its skids on the ground, translational motion of the skid in vertical direction is constrained at all four nodes. This means that airframe will always touch the ground. Similarly, it is necessary to avoid rigid body rotations of the helicopter and this requires imposing further boundary conditions. These considerations led to imposing boundary conditions summarised in Table 4.9.

Table 4.9 : 'Optimum' Boundary Conditions

DOF	***Skid Points Free/Constrained***			
X	P1	P2	P3	P4
	+	-	+	-
Y	P1	P2	P3	P4
	+	+	-	-
Z	P1	P2	P3	P4
	+	+	+	+
Θ_X	P1	P2	P3	P4
	+	+	+	+
Θ_Y	P1	P2	P3	P4
	-	-	-	+
Θ_Z	P1	P2	P3	P4
	-	-	-	+

Modes of the FE model with the BCs listed in Table 4.9 are given in Figure 4.43. It is immediately seen that nearly all the predicted modes within the given frequency range correlate with the modes found experimentally in Section 4.4.

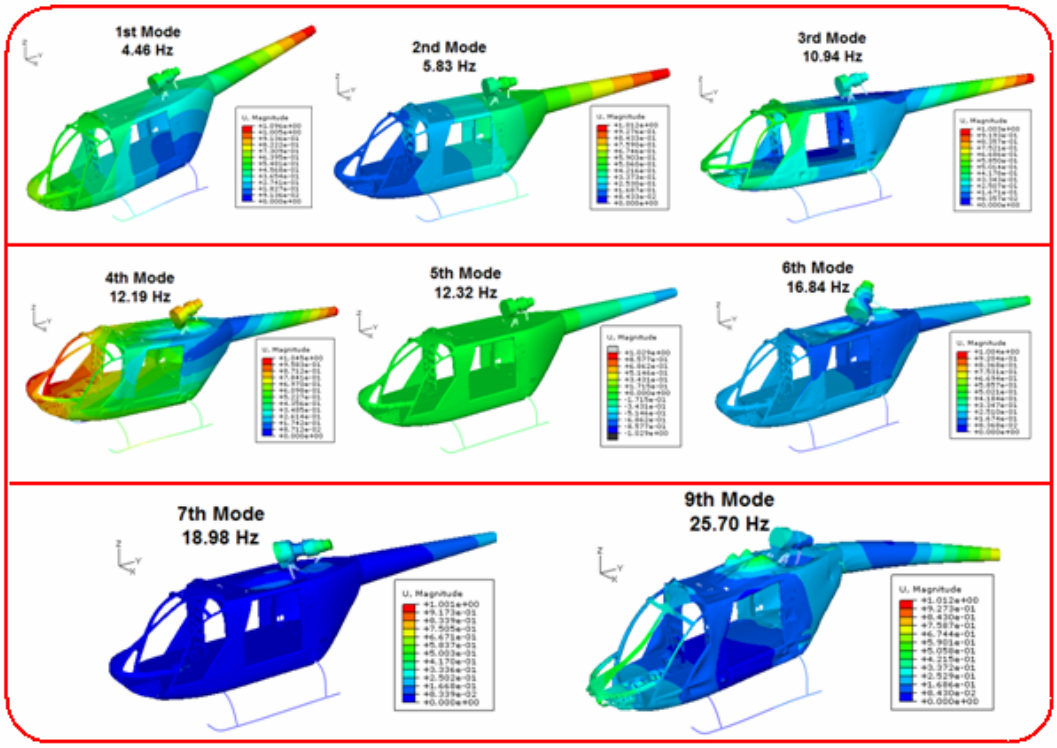

Figure 4.43 : Some Modes of the Latest FE Model of the Helicopter Airframe with Optimum BCs

Results of this latest FE model with appropriate BCs and their correlation with experimental results are summarised in Table 4.10. Comparing to the initial FE models, it is obvious that this latest FE model with appropriate BCs is providing much better results. Within the given frequency range nearly all the modes are correlated with experimental modes although there are some differences in natural frequencies. Only the theoretical 8^{th} mode seems to be different from the experimental 8^{th} mode. It is also noted that the correlation of the modes is not sequential, e.g., 1^{st} theoretical mode is correlated with the 2^{nd} experimental mode and vice versa. Similar observation is made about the 4^{th} and 5^{th} experimental modes. It is worth however that the natural frequencies of these modes are quite close to each other.

It is believed that those discrepancies are due to boundary conditions being approximate, there being still incomplete (missing) parts in the model and also some rivets not being included in the FE model.

Table 4.10 : Comparison of Experimental and Theoretical Results (Optimum BCs)

Exp. Mode No	Exp. Nat. Freq.[Hz]	Theo. Mode No	Theo. Nat. Freq.[Hz]
1	5.48	***2***	5.83
2	5.65	***1***	4.46
3	9.03	***3***	10.94
4	9.27	***5***	12.32
5	9.39	***4***	12.19
6	14.00	***6***	16.84
7	15.90	***7***	18.98
8	17.80	***8***	….*19.64*…..
9	24.35	***9***	25.70

As expected, local modes are not affected by the global BCs. For example, experimentally determined local modes at 143.8 Hz and 144.8 Hz are compared with the results of FE model of the tail cone given in Section 3.4. Corresponding natural frequencies obtained from the FE model of the tail cone are 144.5 and 146.5 Hz, respectively (see Figure 4.44). As seen, nearly the same natural frequencies and mode shapes are obtained.

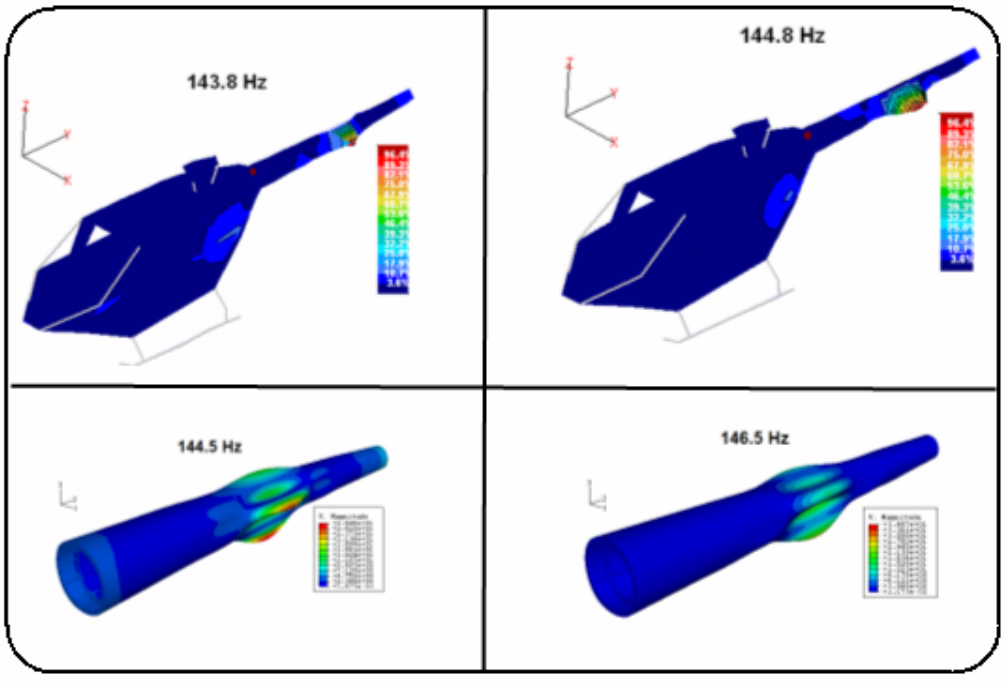

Figure 4.44 : Comparison of Some Experimentally Found Local Modes of the Helicopter Airframe with the FE Results of the Helicopter Tail Cone

4.5.5 Concluding Remarks

In this chapter experimental and theoretical modal analyses of a helicopter airframe were performed. Following some preliminary tests, FRFs are measured on the complete airframe and the engine installed on the airframe. By analysing these measured FRFs, mode shapes, natural frequencies and damping values were determined. Also, starting from initial crude FE models, some FE models of the helicopter airframe were developed. It is seen that imposing appropriate BCs is very important. Utilizing experimental data, methodology of building up FE models of the airframe step by step (so that missing features could be identified) and engineering judgment, a representative FE model of the airframe was developed. In the latest FE mode, appropriate BCs were obtained.

Examining the modal analyses results of the FE model with given BCs in Section 4.5.4, fuselage-ground based modes are affected strongly with respect to BCs as expected. However, engine dominated modes (5^{th} and 6^{th} modes) are not changing as much as the fuselage-ground based modes when BCs are changed. This shows that the error between the theoretical and the experimental results are probably due to imposed BCs as real BCs could not be modelled exactly. Also, it is seen that including further details of the helicopter parts, FE model of the airframe can be improved more and more.

Experimentally obtained modal parameters were used for comparison, correlation and improving theoretical models of the helicopter airframe. Also, as the FRFs were measured on a helicopter airframe, the modal data can be used judging the suitability of the modal behaviour of the helicopter airframe. For example, the frequencies of the first rolling and rocking modes are at 5.48 Hz and 5.65 Hz, respectively while the rotational speed of the main blades of the ITU-LCH is at 318 rpm (5.3 Hz) which is the main excitation source on the airframe.

Although these natural frequencies will change as the other components of the helicopter are installed to the airframe, it is important to control the frequencies (and damping) of the first rolling and rocking modes in order to avoid ground resonance.

5. CONCLUDING REMARKS AND SUGGESTIONS FOR FUTURE WORK

It is found that the numerical models for structures assembled using many riveted joints may contain very significant amount of errors. Therefore, one of the objectives of this thesis was to determine whether an acceptable linear Finite Element (FE) model could be built by adjusting the FE models using the measured modal properties of structures with riveted joints. It has been found that this can be achieved if the objective is to predict the natural frequencies and mode shapes with a few percent errors for the lower modes. It has also been found that adjusting the so-called Effective Clamping Diameter (ECD) of the rivet model can be an effective way of tuning the FE model. In the test cases presented in this thesis, the optimum value of ECD appears to be very comparable with the cross sectional and head diameter of the rivets. However, this may depend on the types of rivets and the methods of construction.

Following the validation of the theoretical (FE) models of some relatively simpler riveted structures, detailed modal test are performed on a tail boom section and some FE models of the tail boom section are developed. At the end, validated FE model for riveted joints is successfully applied to this quite complex helicopter structure. On the other hand, it is worth stating that incorporating the damping mechanism in riveted joints in theoretical models of structures with huge number of rivets is still a challenging problem.

The helicopter tail boom is one of the most important components of airframe structures. As the helicopter tail boom has similar components with all other helicopter structures and it is quite complex, obtaining a validated FE model of this structure is important. For this, very detailed and sophisticated tests are performed on a helicopter tail boom. Firstly, a preliminary set of FRFs is obtained so as to plan the final FRF measurements. Some relatively simple but functional FE models of the tail boom are developed. Using the preliminary test results and the first FE models, sophisticated modal tests are planned for the tail boom. Although the first FE models

of the structure can only represent the lower modes of the structure with a few percent accuracy, using validated FE approach for riveted structures, an improved FE model of tail boom containing thousands of rivets is developed. Comparison and correlation studies are performed in terms of both natural frequencies and mode shapes.

Helicopter airframes are quite complex structures and determination of their dynamic behaviours is not easy. In this thesis, modal tests are performed on a real helicopter prototype structure in order to determine the dynamic behaviour. Using the measured data, fundamental modes of the airframe are determined experimentally. Utilizing the experimental data and the experience gained from previous studies, various FE models of the helicopter airframe are developed. This helicopter structure consists of a fuselage, tail boom, skid, nose and an engine mounted.

Firstly, an initial FE model of the helicopter airframe is developed. In this model, only the most significant components of the helicopter airframe are modelled. However, connections/joints of the structural parts are not considered in detail. Also, the engine is not included in this initial FE model. Comparing the results of the initial FE model with experimental results; it is found that the first FE model developed for the helicopter airframe should be revised. It is found that there are problems even in assembling the main structural parts such as joining the skid and tail to the fuselage. In improved FE model of the helicopter airframe, the engine is also included in the FE model using some simple models for engine installation to the airframe. Although this model is better than the initial models, this model is improved further by joining the structural parts to the fuselage with improved joint constraints. To obtain further improvement of the FE model of the helicopter airframe, the connection of the engine to the fuselage is refined and incomplete parts and rivets are also included in the FE model of the airframe.

As mentioned before vibration tests were performed on the helicopter airframe when the helicopter was on its skids on the ground. Obviously, modelling the real BCs is not easy and it has been observed that BCs have very significant effects on the FE results. At the end of the modelling process, some optimum BCs were determined for the helicopter airframe on which the FRFs were measured. As a result, a representative FE model of the helicopter airframe with approximate BCs was

obtained. Although there are some differences between the experimental and theoretical results they are believed to be mainly due to BCs. In future works, it is suggested to model the contact condition of the skid of the helicopter and ground with some springs whose coefficients obtained anyway. Also, including further details of some airframe parts in the FE model, more realistic FE model of the helicopter airframe can be obtained.

One of the most important outcomes of this thesis was the determination of properties of the lower modes of the real helicopter airframe. It is well known that these modes are critical from ground resonance point of view. Utilizing obtained experimental data and developed theoretical (FE) models of the helicopter airframe, the designs of some helicopter structures can be redesigned or optimized, such as optimising the connection of the skid to the fuselage so as to avoid resonance and provide the required damping. Also, obtained theoretical models of the helicopter airframe can be used for certification purposes.

As mentioned before, there are some incomplete parts and rivets which were not included even in the latest FE model. These parts should be modelled and included in the future FE models of the helicopter airframe. It has been found that proper modelling of rivets in riveted structures is essential. Rivet modelling parameters should be revised and proper values of effective clamping diameter with appropriate weighting should be used. Material properties of all the parts, especially those of honeycomb and epoxy should be controlled in the future FE models. Also, the connections of the skid and engine to the fuselage can be improved further by utilizing experimental data.

REFERENCES

[1] **Fabunmi, J. A.**, 1986. Developments in Helicopter Ground Vibration Testing, *the Fourth International Modal Analysis Conference*, Los Angeles, California, USA, February 1986.

[2] **Crawford, A.R. and Crawford, S.**, 1992. The Simplified Handbook of Vibration Analysis, Volume 1: Introduction to Vibration Analysis Fundamental, Computational Systems, Inc., USA.

[3] **Johnson, W.**, 1994. Helicopter Theory, Dover Publications, Inc., New York, USA.

[4] **Bayar, F. M.**, 2007. Design and Analysis of Fixturing in Assembly of Sheet Metal Components of Helicopters, *M.Sc.Thesis*, Middle East Technical University, Ankara, Turkey.

[5] **Leishman, J. G.**, 2006. Principles of Helicopter Aerodynamics, Second Edition, Cambridge University Press, New York, USA.

[6] **Mühendis ve Makina**, 2002. Helikopterler, TMMOB, Makina Mühendisleri Odası, Şubat, Sayı **505,** Ankara, Türkiye.

[7] **Prouty, R. W**., 1998. Military Helicopter Design Technology, Krieger Publishing Company, Malabar, Florida, USA.

[8] **Bielawa, R. L.**, 2006. Rotary Wing Structural Dynamics and Aeroelasticity, Second Edition, American Institute of Aeronautics and Astronautics Inc., Reston, Virginia.

[9] **Coyle, S.**, 1996. The Art and Science of Flying Helicopters, Arnold, London, Great Britain.

[10] **Cooke, A. K., and Fitzpatrick, E.W.H**, 2002. Institute of Aeronautics and Astronautics Inc., Reston, Virginia, USA.

[11] **Khalid, A. S.**, 2006. Development and Implementation of Rotorcraft Preliminary Design Methodologies Using Multidisciplinary Design Optimization, M. *Sc. Thesis*, Georgia Institute of Technology, USA.

[12] **Hanson, T. F.**, 1998. A Designer Friendly Handbook of Helicopter Rotor Hub.

[13] **Gabel, R., Reed, D., Ricks, R. and Kesack, W.**, 1984. Planning, Creating and Documenting a NASTRAN Finite Element Model of a Modern Helicopter, *Second Decennial Specialist's Meeting on Rotorcraft Dynamics*, AHS/NASA Ames, Moffett Field, California, USA, November 8 1984.

[14] **Howland, G. R., Durno, J. A. and Twomey, W. J.**, 1990. Ground Shake Test of the UH-60A Helicopter Airframe and Comparison with Nastran Finite Element Model Predictions, *NASA Contractor Report,* **181993**, NASA, Langley Research Center, Hampton, Virginia.

[15] **Idosor, F. and Seible, F.**, 1990. Comparison of NASTRAN Analysis with Ground Vibration Results of UH-60A NASA/AEFA Test Configuration, *Final Contractor Report for NASA ARC Contract NCC2-598*, **SSRP-90/3**, University of California, San Diego, California, USA.

[16] **Idosor, F.R. and Seible, F**., 1993. NASTRAN Modelling of flight test components for UH-60A Airloads Program Test Configuration, *Final Report*, NASA Research Grant Number NCC2-712, **SSRP-93/03** University of California, San Diego, California, USA.

[17] **Dompka, R.V.**, 1988. Investigation of Difficult-Component Effects on Finite-Element-Model Vibration Prediction for the AH-1G Helicopter, *44th Annual Forum and Technology Display of the American Society*, Washington, D.C., June 16-18.

[18] **Bisagni, C.**, 2002. Crashworthiness of helicopter subfloor structures, *International of Journal of Impact Engineering*, **27**, 1067-1082.

[19] **Langrand, B., Patronelli, L., Markiewicz, E. and Drazetic, P.**, 2002. An alternative numerical approach for full scale characterization for riveted joint design, *Aerospace Science and Technology*, **6**,343-354.

[20] **Langrand, E., Deletombe, E., Markiewicz, E. and Drazetic, P.**, 2001. Riveted joint modeling for numerical analysis of airframe crashworthiness, *Finite Element Analysis and Design*, **38**, 21-44.

[21] **Simmons, M. C. and Schleyer, G. K.**, 2006. Pulse pressure loading of aircraft structural panels, Thin-Walled Structures, **44**, 496-506.

[22] **Karaoğlu, Ç. and Kuralay, N. S.**, 2002. Stress analysis of a truck chassis with riveted joints, *Finite Element in Analysis and Design*, **38**, 1115-1130.

[23] **Urban, M.R.**, 2003. Analysis of the fatigue life of riveted sheet metal helicopter airframe joints, *International Journal of Fatigue*, **25**, 1013-1026.

[24] **Huang, J. W. and Sin, H. F.**, 2001. Aluminum Rail Rivet and Steel Rail Weld DOE and CAE Studies for NVH, **2001-01-1608**, Society of Automotive Engineers, Inc.

[25] **Jalali, H., Ahmadian, H. and Mottershead J.E.,** 2007. Identification of nonlinear bolted lap-joint parameters by force-state mapping, *International Journal of Solids and Structures*, **44**, 1181-1191.

[26] **Al-Emrani, M. and Kliger, R.**, 2003. FE analysis of stringer-to-floor-beam connections in riveted railway bridges, *Journal of Construction Steel Research*, **59**, 803-818.

[27] **Yun, S.H. and Bauchau, O.A.**, 1998. Improving Modal Parameters Predictions for Jointed Airframe Panels, Part I: Experiments, *Journal of the American Helicopter Society*, **43**, 156-163.

[28] **Yun, S.H. and Bauchau, O.A.**, 1998. Improving Modal Parameters Predictions for Jointed Airframe Panels, Part II: Improved Numerical Model, *Journal of the American Helicopter Society*, **43**, 164-171.

[29] **Buehrle, R.D., Fleming, G.A., Pappa, R.S. and Grosveld, F.W.**, 2000. Finite Element Model Development and Validation for Aircraft Fuselage Structures, *18th International Modal Analysis Conference*, San Antonio, Texas, February 7-10.

[30] **Ewins, D.J.**, 2000. Modal Testing: Theory, Practice and Applications. Second Edition, Research Studies Press, London, England.

[31] **Inman, D. J**., 2001. Engineering Vibration, Prentice Hall International, Inc., USA.

[32] **Pickrel, C. R.**, 1999, A Practical Approach to Modal Pretest Design, *Mechanical Systems and Signal Processing*, **13(2)**, 271-295.

[33] **Pavic, A. and Reynolds, P.**, 2003. Modal testing and dynamic FE model correlation and updating of a prototype high-strength concrete floor, *Cement & Concrete Composites*, **25,** 787-799.

[34] **Giansante, N. and Flannelly, W.G.**, 1974. Identification of Structural Parameters from Helicopter Dynamic Test Data, *ASH National Specialist's Meeting on Rotorcraft Dynamics*, February 13-15, 1974.

[35] **Kenigsberg, I. J., Dean, M. W. and Malatino, R.**, 1974. Correlation of Finite-Element Structural Dynamic Analysis with Measured Free Vibration Characteristics for a Full-Scale Helicopter Fuselage, *AHS/NASA-Ames Specialist's Meeting on Rotorcraft Dynamics*, February 13-15, 1974.

[36] **Reed, D.A. and Gabel, R.**, 1989. Ground Shake Test of the Boeing Model 360 Helicopter Airframe, *NASA Contract NASA Contractor Report,* **181766**, NASA Langley Research Center, Hampton, Virginia.

[37] **Mielczarek, A., Fischer, H. and Riehemann W.**, 2006. Amplitude-dependent damping of PSZ with sinter defects, *Materials Science and Engineering*, **442**, 488–491.

[38] **Li, Q.S., Liu, D.K., Fang, J.Q., Jeary, A.P. and Wong, C.K.**, 2000. Damping in buildings: its neural network model and AR model, *Engineering Structures*, **22**, 1216–1223.

[39] **Lamarque, C.H. Pernot, S. and Cuer, A.**, 2000. Damping Identification in Multi-Degree-of-Freedom Systems via a Wavelet-Logarithmic Decrement-Part 1: Theory, *Journal of Sound and Vibration*, **235(3)**, 375-403(29).

[40] **Huang, F. L., Wang, X. M., Chen, Z. Q., He, X. H. and Ni, Y. Q.**, 2007. A new approach to identification of structural damping ratios, *Journal of Sound and Vibration*, **303**,144-153.

[41] **Beards, C.E.**, 1996. Structural Vibration: Analysis and Damping, John Wiley&Sons Inc., New York, USA.

[42] **Rodriguez, M.M.**, 2006, Analysis of Structural Damping, *M.Sc. Thesis*, Lulea University of Technology, Sweden.

[43] **Imamovic, N.**, 1998. Validation of Large Structural Dynamics Models Using Modal Test Data, *PhD Thesis*, Imperial College of Science, Technology & Medicine, London, U.K.

[44] **Fotsch, D.W.**, 2001. Development of Valid FE Models for Structural Dynamic Design, *PhD Thesis*, Imperial College of Science, Technology & Medicine, London, U.K.

[45] **Visser, W.J.**, 1992. Updating Structural Dynamics Models Using Frequency Response Data, *PhD Thesis*, Imperial College of Science, Technology&Medicine, London, U.K.

[46] **Jung, H.**, 1992. Structural Dynamic Model Updating Using Eigensensitivity Analysis, P*hD Thesis*, Imperial College of Science, Technology & Medicine, London, U.K.

[47] **Zivanovic, S., Pavic, A. and Reynolds, P.**, 2006. Modal testing and FE model tuning of a lively footbridge structure, *Engineering Structures,***28**, 857–868.

[48] **Kaewunruen, S. and Remennikov, A. M.**, 2007, Field trials for dynamic characteristics of railway track and its components using impact excitation technique, *NDT&E International*, **40**, 510–519.

[49] **Göge, D.**, 2003. Automatic updating of large aircraft models using experimental data from ground vibration testing, *Aerospace Science and Technology*, **7**, 33-45.

[50] **Zivanovic, S., Pavic, A., and Reynolds, P.**, 2006. Finite element modelling and updating of a lively footbridge: The complete process, *Journal of Sound and Vibration*, **301**, 126-145.

[51] **Kozak, M.T., Cömert, M.D. and Özgüven, H. N.**, 2007. Titreşim Analizinde Kullanılan Sonlu Eleman Modeli Güncelleme Yöntemlerinin İncelenmesi ve Gerçek Yapılara Uygulanması, *13. Ulusal Makine Teorisi Sempozyumu*, Cumhuriyet Üniversitesi, Sivas, 07 -09 Haziran, s.83 – 90.

[52] **Twomey, W.J, Chen, T.L.C., Ojalvo, I.U. and Ting, T.**, 1989. A General Method for Modifying a Finite-Element Model to Correlate with Modal Test Data, *ASH National Specialist's Meeting on Rotorcraft Dynamics*, Texas, November.

[53] **Gürgöze, M.**, 1984. Analitik Metotlarla Titreşimlerin Etüdü, İTÜ, Elektrik – Elektronik Fakültesi, Ofset Baskı Atölyesİ, İstanbul.

[54] **Meirovitch, L.**, 1967. Methods of Analytical Dynamics, McGraw-Hill, New York.

[55] **Şanlıtürk, K.Y.**, 2008. Finite Element Method, Lecture Notes, Istanbul, Turkey.

[56] **Chandrupatla, T. R. and Belegundu, A. D.**, 2001, Introduction to Finite Elements in Engineering, Third Edition, Prentice Hall, New Jersey.

[57] **Mecitoğlu, Z.**, 2005. Finite Element Analysis in Structures, Lecture Notes, Istanbul.

[58] **Pasin, F.**, 1994. Mekanik Sistemler Dinamiği, İTÜ Rektörlüğü Yayını, İstanbul.

[59] **Cüzdan, H.**, 2005, Sönüm Kabiliyetine Sahip Sonlu Eleman Geliştirilmesi, *Yüksek Lisans Tezi*, İTÜ Fen Bilimleri Enstitüsü, Istanbul.

[60] **Kardestuncer, H., Norrie, D. H. and at. all,** 1987. Finite Element Handbook, McGraww-Hill Book Company, USA.

[61] Abaqus Theory Manual, 2007. Version 6.6.1.

[62] Abaqus Getting Started, 2007. Version 6.6.1.

[63] **Beachley, N. H. and Harrison, H.L.**, 1978. Introduction to Dynamic System Analysis, Harper & Row, Publishers, Inc., New York.

[64] **De Silva, C.W.**, 2006. Use of frequency-domain concepts in the analysis and design of mechnical vibrating systems, ijmee, *International Journal of Mechanical Engineering Education*, **34 (3),** 233-255.

[65] **Ewins, D.**, 2007. Modal Analysis and Noise: Some History, Developments and Applications, *INTER-NOISE 2007*, 28-31 August, Istanbul, Turkey.

[66] **Gürbüzer, G.**, 2005. Sayısal Titreşim Modellerinin Deneysel Verilerle Güncellenmesi, *Yüksek Lisans Tezi*, İTÜ Fen Bilimleri Enstitüsü, Istanbul.

[67] **Heylen, W. and Avitabile, P.**, 1998. Correlation Consideration – Part 5 (Degree of Freedom Correlation Techniques), *Proceedings of the 16th IMAC*, 207-214.

[68] **Avitabile, P. and Pechinsky, F.**, 1994. Coordinate Orthogonality Check (CORTHOG), *Proceedings of the 12th IMAC*, 753-760.

[69] **O'Callahan, J.**, 1998. Correlation Considerations – Part 4 (Modal Vector Correlation Techniques), *Proceedings of the 16th IMAC*, 197-206.

[70] Analysis User's Manual, 2006. Version 6.6.1.

[71] ICATS : Imperail Collage Testing Analysis and Software, Imperial Collage, 2006, London.

[72] MIL-HDBK-5H, 1998. Military Handbook: Metallic Materials and Element for Aerospace Vehicle Structures.

[73] **Çakar, O. and Sanliturk, K.Y.**, 2002, Elimination of Noise and Transducer Effects from Measured Response Data, *Prococeedings of the 6th Biennial Conference on Engineering Systems Design and Analysis*, Istanbul, Turkey, 8-11 July.

[74] Bruel&Kjaer Pulse 7.0 User Guide, 2006.

[75] Fines User Guide, 2006.

[76] **Sanliturk K. Y. and Ewins D. J.**, 1996. Modelling Two-Dimensional Friction Contact and ItsApplication Using Harmonic Balance Method, *Journal of Sound and Vibration*, **193(2)**, 511-523.

[77] **Sanliturk K. Y., Stanbridge A. B. and Ewins D. J.**, 1996. Frictiondamper Optimisation for Turbine Blades: Experiments and Theoretical Predictions, Proceedings of 6th Int. Conference on Vibrations in Rotating Machinery, Oxford, 9-12 September.

[78] **Stanbridge A. B., Sanliturk K. Y. and Ewins D. J.**, 1999,. Measurement and Analysis of High-Temperature FrictionDamper Properties, *the 4th National Turbine Engine High Cycle Fatique (HCF) Conference*, Naval Postgraduate School, Monterey, California, USA, 9-11 February.

[79] Handbook on Guidelines to Best Practice: Modal Testing, 1999. The Dynamic Testing Agency.

CIRRUCULUM VITAE

Hasan KÖRÜK was born in Afşin, K.Maraş in 1981. He graduated from Istanbul Technical University (ITU), Mechanical Engineering Faculty with Bachelor of Science, Mechanical Engineer in 2005. Same year, he started his Master of Science education at ITU, Machine Dynamics, Vibration & Acoustics program. He is working as a research assistant in Division of Machine Theory, System Dynamics and Control in ITU.